



Geoscience BC

SUMMARY OF ACTIVITIES **2018:**
Minerals and Mining

**GEOSCIENCE BC
SUMMARY OF ACTIVITIES 2018:
MINERALS AND MINING**

© 2019 by Geoscience BC.

All rights reserved. Electronic edition published 2019.

This publication is also available, free of charge, as colour digital files in Adobe Acrobat® PDF format from the Geoscience BC website: <http://www.geosciencebc.com/s/SummaryofActivities.asp>.

Every reasonable effort is made to ensure the accuracy of the information contained in this report, but Geoscience BC does not assume any liability for errors that may occur. Source references are included in the report and the user should verify critical information.

When using information from this publication in other publications or presentations, due acknowledgment should be given to Geoscience BC. The recommended reference is included on the title page of each paper. The complete volume should be referenced as follows:

Geoscience BC (2019): Geoscience BC Summary of Activities 2018: Minerals and Mining; Geoscience BC, Report 2019-1, 118 p.

Summary of Activities: Minerals and Mining (Geoscience BC)

Annual publication

ISSN 2561-4584 (Print)

ISSN 2561-4592 (Online)

Geoscience BC

1101–750 West Pender Street

Vancouver, British Columbia V6C 2T7

Canada

Foreword

Geoscience BC is pleased to once again present results from our ongoing projects in our annual *Summary of Activities* publication. Following on from last year, we are publishing the papers in two separate volumes: *Energy and Water*, and this volume, *Minerals and Mining*. Both volumes are available in print and online via www.geosciencebc.com.

Summary of Activities 2018: Minerals and Mining

This volume, *Summary of Activities 2018: Minerals and Mining*, contains 12 papers from Geoscience BC–funded projects or 2018 scholarship recipients that are within Geoscience BC’s strategic focus area of minerals. The papers are divided into three sections, based on Geoscience BC’s strategic objectives of

- 1) Identifying New Natural Resource Opportunities;
- 2) Advancing Science and Innovative Geoscience Technologies; and
- 3) Facilitating Responsible Natural Resource Development.

In the first section, *Identifying New Natural Resource Opportunities*, Rioseco et al. discuss ongoing work interpreting structure, metamorphism and exhumation to provide context for mineral deposits in the interface between the Purcell Anticlinorium and the Kootenay Arc in southeastern British Columbia (BC). Simister et al. (including scholarship recipient Iulianella Phillips) provide an update on using microbial-community fingerprinting in mineral-deposit exploration, and scholarship recipient Luck (et al.) discusses the use of hydrocarbon-pathfinder techniques as a geochemical means to explore for Cu-porphyry and related deposits in BC. Kuppusamy and Holuszko examine rare-earth elements in BC coalfield samples, and present preliminary characterization and extraction findings.

In the *Advancing Science and Innovative Geoscience Technologies* section, Bouzari and Hart identify key features of zircon that are indicative of porphyry-fertile plutons in BC. Scholarship recipients Binner (et al.) and Graham (et al.) highlight mineral-deposit studies of the IKE and Iron Cap deposits, respectively. Scholarship recipient Miller (et al.) presents preliminary lithological descriptions, stratigraphic sequences and structural work near the Big Bulk Au-Cu porphyry system and Red Mountain Au deposit in northwestern BC. Finally, Mackay et al. give an update on using Roben Jig technology to clean coal, this year’s refinement of the washing capabilities benefiting from a rare single-seam run at an operating industrial-washing plant that enabled a direct comparison with the laboratory results.

Finally, in the *Facilitating Responsible Natural Resource Development* section, Fraser introduces two new Geoscience BC–supported projects that will tackle microbial health and biodiversity as part of mine-site reclamation. Scholarship recipient Vanderzee (et al.) presents carbon-sequestration research focused on the Baptiste minesite in central BC.

Geoscience BC Minerals and Mining Publications 2018

In addition to the two *Summary of Activities* volumes, Geoscience BC releases interim and final products from our projects as Geoscience BC reports. The following thirteen Minerals and Mining reports were published in 2018:

- Eleven technical papers in the *Geoscience BC Summary of Activities 2017: Minerals and Mining* volume (Geoscience BC Report 2018-01)
- **Midas High Resolution Magnetic and Radiometric Survey: Search Project Phase III**, by CGG (Geoscience BC Report 2018-03)
- **Producing Clean Coal from Western Canadian Coal Fields Using the Water-Based Roben Jig**, by M. Mackay, R. Leeder, L. Giroux, M. Holuszko, H. Dexter and D. Thomas (Geoscience BC Report 2018-03)
- **Enhancing Geochemical Precision by Analyzing the Clay Fraction in Till: Cost-Benefit Study from the TREK Project Area, British Columbia**, by P.W.G. van Geffen and E.B. Bluemel (Geoscience BC Report 2018-05)
- **Advanced Processing of the TREK Project Geochemical Data: Identifying and Enhancing Geochemical Anomalies in the TREK Project Area Using Sediment Transport Modelling Combined with Multimedia and Multivariate Data Analysis**, by D. Sacco, R. Lett, W. Jackaman and B. Elder (Geoscience BC Report 2018-07)
- **Merging Geological, Seismic Reflection and Magnetotelluric Data in the Purcell Anticlinorium**, by F.A. Cook (Geoscience BC Report 2018-09)

- **Adding Value to Regional Till Geochemical Data through Exploratory Data Analysis, TREK Project Area, Central BC: Final Results**, by E.B. Bluemel (Geoscience BC Report 2018-10)
- **Geology of the Greenwood Map Sheet (NTS 082E/02)**, by T. Höy (Geoscience BC Map 2018-11)
- **Geology and Mineral Potential of the TREK Area, Northern Interior Plateau, Central British Columbia, Parts of 1:250,000 NTS Sheets 093B, C, F and G**, by J.J. Angen, C.J.R. Hart, R.S. Kim and M. Rahimi (Geoscience BC Report 2018-12)
- **Integrated Assessment of Regional Stream-Sediment Geochemistry for Metallic Deposits in Northwestern British Columbia (Parts of NTS 093, 094, 103, 104), Canada**, by CSA Global Canada Geosciences Ltd. (Geoscience BC Report 2018-14)
- **A Compilation of Quality Control Data from Geoscience BC Regional Geochemical Survey (RGS) Initiatives**, by W. Jackaman (Geoscience BC Report 2018-15)
- **Mineralogical and Geochemical Characteristics of Porphyry-Fertile Plutons: Guichon Creek, Takomkane and Granite Mountain Batholiths, South-Central British Columbia (NTS 092I, P, 093A, B)**, by F. Bouzari, C.J.R. Hart, T. Bissig and G. Lesage (Geoscience BC Report 2018-17)
- **Detrital Gold as a Deposit-Specific Indicator Mineral by LA-ICP-MS Analysis**, by D.A. Banks, R.J. Chapman and C. Spence-Jones (Geoscience BC Report 2018-21)

All releases of Geoscience BC reports and data are published on our website and are announced through our website and e-mail updates. Most final reports and data can also be viewed or accessed through our Earth Science Viewer at <http://www.geosciencebc.com/s/WebMaps.asp>.

Acknowledgments

Geoscience BC would like to thank all authors and reviewers of the *Summary of Activities* for their contributions to this volume. RnD Technical is also acknowledged for its work in editing and assembling both volumes. As well, Geoscience BC would like to acknowledge the Province of British Columbia and our project-funding partners for their ongoing support of public geoscience, and express our appreciation for the leaders and volunteers in British Columbia's mineral exploration, mining and energy sectors who support our organization through their guidance, use and recognition of the information that we collect and distribute.

Christa Pellett
Project Co-ordinator
Geoscience BC
www.geosciencebc.com

Contents

Identifying New Natural Resource Opportunities

- N.A. Rioseco, D.R.M. Pattison and R.E. Ashton:** Relationship between deformation and metamorphism in the interface between the Purcell Anticlinorium and the Kootenay Arc, southeastern British Columbia 1
- R.L. Simister, B.P. Iulianella Phillips, P.A. Winterburn and S.A. Crowe:** Microbial-community fingerprints as indicators for buried mineralization, southern British Columbia. 15
- P.M. Luck, R.L. Chouinard and P.A. Winterburn:** Organic-compound pathfinders in soil for base- and precious-metal exploration in British Columbia 27
- V.K. Kuppasamy and M.E. Holuszko:** Characterization and extraction of rare-earth elements from East Kootenay coalfield samples, southeastern British Columbia. 33

Advancing Science and Innovative Geoscience Technologies

- F. Bouzari and C.J.R. Hart:** Assessing British Columbia porphyry fertility using zircons. 45
- M.M. Binner, D.D. Marshall, C.M. Rebagliati and K.B. Riedell:** IKE copper-molybdenum-silver porphyry deposit, southwestern British Columbia: early halo-type veins as a tool for vectoring toward higher grade mineralization. 55

- H.C. Graham, D.J. Morgan, R.J. Chapman and D.A. Banks:** Evolution of porphyry-epithermal gold systems using trace elements: insights from the Iron Cap deposit, Kerr-Sulphurets-Mitchell district, northwestern British Columbia 67
- E.A. Miller, L. Kennedy and B.I. van Straaten:** Preliminary field results from Kinskuch Lake, northwestern British Columbia: a study of the Boundary between the Stuhini and Hazelton groups. . . 75
- M.L. Mackay, L. Giroux, R.L. Leeder, H. Dexter, J. Halko, M. Holuszko, and D. Thomas:** Producing clean coal from western Canadian coalfields using the water-based Roben Jig process: refining the process. 87

Facilitating Responsible Natural Resource Development

- L.H. Fraser:** Soil amendments in mine closure, New Afton mine, south-central British Columbia: proposed work 101
- L.H. Fraser:** Biodiversity in ecosystem mine reclamation, south-central British Columbia: proposed work 105
- S.S.S. Vanderzee, G.M. Dipple and P.M.D. Bradshaw:** Targeting highly reactive labile magnesium in ultramafic tailings for greenhouse-gas offsets and potential tailings stabilization at the Baptiste deposit, central British Columbia 109

Relationship between Deformation and Metamorphism in the Interface between the Purcell Anticlinorium and the Kootenay Arc, Southeastern British Columbia (NTS 082F, G)

N.A. Rioseco, Department of Geoscience, University of Calgary, Calgary, AB, nicole.rioseco@ucalgary.ca

D.R.M. Pattison, Department of Geoscience, University of Calgary, Calgary, AB

R.E. Ashton, Department of Geoscience, University of Calgary, Calgary, AB

Rioseco, N.A., Pattison, D.R.M. and Ashton, R.E. (2019): Relationship between deformation and metamorphism in the interface between the Purcell Anticlinorium and the Kootenay Arc, southeastern British Columbia (NTS 082F, G); in Geoscience BC Summary of Activities 2018: Minerals and Mining, Geoscience BC, Report 2019-1, p. 1–14.

Introduction

The area between the towns of Kimberley, Creston and Crawford Bay in southeastern British Columbia (BC) encompasses the interface between two major Cordilleran tectonic domains, the Purcell Anticlinorium and the Kootenay Arc. These domains comprise part of the mineralogically rich East Kootenay region. The aim of this project is to elucidate changes in structure, metamorphism and exhumation history across the interface to provide further geological context for the different types of mineral deposits that occur within the region.

Regional Geology

The study area (Figure 1) straddles the interface between marginal rocks of North American affinity (Monger et al., 1982) to the east, and pericratonic and accreted island-arc rocks (Monger et al., 1982; Unterschutz et al., 2002) to the west. This region owes its complexity to a history of geological evolution that spanned roughly 1.4 billion years, from the Mesoproterozoic to the Eocene. The eastern portion of the field area is dominated by the Purcell Anticlinorium, a regional-scale, northwest-plunging anticlinal structure that is cored by rocks of the Belt-Purcell Supergroup (BPSG). This regional structure transitions westward into the Kootenay Arc, an arcuate salient composed of Neoproterozoic through Paleozoic pericratonic and accreted island-arc rocks.

The study area is primarily situated within rocks of the BPSG that occupy the core of the Purcell Anticlinorium (Figure 2). The BPSG comprises rift-related clastic rocks and synsedimentary mafic sills interpreted to have been deposited in an intracratonic rift basin (Price, 1964; Harrison, 1972). The lowermost unit of the BPSG, the Aldridge Formation, comprises predominantly turbiditic deposits. The

age of clastic rocks of the BPSG is constrained by the age of the Moyie Sills that are hosted in rocks of the Aldridge Formation (Höy, 1989). On the flanks of the Purcell Anticlinorium, Belt-Purcell strata are unconformably overlain by a Neoproterozoic sequence of sandstone and conglomerate interbedded with pelitic and carbonate rocks known as the Windermere Supergroup (WSG). On the western flank of the Purcell Anticlinorium, where it transitions into the Kootenay Arc, the WSG is unconformably overlain by pericratonic, coarse clastic and carbonate Paleozoic rocks that are part of the Kootenay Arc (Bond et al., 1985; Warren, 1997; Colpron et al., 2002).

In addition to a younging of stratigraphy, the westward transition from the Purcell Anticlinorium into the Kootenay Arc is marked by a change in structural style, metamorphic grade, and cooling history. The Purcell Anticlinorium contains some of the oldest rock exposures in the Cordillera and preserves evidence of structures and metamorphism that are stratigraphically restricted to rocks of Mesoproterozoic age. The Purcell Anticlinorium was affected by three cryptic, Proterozoic orogenic events, the ca. 1350–1300 Ma East Kootenay orogeny, a ca. 1050 Ma Grenville-age event and the ca. 900–800 Ma Goat River orogeny (Leech, 1962; McMechan and Price, 1982; McFarlane and Pattison, 2000; McFarlane, 2015). Despite this orogenic history, and the later effects of Cordilleran deformation that created the Purcell Anticlinorium, Belt–Purcell rocks in the core of the Purcell Anticlinorium preserve primary sedimentary structures and appear to be generally undeformed.

One of the primary features of the transition from the Purcell Anticlinorium to the Kootenay Arc is a change in structural style. The Kootenay Arc preserves evidence of at least three phases of intense structural modification regionally, and up to five locally, which took place during the Mesozoic (Moynihan and Pattison, 2013; Webster and Pattison, 2018). These rocks are characterized by more ductile deformation and higher grades of metamorphism attributed to Cordilleran orogenic processes spanning the Early Jurassic

This publication is also available, free of charge, as colour digital files in Adobe Acrobat® PDF format from the Geoscience BC website: <http://www.geosciencebc.com/s/SummaryofActivities.asp>.

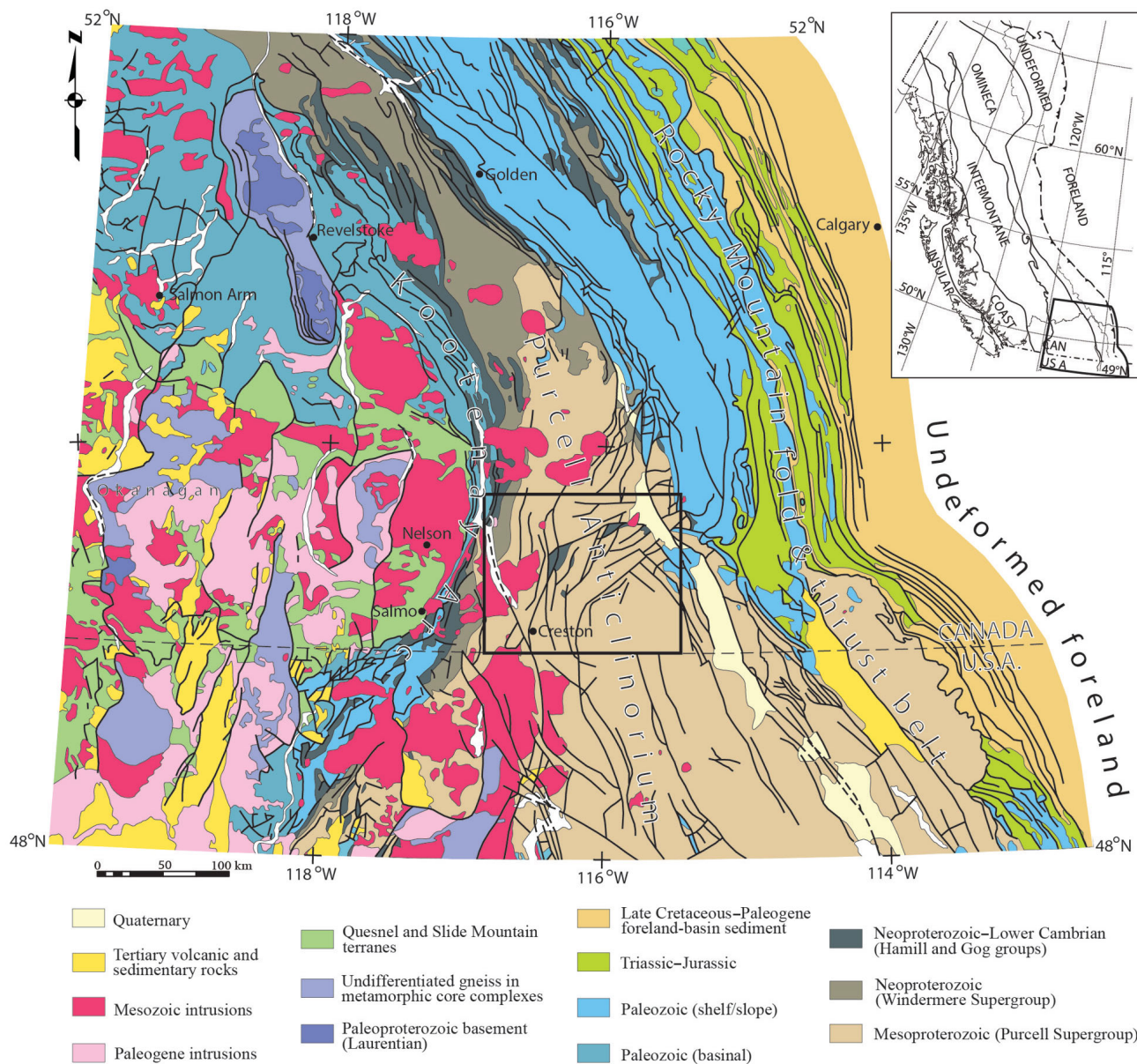


Figure 1. Regional geology of the southeastern Canadian Cordillera in southeastern British Columbia. Study area indicated by black outline. Map modified from Webster and Pattison (2018), originally after Wheeler and McFeely (1991).

through Eocene. The extent to which Mesozoic deformation and metamorphism associated with the Kootenay Arc impinged upon the Purcell Anticlinorium is poorly understood and is the focus of this study.

The metamorphic grade of BPSG rocks within the Purcell Anticlinorium is relatively low, within the chlorite and biotite subzones of the greenschist and lower amphibolite facies (Leech, 1962; Read et al., 1991; Pattison and Seitz, 2012). High grade rocks (andalusite-sillimanite zone) within the Purcell Anticlinorium are restricted to the Matthew Creek metamorphic zone (MCMZ), a fault bounded domain west of Kimberley, BC. These rocks are interpreted to have resulted from a local thermal perturbation, likely as-

sociated with mafic intrusions during the East Kootenay orogeny (McMechan and Price, 1982; McFarlane and Pattison, 2000; McFarlane, 2015). Westward into the Kootenay Arc, there is a contrasting metamorphic history, in which the rocks were ductilely deformed, metamorphosed and intruded over several pulses between 180 and 50 Ma (Archibald et al., 1983, 1984; Klepacki, 1985; Leclair et al., 1993; Moynihan and Pattison, 2013; Webster and Pattison, 2018). Regional metamorphic grade within the Kootenay Arc ranges from greenschist to middle amphibolite facies. Evidence of amphibolite-grade metamorphism is represented by Barrovian (kyanite-sillimanite-type) metamor-

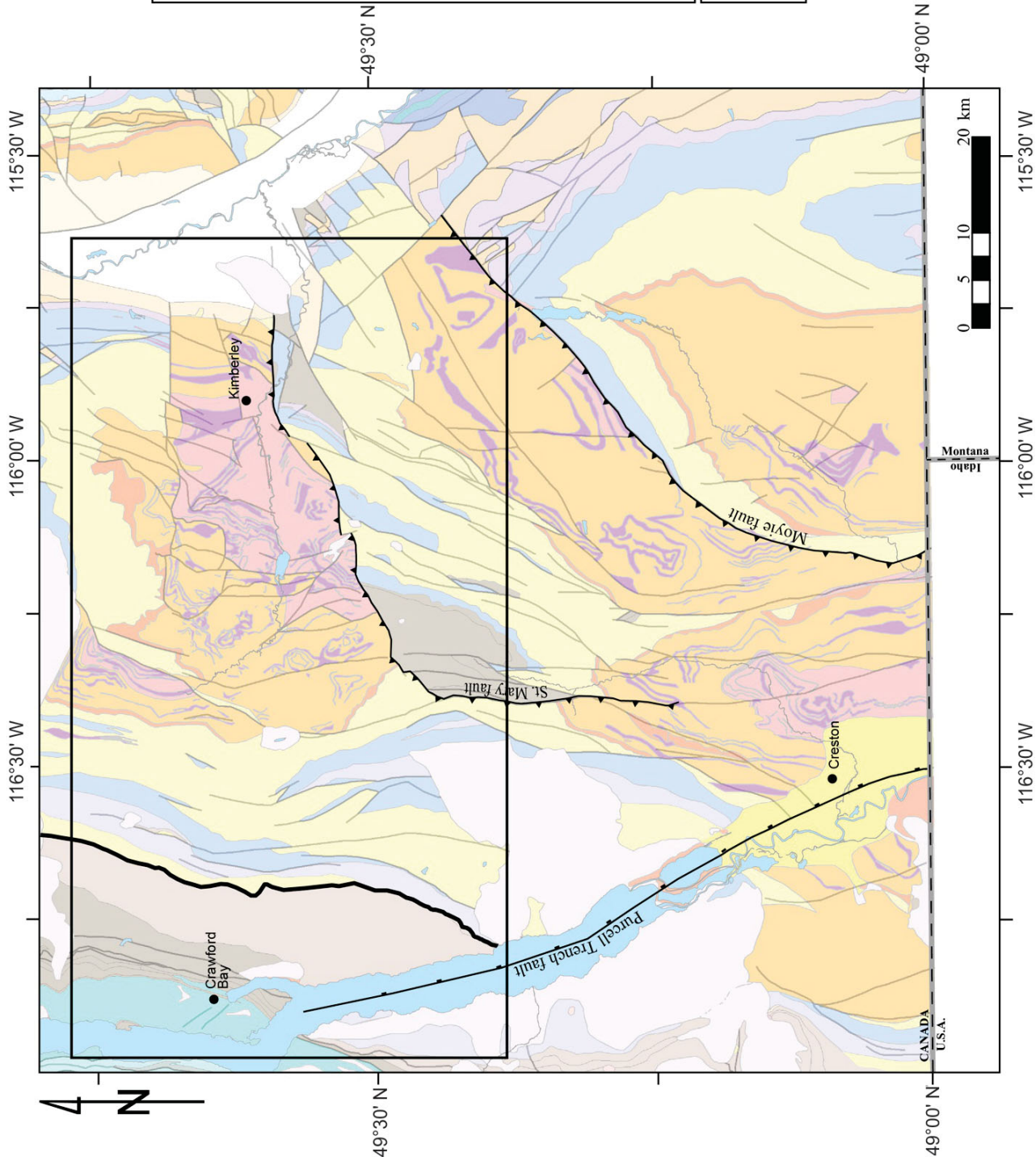


Figure 2. Geological map of the field area, emphasizing the unconformable contact between Belt-Purcell Supergroup (BPSG) and Windermere Supergroup (WSG) and younger rocks. Map modified from Hoy et al. (1995). Structure maps in Figure 6 indicated by black outline.

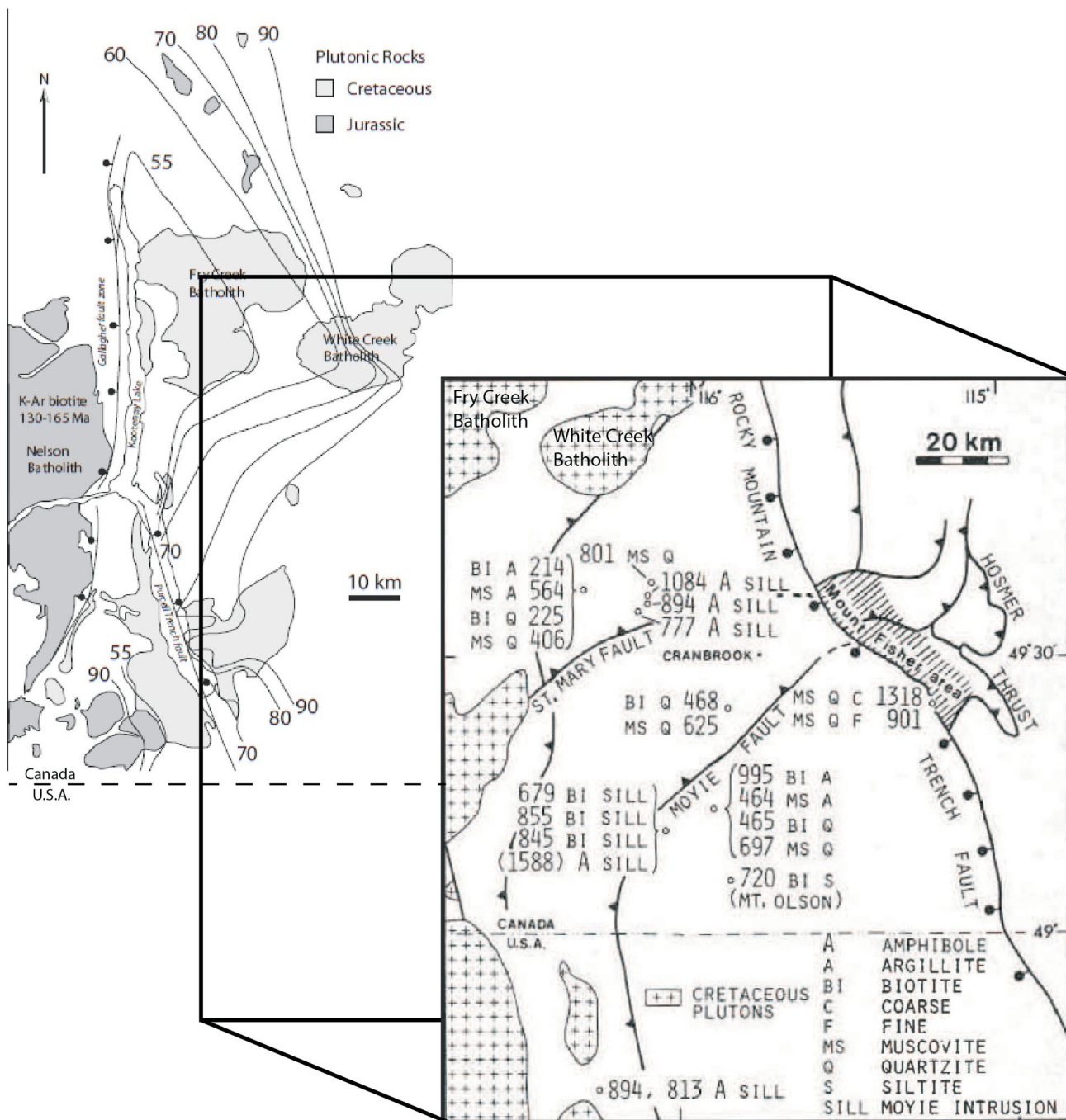


Figure 3. (Left) Potassium-argon cooling ages in biotite from the Kootenay Arc (from Archibald et al., 1984); contour interval 10 million years. **(Right)** Potassium-argon cooling ages from the Purcell Anticlinorium (from McMechan and Price, 1982). Location of figures shown on Figure 1, indicated by black outline.

phic zones that locally reach sillimanite+potassium-feldspar grade (Leclair, 1982; Moynihan and Pattison, 2013; Webster and Pattison, 2018).

A prominent westward decrease in K-Ar and Ar/Ar cooling ages in hornblende and micas (Figure 3) indicates that peak metamorphism within the Purcell Anticlinorium is much older than that of the Kootenay Arc. Hunt (1962) and McMechan and Price (1982) reported K-Ar ages in hornblende and micas in the range 1318–600 Ma. Metamorphic

mineral growth in the core of the Purcell Anticlinorium must have happened prior to exhumation of these rocks, and therefore is restricted to the Proterozoic. In contrast, metamorphosed Neoproterozoic through Paleozoic strata in the Kootenay Arc, where they interface with the Purcell Anticlinorium, yield K-Ar and Ar/Ar ages in the range of 90–45 Ma, indicating much younger, Mesozoic and Cenozoic, metamorphism and exhumation (Figure 3; Archibald et al., 1983, 1984; Webster and Pattison, 2018).

Structure

There is a change in structural style that occurs across the interface between the Purcell Anticlinorium and the Kootenay Arc. A distinction is made between Purcell Anticlinorium-type structures, which are characteristic of rocks of the BPSG in the core of the Purcell Anticlinorium, and Kootenay Arc-type structures, which are associated with Cordilleran orogenesis. The following sections utilize the subscripts ‘ $_{PA}$ ’ and ‘ $_{KA}$ ’ to differentiate between Purcell Anticlinorium-type and Kootenay Arc-type structures.

Purcell Anticlinorium-Type Structures

Rocks of the lower, middle and upper Aldridge Formation occur as thick, planar-bedded, turbiditic deposits. These strata consist predominantly of massive sandy units, which range from 0.5–1 m in thickness, and are irregularly interbedded with thinner (5–10 cm) silty layers (Figure 4a). The Moyie Sills occur mainly in lower and middle Aldridge rocks; they are typically massive and commonly preserve

ophitic, igneous textures (Figure 4b). These units are typically on the order of 6–10 m thick.

Bedding (S_0), as well as primary sedimentary structures, are well preserved within Belt–Purcell rocks in the core of the Purcell Anticlinorium (Figure 4c). An S_1 penetrative, slaty cleavage (Figure 4d) is present throughout the pelitic portions of the Aldridge Formation. This cleavage is referred to as S_{1PA} , and generally dips within a range of 15–30° from that of S_0 . The S_{1PA} cleavage is stratigraphically restricted to rocks of the Belt–Purcell Supergroup, indicating that cleavage development occurred prior to deposition of the Windermere Supergroup. Leech (1962) noted that there is a lack of recognizable fold structures that can be related to S_{1PA} . Although referred to here as S_{1PA} , this cleavage is a structure that is intrinsic to rocks of the Belt–Purcell Supergroup in parts of the Purcell Anticlinorium that have not been overprinted by Kootenay Arc-type structures.

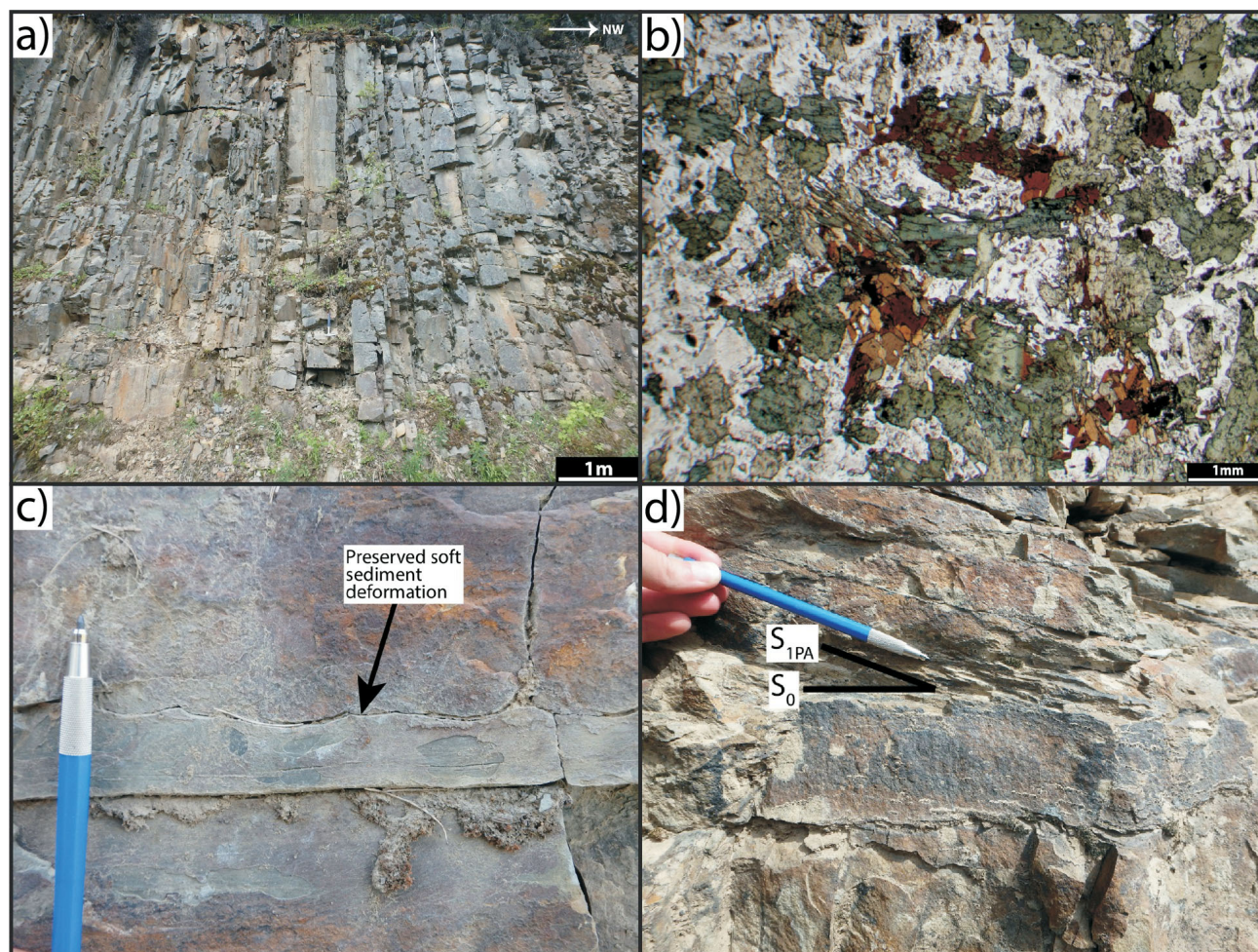


Figure 4. Photos and photomicrographs of representative units and structures in the study area: **a)** exposure of the Aldridge Formation from within the core of the Purcell Anticlinorium near Kitchener, BC; **b)** photomicrograph of a typical Moyie Sills sample collected near St. Mary Lake, BC; **c)** soft-sediment deformation observed near Lumberton, BC; **d)** S_{1PA} cleavage developed within the pelitic interbeds of the Aldridge Formation near Yahk, BC.

Kootenay Arc–Type Structures

Evidence of three deformation events in the Kootenay Arc was observed in rocks of the Windermere Supergroup, as well as in younger, coarse Paleozoic clastic rocks that comprise the easternmost portion of the Kootenay Arc. The primary fabric of these rocks is a steeply dipping, penetrative cleavage (S_{1KA}) that is manifested as a phyllitic fabric, which is subparallel to bedding. The S_{1KA} cleavage is overprinted by a spaced cleavage (S_{2KA}) that dips moderately to the east (Figure 5a) and is axial planar to folds of S_{1KA} (Figure 5b). Sub-horizontal lineations (L_{2KA}) present on the surface of S_{1KA} are generally north trending and are coincident with the constructed F_2 fold axis in both S_0 measured in WSG and younger strata, as well as in S_{1KA} (Figure 5c). A third deformation phase (D_3) resulted in the crenulation of the S_{2KA} surface (Figure 5d), and is manifested as a near-vertical, south-southwest-trending lineation (L_{3KA}) on the surface of S_{1KA} (Figure 5c).

Impingement of Kootenay Arc–Type Structures on the Western Flank of the Purcell Anticlinorium

Kootenay Arc–type structures are restricted to the northern portion of the field area (Figure 6a–c). The Gray Creek Road, which connects the towns of Kimberley and Crawford Bay, BC, allows for an examination of the change in structural style across the interface between the Purcell Anticlinorium, in which S_0 and S_{1PA} (Mesoproterozoic) are the dominant structures, and the Kootenay Arc, which is characterized by a series of three overprinting Mesozoic structures.

Kootenay Arc–type structures are measured in Belt–Purcell rocks on the western flank of the Purcell Anticlinorium. The most easterly indication of Mesozoic structural modification within the Purcell Anticlinorium occurs near St. Mary Lake within the lower Aldridge Formation

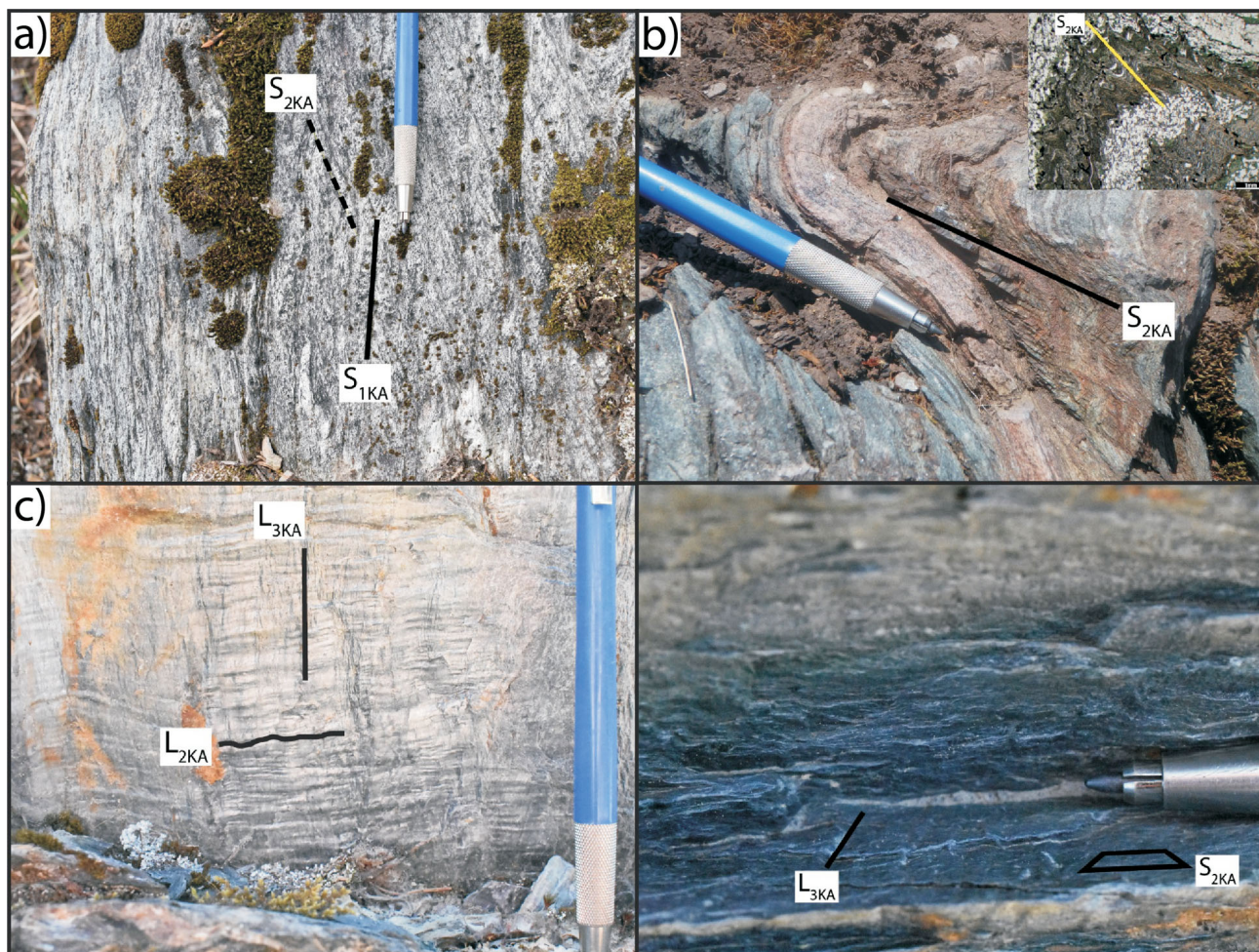


Figure 5. Photos and photomicrographs of representative units and structures in the study area: **a)** relationship between phyllitic fabric (S_{1KA}) and spaced cleavage (S_{2KA}) in rocks of the Windermere Supergroup along the western side of the Gray Creek transect near Crawford Bay; **b)** fold in rocks of the Windermere Supergroup along the western side of the Gray Creek transect, with an axial-planar S_{2KA} cleavage (S_{2KA}), and inset of photomicrograph of small-scale fold and S_{2KA} cleavage from the same locality; **c)** exposure of L_{2KA} and L_{3KA} in phyllite along the western side of the Gray Creek transect; **d)** crenulation (L_{3KA}) of the S_{2KA} surface along the western side of the Gray Creek transect.

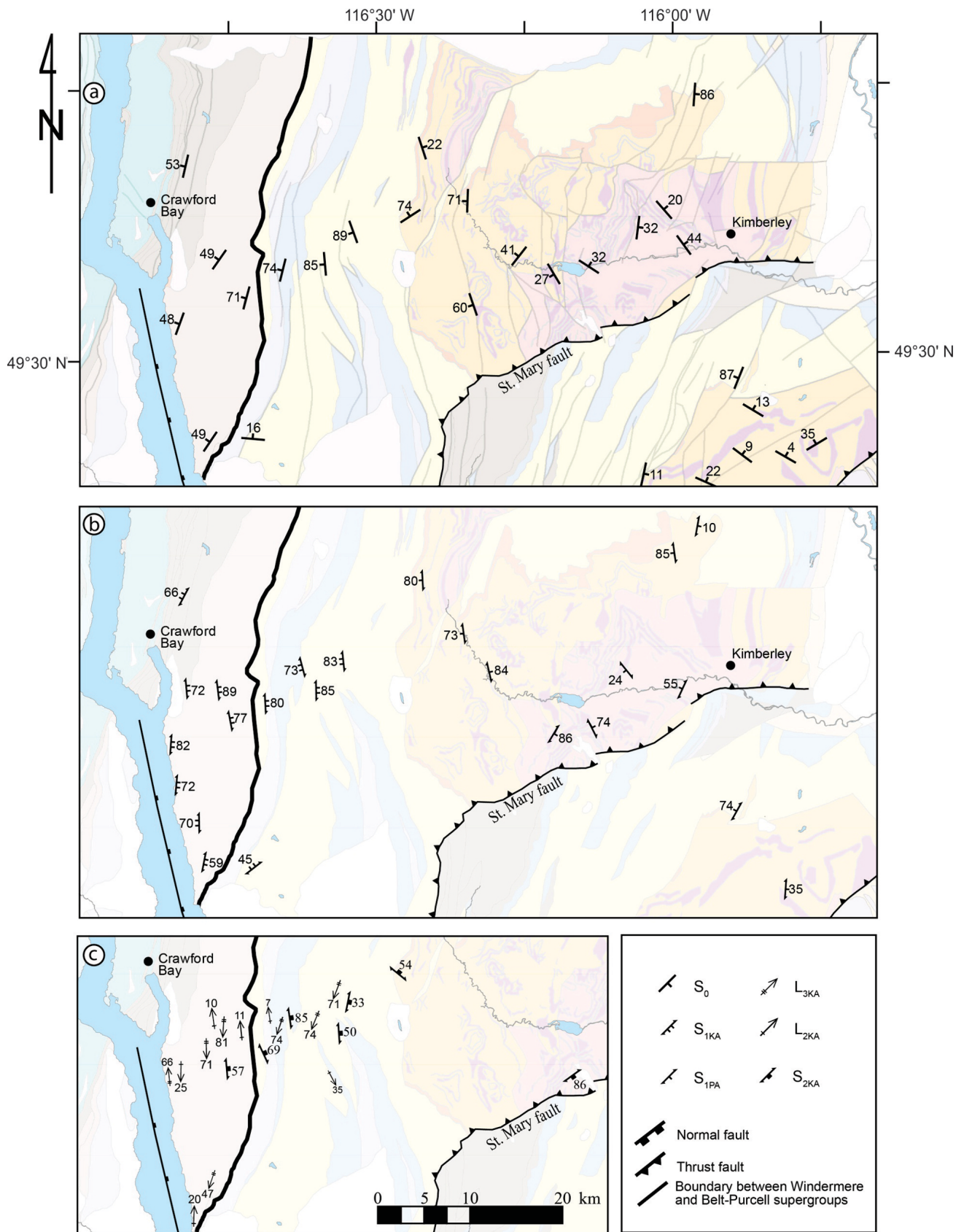


Figure 6. Structures observed across the Purcell Anticlinorium–Kootenay Arc transition in the study area. Maps show **a)** bedding orientations; **b)** fabrics S_{1PA} (one tick on symbol) and S_{1KA} (two ticks on symbol); **c)** structures associated with D_{2KA} (S_{2KA} and L_{2KA}) and D₃ (L_{3KA}). Map modified after Höy et al. (1995).

where folding and crenulations of S_{1PA} occur, as well as within the MCMZ west of Kimberley (McFarlane and Pattison, 2000). Within the westernmost exposures of the Aldridge Formation, as well as in younger Belt–Purcell rocks, S_{2KA} crenulations are intensified into a pervasive S_{2KA} schistosity. Locally, L_{3KA} is also developed in rocks of both the Belt–Purcell and Windermere Supergroups. Stereonet analysis indicates that large-scale folding of the Purcell Anticlinorium is related to the D_{2KA} , Mesozoic deformation that is responsible for the development of S_{2KA} and L_{2KA} . Constructed fold axes defined by S_0 in Belt–Purcell rocks and S_{1PA} are roughly coincident with the cluster of axes of L_{2KA} crenulations of S_{1PA} . The same is true for constructed fold axes defined by S_0 in WSG and younger rocks, as well as S_{1KA} measured in both BPSG and WSG and younger rocks, although the former plunge shallowly south rather than shallowly north (Figure 7).

The occurrence of overprinting Mesozoic structures characteristic of the Kootenay Arc within Belt–Purcell Supergroup rocks in the western margin of the Purcell Anticlinorium suggests that Kootenay Arc–type deformation propagated across the Windermere–Belt–Purcell unconformity into these older rocks. Although Kootenay Arc–type crenulations (S_{2KA}) are found near the St. Mary Lake area, the structural interface between the Purcell Anticlinorium and the Kootenay Arc is interpreted as the easternmost development of S_{1KA} , which occurs farther west, within 10–15 km east of the Windermere–Belt–Purcell unconformity. Here, S_{1KA} , the penetrative phyllitic schistosity that is characteristic of Kootenay Arc–type deformation, is the dominant fabric in rocks of the uppermost units of the Belt–Purcell Supergroup. By contrast, S_{2KA} , is developed throughout the region and overprints both S_{1KA} and S_{1PA} .

Metamorphism

Evidence of metamorphic grade across the interface is primarily restricted to argillaceous rocks of the Belt–Purcell and Windermere supergroups, whose bulk compositions are favourable for porphyroblast growth. Metamorphic grade in the Purcell Anticlinorium falls within the chlorite and biotite subzones of the greenschist and lower amphibolite facies (Figure 8), rocks are characterized by the assemblage plagioclase+quartz±muscovite±chlorite±biotite. There is no significant variation in the distribution of mineral assemblages across the Purcell Anticlinorium, indicating that the five samples that lack biotite are the result of restricted bulk compositions rather than a lower metamorphic grade. Similarly, the Moyie Sills, which are restricted to the lower and middle Aldridge Formation, do not show any significant variation in metamorphic grade across the Purcell Anticlinorium, and are characterized by the mineral assemblage plagioclase+quartz±chlorite±biotite±hornblende±actinolite±epidote. Variable occurrences of garnet

in the Purcell Anticlinorium will be discussed in more detail below.

The Kootenay Arc is characterized by three distinct episodes of metamorphism spanning the Middle Jurassic to the Late Cretaceous (Moynihan and Pattison, 2013; Webster and Pattison, 2018). The easternmost edge of the Kootenay Arc, where it interfaces with the Purcell Anticlinorium, is characterized by an elongate belt of regional, Barrovian metamorphism (Figure 8). East of Kootenay Lake, metamorphic grade decreases eastward from sillimanite+potassium-feldspar to biotite zone within Windermere and younger rocks. Peak metamorphic grade is about the same (biotite zone) as that of older metamorphic rocks of the BPSG beneath the Windermere unconformity (Moynihan and Pattison, 2013). For this reason, an investigation of mineral growth with respect to microstructures is necessary to determine the timing of metamorphism across the region.

Metamorphism with Respect to Deformation

Within the northern portion of the field area, consisting of argillaceous rocks of the Aldridge Formation, porphyroblasts of chlorite show evidence of internal deformation, as well as alignment within the plane of the S_{1PA} foliation (Figure 9a, b). These fabrics indicate that porphyroblast growth occurred prior to the development of S_{1PA} ; metamorphic conditions responsible for the growth of these minerals must have occurred during the Proterozoic. The last occurrence of porphyroblasts in Belt–Purcell rocks that predate the development of S_{1PA} roughly coincides with the first signs of Kootenay Arc–type structures. Within rocks of both the Belt–Purcell (Figure 9c), and Windermere supergroups (Figure 9d, e) that exhibit Kootenay Arc–type deformation, porphyroblast growth appears to be intertectonic, between D_{1KA} and D_{2KA} , meaning biotite of this type cannot be Mesoproterozoic. The S_{1KA} cleavage is folded into microlithons between the cleavage planes of S_{2KA} . Straight inclusion trails in biotite porphyroblasts indicate that mineral development preceded folding associated with S_{2KA} . Additionally, the spaced S_{2KA} cleavage wraps biotite porphyroblasts (Figure 9c–e). In the westernmost portion of the field area, along the eastern shoreline of Kootenay Lake, pre- S_{2KA} biotite occurs both as large porphyroblasts that are wrapped by S_{2KA} (Figure 9e), and as finer grains that were folded with S_{1KA} (Figure 9f). In both cases, biotite growth preceded the development of S_{2KA} . Microstructural analysis implies that some of the biotite in Belt–Purcell rocks, specifically those close to the interface with the Kootenay Arc, developed during the Mesozoic, not the Mesoproterozoic. Therefore, biotite of Mesoproterozoic age does not extend westward all the way to the Windermere unconformity and Mesozoic metamorphism affected Belt–Purcell rocks in the Purcell Anticlinorium.

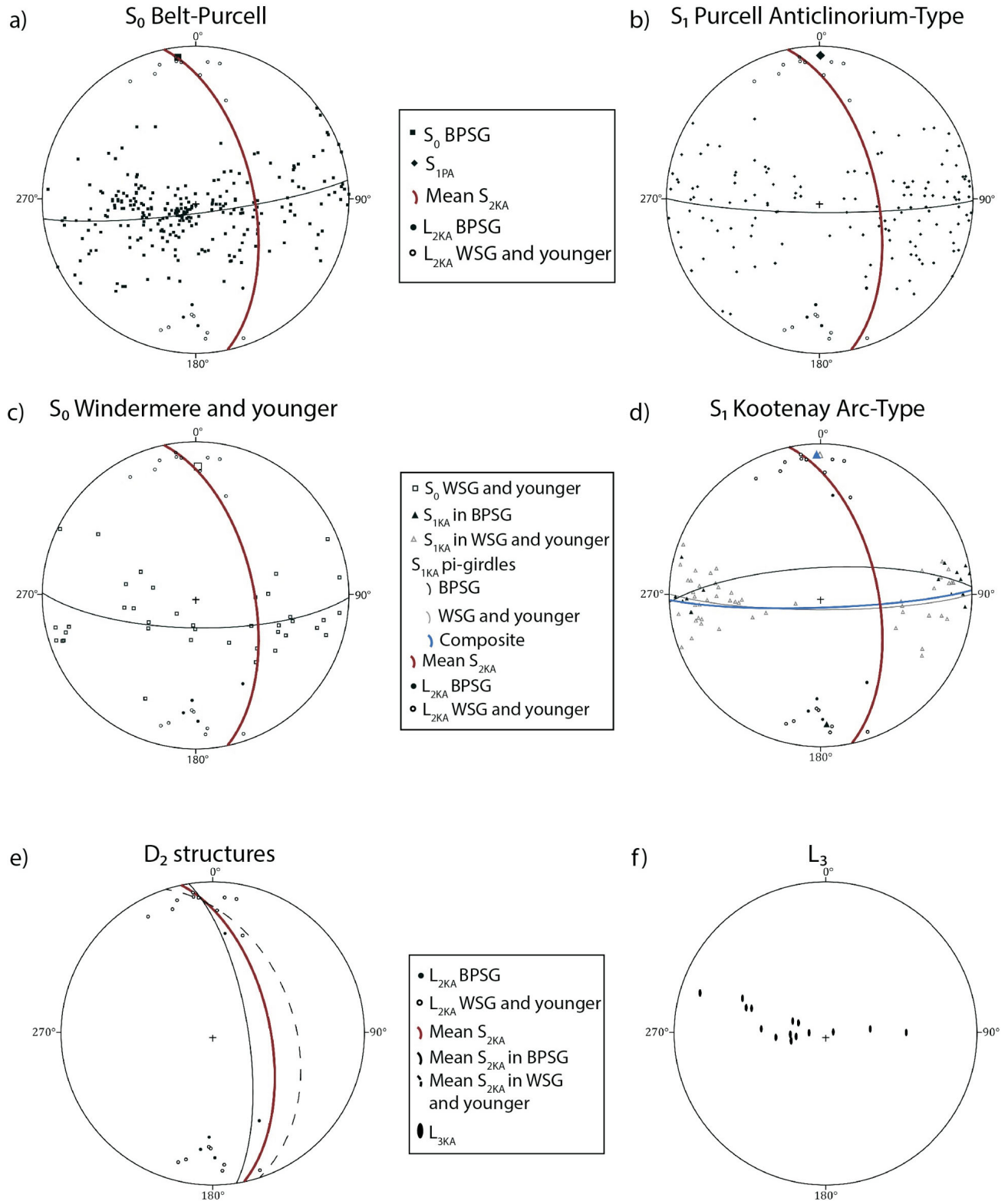


Figure 7. Stereonet analysis of all measured structures (equal angle projections, lower hemisphere): **a)** poles to S_0 in Belt-Purcell rocks with associated D_{2KA} structures; **b)** poles to S_{1PA} with associated D_{2KA} structures; **c)** poles to S_0 in Windermere and younger strata with associated D_{2KA} structures; **d)** poles to S_{1KA} with associated D_{2KA} structures; **e)** D_{2KA} structures: overall mean S_{2KA} , mean S_{2KA} measured in the Belt-Purcell Supergroup (BPSG), mean S_{2KA} measured in the Windermere Supergroup (WSG) and younger rocks, and L_{2KA} lineations; **f)** D_3 lineations.

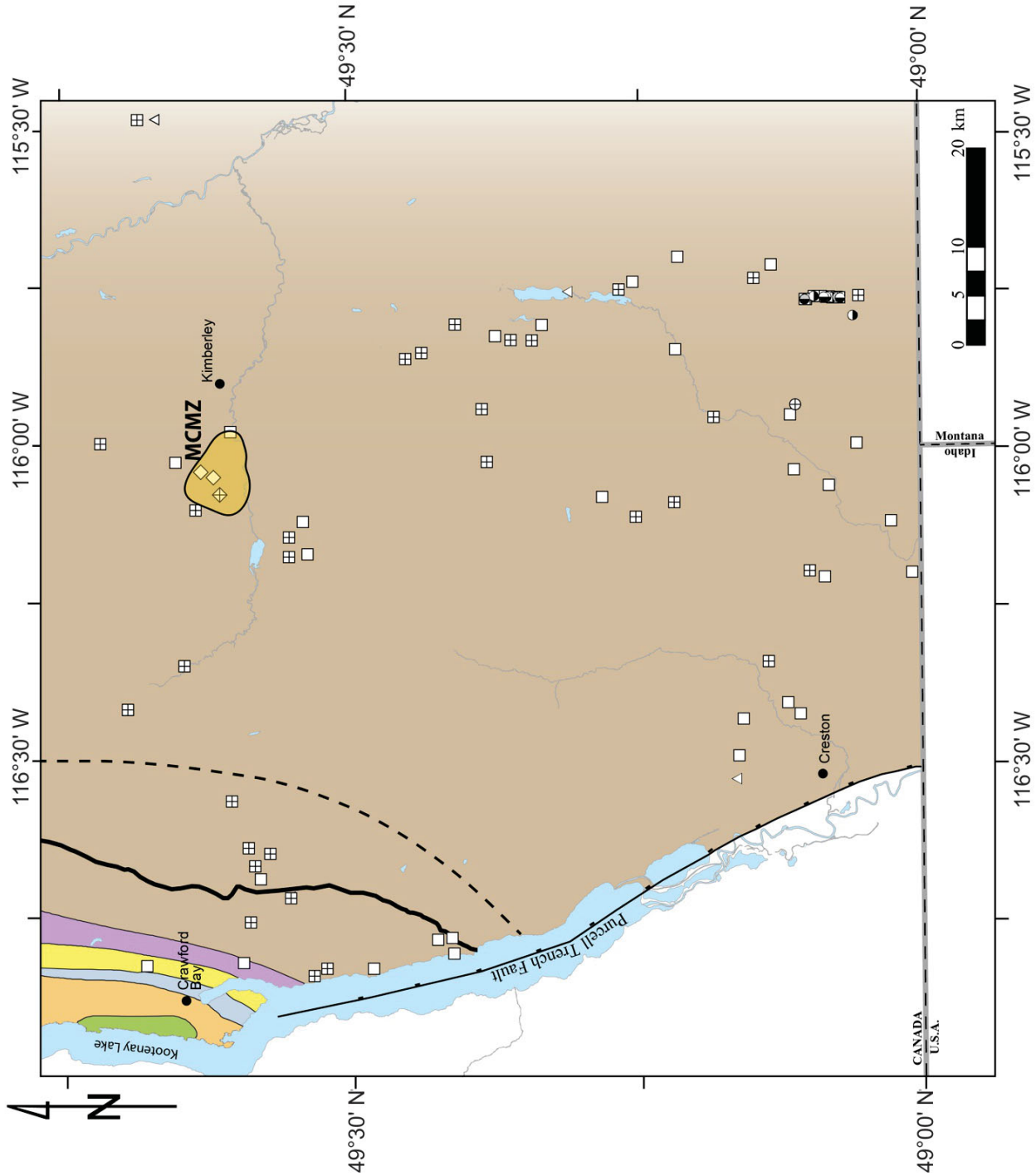


Figure 8. Map of mineral assemblages in sedimentary rocks across the Purcell Anticlinorium in the study area, with metamorphic zones from Moynihan and Pattison (2013). Abbreviation: MCMZ, Matthew Creek metamorphic zone.

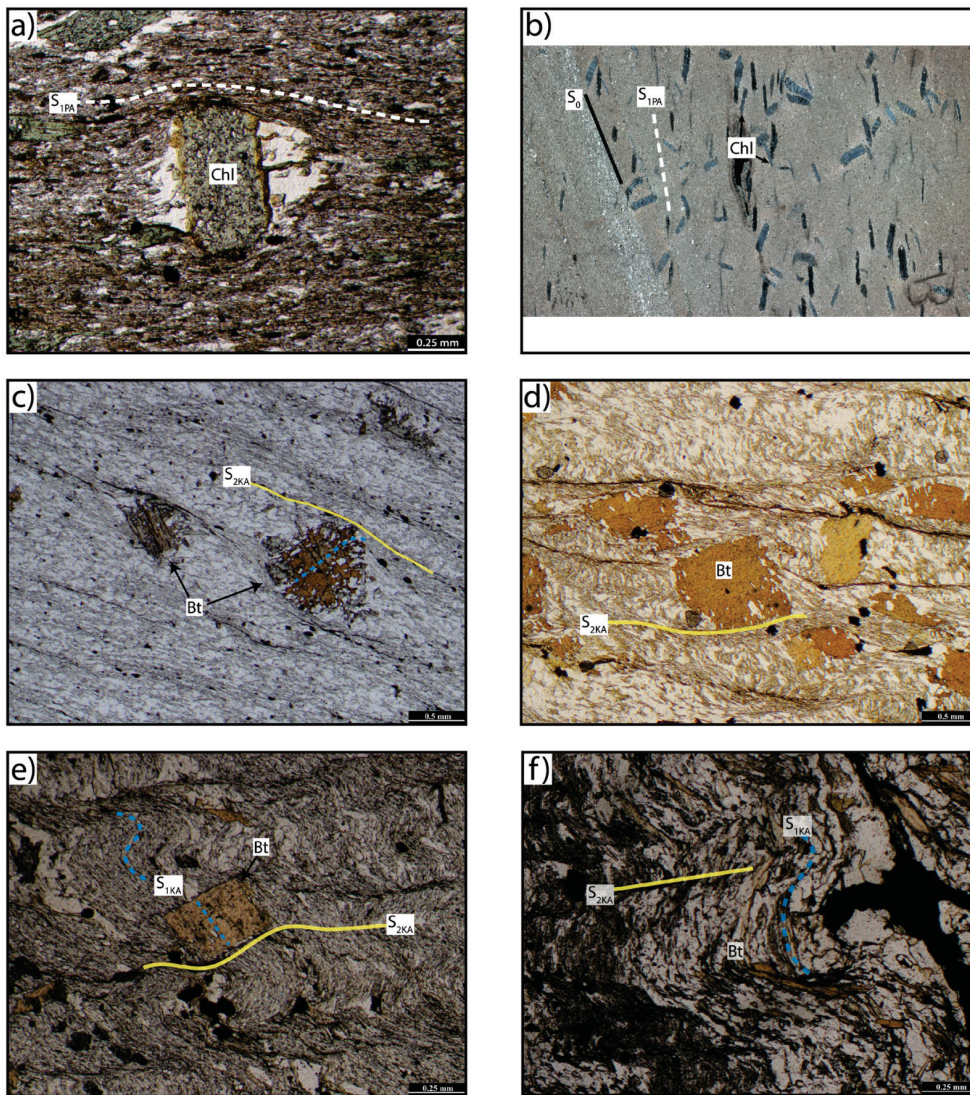
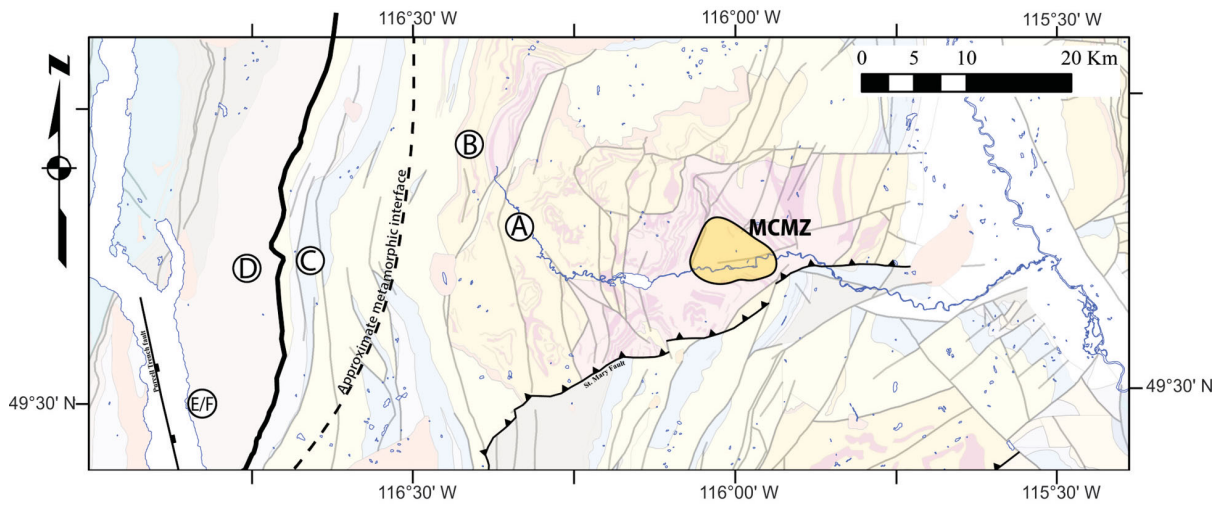


Figure 9. Photomicrographs indicating the relationship between porphyroblasts and rock fabrics, along with a map indicating sample locations (letters match those identifying the photomicrographs) in the study area: **a)** pre-tectonic chlorite from the Aldridge Formation; **b)** pre-tectonic chlorite from the Aldridge Formation; **c)** inter-tectonic biotite from the uppermost units of the Belt–Purcell Supergroup; **d)** inter-tectonic biotite from the Windermere Supergroup; **e)** inter-tectonic biotite from the Windermere Supergroup; **f)** pre S_{2KA} biotite from the Windermere Supergroup. Abbreviations: Bt, biotite; Chl, chlorite; MCMZ, Matthew Creek metamorphic zone.

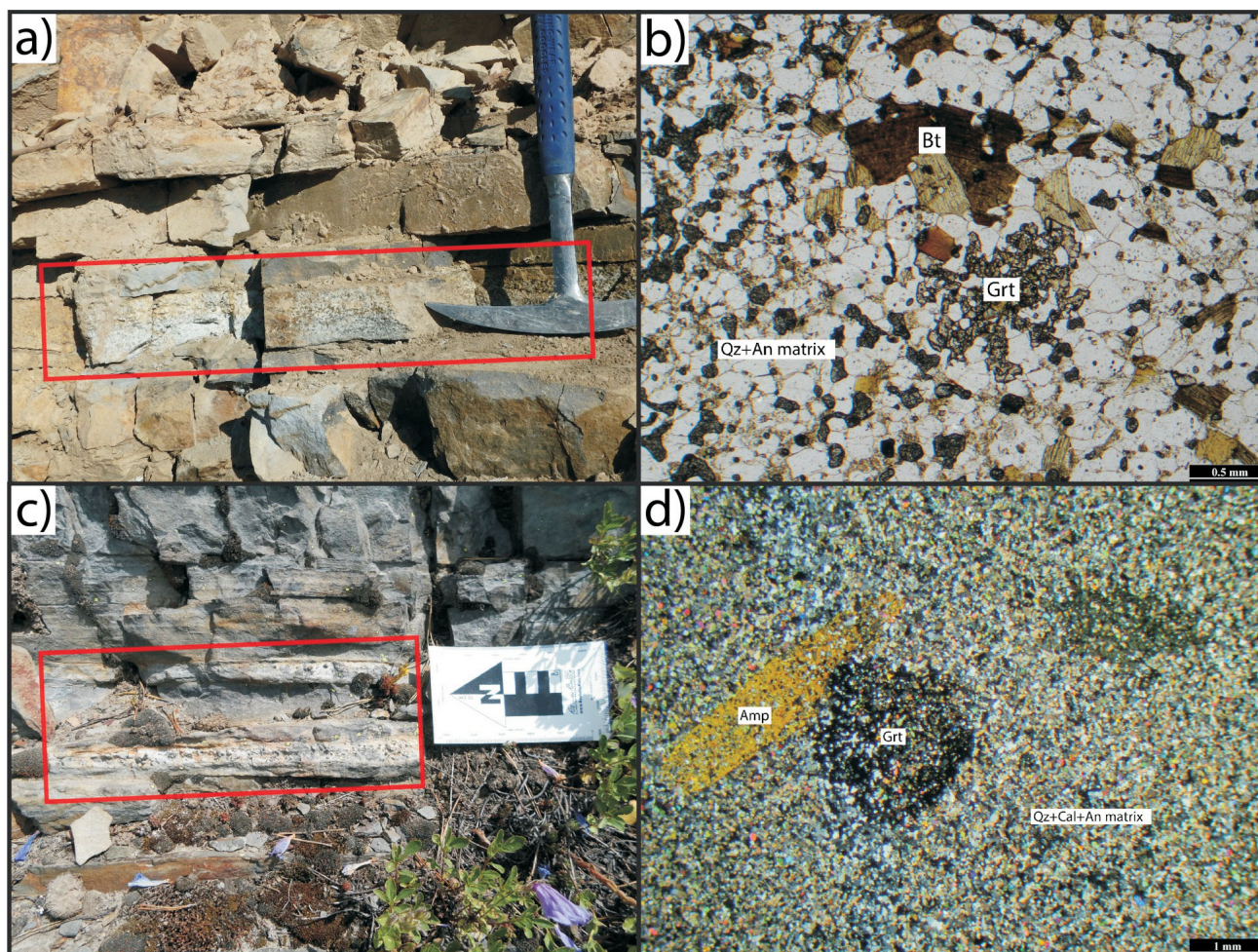


Figure 10. Garnet-bearing rocks in the Purcell Anticlinorium in the study area: **a)** field setting of garnet-bearing rocks on Mount Mahon; **b)** photomicrograph of garnet-biotite rock from Mount Mahon; **c)** field setting of garnet-amphibole rocks near Mount Olson; **d)** photomicrograph of garnet-amphibole rock near Mount Olson. Abbreviations: Amp, amphibole; An, anorthite; Bt, biotite; Cal, calcite; Grt, garnet; Qz, quartz.

Garnet in the Purcell Anticlinorium

Five occurrences of garnet-bearing rocks have been identified within the Purcell Anticlinorium. They include: 1) the MCMZ west of Kimberley (McFarlane and Pattison, 2000), 2) the Sullivan mine northwest of Kimberley (DePaoli and Pattison, 2000), 3) the St. Eugene mine in Moyie (Pattison and Seitz, 2012), 4) Mount Mahon west of Yahk (Read et al., 1991; Brown and Stinson, 1995), and 5) near Mount Olson east of Yahk (Leech, 1967; Read et al., 1991). Previous studies indicate that garnet-bearing mineral assemblages within the Purcell Anticlinorium are due to either unusual bulk compositions favourable to garnet growth (DePaoli and Pattison, 2000; Pattison and Seitz, 2012) or domains of higher metamorphic grade (e.g., MCMZ; cf. McFarlane and Pattison, 2000). The presence of garnet within the Purcell Anticlinorium is of interest because anomalous garnet-bearing assemblages in metasedimentary rocks of low metamorphic grade have been asso-

ciated with prolific mineral deposits within the area (e.g., Sullivan and St. Eugene deposits).

Garnet-bearing rocks in the middle Aldridge Formation at Mount Mahon were identified in a single (though there may be more) layer ~10 cm thick (Figure 10a) and contain the mineral assemblage garnet+biotite+quartz+plagioclase+clay as an alteration product (Figure 10b). Near Mount Olson, within the lower Aldridge Formation, garnet-bearing layers ranging in thickness from 5 to 30 cm and with a maximum stratigraphic separation of ~15 m were identified in the field (Figure 10c). These rocks contain garnet+amphibole+plagioclase+quartz+ilmenite, with either calcite or chlorite (Figure 10d). A reaction that accounts for garnet growth at Mount Mahon and Mount Olson is:



In both localities, garnet-bearing layers are interlayered with typical biotite-bearing argillaceous rocks of the Aldridge Formation. Therefore, localized garnet growth is

not the result of higher metamorphic grade and is instead attributed to unusual calcareous bulk compositions. There is no evidence of mineralization associated with these layers.

Summary

Difficulty in defining the interface between the western edge of the Purcell Anticlinorium, and the eastern edge of the Kootenay Arc within the study area is attributed to the fact that the boundary between the two domains can be described in terms of stratigraphy, structure, metamorphism and exhumation history. Overall, there is a younging of stratigraphy as the Kootenay Arc is entered, from Mesoproterozoic BPSG rocks in the core of the Purcell Anticlinorium to Neoproterozoic and Paleozoic strata in the Kootenay Arc. However, structurally the interface occurs east of the unconformity between the WSG and the BPSG, as indicated by the development of Kootenay Arc-type structures, which are developed within BPSG rocks beneath the unconformity. In terms of metamorphism, there is no discernable change in metamorphic grade across the unconformity between the WSG and BPSG, both regions falling in the biotite zone. Constraining the timing of peak metamorphism in the interface zone is underpinned by the interplay between porphyroblast growth and deformation. Based on these relationships, the metamorphic interface roughly coincides with the structural interface. However, the absence of porphyroblasts makes it difficult to tightly constrain the metamorphic interface within this region. Work in progress on Ar/Ar cooling ages in biotite and muscovite from across the study area will further constrain the location and nature of this multifaceted interface.

Future Work

Kootenay Arc-type structures observed during fieldwork associated with this project require correlation with structures identified in previous studies of deformation within the Kootenay Arc by Moynihan and Pattison (2013), and Webster and Pattison (2018). Synthesizing observations presented in this paper with those of Moynihan and Pattison (2013), and Webster and Pattison (2018) will more tightly constrain the timing of metamorphism. The aim is to understand the way in which Mesozoic metamorphism affected rocks along the margin of North America at the time of Cordilleran orogenesis. Recently acquired Ar/Ar ages in biotite and muscovite across the field area will allow for an assessment of the marked contrast in exhumation history across the Kootenay Arc–Purcell Anticlinorium interface, and how it relates to the stratigraphic, structural and metamorphic changes across the transition. This improved understanding will provide better constraints on the deformational, metamorphic and cooling histories of these two adjacent, regional-scale structural domains. In turn, elucidating their geological evolution will provide better constraints on the formation of the many mineral deposits in the

region and improve the understanding of the different types of mineralization that occur across the interface.

Acknowledgments

The authors would like to thank Geoscience BC for their continued support of this study. This work was funded by a Geoscience BC grant to D. Pattison and N. Rioseco, and a Natural Sciences and Engineering Research Council of Canada (NSERC) Discovery Grant to D. Pattison. They would also like to thank J. Forshaw and C. Padget for reviewing this manuscript, as well as G. Costigan and M. Lazarotto for additional help and insightful conversation.

References

- Archibald, D.A., Glover, J.K., Price, R.A., Farrar, E. and Carmichael, D.M. (1983): Geochronology and tectonic implications of magmatism and metamorphism, southern Kootenay Arc and neighbouring regions, southeastern British Columbia, part I: Jurassic to mid-Cretaceous; Canadian Journal of Earth Sciences, v. 20, p. 1891–1913.
- Archibald, D.A., Krough, T.E., Armstrong, R.L. and Farrar, E. (1984): Geochronology and tectonic implications of magmatism and metamorphism, southern Kootenay Arc and neighbouring regions, southeastern British Columbia, part II: Mid-Cretaceous to Eocene; Canadian Journal of Earth Sciences, v. 21, p. 567–583.
- Bond, G.C., Christie-Blick, N., Kominz, M.A. and Devlin, W.J. (1985): An early Cambrian rift to post-rift transition in the Cordillera of western North America; Nature, v. 315, p. 742–746.
- Brown, D.A. and Stinson, P. (1995): Geological Mapping of the Yahk Map Area, southeastern British Columbia: an update (82F/1); BC Ministry of Energy, Mines and Petroleum Resources, BC Geological Survey, Geological Fieldwork 1994, Paper 1995-1, p. 111–125.
- Colpron, M., Logan, J.L. and Mortensen, J.K. (2002): U-Pb zircon age constraint for late Neoproterozoic rifting and initiation of the lower Paleozoic passive margin of western Laurentia; Canadian Journal of Earth Sciences, v. 39, p. 133–143.
- De Paoli, G.R. and Pattison, D.R.M. (2000): Thermobarometric calculation of peak metamorphic conditions of the Sullivan deposit; *in* The Geological Environment of the Sullivan Deposit, British Columbia, J.W. Lydon, J.F. Stack, T. Höy and M.E. Knapp (ed.), Geological Association of Canada, Mineral Deposits Division Special Volume No. 1, p. 272–280.
- Harrison, J.E. (1972): Precambrian Belt basin of northwestern United States: its geometry, sedimentation and copper occurrences; Geological Society of America Bulletin, v. 83, p. 1215–1240.
- Höy, T. (1989): The age, chemistry and tectonic setting of the Middle Proterozoic Moyie sills, Purcell Supergroup, southeastern British Columbia; Canadian Journal of Earth Sciences, v. 26, p. 2305–2317.
- Höy, T., Price, R.A., Legun, A., Grant, B. and Brown, D. (1995): Purcell Supergroup, southwestern British Columbia (NTS 82G, F, E; 82J/SW, 82K/SE); BC Ministry of Energy, Mines and Petroleum Resources, BC Geological Survey, Geoscience Map 1995-1, scale 1:250 000.

- Hunt, G. (1962): Time of Purcell eruption in southeastern British Columbia and southwestern Alberta; *Bulletin of Canadian Petroleum Geology*, v. 10, p. 438–442.
- Klepacki, D.W. (1985): Stratigraphy and structural geology of the Goat Range area, southeastern British Columbia; Ph.D. thesis, Massachusetts Institute of Technology, Cambridge, Massachusetts, 268 p.
- Leclair, A.D. (1982): Preliminary results on the stratigraphy, structure, and metamorphism of central Kootenay Arc rocks, southeastern British Columbia; *in* Current Research, Part A, Geological Survey of Canada, Paper 82-1A, p. 45–49.
- Leclair, A.D., Parrish, R.R. and Archibald, D.A. (1993): Evidence for Cretaceous deformation in the Kootenay Arc based on U-Pb and $^{40}\text{Ar}/^{39}\text{Ar}$ dating, southeastern British Columbia; *in* Current Research, Part A, Geological Survey of Canada, Paper 93-1A, p. 207–220.
- Leech, G.B. (1962): Metamorphism and granitic intrusions of Precambrian age in southeastern British Columbia; Geological Survey of Canada, Paper 62-13, 11 p.
- Leech, G.B. (1967): K-Ar Isotopic Ages, Report 7, British Columbia; *in* Age Determinations and Geological Studies, R.K. Wanless, R.D. Stevens, G.R. Lachance, C.M. Edmonds (ed.), Geological Survey of Canada, Paper 66-17, p. 9–10.
- McFarlane, C.R.M. (2015): A geochronological framework for sedimentation and Mesoproterozoic tectonomagmatic activity in lower Belt-Purcell rocks exposed west of Kimberley, British Columbia; *Canadian Journal of Earth Sciences*, v. 52, p. 444–465, URL <<https://doi.org/10.1139/cjes-2014-0215>> [November 2018].
- McFarlane, C.R.M. and Pattison, D.R.M. (2000): Geology of the Matthew Creek metamorphic zone, southeast British Columbia: a window into Middle Proterozoic metamorphism in the Purcell Basin; *Canadian Journal of Earth Sciences*, v. 37, p. 1073–1092, URL <<https://doi.org/10.1139/e00-018>> [November 2018].
- McMechan, M.E. and Price, R.A. (1982): Superimposed low-grade metamorphism in the Mount Fisher area, southeastern British Columbia—implications for the East Kootenay orogeny; *Canadian Journal of Earth Sciences*, v. 19, p. 476–489.
- Monger, J.W.H., Price, R.A. and Templeman-Kluit, D.J. (1982): Tectonic accretion and the origin of the two major metamorphic and plutonic belts in the Canadian Cordillera; *Geology*, v. 10, p. 70–75.
- Moynihan, D.P. and Pattison, D.R.M. (2013): Barrovian metamorphism in the central Kootenay Arc, British Columbia: petrology and isograd geometry; *Canadian Journal of Earth Sciences*, v. 50, p. 769–794, URL <<https://doi.org/10.1139/cjes-2012-0083>> [November 2018].
- Pattison, D.R.M. and Seitz, J.D. (2012): Stabilization of garnet in metamorphosed altered turbidites near the St. Eugene lead-zinc deposit, southeastern British Columbia: equilibrium and kinetic controls; *Lithos*, v. 134–135, p. 221–235, URL <<https://doi.org/10.1016/j.lithos.2011.12.007>> [November 2018].
- Price, R.A. (1964): The Precambrian Purcell system in the Rocky Mountains of southern Alberta and British Columbia; *Bulletin of Canadian Petroleum Geology*, v. 12, p. 399–426.
- Read, P.B., Woodsworth, G.J., Greenwood, H.J., Ghent, E.D. and Evenchick, C.A. (1991): Metamorphic map of the Canadian Cordillera; Geological Survey of Canada, Map 1714A, scale 1:2 000 000.
- Unterschutz, J.L.E., Creaser, R.A., Erdmer, P., Thompson, R.I. and Daughtry, K.L. (2002): North American margin origin of Quesnel terrane strata in the southern Canadian Cordillera: inferences from geochemical and Nd isotopic characteristics of Triassic metasedimentary rocks; *Geological Society of America Bulletin*, v. 114, no. 4, p. 462–475.
- Warren, M.J. (1997): Crustal extension and subsequent crustal thickening along the Cordilleran rifted margin of ancestral North America, western Purcell Mountains, southeastern British Columbia; Ph.D. thesis, Queen’s University, 477 p.
- Webster, E.R. and Pattison, D. (2018): Spatially overlapping episodes of deformation, metamorphism, and magmatism in the southern Omineca belt, southeastern British Columbia; *Canadian Journal of Earth Sciences*, v. 55, no. 1, p. 84–110, URL <<https://doi.org/10.1139/cjes-2017-0036>> [November 2018].
- Wheeler, J.O. and McFeely, P. (1991): Tectonic assemblage map of the Canadian Cordillera and adjacent parts of the United States of America; Geological Survey of Canada, Map 1712A, scale 1:2 000 000, URL <<https://doi.org/10.4095/133549>> [November 2018].

Microbial-Community Fingerprints as Indicators for Buried Mineralization, Southern British Columbia

R.L. Simister, Department of Microbiology and Immunology, The University of British Columbia, Vancouver, BC, rlsimister@gmail.com

B.P. Iulianella Phillips, Mineral Deposits Research Unit (MDRU), Department of Earth, Ocean and Atmospheric Sciences, The University of British Columbia, Vancouver, BC

P.A. Winterburn, Mineral Deposits Research Unit (MDRU), Department of Earth, Ocean and Atmospheric Sciences, The University of British Columbia, Vancouver, BC

S.A. Crowe, Departments of Microbiology and Immunology, and Earth, Ocean and Atmospheric Sciences, The University of British Columbia, Vancouver, BC

Simister, R.L., Iulianella Phillips, B.P., Winterburn, P.A. and Crowe, S.A. (2019): Microbial-community fingerprints as indicators for buried mineralization, southern British Columbia; *in* Geoscience BC Summary of Activities 2018: Minerals and Mining, Geoscience BC, Report 2019-1, p. 15–26.

Introduction

As global population grows and modernizes, demand for mineral resources is expanding (Kesler, 2007). At the same time, existing orebodies are being exhausted, while the frequency of new discoveries of exposed or partially exposed deposits diminishes. Demand for mineral resources must therefore be met through the discovery and development of buried or concealed mineral deposits. Although mineral resource extraction supported the core of the Canadian economy for more than a century—currently contributing \$56 billion to Canada’s GDP and providing 19% of its goods exports (The Mining Association of Canada, 2018)—its ability to do so relies on continued discovery of mineral deposits that may be concealed by overburden. Finding these mineral deposits beneath exotic overburden consisting of glacial and preglacial sediments remains a fundamental and widespread challenge to mineral exploration in Canada (Anderson et al., 2012; Ferbey et al., 2014).

New and innovative techniques that complement, enhance or even surpass traditional techniques to define the surface expression of buried mineralization could minimize the cost of exploration and help in targeting drilling activities (Kelley et al., 2006). Several recent studies in British Columbia (BC) have demonstrated the potential for new surface geochemical techniques to lead to the discovery of concealed orebodies. These include indicator minerals (Plouffe et al., 2013), soil partial-leach and selective-extraction geochemistry on multiple soil horizons (e.g., Bissig and Riquelme, 2010), halogen-element detection (e.g., Heberlein and Dunn, 2017), till geochemistry (Reid et

al., 2009; Reid and Hill, 2010) and biogeochemistry (Reid et al., 2009; Reid and Hill, 2010). Each geochemical technique and media type has both strengths and weaknesses in identifying buried mineralization.

In particular, geochemical signatures generated from orientation surveys over known deposits are typically noisy with poor anomaly to background resolution (Stanley, 2003), show poor reproducibility and have element patterns that are sometimes difficult to reconcile with mineral-deposit chemistry and known trace-element mobility patterns (Heberlein and Samson, 2010). The limited mechanistic understanding of these techniques has led to compromised utility by the mineral exploration industry, resulting in less return on investment than possible. Shortfalls in many of these commercial techniques to repeat performance shown in orientation surveys over known mineralization has, in large part, resulted in questioned use and reliability by major exploration companies. Despite these issues, there is sufficient empirical evidence to indicate causative links between mineralization beneath transported cover and the presence of geochemical gradients in the surface environment (Hamilton, 1998; Kelley et al., 2006; Nordstrom, 2011).

Although much less explored, biological anomalies may be robust indicators of buried mineralization, and such anomalies may be detectable through low-cost, high-throughput geobiological surveys (Kelley et al., 2006). Microorganisms kinetically enhance and exploit thermodynamically favourable geochemical reactions, including the dissolution and formation of diverse minerals, to support their metabolism and growth in nearly every low-temperature geological setting (Falkowski et al., 2008). They are acutely sensitive, often rapidly responding to the dynamics of chemical and physical gradients in the environment. Subtle

This publication is also available, free of charge, as colour digital files in Adobe Acrobat® PDF format from the Geoscience BC website: <http://www.geosciencebc.com/s/SummaryofActivities.asp>.

changes in mineral bioavailability, for example, can be reflected in dramatic shifts in composition and activity of microbial communities (Fierer, 2017). This can be seen at the global scale as marine-phytoplankton communities respond to traces of iron in seawater, a process that can be viewed as chlorophyll plumes via remote sensing (Fuhrman, 2009). Application of modern sequencing technologies allows high-throughput profiling of the taxonomic diversity and metabolic potential of soil microbial communities across subtle, and often poorly resolved, geochemical gradients. Microbial-community profiles thus have a strong potential to resolve chemical and physical differences in sample suites that are not readily discernible through conventional geochemical and geophysical surveys. In residual terrains, for example, where chemical gradients are high, changes in bacterial population have been clearly demonstrated (e.g., Southam and Saunders, 2005; Reith and Rogers, 2008).

Even outdated techniques with low throughput and resolution, such as Denaturing Gradient Gel Electrophoresis (DGGE), that can produce a crude microbial-community ‘fingerprint’ (Wakelin et al., 2012) reveal changes in bacterial communities in soils over buried volcanogenic massive-sulphide (VMS) deposits. The advent of high-throughput next-generation sequencing (NGS) platforms over the last decade has transformed the capacity to interrogate the molecular fingerprints of microbial communities (Binladen et al., 2007; Zhou et al., 2015). Application of NGS technologies thus allows profiling of the taxonomic diversity and metabolic potential of soil microbial communities across defined survey areas. Given that each soil sample comprises thousands of microbial taxa, each containing hundreds to thousands of genes sensing and interacting with the surrounding soil environment (Fierer, 2017), the statistical power of this approach to identify anomalies is unprecedented.

The authors therefore propose that high-throughput sequencing technologies may enable use of soil microbial-community profiling as a robust, efficient and cost-effective tool to identify and locate buried mineral deposits in BC. In a pilot study, the use of soil microbial-community fingerprinting with modern DNA sequencing technologies was employed to find buried mineral deposits (Simister et al., 2017). This pilot study has shown that exposure of soil microbial communities to constituents commonly associated with mineral deposits elicits a response detectable on laboratory time scales of several weeks. The strong microbial responses observed are encouraging signs for the use of microbial-community fingerprinting in mineral-deposit exploration.

British Columbia is host to numerous mineral deposits of economic value, including a wealth of Cu-porphyry mineralization. Successful exploration for these deposits is de-

pendent on technologies that can detect mineralization through thick sequences of Quaternary glacial sediments. The province is an ideal region to evaluate microbial-community sequencing as an exploration methodology for ‘seeing’ through overburden, as multiple field sites can be tested. Data have been collected from three different Cu-porphyry systems (Figure 1): 1) the Deerhorn Cu-Au porphyry of Consolidated Woodjam Copper Corp. in central BC, 2) the Highland Valley Copper Highmont South Cu-Mo porphyry of Teck Resources Ltd. in south-central BC, and 3) the Mount Washington Cu-Au porphyry on Vancouver Island.

Methodology

Field Locations

Sampling for geochemical and microbiological analysis was completed in July 2017 for both the Deerhorn Cu-Au porphyry and the Highland Valley Copper (HVC) Highmont South Cu-Mo porphyry. An additional Cu-Au porphyry at Mount Washington on Vancouver Island has recently been sampled, with fieldwork concluding in mid-October 2018.

The Deerhorn survey consisted of three transects across subsurface mineralization (Figure 2), with overlying glacial sediments ranging from 10 to 60 m in thickness and an extremely variable surficial environment with respect to regolith and vegetation (Rich, 2016). Mineralization is hosted primarily in monzonite intrusions as disseminated and vein-hosted Cu and Au, with the main zone of mineralization located beneath the thick glacial overburden (Rich, 2016).

The Highland Valley sampling program, consisting of three transects perpendicular to the main mineralized cores in the

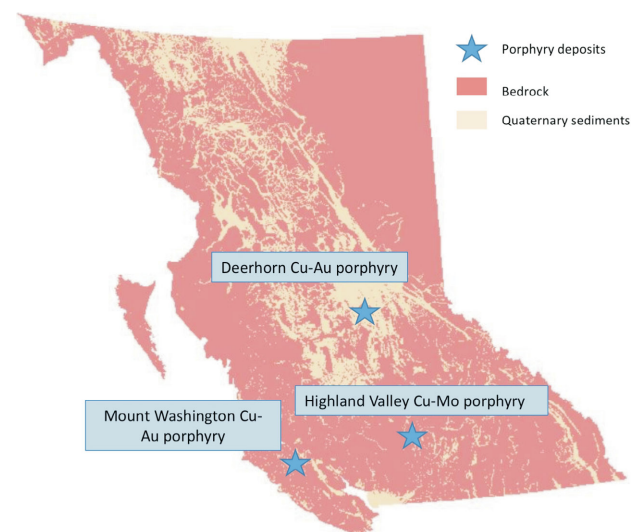


Figure 1: Locations of deposits from which data have been collected for this study.

Highmont South region (Figure 3), was carried out over two separate field surveys. The mineralization is expressed in a gradational change from Cu-sulphide-rich minerals in the centre (bornite, chalcopyrite) to a primarily Fe-sulphide (pyrite only)-rich outer zone (Chouinard, 2018), with an

average till thickness above mineralization of 5 m. Sample sites were selective, as the till in the region was variable, with changes in vegetation, anthropogenic influences and areas that have been appreciably waterlogged (Chouinard, 2018).

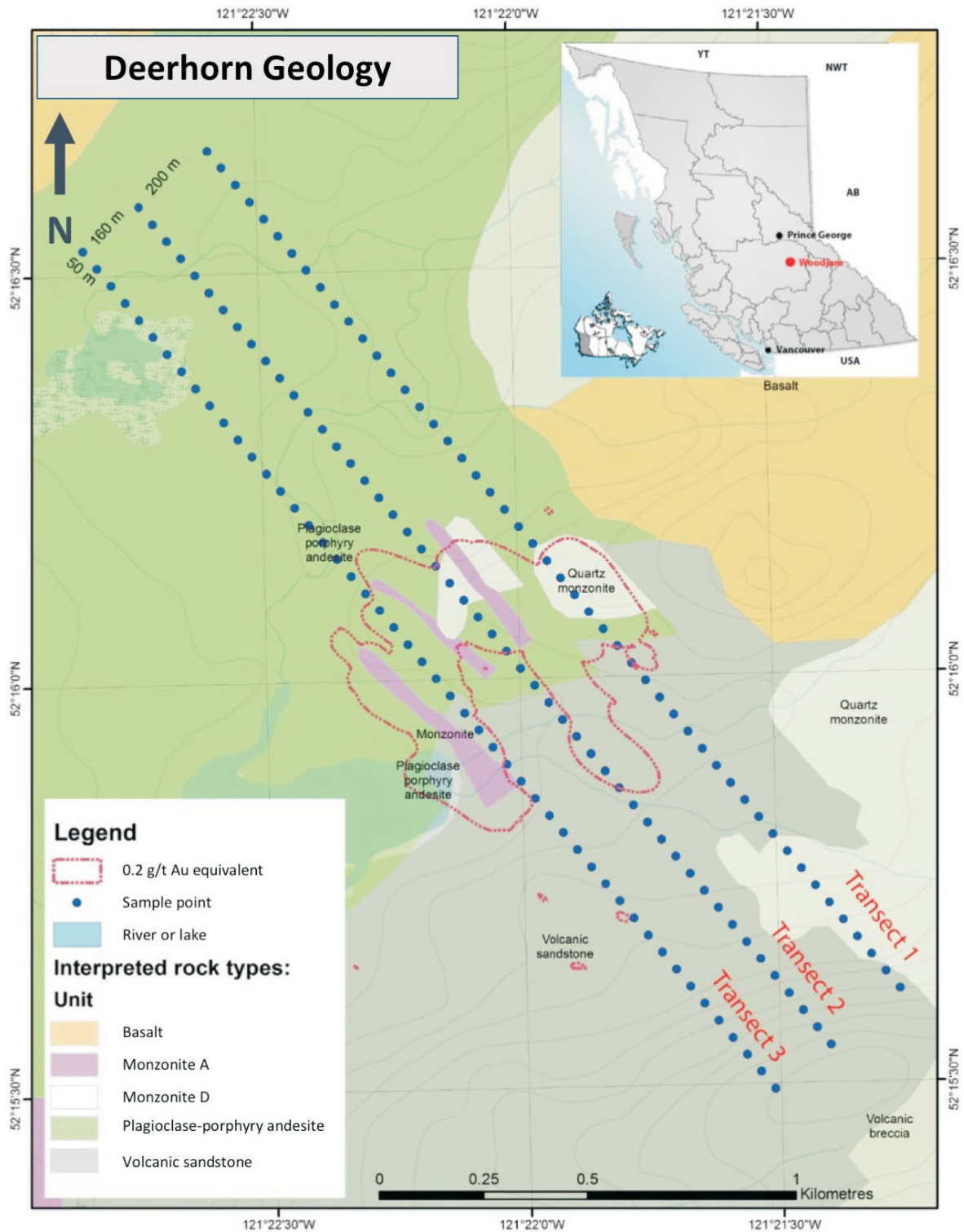


Figure 2: Bedrock geology of the Deerhorn Cu-Au–porphyry deposit of Consolidated Woodjam Copper Corp. (Rich and Winterburn, 2016). Microbial analysis was performed on every sample point.

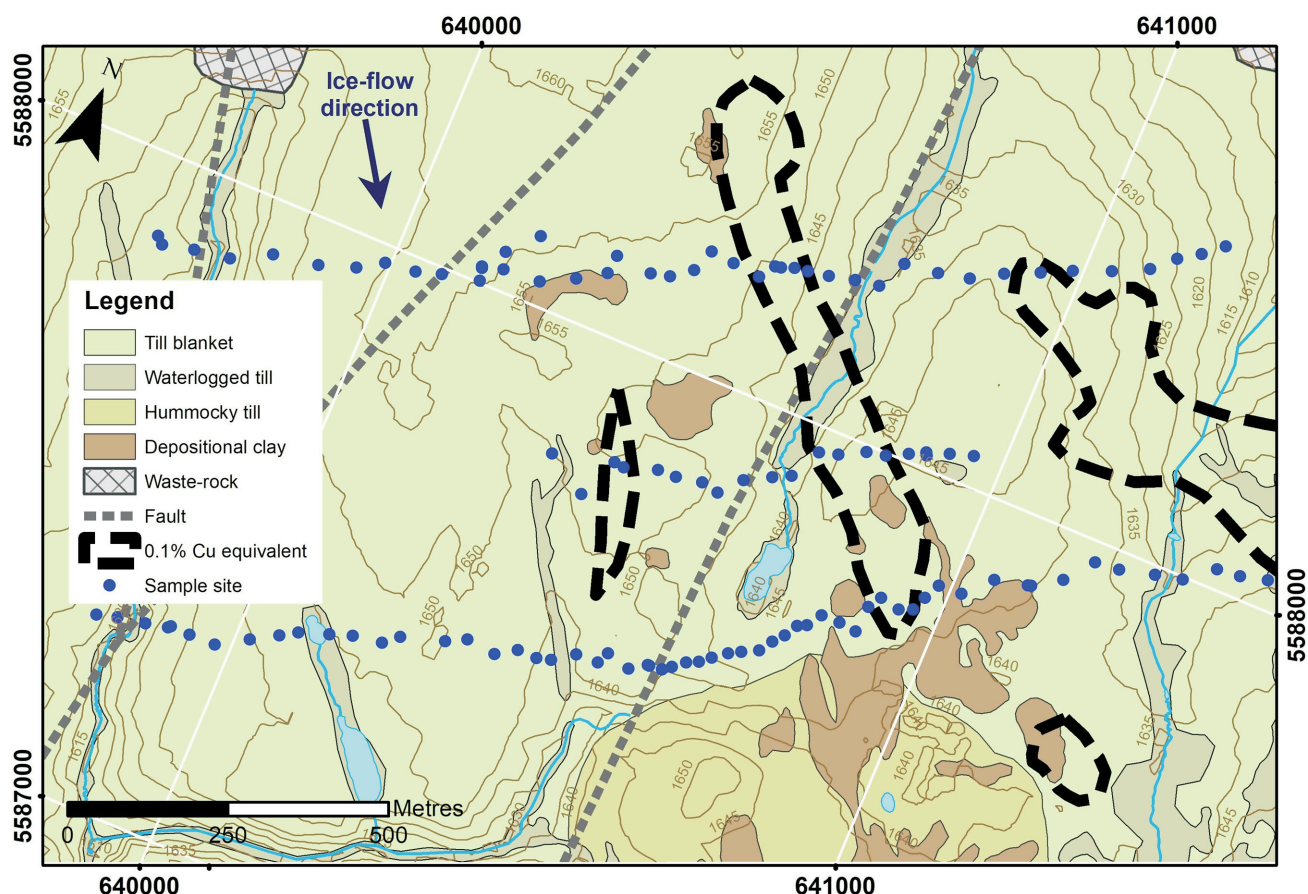


Figure 3: Surficial deposits in the Highmont South region of the Highland Valley Copper Cu-Mo–porphyry deposit of Teck Resources Ltd. (modified from Chouinard, 2018). Microbial analysis was performed on every site.

Soil Sampling

Soils for microbial-community analysis were sampled with sterilized equipment without field screening, to preserve the microbial community as much as possible. Descriptions were documented for in situ physicochemical variables at each sample site for every observed soil horizon in the profile. Soils at the field sites are derived from the breakdown of till by surface-weathering processes in situ, so the soils are considered residual weathering products of the till blanket. The B-horizon soils (Figure 4) were targeted for microbial soil samples, although multiple horizons (including O, Ah, Ae, and C) were taken where possible. Soil samples were also collected for geochemical analysis. Field measurements consisted of slurry tests for pH and oxidation-reduction potential (ORP) after field sieving through a 6 mm screen. Geochemical samples for each site were sent to either Bureau Veritas Minerals (Vancouver, BC) or ALS Chemex (Vancouver, BC) for acid-digestion and subsequent analysis via ICP-MS, and the microbial samples were frozen at -4°C upon return to the laboratory at The University of British Columbia (UBC) prior to DNA extraction. A subset of the Mount Washington microbial samples has been preserved to perform a cell-count analysis. A small amount of each soil sample was transferred with aseptic in-

struments into smaller vials containing an RNA preservative.

DNA Extraction

Microbial-community DNA was extracted from samples using a MO BIO Laboratories Inc. PowerMax[®] Soil DNA Isolation Kit; as per manufacturer’s instructions, approximately 0.25 g of soil was used. Resulting DNA was stored at -20°C . The quality and quantity of genomic DNA were measured on a ThermoFisher Scientific NanoDrop[®] ND-1000 spectrophotometer and by using Invitrogen[™] PicoGreen[™] (Quant-iT[™] dsDNA Assay Kit) dye.

Small Subunit Ribosomal RNA (SSU rRNA) Gene Amplification and iTag Sequencing

Bacterial and archaeal 16S rRNA gene fragments from the extracted genomic DNA were amplified using primers 515f and 806r (Apprill et al., 2015). Sample preparation for amplicon sequencing was performed as described by Kozich et al. (2013). In brief, the aforementioned 16S rRNA gene-targeting primers, complete with Illumina adapter, an 8-nucleotide index sequence, a 10-nucleotide pad sequence, a 2-nucleotide linker and the gene-specific primer, were used in equimolar concentrations together with



Figure 4. Typical soil profiles for porphyry deposits: **a)** horizons at the Deerhorn Cu-Au porphyry deposit of Consolidated Woodjam Copper Corp., and **b)** Highmont South property at the Highland Valley Copper Cu-Mo–porphyry deposit of Teck Resources Ltd. (Chouinard, 2018; Rich, 2016).

Deoxynucleotide triphosphate (dNTPs), Polymerase chain reaction (PCR) buffer, MgSO_4 , $2\text{U}/\mu\text{L}$ ThermoFisher high-fidelity platinum Taq DNA polymerase and PCR-certified water to a final volume of $50\ \mu\text{L}$. PCR amplification was performed with an initial denaturing step of 95°C for 2 min, followed by 30 cycles of denaturation (95°C for 20 s), annealing (55°C for 15 s) and elongation (72°C for 5 min), with a final elongation step at 72°C for 10 min. Equimolar concentrations of amplicons were pooled into a single library. The amplicon library was analyzed on an Agilent Bioanalyzer using the High-Sensitivity DS DNA Assay to determine approximate library fragment size, and to verify library integrity. Library pools were diluted to $4\ \text{nM}$ and denatured into single strands using fresh $0.2\ \text{N}$ NaOH, as recommended by Illumina. The final library was loaded at a concentration of $8\ \text{pM}$, with an additional PhiX spike-in of 5–20%. Sequencing was conducted on the MiSeq platform at the Sequencing + Bioinformatics Consortium, The University of British Columbia, Vancouver, BC (The University of British Columbia, 2018).

Informatics

Sequences were processed using the mothur (Schloss et al., 2009) MiSeq protocol (Kozich et al., 2013). Briefly, sequences were removed from the analysis if they contained ambiguous characters, had homopolymers longer than 8 base pairs and did not align to a reference alignment of the correct sequencing region. Unique sequences, and their frequency in each sample, were identified and then a pre-clustering algorithm was used to further de-noise sequences within each sample (Schloss et al., 2011). Unique sequences were identified and aligned against a SILVA alignment (mothur Project, 2018a). Sequences were chimera checked using VSEARCH (Rognes et al., 2016) and reads were then clustered into 97% operational taxonomic units (OTUs) using the Matthews correlation coefficient (MCC; Westcott and Schloss, 2017). Operational taxonomic units were classified using the SILVA reference taxonomy database (release 132; mothur Project, 2018b).

Results and Discussion

Soil is one of the most complex and diverse microbial habitats, with merely 1 g containing up to 10^{10} cells and 10^4 bacterial species (Torsvik and Øvreås, 2002; Roesch et al., 2007). The current study’s approach relies on the ability to capture this diversity through next-generation sequencing technologies. In microbiology, the assessment of diversity often involves calculation of species richness (number of species present in a sample; Magurran, 2013). The most common approach is to assign 16S rRNA sequences into OTUs and represent these as rarefaction curves, which plot the cumulative number of OTUs captured as a function of sampling effort, and therefore indicate the OTU richness in a given set of samples. Other common methods include

nonparametric analysis, such as Chao1, which estimates the overall sample diversity (also known as alpha diversity; Hughes et al., 2001).

The current study extracted microbial-community DNA from soil transects at Deerhorn and Highland Valley Copper (Figures 2, 3) and sequenced the 16S rRNA gene. Samples taken from Mount Washington (Figure 1) are currently undergoing DNA extraction. Analysis of these sequences reveals that the number of observed OTUs (hereafter referred to as species) is 2417 ± 344 (range 1041–3044), with an alpha diversity (Chao1 index) of 4015 ± 814 (range

1784–5666; Figure 5a, b), at Deerhorn and 2671 ± 445 (range 1068–3768), with an alpha diversity (Chao1 index) of 4066 ± 710 (range 1663–5763) (Figure 4a, b), at Highland Valley Copper, indicating that the sequencing coverage was sufficient to capture 65% of the microbial-community diversity. These levels of diversity are well in line with diversity commonly observed in soils (Thompson et al., 2017). These measurements dispel the dogma that extremely high diversity in soil microbial communities renders them intractable to molecular-based microbial-community analysis. There was no pronounced difference in

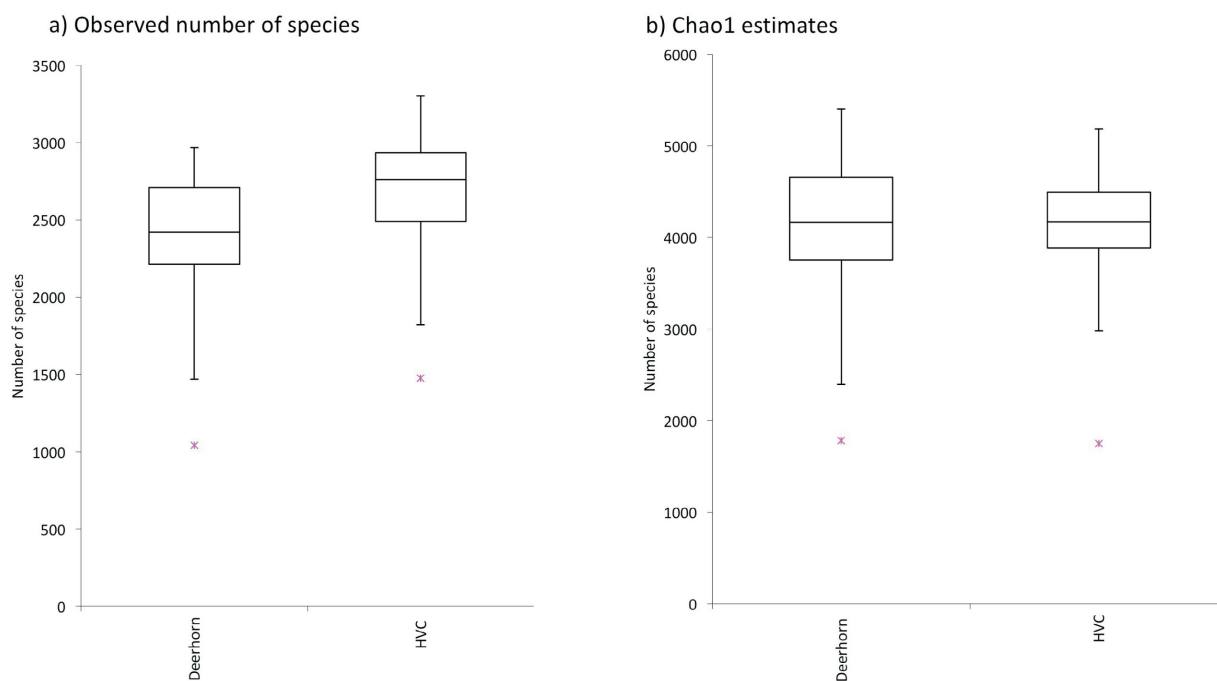


Figure 5. Boxplots for Deerhorn and Highland Valley Copper sites of **a)** observed number of species, and **b)** Chao1 richness estimates. Outliers indicated by pink 'x' symbols.

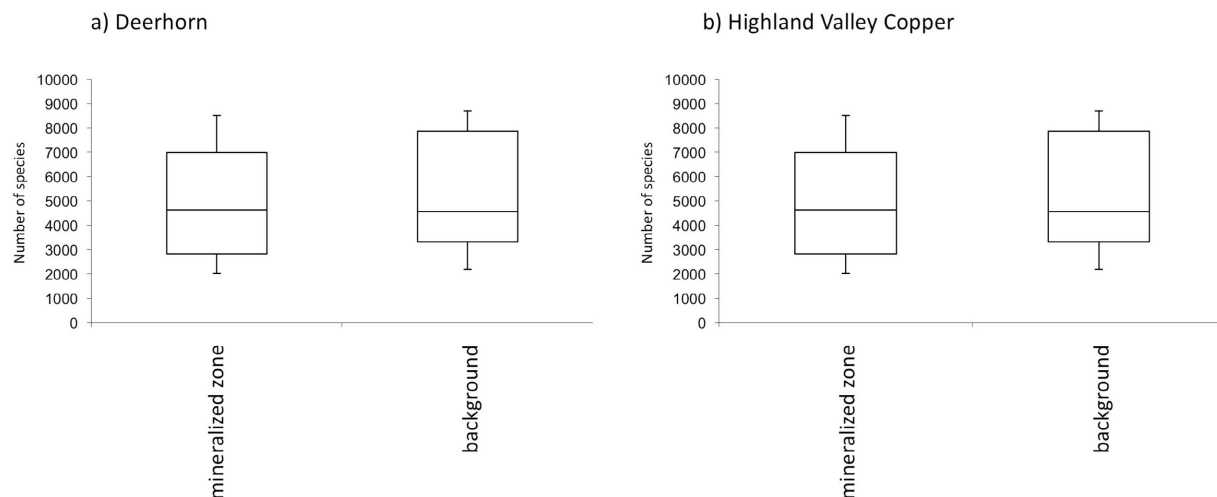


Figure 6. Boxplots of observed number of species in the mineralized zone compared to the rest of the site for **a)** Deerhorn, and **b)** Highland Valley Copper.

species richness (i.e., the number of species in a given sample) across the mineralized zone at both Deerhorn and Highland Valley Copper (Figure 6). The study's measurements demonstrate that soil diversity can be captured through next-generation sequencing technologies, which bodes well for the approach and imparts enormous and unprecedented statistical power to community profiles as anomaly indicators.

The number of reads per microbial phylum was normalized to total read number for a given sample and expressed as a percentage of the total reads from that sample (Figure 7). Most microbial-community members belong to the Proteobacteria, Acidobacteria and Verrucomicrobia phyla at both sites (Figure 7). The relative proportions are consistent with previous studies on soil ecosystems (Choi et al., 2017, Fierer, 2017). This high-level taxonomic analysis reveals strong similarities across all samples, thus giving confidence that the analyses are not overwhelmed by intersample variability arising because of the very high levels of microbial diversity and chemical and physical heterogeneity commonly found in soils. As found with the incubation experiments (Simister et al., 2017); however, the similarity across the samples suggests that discrimination between background and anomalous soils may be more sensitive with analyses at the genus or species level rather than at the phylum level.

Ongoing Work and Conclusions

The same soil microbial-community members that responded to the presence of mineralization in the field samples will be identified using the profiled microbiome compositions from the incubation experiments. For example, the species that increased in response to chalcopyrite ore and copper amendment relative to controls included *Rhodanobacteria* sp., SC-I-84 sp. and *Acidimicrobiales* sp. Therefore, particular attention will be paid to any anomalous abundances of these species over the mineralized zone at the field sites. Furthermore, work is progressing on standard hierarchical-clustering analysis of the samples to discriminate between background and anomalous values. Specifically, anomalous versus background communities will be identified using the multivariate statistical analyses (UniFrac, ANOSIM) commonly employed in microbial ecology (Lozupone and Knight, 2005; Ramette, 2007). Indicator analyses will be used to identify microbial taxa responsible for these community anomalies, an example of which is shown in Figure 8.

Application of modern sequencing technologies enabled profiling of the taxonomic diversity of soil microbiomes across subtle, and often poorly resolved, geochemical gradients that can develop in soils in response to mineralization beneath cover. Given that each soil sample comprises thousands of microbial taxa, each containing hundreds to

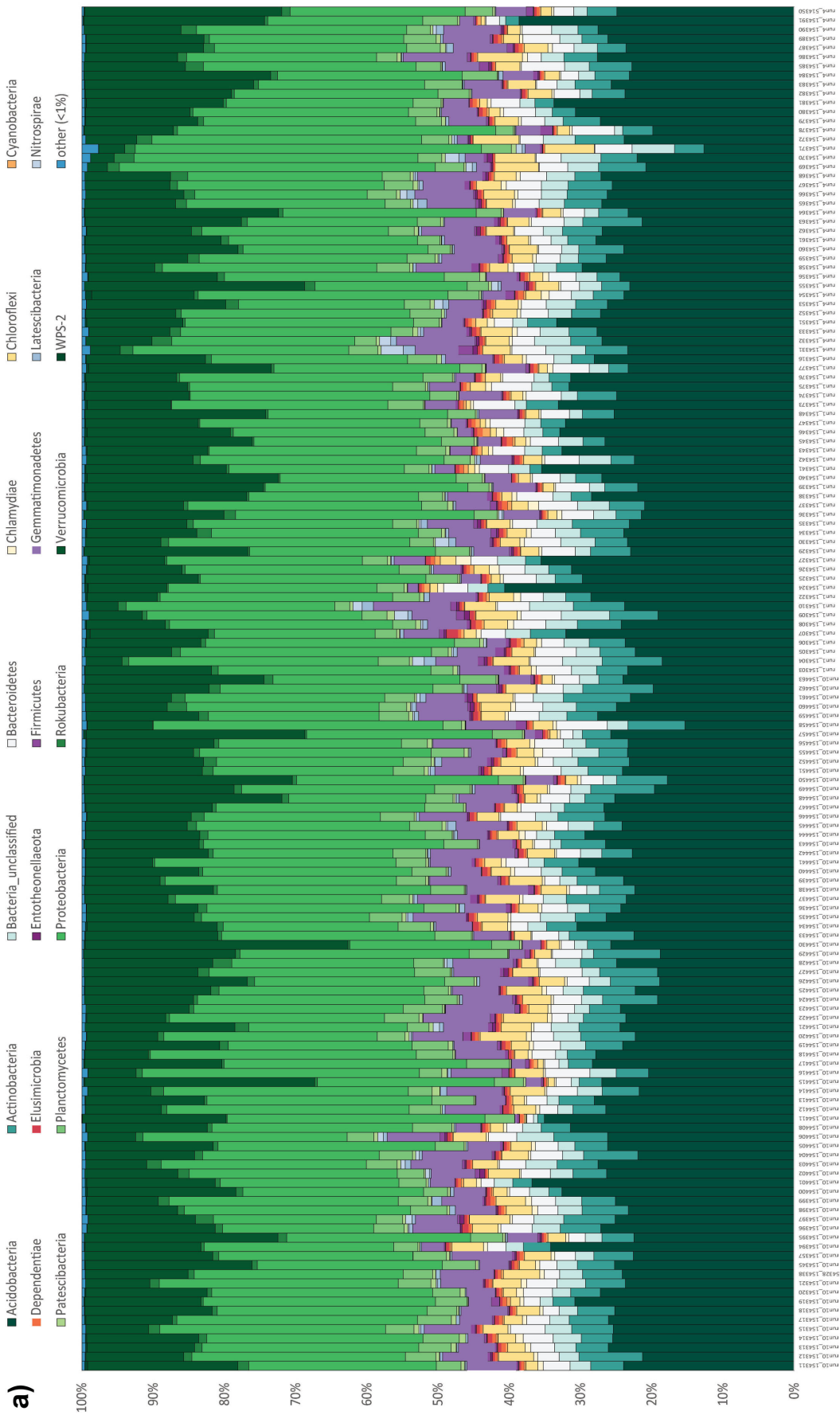
thousands of genes, the statistical power of this approach to identifying anomalies is unprecedented.

Acknowledgments

The first two authors contributed equally to the paper, the second author being the recipient of a 2018 Geoscience BC Student Scholarship. The authors thank S. Rich and R. Chouinard for sample collection and P. Kenward for peer review of the paper. Funding was provided by Geoscience BC.

References

- Anderson, R., Plouffe, A., Ferbey, T. and Dunn, C. (2012): The search for surficial expressions of buried Cordilleran porphyry deposits; background and progress in a new TGI-4 activity in the southern Canadian Cordillera; Geological Survey of Canada, Current Research 2012-7, 19 p., URL <<https://doi.org/10.4095/290295>> [December 2018].
- Apprill, A., McNally, S., Parsons, R. and Weber, L. (2015): Minor revision to V4 region SSU rRNA 806R gene primer greatly increases detection of SAR11 bacterioplankton; Aquatic Microbial Ecology, v. 75, no. 2, p. 129–137, URL <<https://doi.org/10.3354/ame01753>> [December 2018].
- Binladen, J., Gilbert, M.T.P., Bollback, J.P., Panitz, F., Bendixen, C., Nielsen, R. and Willerslev, E. (2007): The use of coded PCR primers enables high-throughput sequencing of multiple homolog amplification products by 454 parallel sequencing; PloS one, v. 2, no. 2, e197, URL <<https://doi.org/10.1371/journal.pone.0000197>> [December 2018].
- Bissig, T. and Riquelme, R. (2010): Andean uplift and climate evolution in the southern Atacama Desert deduced from geomorphology and supergene alunite-group minerals; Earth and Planetary Science Letters, v. 299, p. 447–457, URL <<https://pdfs.semanticscholar.org/544a/68c71f3e5c11447433bfa6543673542ebbeb.pdf>> [December 2018].
- Choi, J., Yang, F., Stepanauskas, R., Cardenas, E., Garoutte, A., Williams, R., Flater, J., Tiedje, J.M., Hofmockel, K.S. and Gelder, B. (2017): Strategies to improve reference databases for soil microbiomes; The ISME journal, v. 11, no. p. 829–834, URL <<https://www.ncbi.nlm.nih.gov/pmc/articles/PMC5364351/>> [December 2018].
- Chouinard, R.L.M. (2018): Surficial geochemical tools for Cu-Mo porphyry exploration in till-covered terrain; M.Sc. thesis, The University of British Columbia, URL <<https://open.library.ubc.ca/cIRcle/collections/ubctheses/24/items/1.0370934>> [December 2018].
- Falkowski, P.G., Fenchel, T. and Delong, E.F. (2008): The microbial engines that drive Earth's biogeochemical cycles; Science, v. 320, no. 5879, p. 1034–1039, URL <<http://www.sciencemag.org/cgi/pmidlookup?view=long&pmid=18497287>> [December 2018].
- Ferbey, T., Anderson, R.G. and Plouffe, A. (2014): An integrated approach to search for buried porphyry-style mineralization in central British Columbia using geochemistry and mineralogy: a TGI-4 project; Geological Survey of Canada, Current Research 2014-2, 15 p., URL <<https://doi.org/10.4095/293130>> [December 2018].
- Fierer, N. (2017): Embracing the unknown: disentangling the complexities of the soil microbiome; Nature Reviews Mi-



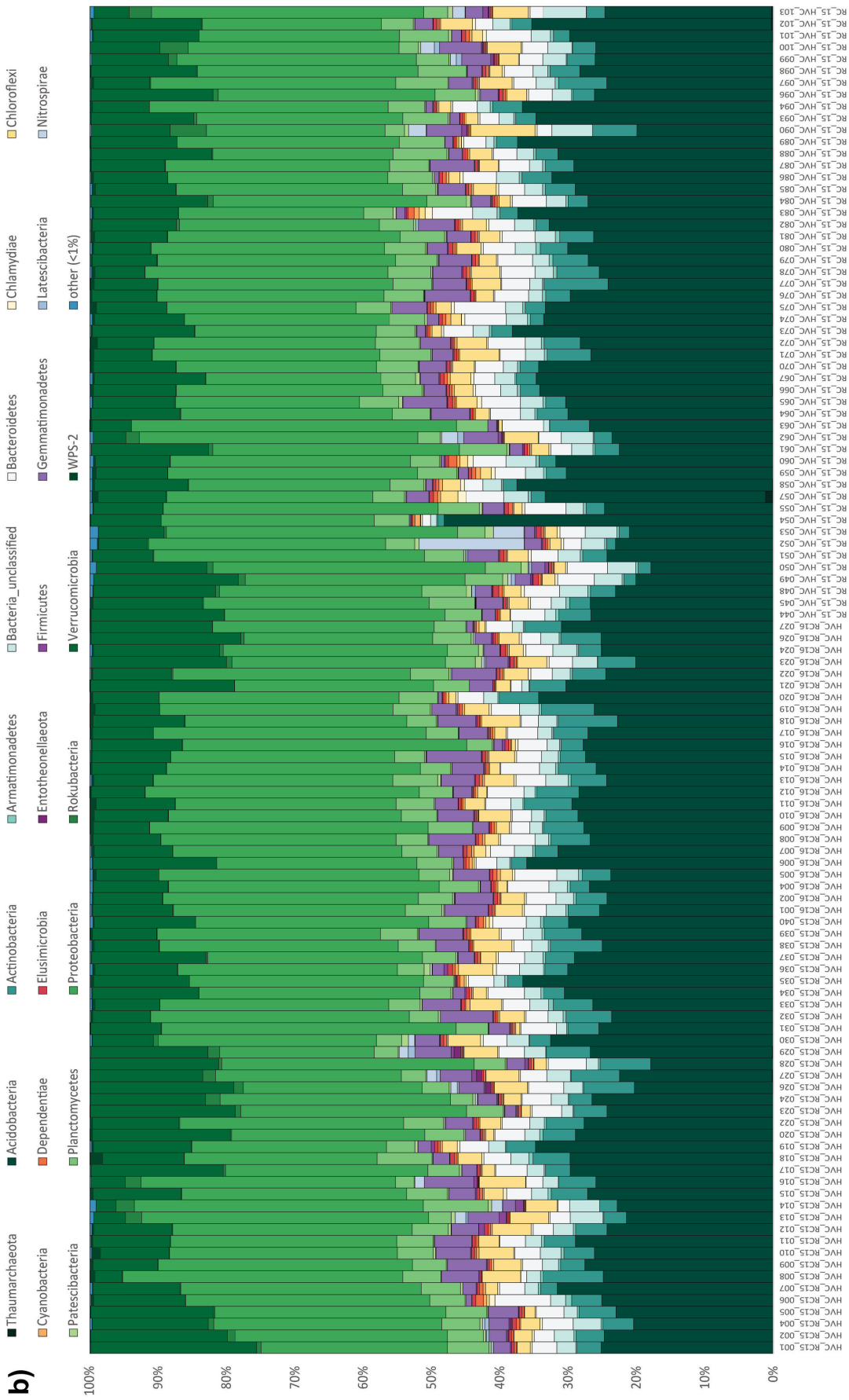


Figure 7. Distribution of 16S rRNA reads per phylum for each sample from **a)** Deerhorn, and **b)** Highland Valley Copper. The number of reads per phylum is calculated as a percentage of the total reads for each sample. The 'Other' grouping represents summed phyla that individually contributed <0.5% of the total number of reads per sample.

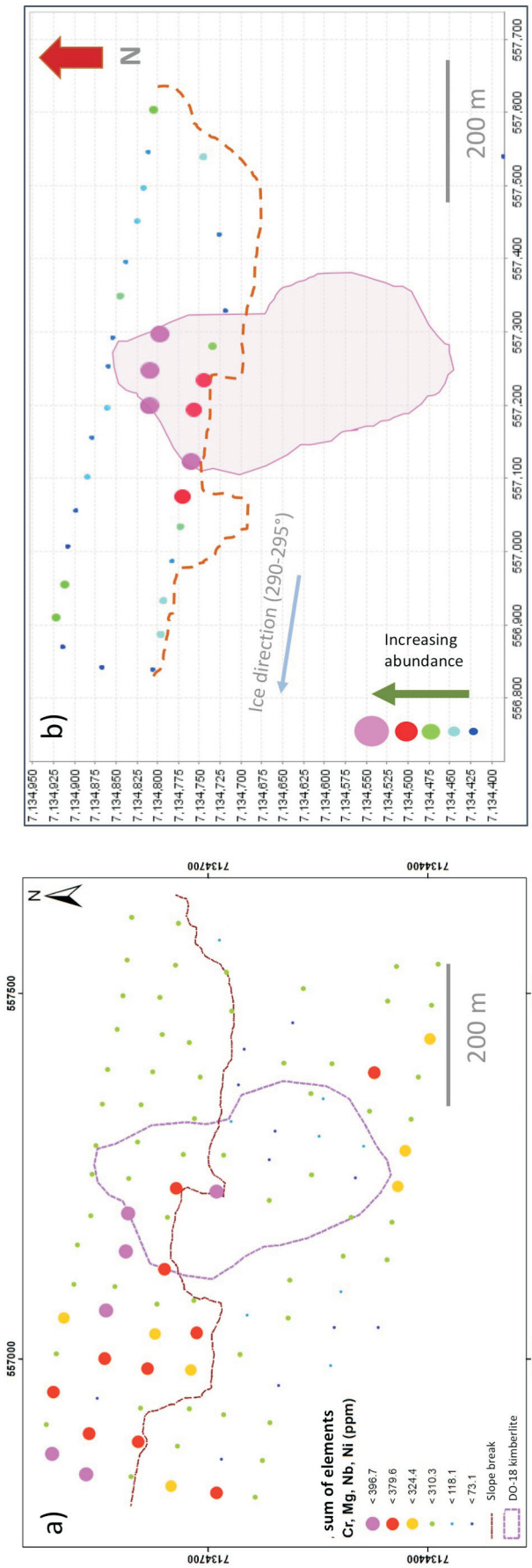


Figure 8. Microbial-community fingerprinting of data from the DO-18 diamondiferous kimberlite at Lac de Gras, Northwest Territories, shown with sample sites overlain on **a)** multi-element anomaly map for anomalous populations of Cr+Mg+Nb+Ni extracted by aqua regia, and **b)** anomaly map based on microbial 16S rRNA sequencing data. The community shift indicative of buried mineralization occurs directly over the kimberlite **(b)**, which contrasts with the traditional multi-element geochemical approach in which the kimberlite is picked up primarily down ice from the kimberlite **(a)**.

- crobiology, v. 15, p. 579–590, URL <<https://www.nature.com/articles/nrmicro.2017.87>> [December 2018].
- Fuhrman, J.A. (2009): Microbial community structure and its functional implications; *Nature*, v. 459, p. 193–199, URL <<https://www.nature.com/articles/nature08058>> [December 2018].
- Hamilton, S. (1998): Electrochemical mass-transport in overburden: a new model to account for the formation of selective leach geochemical anomalies in glacial terrain; *Journal of Geochemical Exploration*, v. 63, no. 3, p. 155–172, URL <<https://www.sciencedirect.com/science/article/pii/S0375674298000521>> [December 2018].
- Heberlein, D.R. and Dunn, C.E. (2017): Preliminary results of a geochemical investigation of halogen and other volatile compounds related to mineralization, part 2: Mount Washington epithermal gold prospect; *in* Geoscience BC Summary of Activities 2016, Geoscience BC, Report 2017-1, p. 151–159, URL <<http://www.geosciencebc.com/SummaryofActivities.asp>> [December 2018].
- Heberlein, D.R. and Samson, H. (2010): An assessment of soil geochemical methods for detecting copper-gold porphyry mineralization through Quaternary glaciofluvial sediments at the Kwanika central zone, north-central British Columbia; Geoscience BC, Report 2010-03, 89 p., URL <http://cdn.geosciencebc.com/project_data/GBC_Report2010-3/GBC_Report2010-03_Report.pdf> [December 2018].
- Kelley, D.L., Kelley, K.D., Coker, W.B., Caughlin, B. and Doherty, M.E. (2006): Beyond the obvious limits of ore deposits: the use of mineralogical, geochemical, and biological features for the remote detection of mineralization; *Economic Geology*, v. 101, p. 729–752, URL <<https://pubs.er.usgs.gov/publication/70030241>> [December 2018].
- Kesler, S.E. (2007): Mineral supply and demand into the 21st century; *in* Proceedings for a Workshop on Deposit Modeling, Mineral Resource Assessment, and Their Role in Sustainable Development, v. 1294 p. 55–62, URL <<https://pubs.usgs.gov/circ/2007/1294/reports/paper9.pdf>> [December 2018].
- Kozich, J.J., Westcott, S.L., Baxter, N.T., Highlander, S.K. and Schloss P.D. (2013): Development of a dual-index sequencing strategy and curation pipeline for analyzing amplicon sequence data on the MiSeq Illumina sequencing platform; *Applied and Environmental Microbiology*, v. 79, p. 5112–5120, URL <<https://www.ncbi.nlm.nih.gov/pmc/articles/PMC3753973/>> [December 2018].
- Lozupone, C. and Knight, R. (2005): UniFrac: a new phylogenetic method for comparing microbial communities; *Applied and Environmental Microbiology*, v. 71, p. 8228–8235, URL <<https://aem.asm.org/content/71/12/8228>> [December 2018].
- Magurran, A.E. (2013): *Measuring biological diversity*, Blackwell Science Ltd, John Wiley & Sons, Malden, Massachusetts, 264 p.
- mothur Project (2018a): Silva reference alignment; mothur Project, URL <http://www.mothur.org/wiki/Silva_reference_alignment> [November 2018].
- mothur Project (2018b): Silva reference files; mothur Project, URL <http://www.mothur.org/wiki/Silva_reference_files> [November 2018].
- Nordstrom, D.K. (2011): Hydrogeochemical processes governing the origin, transport and fate of major and trace elements from mine wastes and mineralized rock to surface waters; *Applied Geochemistry*, v. 26, p. 1777–1791, URL <<https://doi.org/10.1016/j.apgeochem.2011.06.002>> [December 2018].
- Plouffe, A., Ferbey, T., Anderson, R., Hashmi, S. and Ward, B. (2013): New TGI-4 till geochemistry and mineralogy results near the Highland Valley, Gibraltar, and Mount Polley mines, and Woodjam District: an aid to search for buried porphyry deposits; *in* Geological Survey of Canada, Open File 7473, 58 p., URL <<https://doi.org/10.4095/292907>> [December 2018].
- Ramette, A. (2007): Multivariate analyses in microbial ecology; *FEMS Microbiology Ecology*, v. 62, p. 142–160, URL <<https://www.ncbi.nlm.nih.gov/pmc/articles/PMC2121141/>> [December 2018].
- Reid, N. and Hill, S. (2010): Biogeochemical sampling for mineral exploration in arid terrains: Tanami gold province, Australia; *Journal of Geochemical Exploration*, v. 104, no. 3, p. 105–117, URL <<https://doi.org/10.1016/j.gexplo.2010.01.004>> [December 2018].
- Reid, N., Hill, S. and Lewis, D. (2009): Biogeochemical expression of buried gold mineralization in semi-arid northern Australia: penetration of transported cover at the Titania gold prospect, Tanami Desert, Australia; *Geochemistry: Exploration, Environment, Analysis*, v. 9, p. 267–273, URL <<https://doi.org/10.1144/1467-7873/09-194>> [December 2018].
- Reith, F. and Rogers, S. (2008): Assessment of bacterial communities in auriferous and non-auriferous soils using genetic and functional fingerprinting; *Geomicrobiology Journal*, v. 25, p. 203–215, URL <<https://www.tandfonline.com/doi/abs/10.1080/01490450802081846>> [December 2018].
- Rich, S. (2016): Geochemical mapping of porphyry deposits and associated alteration through transported overburden; M.Sc. thesis, The University of British Columbia, 467 p., URL <<https://open.library.ubc.ca/cIRcle/collections/ubctheses/24/items/1.0307413>> [December 2018].
- Roesch, L.F., Fulthorpe, R.R., Riva, A., Casella, G., Hadwin, A.K., Kent, A.D., Daroub, S.H., Camargo, F.A., Farmerie, W.G. and Triplett, E.W. (2007): Pyrosequencing enumerates and contrasts soil microbial diversity; *The ISME Journal*, v. 1, no. 4, p. 283–290, URL <<https://www.ncbi.nlm.nih.gov/pmc/articles/PMC2970868/>> [December 2018].
- Rognes, T., Flouri, T., Nichols, B., Quince, C. and Mahé, F. (2016): VSEARCH: a versatile open source tool for metagenomics; *PeerJ*, v. 4, p. 2584, URL <<https://peerj.com/articles/2584/>> [December 2018].
- Schloss, P.D., Gevers, D. and Westcott, S.L. (2011): Reducing the effects of PCR amplification and sequencing artifacts on 16S rRNA-based studies; *PloS one*, v. 6, p. 27310, URL <<https://journals.plos.org/plosone/article?id=10.1371/journal.pone.0027310>> [December 2018].
- Schloss, P.D., Westcott, S.L., Ryabin, T., Hall, J.R., Hartmann, M., Hollister, E.B., Lesniewski, R.A., Oakley, B.B., Parks, D.H. and Robinson, C.J. (2009): Introducing mothur: open-source, platform-independent, community-supported software for describing and comparing microbial communities; *Applied and Environmental Microbiology*, v. 75, p. 7437–7541, URL <<https://www.ncbi.nlm.nih.gov/pmc/articles/PMC2786419/>> [December 2018].
- Simister, R.L., Winterburn, P.A. and Crowe, S.A. (2017): Responses of the soil microbial community to weathering of ore minerals; *in* Geoscience BC Summary of Activities 2017: Minerals and Mining, Geoscience BC, Report 2018-1,

- p. 57–68, URL <http://cdn.geosciencebc.com/pdf/SummaryofActivities2017/MM/SoA2017_MM_Simister.pdf> [December 2018].
- Southam, G. and Saunders, J.A. (2005): The geomicrobiology of ore deposits; *Economic Geology*, v. 100, no. 6, p. 1067–1084, URL <<https://pubs.geoscienceworld.org/segweb/economicgeology/article/100/6/1067/127646/the-geomicrobiology-of-ore-deposits4>> [December 2018].
- Stanley, C. (2003): Statistical evaluation of anomaly recognition performance; *Geochemistry: Exploration, Environment, Analysis*, v. 3, p. 3–12, URL <<http://geea.lyellcollection.org/content/3/1/3/tab-figures-data>> [December 2018].
- The Mining Association of Canada (2018): Mining facts; The Mining Association of Canada, URL <<http://mining.ca/resources/mining-facts>> [November 2018].
- The University of British Columbia (2018): Sequencing + Bioinformatics Consortium; The University of British Columbia, URL <<https://sequencing.ubc.ca/>> [November 2018].
- Thompson, L.R., Sanders, J.G., McDonald, D., Amir, A., Ladau, J., Locey, K.J., Prill, R.J., Tripathi, A., Gibbons, S.M., Ackermann, G., Navas-Molina, J.A., Janssen, F., Kopylova, E., Vázquez-Baeza, Y., González, A., Morton, J.T., Mirarab, S., Xu, Z.Z., Jiang, L., Haroon, M.F., Kanbar, J., Zhu, Q., Song, S.J., Kosciulek, T., Bokulich, N.A., Lefler, J., Brislawn, C.J., Humphrey, G., Owens, S.M., Hampton Marcell, J., Berg-Lyons, D., McKenzie, V., Fierer, N., Fuhrman, J.A., Clauset, A., Stevens, R.L., Shade, A., Polard, K.S., Goodwin, K.D., Jansson, J.K., Gilbert, J.A., Knight, R. and the Earth Microbiome Project Consortium (2017): A communal catalogue reveals Earth’s multiscale microbial diversity; *Nature*, article 24621, URL <<https://www.nature.com/articles/nature24621>> [November 2018].
- Torsvik, V. and Øvreås, L. (2002): Microbial diversity and function in soil: from genes to ecosystems; *Current Opinion in Microbiology*, v. 5, p. 240–245, URL <<https://www.scienceirect.com/science/article/pii/S1369527402003247?via%3Dihub>> [December 2018].
- Wakelin, S., Anand, R.R., Macfarlane, C., Reith, F., Noble, R. and Rogers, S. (2012): Assessing microbiological surface expression over an overburden-covered VMS deposit; *Journal of Geochemical Exploration*, v. 112, p. 262–271, URL <http://www.academia.edu/23252666/Assessing_microbiological_surface_expression_over_an_overburden-covered_VMS_deposit> [December 2018].
- Westcott, S.L. and Schloss, P.D. (2017): OptiClust, an improved method for assigning amplicon-based sequence data to operational taxonomic units; *mSphere*, v. 2, URL <<https://www.ncbi.nlm.nih.gov/pmc/articles/PMC5343174>> [December 2018].
- Zhou, J., He, Z., Yang, Y., Deng, Y., Tringe, S.G. and Alvarez-Cohen, L. (2015): High-throughput metagenomic technologies for complex microbial community analysis: open and closed formats; *MBio*, v. 6, URL <<https://www.ncbi.nlm.nih.gov/pmc/articles/PMC4324309/>> [December 2018].

Organic-Compound Pathfinders in Soil for Base- and Precious-Metal Exploration in British Columbia

P.M. Luck, Mineral Deposit Research Unit, The University of British Columbia, Vancouver, BC, pluck@eoas.ubc.ca

R.L. Chouinard, Mineral Deposit Research Unit, The University of British Columbia, Vancouver, BC

P.A. Winterburn, Mineral Deposit Research Unit, The University of British Columbia, Vancouver, BC

Luck, P.M., Chouinard, R.L. and Winterburn, P.A. (2019): Organic-compound pathfinders in soil for base- and precious-metal exploration in British Columbia; in Geoscience BC Summary of Activities 2018: Minerals and Mining, Geoscience BC, Report 2019-1, p. 27–32.

Introduction

Hydrocarbon pathfinders are a promising and under-researched tool for nonpetroleum-based mineral exploration through cover. Historically, most economic mineral deposits were discovered as showings of visibly altered or mineralized outcrop. Currently in British Columbia (BC), economic geologists explore for deposits in terrain that may be covered by tens to hundreds of metres of till and glaciolacustrine deposits. Traditionally, commodity and pathfinder elements analyzed by a variety of partial-extraction techniques were integrated with other information, such as geophysical or geological evidence, to potentially improve drilling outcomes. When sampling soils that developed over poorly understood glacially derived surface sediments, geochemical signals may be complex and far travelled. This challenge has driven innovation and development of other exploration techniques to explore through transported overburden. Hydrocarbon concentrations in soil may increase in response to economic mineralization and have the potential to identify targets beneath cover.

The purpose of this research is the advancement of hydrocarbon-pathfinder techniques as an open geochemical exploration tool to explore for Cu-porphyry and related deposits in BC. The goals of this project are to

- identify the physical, chemical and biological links between buried economic mineralization and hydrocarbon concentrations and compositions at surface;
- develop robust, commercially viable and cost-effective analytical techniques for hydrocarbon analysis; and
- optimize hydrocarbon-sampling methodologies and strategies.

This research draws on datasets and sample suites generated by previous research in the Exploration Geochemistry Initiative research group at the Mineral Deposit Research

Unit (MDRU), primarily from soils overlying the Highmont South Cu-Mo calcalkalic porphyry deposit in south-

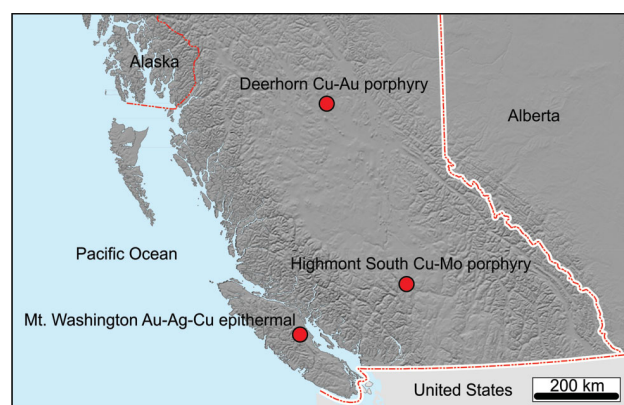


Figure 1. Locations of orientation studies for organic compounds in base- and precious-metals exploration, southern British Columbia.

central BC (Chouinard, 2018) and the Deerhorn Cu-Au alkaline porphyry deposit (Rich, 2016) in central BC (Figure 1). An integrated study of available traditional geochemistry, bedrock and Quaternary geology, and physiography data for these study areas will define hydrocarbon behaviour in proximity to mineralized systems. Data analysis aims to discriminate areas with elevated hydrocarbon abundances generated by barren geology from those of economic interest. Additionally, new fieldwork to be undertaken in the fourth quarter 2018 at the Mount Washington epithermal Au-Cu-Ag deposit on Vancouver Island will test the applicability of organic-compound pathfinders across the continuum of Cu-porphyry systems.

Methods

Pioneering research in organic-compound pathfinders demonstrated changes in the abundance of organic compounds in soil related to underlying hydrocarbon resources, geothermal anomalies and mineral deposits (Klusman, 1993).

This publication is also available, free of charge, as colour digital files in Adobe Acrobat® PDF format from the Geoscience BC website: <http://www.geosciencebc.com/s/SummaryofActivities.asp>.

There are two strategies utilizing organic-compound pathfinders that are currently practised in mineral exploration: passive and soil sampling. The passive-sampling technique utilizes collectors made of various sorbents, such as activated charcoal, encased in a water-resistant casing. With this approach, sampling is conducted by auguring a 60–100 cm deep hole in the soil, in which the sampler is buried for 120 days or more. Upon retrieval, the passive sampler is analyzed by thermal-desorption gas chromatography–mass spectrometry (GC-MS). Amplified Geochemical Imaging LLC (AGI) distributes collectors that were once termed ‘Gore Sorbers’ (Figure 2), and it also performs the C2–C20 analysis. At the Miitel Ni-sulphide deposit in western Australia, 2-methylbutane, 1-pentene and pentane were reported as being anomalous above known mineralization using this method (Noble et al., 2017).

In the soil-sampling technique, the B horizon is typically used as sampling medium (Hamilton, 2007), although lake bottom sediments, peat and humus have also been evaluated (Sutherland, 2007). Samples undergo a hexane-acetone leach to extract surface-bound hydrocarbons, and concentrations are determined by GC-MS (Cayer, 2017). This method type is sometimes referred to as a time-integrated technique, as it is considered that the organic compounds accumulate in soil over time. Soil techniques have the advantage over passive techniques of requiring only a single visit to the field and a faster turnaround time. The Activation Laboratories Ltd. proprietary Spatiotemporal Geochemical Hydrocarbons (SGH) technique, as evaluated at the Mount Milligan Cu-Au porphyry (Heberlein, 2010), is one such technique. Historically, SGH results were reported as generic compound classes, rather than compound-specific results. Currently, the SGH technique results are reported as a contoured interpretation map; no compound concentrations are shared with the end user.

Biogeochemical Links Between Organic Compounds and Ore Deposits

A growing body of evidence suggests that organic compounds form and accumulate in mineralized environments through microbial biosynthesis. A number of bacterial species have been identified in acid mine-drainage leachates (Southam and Saunders, 2005; Harneit et al., 2006), where they commonly grow as biofilms on the surfaces of sulphide minerals. Examples include the sulphide oxidizer *Acidithiobacillus thiooxidans*, iron and sulphide oxidizer *A. ferrooxidans* and iron oxidizer *Leptospirillum ferrooxidans* (Edwards et al., 1999). These bacteria enhance sulphide dissolution, playing a crucial role in supergene environments (Enders et al., 2006).

Sulphur- and iron-oxidizing bacteria use extracellular polymeric substances (EPS) to attach themselves to mineral surfaces (Harneit et al., 2006; Konhauser, 2007). For



Figure 2. An AGI Gore Module activated-charcoal organic-compound collector being retrieved after two months (Image: M. Bodner).

A. ferrooxidans, the EPS and outer cell membrane contain lipopolysaccharide (LPS; Figure 3), which has a slight positive charge under acidic conditions that results in an attraction to the negative surface charge of sulphide grains. As the LPS degrades, the lipid functional groups may contribute to the concentration of alkanes in the subsurface and soils.

In a sediment-column copper-sulphide bioleaching experiment (Luca et al., 2008), hydrocarbons formed as byproducts of bacterial metabolism. Columns were spiked with Cu-bearing ore from the Andina hydrothermal breccia and El Teniente Cu-porphyry deposits in Chile. A bacterial consortium taken from the El Teniente ore leachate and a pure strain of *A. ferrooxidans* were used to inoculate the sediment columns. Gas exiting the column was passed through

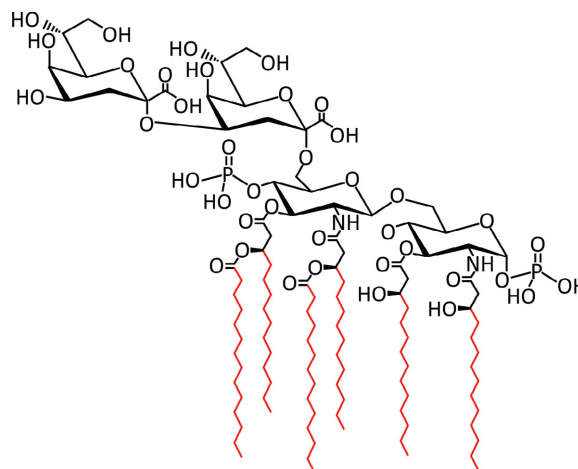


Figure 3. Lewis diagram of lipopolysaccharide (LPS), with lipid functional groups shown in red. This compound is part of the outer cell membrane of microbes, such as *Acidithiobacillus ferrooxidans*, that enable them to adhere to sulphide grains. After decomposition, the lipid functional groups may contribute to alkane concentrations in soil. Alkanes, such as decane, dodecane and tridecane, are pathfinders for sulphide-bearing ore deposits.

an adsorbent for 90 days. Bacterial species were identified with terminal-restriction fragment-length polymorphism analysis. The autotrophs *A. ferrooxidans* and other bacterial species were identified. Organic compounds in the adsorbent material were analyzed by Activation Laboratories Ltd. using GC-MS (Luca et al., 2008). Measurable concentrations of methyl-benzenes (20–350 ppt) and branched alkanes (10–120 ppt) were observed (Luca et al., 2008).

Previous MDRU Studies

Highmont South Cu-Mo Porphyry Deposit, Highland Valley Copper District, South-Central BC

High-molecular-weight alkanes, such as decane ($C_{10}H_{22}$), dodecane ($C_{12}H_{26}$) and tridecane ($C_{13}H_{28}$), are elevated in the surface B-horizon soil over mineralization in the southern section of the study area (Chouinard, 2018). Anomalous high concentrations also occur in areas overlying bedrock-fault projections to surface and topographic lows where soils are saturated with water (Figure 4). Fault zones are known to transport fluids containing trace amounts of organic compounds (Klusman, 1993).

Deerhorn Cu-Au Porphyry Deposit, Woodjam Cu-Au-Mo Porphyry District, Central BC

At the Deerhorn-Cu-Au porphyry deposit, one of three north-northwest-trending passive-gas transects showed anomalous hydrocarbon concentrations at the margins of the mineralization (Figure 5; Rich, 2016). Dodecane concentrations were highest in two samples directly northeast of the deposit footprint. Concentrations of the branched alkanes 2-methylbutane and 1-ethyl-2/3-methylbenzene were anomalous in samples adjacent to mineralization in the northwest and southeast. The cyclic compounds cyclopentene and o-xylene, which have a moderate correlation across the dataset ($R^2 = 0.7$), share a similar ‘rabbit-ears’-style anomaly pattern with respect to the deposit.

The inconsistent results between the three transects suggests that the passive samplers did not reach equilibrium with soil gasses. The samplers were deployed for a period of 63 days. Since then, the manufacturer has suggested a sampling interval of at least 120 days. Additional evaluation is required to make this methodology logistically feasible in an exploration setting.

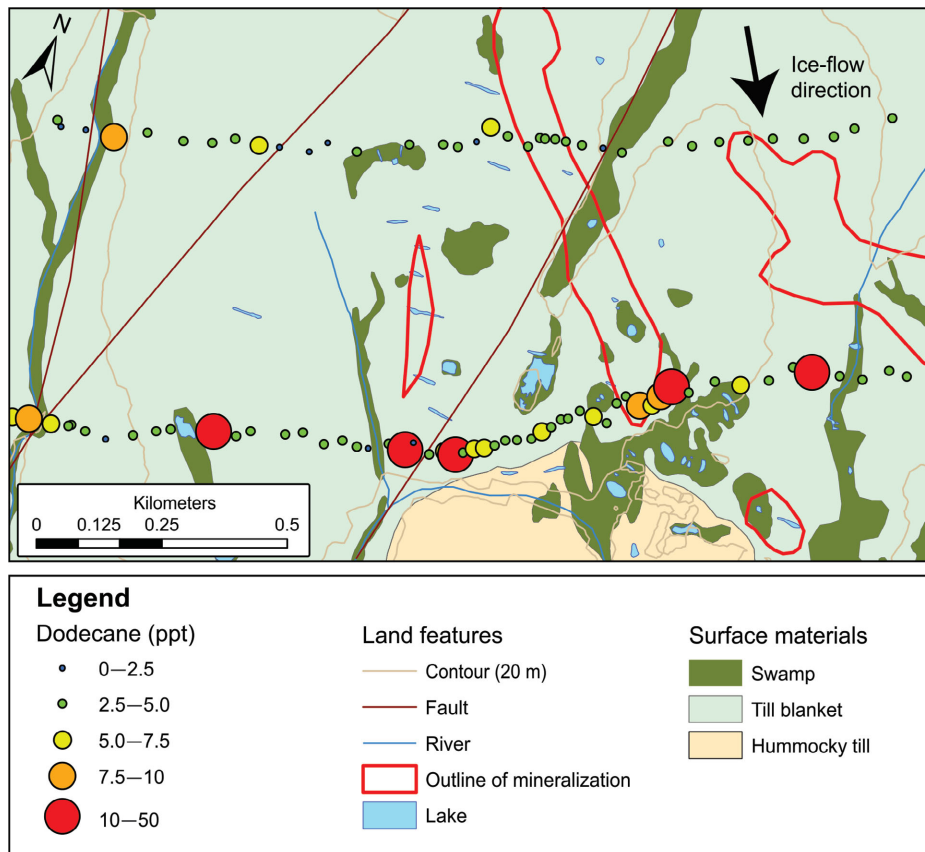


Figure 4. Passive sampler transects of the Highmont South Cu-Mo porphyry deposit. An anomalous response in dodecane detected the mineralized outline on the southern transect. Data from Chouinard (2018).

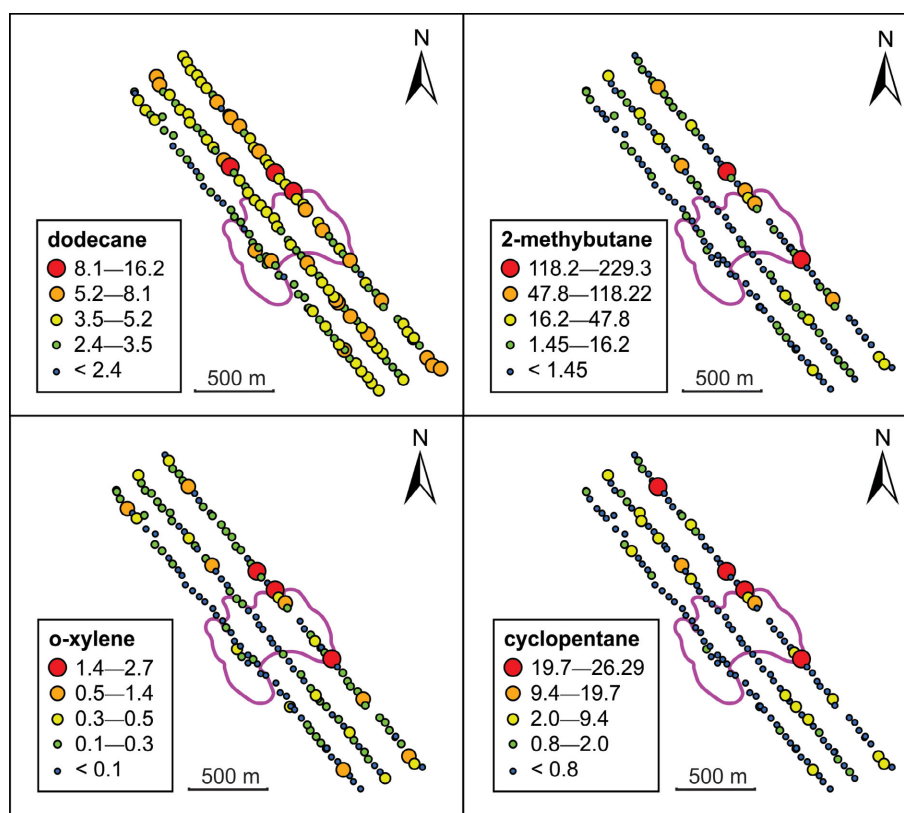


Figure 5. Results (in ppt) for AGI passive-sampler survey at the Deerhorn Cu-Au porphyry deposit. In total, 152 samplers were deployed for 63 days. Data from Rich (2016).

Current Research Directions

The Mount Washington high-sulphidation, epithermal Au-Ag-Cu deposit has historically produced 381 733 tonnes grading 0.34 g/t Au, 19 g/t Ag and 0.93% Cu (Houle, 2013, 2014). The main geological units in the study area include Triassic Karmutsen Group basalts, Cretaceous Nanaimo Group sedimentary rocks and the Eocene Mount Washington Plutonic Suite (Muller, 1998; Massey et al., 2005; Figure 6). These units are cut by a series of north-northwest-striking extension faults. The Lakeview-Domineer resource area contains a mineralized breccia zone and the Domineer vein (Houle, 2013). A previous geochemical orientation study at Mount Washington tested the response of halogens and volatile compounds in soil, snow, mountain hemlock and yellow cedar to mineralization (Heberlein et al., 2017).

As part of this project, a soil geochemical survey was carried out to test the hydrocarbon response over the Mount Washington mineralization. The grid design runs perpendicular to the strike of country rock and extends beyond the extension faults to the east and west of mineralization. A grid spacing of 50 m was centred over a mineralized breccia zone. Sample sites were selected to favour undisturbed soils, as the area is cut by a network of resource roads. At each sampling station, site duplicates were collected for

four-acid and aqua-regia ICP-MS, organic compounds and genomics analysis. Five sites were selected for vertical-profile sampling. At these sites, representative samples were taken from each soil horizon. In the Bm horizon, where practical, samples were taken at 10 cm intervals to a depth of 1 m (Figure 7). Additionally, sulphide-mineralized surface-rock samples were collected for hydrocarbon analysis. For this study, samples will be extracted in a hexane-based solvent followed by GC-MS analysis of the extract for C2–C20 hydrocarbons.

Conclusion

While results thus far have been promising, the use of organic-compound pathfinders in exploration for mineral deposits beneath cover requires more research to evaluate the hydrocarbon link between the buried mineral deposit and surface, and also to establish that anomalies are reproducible through analysis-of-variance experiments. Orientation studies by the MDRU Exploration Geochemistry Initiative have shown the effectiveness of passive collectors for identifying Cu-porphyry mineralization through cover. Key organic compounds, including long-chain alkanes, branched alkanes and aromatic compounds, show anomalous responses in soils above and adjacent to ore-deposit footprints. These compounds are linked to mineralization by microorganisms such as *Acidithiobacillus ferrooxidans*,

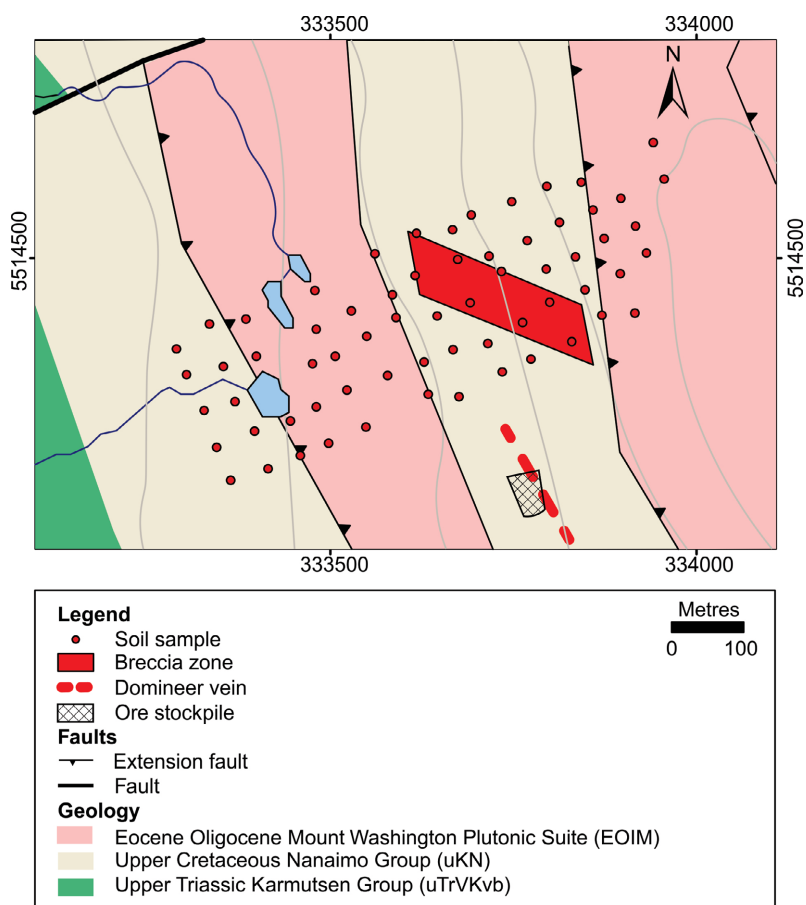


Figure 6. Geology of the Mount Washington Au-Ag-Cu epithermal deposit after Muller (1998) and Massey et al. (2005). Mineralized footprint after McDougal (1987) and Heberlein et al. (2017). A grid spacing of 50 m perpendicular to strike was chosen to target the deposit footprint and test the response of faults cutting mineralized and barren geology.

which attach to sulphides and gain energy by facilitating redox-based sulphide dissolution. Further research aims to develop and improve solvent-extraction methodologies so that organic-compound analyses may be integrated with traditional soil-sampling workflows. Upcoming results from the Mount Washington Au-Ag-Cu epithermal deposit will test the applicability of organic compounds across the Cu-porphry continuum.

Acknowledgments

This project is part of the Mineral Deposit Research Unit's Exploration Geochemistry Initiative, with funding from the Natural Sciences and Engineering Research Council and Bureau Veritas. The author thanks D. Seneshen for improving an earlier version of the manuscript. B.P. Iulianella Phillips, R. Shaw, A. Wickham and R. Simister were indispensable during field activities for this project. The study benefited by support from the Society of Economic Geologists and the Canadian Institute of Mining, Metallurgy and Petroleum.

References

- Cayer, E.M. (2017): The development of surface geochemical technologies for the detection of kimberlites concealed by glacial drift in the Northwest Territories, Canada; M.Sc. thesis, The University of British Columbia, Vancouver, BC, 682 p., URL <<https://open.library.ubc.ca/cIRcle/collections/ubctheses/24/items/1.0357236>> [November 2018].
- Chouinard, R.L.M. (2018): Surficial geochemical exploration tools for porphyry Cu-Mo mineralisation in till-covered terrain, south-central British Columbia; M.Sc. thesis The University of British Columbia, Vancouver, BC.
- Edwards, K.J., Gihring, T.M. and Banfield, J.F. (1999): Seasonal variations in microbial populations and environmental conditions in an extreme acid mine drainage environment; Applied and Environmental Microbiology, v. 65, no. 8, p. 3627–3632, URL <<https://www.ncbi.nlm.nih.gov/pmc/articles/PMC91544/>> [October 2018].
- Enders, M.S., Knickerbocker, C., Titley, S.R. and Southam, G. (2006): The role of bacteria in the supergene environment of the Morenci porphyry copper deposit, Greenlee County, Arizona; Economic Geology, v. 101, no. 1, p. 59–70, URL <<https://trove.nla.gov.au/version/198100084>> [October 2018].

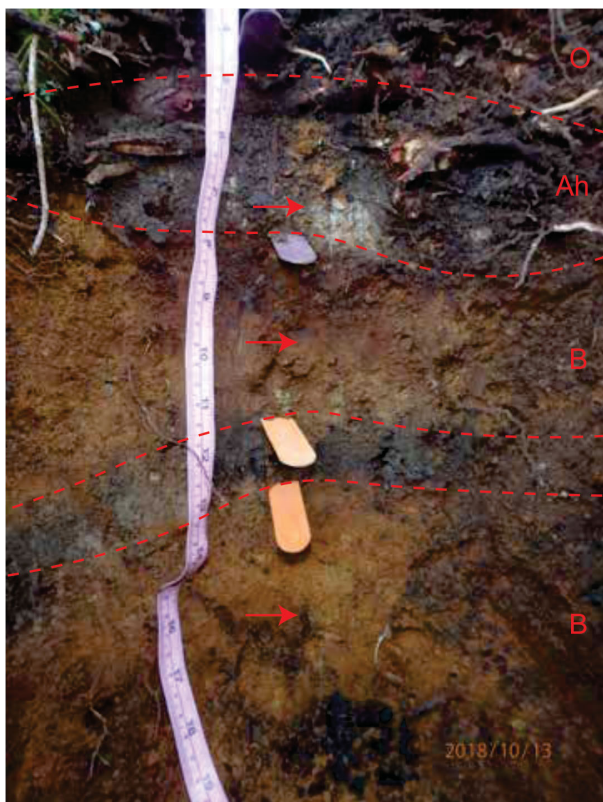


Figure 7. Representative soil profile at the Mount Washington Au-Ag-Cu epithermal deposit. Each horizon was sampled; where horizon thickness allowed, additional samples were taken at 10 cm intervals.

Hamilton, S.M. (2007): Major advances in soil geochemical exploration methods for areas of thick glacial drift cover; Proceedings of Exploration 07: Fifth Decennial International Conference on Mineral Exploration, B. Milkereit (ed.), p. 263–280, URL <<http://www.dmec.ca/ex07-dvd/E07/pdfs/13.pdf>> [October 2018].

Harneit, K., Göksel, A., Kock, D., Klock, J.H., Gehrke, T. and Sand, W. (2006): Adhesion to metal sulfide surfaces by cells of *Acidithiobacillus ferrooxidans*, *Acidithiobacillus thiooxidans* and *Leptospirillum ferrooxidans*; Hydrometallurgy, v. 83, no. 1–4, p. 245–254, URL <<https://doi.org/10.1016/j.hydromet.2006.03.044>> [October 2018].

Heberlein, D. (2010): An assessment of soil geochemical methods for detecting copper-gold porphyry mineralization through Quaternary glaciofluvial sediments at the WBX-MBX and 66 zones, Mt. Milligan, north-central British Columbia; Geoscience BC, Report 2010-08, 68 p., URL, <http://www.geosciencebc.com/i/project_data/GBC_Report2010-8/GBC_Report2010-8_Report.pdf> [October 2018].

Heberlein, D.R., Dunn, C.E. and Rice, S. (2017): Halogens and other volatile compounds in surface sample media as indicators of mineralization, part 2: Mount Washington epithermal Au-Cu-Ag prospect, Vancouver Island, BC (NTS 092F/14); Geoscience BC, Report 2017–12, URL <http://www.geosciencebc.com/i/project_data/GBCReport2017-12/GBCR2017-12_MW_Rpt.pdf> [October 2018].

Houle, J. (2013): Geochemical and prospecting technical assessment report on the Mount Washington property for North Bay Resources Inc., Nanaimo Mining Division, BC; BC Ministry of Energy, Mines and Petroleum Resources, Assessment Report 34200, 206 p. URL <<https://aris.empr.gov.bc.ca/ArisReports/34200.PDF>> [October 2018].

Houle, J. (2014): NI 43-101 technical report on the Mount Washington property, Vancouver Island, British Columbia; NI 43-101 technical report prepared for North Bay Resources Inc., 92 p.

Klusman, R.W. (1993): Soil-gas and related methods for natural resource exploration; John Wiley and Sons, New York, New York, 483 p.

Konhauser, K.O. (2007): Introduction to Geomicrobiology; Blackwell Science Ltd., Oxford, United Kingdom, 440 p.

Luca, R., Townley, B., Escobar, B. and Vargas, T. (2008): Formation of hydrocarbon gaseous compounds during bioleaching of copper sulphide minerals with mesophilic microorganisms; Hydrometallurgy, v. 94, no. 1, p. 54–57, URL <<https://www.sciencedirect.com/science/article/abs/pii/S0304386X08001928>> [October 2018].

Massey, N.W.D., MacIntyre, D.G., Desjardins, P.J., and Cooney, R.T. (2005): Geology of British Columbia; BC Ministry of Energy, Mines and Petroleum Resources, Geoscience Map 2005-3, (3 sheets), scale 1:1 000 000. URL <<http://www.empr.gov.bc.ca/mining/geoscience/publications/catalogue/maps/geoscience/Pages/2005-3.aspx>> [October 2018].

McDougall, J.J. (1987): Summary report on the Mt. Washington gold property; Better Resources Limited, February 1987.

Muller, J.E. (1989): Tertiary low angle faulting and related gold and copper mineralization on Mount Washington, Vancouver Island (92F/11, 14); in Geological Fieldwork 1988, BC Ministry of Energy, Mines and Petroleum Resources, BC Geological Survey, Paper 1989-1, p. 81–91, URL <<https://pdfs.semanticscholar.org/ca1d/2d443f24f9fb4f807e52ab9038ff87807f09.pdf>> [October 2018].

Noble, R.R.P., Seneshen, D.M., Lintern, M.J., Anand, R.R., Pagès, A. and Pinchand, G.T. (2017): Soil-gas and weak partial soil extractions for nickel exploration through transported cover in Western Australia; Geochemistry: Exploration, Environment, Analysis, v. 18, no. 1, p. 31–45, URL <<https://pubs.geoscienceworld.org/geea/article-abstract/18/1/31/519235/soil-gas-and-weak-partial-soil-extractions-for?redirectedFrom=fulltext>> [October 2018].

Rich, S.D. (2016): Geochemical mapping of porphyry deposits and associated alteration through transported overburden; M.Sc. thesis, The University of British Columbia, Vancouver, BC.

Southam, G. and Saunders, J.A. (2005): The geomicrobiology of ore deposits; Economic Geology, v. 100, no. 6, p. 1067–1084, URL <<http://dx.doi.org/10.2113/gsecongeo.100.6.1067>> [October 2018].

Sutherland, D.A. (2007): Cutting edge geochemistry detects organic signatures in surficial samples originating from bacterial-mineral interactions to locate and identify deeply buried exploration targets; in Proceedings of Exploration 07: Fifth Decennial International Conference on Mineral Exploration, B. Milkereit (ed.), Paper 82, p. 989–992.

Sutherland, D.A. (2009): Robust ‘organic’ geochemistry identifies and vectors to deeply buried exploration targets; in Proceedings of the 24th International Applied Geochemistry Symposium, Volume 1, D.R. Lentz, K.G. Thorne and K.L. Beal (ed.), p. 97–100, URL <https://www.appliedgeochemists.org/images/stories/IAGS_2009/24th_IAGS_Abstracts_Vol1_ALL_revised.pdf> [October 2018].

Characterization and Extraction of Rare-Earth Elements from East Kootenay Coalfield Samples, Southeastern British Columbia

V.K. Kuppusamy, Norman B. Keevil Institute of Mining Engineering, The University of British Columbia, Vancouver, BC, vinothkumar@alumni.ubc.ca

M.E. Holuszko, Norman B. Keevil Institute of Mining Engineering, The University of British Columbia, Vancouver, BC

Kuppusamy, V.K., and Holuszko, M.E. (2019): Characterization and extraction of rare-earth elements from East Kootenay coalfield samples, southeastern British Columbia; in *Geoscience BC Summary of Activities 2018: Minerals and Mining*, Geoscience BC, Report 2019-1, p. 33–44.

Introduction

Rare-earth elements (REE) make up a group of 17 elements in the periodic table, including 15 lanthanides and 2 chemically similar transition metals, Sc and Y. Using the atomic number, REE are classified as heavy REE and light REE, with elements from Tb to Lu and Y belonging to the former group and La to Gd and Sc belonging to the latter group (Moldoveanu and Papangelakis, 2013; Zhang et al., 2015). With the emergence of new clean energy and defense-related technologies, consumption of rare-earth elements (REE) has increased rapidly (Tse, 2011). For example, it is projected that the demand for Dy, one of the REE, is expected to increase as much as 2600% by 2025 (Standing Committee on Natural Resources, 2014). In addition, traditional rare-earth ore deposits are quickly being depleted and are expected to meet the demand for only the next 15–20 years (Seredin and Dai, 2012). Based on supply and demand, REE are classified as critical elements by the United States and the European Union due to their importance in clean energy and defense applications (United States Department of Energy, 2010; European Commission, 2017). The National Energy Technology Laboratory in the United States has conducted a prospective analysis of coal deposits as a source of REE using the United States Geological Survey coal database, which contains the concentrations of rare-earth elements across United States coalfields (Bryan et al., 2015). Further, the United States Department of Energy has committed US\$10 million to several projects researching the techno-economic feasibility of domestic separation technologies of REE from coal and/or its byproducts containing a minimum of 300 ppm total REE and concentrating the REE to a level greater than or equal to 2% (by weight) in processed streams (United States Department of Energy, 2016).

There is an indication of the presence of REE in some Canadian coal deposits, especially in British Columbia (BC) coalfields (Goodarzi, 1988; Birk and White, 1991; Goodarzi et al., 2009); however, there is no proper quantification, characterization and extraction analysis currently available for coal deposits in BC or in other coal deposits across Canada. The purpose of this ongoing research is to characterize and quantify the REE and their mode of occurrence in BC coal deposits and in different processing products of coal for possible extraction study. Some of the initial results of the study were reported previously (Kumar et al., 2018). This paper shows the preliminary characterization and extraction results conducted on a sample received from a southeastern BC coal mine.

Materials and Methods

Sample

Samples and the method used in this study is part of the continuing research published in *Summary of Activities Report 2017: Minerals and Mining* (Kumar et al., 2018). As described by Kumar et al. (2018), a run-of-mine (ROM) coal sample of approximately 300 kg was collected from a mine in the East Kootenay coalfield, southeastern BC, and shipped in barrels to the Coal and Mineral Processing Laboratory at The University of British Columbia. Representative samples were obtained for further testing using the standard procedure for coal sample preparation, ASTM D2013/D2013M-12 (2012). Proximate analysis was conducted on the representative samples in duplicates using the standard methods ASTM D3174-12 (2012), ASTM D3172-13 (2013), ASTM D3173/D3173M-17a (2017) and ASTM D3175-17 (2017).

Tree Release Analysis

A tree release analysis procedure (Figure 1) can be used to generate an optimum separation performance curve for the flotation process, which is used for cleaning fine coal (Mohanty et al., 1998). A representative feed sample of 300 g was crushed to $-500\ \mu\text{m}$. Flotation tests were con-

This publication is also available, free of charge, as colour digital files in Adobe Acrobat® PDF format from the Geoscience BC website: <http://www.geosciencebc.com/s/SummaryofActivities.asp>.

ducted on the 2 L Denver laboratory cell with an initial slurry content of 14.3%. The coal sample was wetted for 5 minutes with an impeller speed of 1300 rpm. A flotation reagent emulsion of 25 g/t of methyl isobutyl carbinol (MIBC) and 50 g/t of kerosene in 200 mL of water was made using a high-speed laboratory blender and added to the flotation cell. The coal slurry with reagents was further conditioned for 10 minutes, followed by another 25 g/t of MIBC addition and conditioning for 1 minute. Using an aeration rate of 4–5 L/min, the concentrate was collected until the froth was barren. The initial products were each successively refloats twice to obtain eight products, as shown in Figure 1. The final products from the tree release analysis were dried at 65°C, weighed to obtain the yield data and analyzed for ash content. For the feed sample, the tree release analysis was conducted in duplicate. Based on the ash content of the products, three products were selected with low (<10%), middlings (10–60%) and tailings (>60%) to find REE concentration in the flotation products.

Sequential Extraction

Sequential extraction was first developed to analyze particulate trace metals (Tessier et al., 1979). This procedure was later modified for coal (Finkelman et al., 1990; Finkelman, 1994) and successfully applied to REE in coal by Dai et al. (2002). A similar extraction method has also been applied to other trace elements in coal such as arsenic, mercury and selenium (Dai et al., 2004; Zhang et al., 2007; Zheng et al., 2008; Bai et al., 2011; Zhou et al., 2016). Based on these

studies, a simplified three-step procedure was adopted and used in this study, as shown in Table 1.

Alkali-Acid Leach Test

Background

To improve the utilization properties and to mitigate the environmental impacts, the ROM coal is processed to remove undesirable impurities such as mineral matter and sulphur to meet the market quality requirements depending on the final use. Coarse coal particles (>0.5 mm) are processed using gravity-based separation techniques. Fine coal particles (<0.5 mm) of metallurgical coal are generally treated using flotation (Laskowski, 2001). Due to the limited effectiveness of physical beneficiation methods to remove fine dispersed mineral matter in coal, alternative techniques such as chemical leaching processes are used to produce clean coal. Among several alternative processes, alkali-acid leaching has been studied in detail (Meshram et al., 2012). Waugh and Bowling (1984) showed that for Australian coals, alkali-acid leaching can be used to reject more than 90% of ash-forming minerals with a 10% sodium hydroxide (NaOH) solution at 200–300°C under vapour pressure followed by a dilute acid treatment. Wang et al. (1986) achieved 90% reduction in mineral matter for Australian coals using milder temperature conditions at 125–185°C with a 4–80% NaOH solution. Sriamoju et al. (2017) explained the mechanism of the coal chemical leaching process and proposed an acid regeneration method using the pilot scale test.

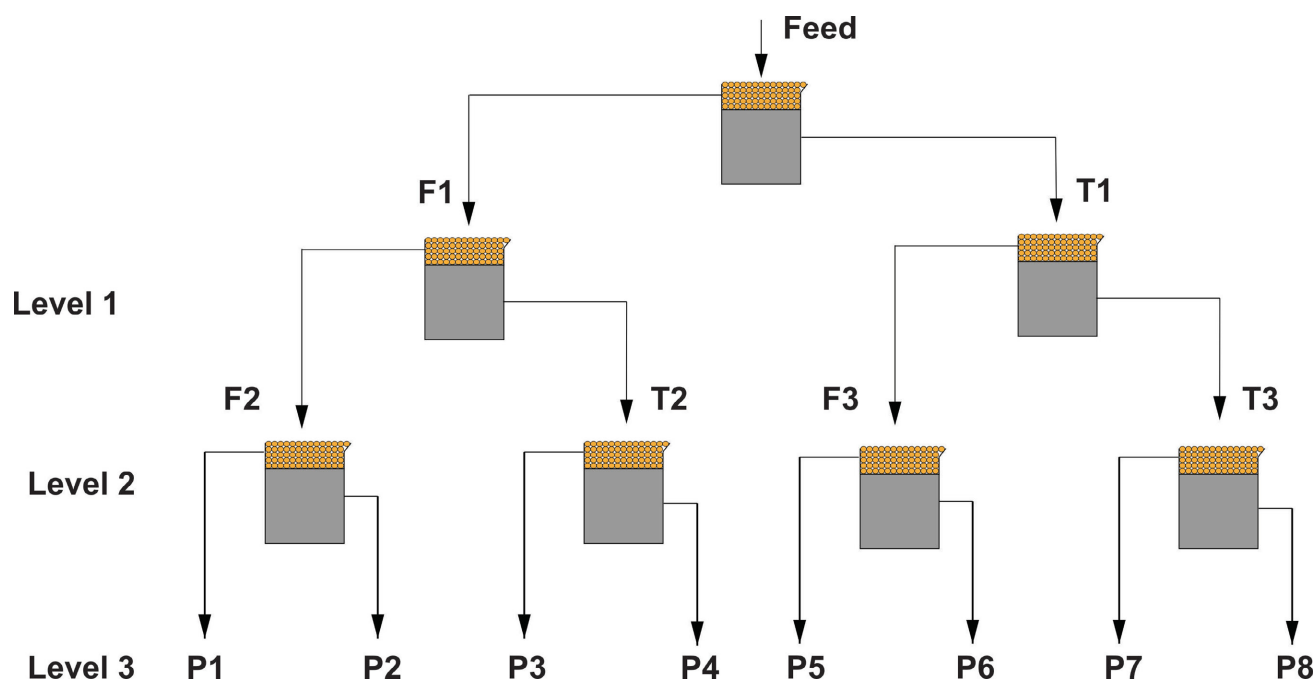
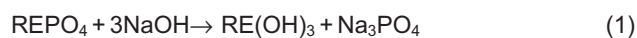


Figure 1. Schematic diagram of tree release analysis procedure. In this test, the coal sample (feed) was first separated using flotation into float F1 and tailings T1 (level 1). In the level 2, both float F1 and tailings T1 were refloats separately to obtain a total of four products: float F2 and tailings T2, and float F3 and tailings T3, respectively. In level 3, the four products from the second stage were again floated to obtain final products, P1 to P8. The yellow bubble and grey portion in the figure represent froth and tailings obtained during flotation, respectively.

There is some similarity between the alkali-acid leach process of coal and processing rare-earth concentrates. Traditional rare-earth concentrates such as monazite and xenotime (rare-earth phosphate minerals) are generally processed using sulphuric acid or sodium hydroxide. In the caustic process, finely ground monazite (<45 µm) is leached at 140–150°C using 60–70% NaOH for 3–4 hours to form insoluble hydroxides of rare-earth elements. These hydroxides are dissolved in acid for subsequent processes (Habashi, 2013; Krishnamurthy and Gupta, 2016). The reaction mechanism is given below:



There is no previous study on using an alkali-acid leach for the simultaneous extraction of REE and clean coal from the coal waste stream. In the present work, alkali-acid leaching was conducted on coal tailings obtained from the ROM coal treated by flotation.

Coal Tailings Sample Preparation

The coal tailings samples for the alkali-acid leach tests were obtained using flotation of the representative ROM sample. For the flotation test, a representative feed sample of approximately 4.5 kg was crushed to obtain a size of –500 µm. Approximately 1 kg of feed coal was used in batches to conduct flotation tests in a 10 L Denver laboratory cell. The coal sample was initially conditioned for 5 minutes at an impeller speed of 1300 rpm. A flotation reagent emulsion of 25 g/t of methyl isobutyl carbinol (MIBC) and 240 g/t of kerosene in 200 mL of water was prepared using a high-speed laboratory blender and added to the flotation cell. Further, the coal slurry with reagents was conditioned for 15 minutes followed by another 25 g/t of frother (MIBC) addition and conditioning for 1 minute. Using an aeration rate of 4.5 L/min, the concentrate was collected until the froth was barren. Tailings were pressure filtered and both the filtered tailings as well as the concentrate were dried at 65°C. After drying, the tailings and concentrate collected from different flotation batches were homogenized and representative samples were split to conduct ash analysis. Tailings from these flotation tests were used as the feed sample for alkali-acid leach tests.

Alkali-Acid Leach Test Procedure

A 15 g representative sample of the coal tailings was mixed with 60 g of solution of different concentrations of NaOH, at 20% solid content. Alkali leaching was performed using a Parr® 4590 micro stirred reactor with 100 mL reactor volume and carried out at appropriate temperatures with vapour pressure for different leaching times. Alkali-leached coal slurry was filtered to obtain the NaOH leach solution and the solid residue was both washed and filtered twice to remove any excess NaOH solution and water-soluble components. The filtered alkali leach residue was repulped and 7.5 wt. % of concentrated hydrochloric acid (HCl) was added to the slurry in a beaker. The beaker was placed in a water bath maintained at 50°C for 30 minutes and the entire set-up was mounted on a magnetic stirrer to agitate the slurry during the acid leaching process. Finally, the acid-leached coal slurry was filtered to obtain the HCl solution and the clean coal residue that was later washed and filtered until the wash water reached a neutral pH. The clean coal (representing residue obtained after alkali-acid leaching) was dried at 65°C and analyzed for ash content. To obtain statistically reliable data at the preliminary stage of the study, experimental runs for leaching tests were obtained by adopting an experimental design using JMP® software with four levels for NaOH concentration (5–30 wt. %), three levels for temperature (130–190°C) and three levels for time (30–120 minutes).

Analytical Methods

For total REE quantification, feed and test product samples (0.2 g) were added to lithium metaborate and lithium tetraborate flux and mixed thoroughly. The samples were then fused in a furnace at 1025°C. Finally, the resulting melts were cooled and digested in an acid mixture containing nitric, hydrochloric and hydrofluoric acids. The digested solutions were then analyzed by inductively coupled plasma–mass spectrometry (ICP-MS). The analytical results were corrected for inter-elemental spectral interference. This analysis was conducted by the MS Analytical laboratory (Langley, BC). In this study, REE in coal are expressed as follows: whole coal basis (REE concentration in the coal sample) and ash basis (REE concentration in the ash of the coal sample).

Table 1. Sequential extraction procedure used in this study. Abbreviation: ICP-MS, inductively coupled plasma–mass spectrometry.

Step	Mode of occurrence	Procedure
1	Ion-exchangeable phase	A 15 g sample was transferred into a 150 mL beaker and 90 mL of 1 N ammonium acetate was added to the beaker. The slurry was magnetically stirred for 24 hours at room temperature and filtered using Whatman grade 42 filter paper. The liquid was labelled and stored for ICP-MS analysis and the solid residue was dried at 65°C.
2	Organic bound	The dried residue from step 1 was mixed with chloroform (1.47 g/cm ³) and was magnetically stirred for 24 hours at room temperature. Then, the mixture was centrifuged at 3500 rpm for 20 minutes to get float and sink fraction. The float fraction (<1.47 g/cm ³) was air dried in the fume hood and stored for ICP-MS analysis.
3	Inorganic bound	The sink fraction (>1.47 g/cm ³) from step 2 was air dried in the fume hood and stored for ICP-MS analysis.

Quantitative X-ray diffraction data were collected on selected samples to identify the mineral phases. The X-ray powder-diffraction data were collected over a range 3–80° of 2θ with CoKα radiation on a Bruker D8 Advance Bragg-Brentano diffractometer equipped with an Fe monochromator foil, 0.6 mm (0.3°) divergence slit, incident- and diffracted-beam Soller slits, and a LYNXEYE XE detector. The long fine-focus Co X-ray tube was operated at 35 kV and 40 mA using a take-off angle of 6°. The X-ray diffractogram was analyzed using the International Centre for Diffraction Data® PDF-4+ 2019 database using the search/match module by Bruker. X-ray powder-diffraction data of the sample were refined with Rietveld program TOPAS 4.2 by Bruker.

Scanning electron microscope–energy X-ray dispersive spectrometry (SEM-EDX) of selected samples was carried out to examine finely disseminated rare-earth minerals and to determine their mineral associations and size using a FEI Quanta™ 650 scanning electron microscope (SEM) operated at 20 kV at a working distance of 10 mm.

Results and Discussion

Proximate Analysis

The result of the proximate analysis of ROM coal and tailings coal generated for leaching tests is listed in Table 2. According to the ASTM D388-17 (2017) standard, feed coal is classified as medium-volatile bituminous coal.

Flotation Behaviour of the Feed Sample and REE Concentration

The tree release analysis provided a separation performance curve achievable under a predetermined set of con-

ditions for flotation of the feed sample. The shape of the performance curve indicates the ability to clean the coal using flotation such as ideal separation, easy cleanability, difficult cleanability and impossible separation (Laskowski, 2001). As shown in Figure 2, at 10% ash, 83% yield of the clean coal can be achieved for feed coal. Figure 2 also shows that the sample exhibits easy cleanability using flotation and its combustible recovery exceeded 99%.

The feed sample and selected three tree release analysis products containing low-ash (<10%), middlings (10–60%) and high-ash (>60%) products were analyzed for rare-earth element concentrations, the results of which are presented in Table 3. The highest concentration of REE on an ash basis was reported in the low-ash flotation product (550 ppm; Table 3). On whole coal basis, however, the concentration of REE in the low-ash flotation product (25 ppm; Table 3) was six times lower than tailings (173 ppm). It shows that the concentration of REE in the tailings enriched during the flotation process, which indicates the association of REE with mineral matter in the feed coal. Further, REE distribution calculated using the mass balance on the low-ash products (<10% ash), middlings (10–60% ash) and tailings (>60% ash) as obtained from the tree release analysis re-

Table 2. Proximate analysis of feed (run-of-mine [ROM] coal) and tailings coal samples.

Sample	ROM coal (as-received)	Tailings (dried)
Moisture (%)	1.33	1.46
Volatile matter (%)	18.22	15.71
Ash (%)	24.82	46.21
Fixed carbon (%)	55.63	36.61

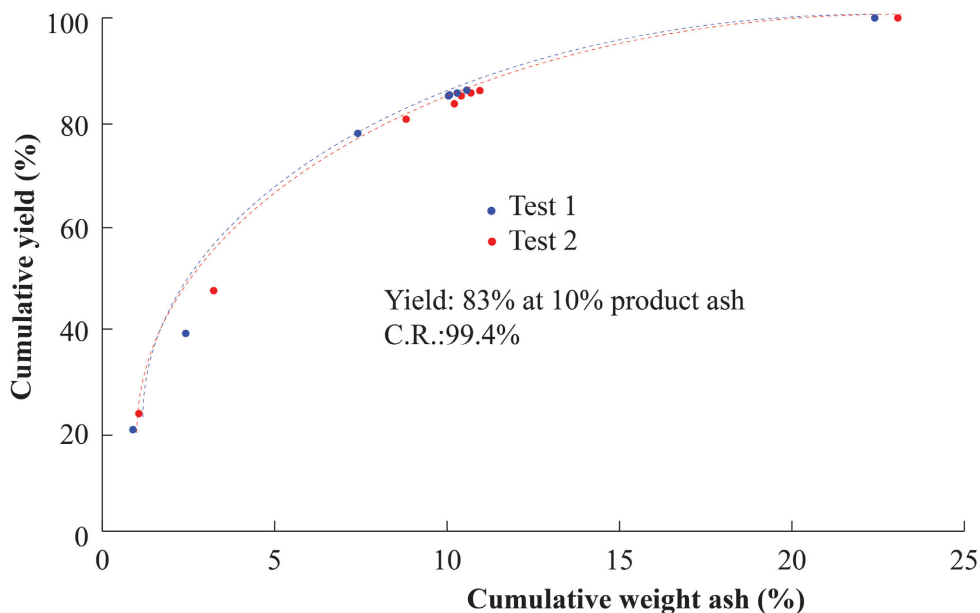


Figure 2. Flotation performance curve obtained from tree release analysis of the feed sample. Test was performed in duplicates as represented by test 1 and test 2 data.

vealed that most of the REE by weight percent was reported to the middlings plus tailings streams, as shown in Figure 3.

Sequential Extraction Results

The results of the sequential extraction of the feed sample is shown in Figure 4. Total recovery of approximately 88% of the REE was reported, whereas the loss is reported as an error in Figure 4, which might be due to cumulative sampling error, analytical error and weight loss during the experiment. The ion exchangeable REE in the sample is negligible and most of the REE were below the detectable limit. The REE associated with the organic and inorganic portions of the coal was found to be approximately 20% and approximately 68%, respectively. As shown in Figure 3, most of the REE is reported in middlings plus tailings, which further validates the result of the sequential extraction.

Dai et al. (2002), using a similar sequential extraction procedure as in this study, showed that coal samples from the Shitanjing, Shizuishan and Fenfeng coalfields contain approximately 90% of REE associated with aluminum silicate minerals. The organically associated REE were re-

ported previously, especially in low-ash and low-rank coals (refers to subbituminous and lignite; Eskenazy, 1987, 1999; Dai and Finkelman, 2018). Because coal in this study belongs to high-ranking coal (bituminous), it can be inferred that not all rare-earth elements in the studied samples of clean coal have an organic association. Further, the density-based sequential extraction process does not account for the fine-grained minerals dispersed within the coal matrix and thus erroneously assigns the organic-associated REE percentage. Direct measurement using SEM and other advanced characterization techniques should, therefore, be incorporated to understand the exact nature of organic-associated REE in the sample.

Figure 5 shows SEM-EDX images of clean coal and tailings. Spot analyses have shown that REE is associated with aluminosilicate minerals (likely clays) in both clean coal and tailings, thus it can be inferred that the actual amount of organic-associated REE in the coal is less than the reported value in the results of the sequential extraction. It can be further concluded that inorganic associations are the dominant mode of REE occurrence in the studied coal samples. REE associated with clays were previously reported in the Jungar coalfield, China; the Huaibei coalfield, China; the

Table 3. Rare-earth element (REE) concentration in feed sample and tree release analysis products (in ppm). Low ash denotes product with <10% ash, middlings denote product with 10–60% ash and tailings denote product with >60% ash.

Sample	Sample name	Ash (%)	Sc	Ce	Dy	Er	Eu	Gd	Ho	La	Lu	Nd	Pr	Sm	Tb	Tm	Y	Yb	Total REE (ash basis)	Total REE (whole coal basis)
S1	Feed coal	24.82	12.1	89.5	7.5	4.6	2.2	8.5	1.7	48.0	0.6	41.5	10.6	8.1	1.3	0.8	48.0	4.9	289.8	71.9
S2	Low ash product	4.5	N/A	177.7	14.7	9.6	4.2	15.8	3.6	97.7	1.3	82.2	21.1	15.3	2.4	1.3	93.3	9.3	549.4	24.7
S3	Middlings	35.92	11.1	76.8	6.7	4.3	1.7	7.1	1.5	41.2	0.6	34.0	9.0	7.0	1.2	0.7	42.9	4.3	250.0	89.8
S4	Tailings	85.55	7.01	64.9	4.9	3.1	1.4	5.6	1.1	35.0	0.5	30.2	7.9	5.9	0.9	0.5	30.9	2.9	202.3	173.1

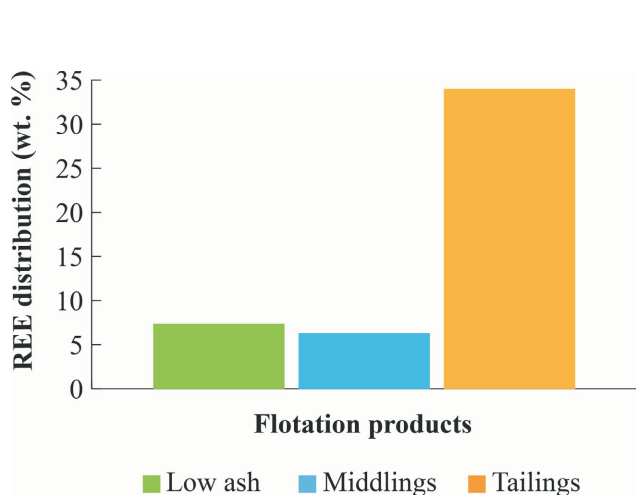


Figure 3. Distribution of rare-earth elements (REE) by weight percent in the tree release analysis flotation products calculated using data shown in Table 3. Low ash denotes product with <10% ash, middlings denote product with 10–60% ash and tailings denote product with >60% ash.

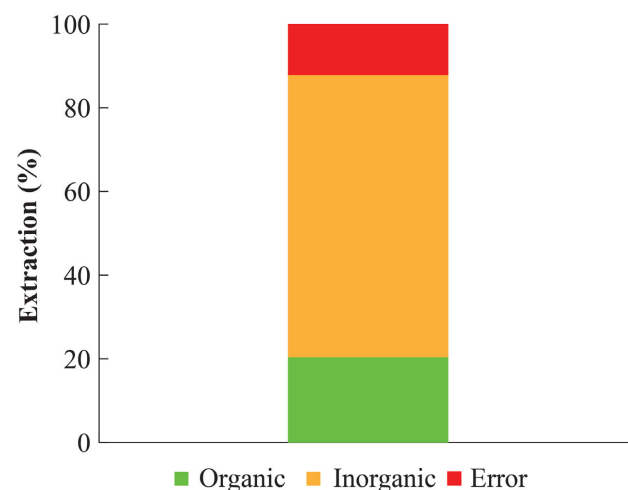


Figure 4. Sequential extraction results of feed sample showing the distribution of rare-earth elements (REE) in various modes of occurrences. Ion-exchangeable REE was below the detectable limit. Error denotes the cumulative sampling error, analytical error and weight loss during the experiment.

Antaibao mining district, China; Far East deposits, Russia; and Fire clay coal, United States (Seredin, 1996; Dai et al., 2012; Zheng et al., 2007; Wang et al., 2008; Hower et al., 2018).

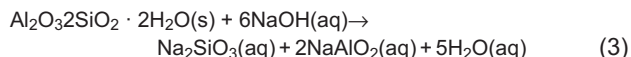
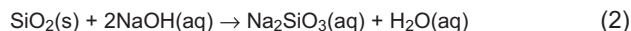
Leaching Test Results

Because it was found that most of the REE by weight percent reported in middlings and tailings, the coal tailings were used for the extraction study. Flotation of the feed coal, as described in section about coal tailings sample preparation, resulted in 10.12% and 46.21% ash with corresponding yields of approximately 58% and approximately 42% in the concentrate and tailings, respectively. Because coal tailings were used for subsequent alkali-acid leaching tests, particle size distribution was performed using the sieve analysis and the P_{80} of the sample was found to be 250 μm . To capture the interaction effect between the factors in the initial stage of the experiment, partial factorial design was adopted for this study. Figure 6 depicts the product ash obtained after the acid leaching stage for 12 experiments. Maximum ash reduction of approximately 70% was observed for test 10 (30% NaOH at 190°C for 30 minutes) with a corresponding product ash content of 14%. Further, fitting the data using the standard least squares model showed that significant factors affecting the product ash were NaOH concentration and temperature, with p-values of 0.00176 and 0.00786, respectively.

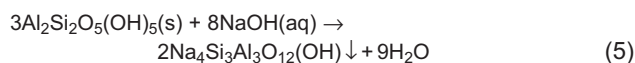
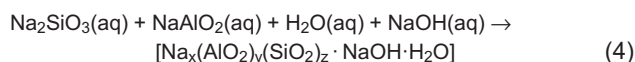
Effect of NaOH Concentration and Temperature

Sodium hydroxide concentration has a significant effect on the product ash, as shown in Figure 7. Irrespective of the temperature, increases in sodium hydroxide concentration proportionately decrease product ash content. The general

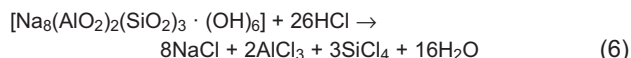
mechanism for alkali-acid leaching of the ash content can be explained in two stages: the alkali stage and the acid stage. During the alkali-acid leaching stage, the mineral matter—such as quartz and clays—reacts with sodium hydroxide to form soluble sodium silicate and sodium aluminate (Vaugh and Bowling, 1984; Mukherjee and Borthakur, 2001; Dash et al., 2013; Behera et al., 2017; Sriramoju et al., 2017).



With the increase in alkali concentration, temperature and leaching time, concentrations of silicate and aluminate ions increase in the leach solution. Beyond the solubility limit, sodium aluminosilicate precipitates out as gel, as shown in the reaction below (Buhl et al., 1997; Mukherjee and Borthakur, 2001; Rahman et al., 2017):



During the acid leaching stage, sodalite formed in the alkali-acid leach stage is dissolved into sodium and aluminum chlorides and silicic acid, as shown below:



From the X-ray diffraction (XRD) analysis, as shown in Figure 8, clays and quartz account for more than 90% of the crystalline mineral matter in the feed coal. The reduction in

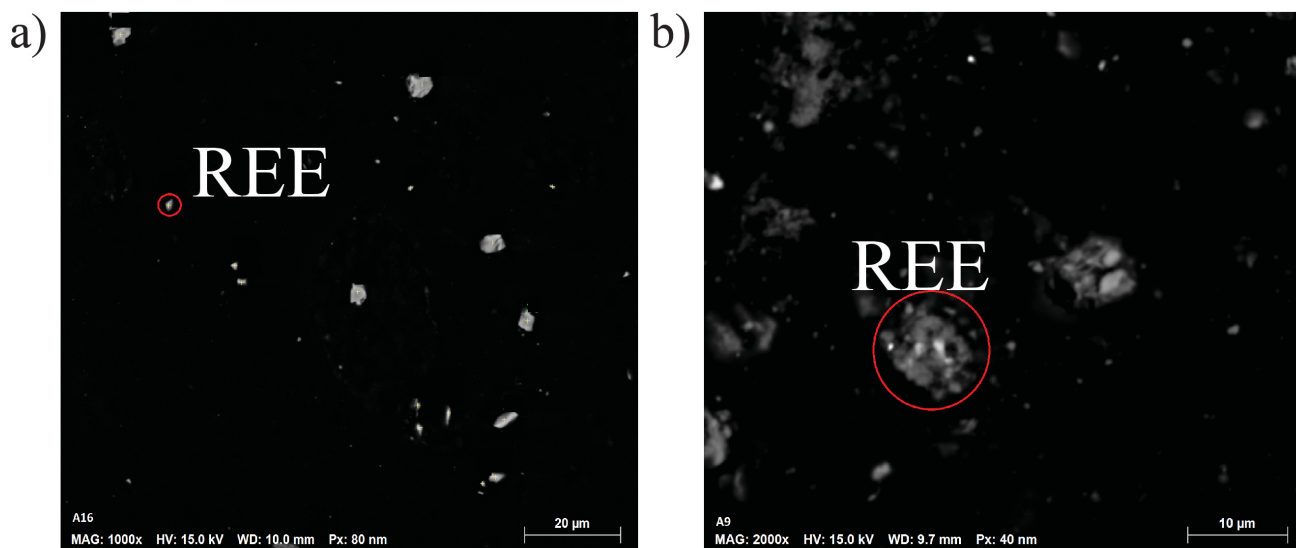


Figure 5. Scanning electron microscope—energy dispersive X-ray spectrometry (SEM-EDX) images of **a)** clean coal; elements observed in highlighted grains: Al, Er and O and **b)** tailings; elements observed in highlighted grains: Al, Ba, Br, Ca, Ce, O, P and Si.

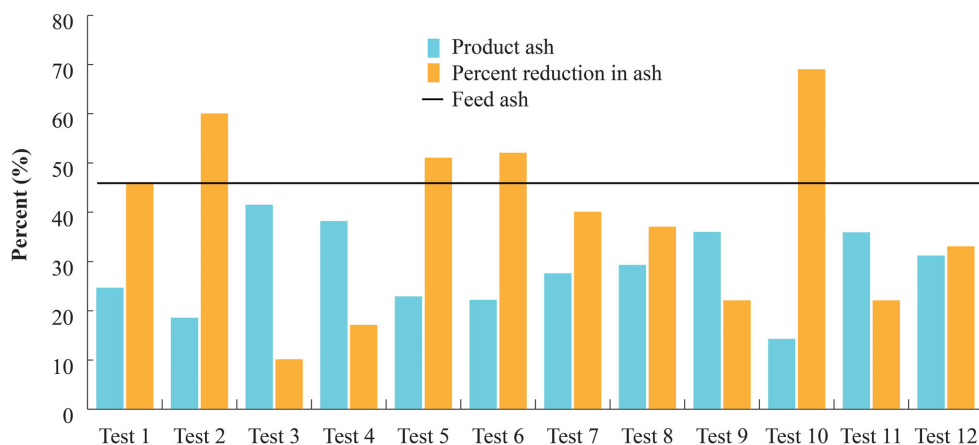


Figure 6. Effect of test conditions on product ash (light blue bar) compared with feed tailings ash (black line). Light orange bar represents percentage reduction of product ash compared with feed tailings ash after the alkali-acid leach test.

ash content of coal tailings treated by alkali-acid leaching, therefore, follows a similar mechanism, as explained in equations 4–8.

Ash reduction was more pronounced when the temperature was increased from 130 to 160°C, as shown in Figure 7. But when the temperature was further increased to 190°C, the ash reduction was comparatively less effective.

Recovery of Rare-Earth Elements

Because alkali-acid leaching of coal leaches clay minerals, and because of the association of REE with clay minerals, it was expected that there might be a relationship between the ash content in clean coal residue and REE recovery. To understand the relationship between ash reduction in the alkali-acid leach test and rare-earth recovery, clean coal residue samples with varying ash percent were selected for REE element analysis. REE recovery was calculated for individual elements using equation 7 and the results are shown in Figure 9. Promethium is extremely rare and generally considered not to exist in nature (Resende and Morais, 2010), and scandium was not assayed, so neither of these elements were included in the calculation.

$$\text{REE recovery (\%)} = 1 - \frac{\text{REE in Residue}}{\text{REE in Feed}} \times 100 \quad (7)$$

The highest recovery of REE was observed in test 1 and the corresponding ash content of the clean coal was 24.6%. Even though test 13 resulted in the lowest ash content for clean coal, the REE recovery was comparatively lower than in test 1. This observation implies that the recovery of REE was not increasing with the decreasing percent of ash in the clean coal; consequently, no correlation exists between the clean coal ash (as produced from alkali-acid leaching) and the REE recoveries. The REE extraction during the al-

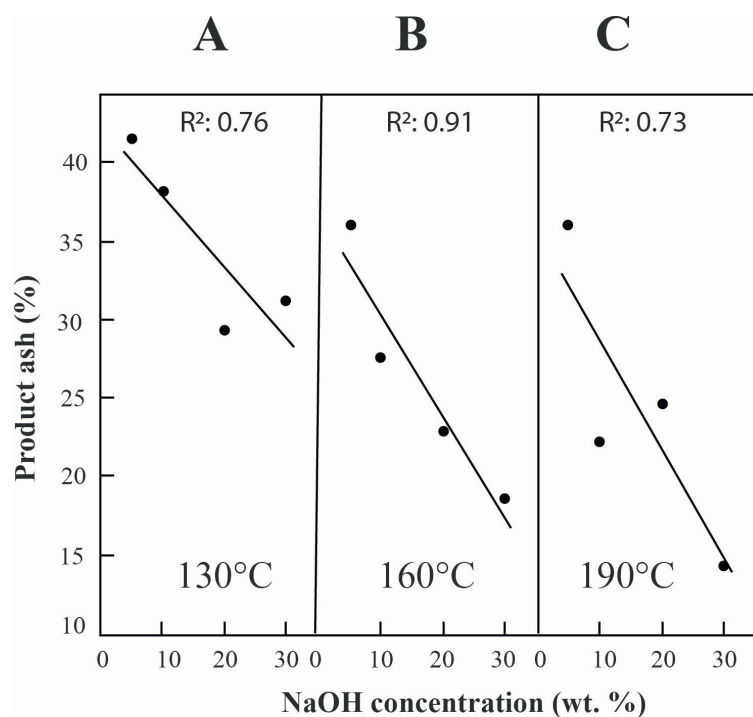
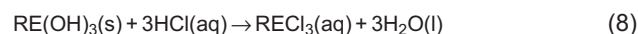


Figure 7. Effect of sodium hydroxide concentration on product ash (%) for various temperatures: A (130°C), B (160°C), C (190°C).

kali-acid leaching of coal can be explained using traditional REE phosphate mineral-leaching mechanism. During the alkali leaching of coal, the REE phosphate is converted to an insoluble rare-earth hydroxide, as explained in equation 1. During the acid leaching stage, rare-earth hydroxide is leached into rare-earth chloride, as shown below:



A previous study on monazite concentrate showed that phosphate dissolution increases with NaOH concentration, temperature and time (Panda et al., 2014). Figure 9 shows that the highest recovery of REE corresponds to 20 wt. % NaOH concentration, a temperature of 190°C and 60 min-

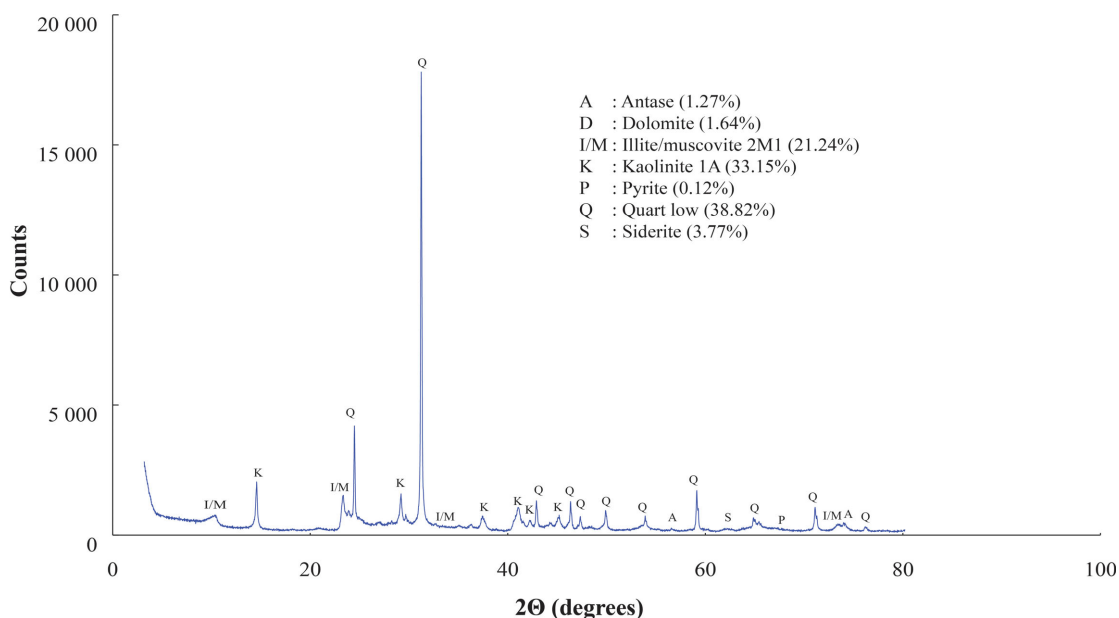


Figure 8. Quantitative X-ray diffraction (XRD) analysis of feed coal sample used for the alkali-acid leach test.

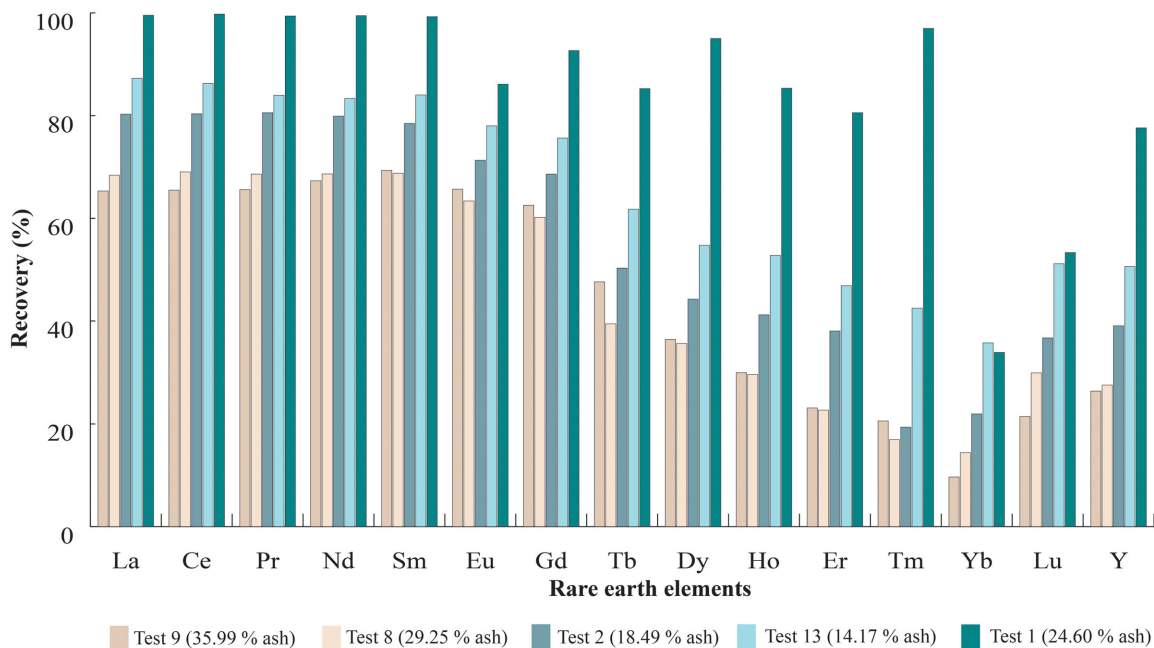


Figure 9. Individual rare-earth element (REE) recovery in selected clean coal residue with varying ash content (low to high) obtained after the alkali-acid leaching test. Results are displayed in increasing order of REE recovery. Sc and Pm were not included in the results shown.

utes of leaching. The lowest recovery of REE corresponds to test 9 and test 8, which have lower concentrations of NaOH (5%) and temperature (130°C), respectively. Using ICP-MS analysis of the leach solution, the amount of REE in the HCl leach solution was found to be significantly higher than that in the NaOH leach solution for test 1. These data indicate that REE dissolution might follow the mechanism for traditional rare-earth phosphate leaching, as explained previously in equation 1. Further, it is observed that

recoveries of light REE are higher than those of heavy REE for all tests.

Conclusions

Coal and its byproducts are viewed as a potential alternative for traditional rare-earth deposits. In this regard, several studies are being conducted for the characterization and extraction of rare-earth elements from coal sources. To understand the nature of REE association in coal as well as

to estimate the enrichment of rare-earth elements during coal beneficiation in East Kootenay coalfield samples, the feed sample was subjected to tree release analysis. Sequential extraction and mineralogical study using SEM-EDX identified REE associated with clays in both clean coal concentrate and tailings. The identification of REE associated with clays in the low-ash product reiterate the dominance of inorganic-associated REE in the samples.

Coal tailings generated using ROM samples from the East Kootenay coalfield in British Columbia were studied using an alkali-acid leaching process for the simultaneous extraction of clean coal and rare-earth elements. An approximate 70% reduction in the ash content of coal tailings was achieved to obtain clean coal. During the coal cleaning process, almost 97% of LREE and 76% of HREE were extracted simultaneously. The possible mechanisms of rare-earth elements extraction were also hypothesized.

There was no valid relationship found between ash reduction in coal (residue after leaching) and rare-earth-element extraction due to different target minerals available for leaching, such as silica and clay, for coal cleaning and rare-earth phosphates for REE extraction. Both processes depend on NaOH concentration, temperature and time. Subsequent study is required to optimize process parameters to maximize coal cleaning and rare-earth-element extraction simultaneously. The coal samples under consideration are of metallurgical quality and the production of clean coal and rare-earth concentrate from the coal tailings will enhance the economic viability of the process.

With the development of cost-effective extraction techniques for REE in coal, these elements will be extracted as byproducts of coal mining, thus strengthening brownfield operations by increasing profitability as well as potential green credits because these REE are used in clean energy technologies. In case of the greenfield operations, the possibility of extracting REE from coal will increase the competitiveness of deposits and more deposits may be feasible for mining and extraction.

Acknowledgments

The authors gratefully acknowledge the Geoscience BC scholarship. The authors also thank M. Mastalerz, Indiana University, and M. Mackay for their valuable comments and suggestions to improve this manuscript.

References

ASTM D2013/D2013M-12 (2012): Standard practice for preparing coal samples for analysis; ASTM International, West Conshohocken, Pennsylvania, URL <https://doi.org/10.1520/D2013_D2013M-12> [November 2018].

ASTM D3172-13 (2013): Standard practice for proximate analysis of coal and coke; ASTM International, West

Conshohocken, Pennsylvania, URL <<https://doi.org/10.1520/D3172>> [November 2018].

ASTM D3173/D3173M-17a (2017): Standard test method for moisture in the analysis sample of coal and coke; ASTM International, West Conshohocken, Pennsylvania, URL <https://doi.org/10.1520/D3173_D3173M-17A> [November 2018].

ASTM D3174-12 (2012): Standard test method for ash in the analysis sample of coal and coke from coal; ASTM International, West Conshohocken, Pennsylvania, URL <<https://doi.org/10.1520/D3174-12>> [November 2018].

ASTM D3175-17 (2017): Standard test method for volatile matter in the analysis sample of coal and coke; ASTM International, West Conshohocken, Pennsylvania, URL <<https://doi.org/10.1520/D3175-17>> [November 2018].

ASTM D388-17 (2017): Standard classification of coals by rank; ASTM International, West Conshohocken, Pennsylvania, URL <<https://doi.org/10.1520/D0388-17>> [November 2018].

Bai, J., Wang, Q., Wei, Y. and Liu, T. (2011): Geochemical occurrences of rare earth elements in oil shale from Huadian; *Journal of Fuel Chemistry and Technology*, v. 39, no. 7, p. 489–494, URL <[https://doi.org/10.1016/S1872-5813\(11\)60032-7](https://doi.org/10.1016/S1872-5813(11)60032-7)> [November 2018].

Behera, S.K., Chakraborty, S. and Meikap, B.C. (2017): Chemical demineralization of high ash Indian coal by using alkali and acid solutions; *Fuel*, v. 196, p. 102–109, URL <<https://doi.org/10.1016/J.FUEL.2017.01.088>> [November 2018].

Birk, D. and White, J.C. (1991): Rare earth elements in bituminous coals and underclays of the Sydney Basin, Nova Scotia: element sites, distribution, mineralogy; *International Journal of Coal Geology*, v. 19, p. 219–251.

Bryan, R.C., Richers, D., Andersen, H.T. and Gray, T. (2015): Assessment of rare earth elemental contents in select United States coal basins; *United States National Energy Technology Laboratory*, 47 p., URL <https://edx.netl.doe.gov/dataset/netl-ree-technical-reports/resource_download/137a0880-7c47-40d1-bc23-80b07264ab13> [November 2018].

Buhl, J.-C., Hoffmann, W., Buckermann, W.A. and Müller-Warmuth, W. (1997): The crystallization kinetics of sodalites grown by the hydrothermal transformation of kaolinite studied by Si MAS NMR; *Solid State Nuclear Magnetic Resonance*, v. 9, no. 2–4, p. 121–128, URL <[https://doi.org/10.1016/S0926-2040\(97\)00052-0](https://doi.org/10.1016/S0926-2040(97)00052-0)> [November 2018].

Dai, S. and Finkelman, R.B. (2018): Coal as a promising source of critical elements: progress and future prospects; *International Journal of Coal Geology*, v. 186, p. 155–164, URL <<https://doi.org/10.1016/J.COAL.2017.06.005>> [November 2018].

Dai, S., Jiang, Y., Ward, C.R., Gu, L., Seredin, V.V., Liu, H., Zhou, D., Wang, X., Sun, Y., Zou, J. and Ren, D. (2012): Mineralogical and geochemical compositions of the coal in the Guanbanwusu mine, Inner Mongolia, China: further evidence for the existence of an Al (Ga and REE) ore deposit in the Jungar coalfield; *International Journal of Coal Geology*, v. 98, p. 10–40.

Dai, S., Li, D., Ren, D., Tang, Y., Shao, L. and Song, H. (2004): Geochemistry of the late Permian No. 30 coal seam, Zhijin coalfield of Southwest China: influence of a siliceous low-temperature hydrothermal fluid; *Applied Geochemistry*

- try, v. 19, no. 8, p. 1315–1330, URL <<https://doi.org/10.1016/j.apgeochem.2003.12.008>> [November 2018].
- Dai, S., Ren, D. and Li, S. (2002): Occurrence and sequential chemical extraction of rare earth elements in coals and Seam roofs; *Journal of China University of Mining & Technology*, v. 31, no. 5, p. 349–353.
- Dash, P.S., Kumar, S.S., Banerjee, P.K. and Ganguly, S. (2013): Chemical leaching of high-ash Indian coals for production of low-ash clean coal; *Mineral Processing and Extractive Metallurgy Review*, v. 34, no. 4, p. 223–239, URL <<https://doi.org/10.1080/08827508.2012.656775>> [November 2018].
- Eskenazy, G.M. (1987): Rare earth elements in a sampled coal from the Pirin deposit, Bulgaria; *International Journal of Coal Geology*, v. 7, p. 301–314.
- Eskenazy, G.M. (1999): Aspects of the geochemistry of rare earth elements in coal: an experimental approach; *International Journal of Coal Geology*, v. 38, p. 285–295.
- European Commission (2017): Study on review of the list of critical raw materials, 92 p., URL <<https://publications.europa.eu/en/publication-detail/-/publication/08fdab5f-9766-11e7-b92d-01aa75ed71a1/language-en>> [November 2018].
- Finkelman, R.B. (1994): Modes of occurrence of potentially hazardous elements in coal: levels of confidence; *Fuel Processing Technology*, v. 39, no. 1–3, p. 21–34, URL <[https://doi.org/10.1016/0378-3820\(94\)90169-4](https://doi.org/10.1016/0378-3820(94)90169-4)> [November 2018].
- Finkelman, R.B., Palmer, C.A., Krasnow, M.R., Aruscavage, P.J., Sellers, G.A. and Dulong, F.T. (1990): Combustion and leaching behavior of elements in the Argonne Premium Coal Samples; *Energy & Fuels*, v. 4, no. 6, p. 755–766, URL <<https://doi.org/10.1021/ef00024a024>> [November 2018].
- Goodarzi, F. (1988): Elemental distribution in coal seams at the Fording coal mine, British Columbia, Canada; *Chemical Geology*, v. 68, no. 1–2, p. 129–154, URL <[https://doi.org/10.1016/0009-2541\(88\)90092-7](https://doi.org/10.1016/0009-2541(88)90092-7)> [November 2018].
- Goodarzi, N.N., Goodarzi, F., Grieve, D.A., Sanei, H. and Gentzis, T. (2009): Geochemistry of coals from the Elk Valley coal-field, British Columbia, Canada; *International Journal of Coal Geology*, v. 77, p. 246–259.
- Habashi, F. (2013): Extractive metallurgy of rare earths; *Canadian Metallurgical Quarterly*, v. 52, no. 3, p. 224–233, URL <<https://doi.org/10.1179/1879139513Y.0000000081>> [November 2018].
- Hower, J.C., Berti, D., Hochella, M.F. and Mardon, S.M. (2018): Rare earth minerals in a “no tonstein” section of the Dean (Fire Clay) coal, Knox County, Kentucky; *International Journal of Coal Geology*, v. 193, p. 73–86, URL <<https://doi.org/10.1016/J.COAL.2018.05.001>> [November 2018].
- Krishnamurthy, N. and Gupta, C. (2016): Extractive metallurgy of rare earths (Second Edition); CRC Taylor and Francis Group, Boca Raton, p. 235–330, URL <<https://www.crcpress.com/Extractive-Metallurgy-of-Rare-Earths/Krishnamurthy-Gupta/p/book/9781466576346>> [November 2018].
- Kumar, V., Kumar, A. and Holuszko, M.E. (2018): Occurrence of rare-earth elements in selected British Columbian coal deposits and their processing products; *in Geoscience BC Summary of Activities 2017: Minerals and Mining, Geoscience BC, Report 2018-1*, p. 87–100, URL <http://cdn.geosciencebc.com/pdf/SummaryofActivities2017/MM/SoA2017_MM_Kumar.pdf> [November 2018].
- Laskowski, J.S. (2001): Coal flotation and fine coal utilization (First Edition); Elsevier, Amsterdam, 368 p.
- Meshram, P., Sinha, M.K., Sahu, S.K. and Pandey, B.D. (2012): Chemical beneficiation of low-grade coal—A review; *in 16th International Conference on Non-ferrous Metals Proceedings*, Abhilash, P. Landge, and T.R. Mankhand (ed.), New Delhi, 13 p., URL <<http://eprints.nmlindia.org/6311/1/13-1—13-13.PDF>> [November 2018].
- Mukherjee, S. and Borthakur, P.C. (2001): Chemical demineralization/desulphurization of high sulphur coal using sodium hydroxide and acid solutions; *Fuel*, v. 80, no. 14, p. 2037–2040, URL <[https://doi.org/10.1016/S0016-2361\(01\)00094-1](https://doi.org/10.1016/S0016-2361(01)00094-1)> [November 2018].
- Mohanty, M.K., Honaker, B.Q., Patwardhan, A. and Ho, K. (1998): Coal flotation washability: an evaluation of the traditional procedures; *Coal Preparation*, v. 19, no. 1–2, p. 33–49, URL <<https://doi.org/10.1080/07349349808945572>> [November 2018].
- Moldoveanu, G. and Papangelakis, V. (2013): Recovery of rare earth elements adsorbed on clay minerals: II. leaching with ammonium sulfate; *Hydrometallurgy*, v. 131, p. 158–166.
- Panda, R., Kumari, A., Jha, M.K., Hait, J., Kumar, V., Rajesh Kumar, J. and Lee, J.Y. (2014): Leaching of rare earth metals (REMs) from Korean monazite concentrate; *Journal of Industrial and Engineering Chemistry*, v. 20, no. 4, p. 2035–2042, URL <<https://doi.org/10.1016/J.JIEC.2013.09.028>> [November 2018].
- Rahman, M., Pudasainee, D. and Gupta, R. (2017): Review on chemical upgrading of coal: production processes, potential applications and recent developments; *Fuel Processing Technology*, v. 158, p. 35–56, URL <<https://doi.org/10.1016/J.FUPROC.2016.12.010>> [November 2018].
- Resende, L.V. and Morais, C.A. (2010): Study of the recovery of rare earth elements from computer monitor scraps – leaching experiments; *Minerals Engineering*, v. 23, p. 277–280.
- Seredin, V.V. (1996): Rare earth element-bearing coals from the Russian Far East deposit; *International Journal of Coal Geology*, v. 30, p. 101–129.
- Seredin, V. and Dai, S. (2012): Coal deposits as potential alternative sources for lanthanides and yttrium; *International Journal of Coal Geology*, v. 94, p. 67–93.
- Sriramoju, S.K., Suresh, A., Lingam, R.K. and Dash, P.S. (2017): Mechanism of a coal chemical-leaching process and recovery of spent chemicals: a pilot-scale study; *International Journal of Coal Preparation and Utilization*, v. 37, no. 6, p. 293–302, URL <<https://doi.org/10.1080/19392699.2016.1179637>> [November 2018].
- Standing Committee on Natural Resources. (2014): The rare earth elements industry in Canada—summary of evidence, 26 p., URL <http://www.ourcommons.ca/Content/Committee/412/RNNR/WebDoc/WD6669744/412_RNNR_reldoc_PDf/RareEarthElements-Summary-e.pdf> [November 2018].
- Tessier, A., Campbell, P.G.C. and Bisson, M. (1979): Sequential extraction procedure for the speciation of particulate trace metals; *Analytical Chemistry*, v. 51, no. 7, p. 844–851, URL <<https://doi.org/10.1021/ac50043a017>> [November 2018].
- Tse, P.K. (2011): China’s rare-earth industry; *United States Geological Survey Open-File Report 2011-1042*, 11 p., URL <<https://pubs.usgs.gov/of/2011/1042/of2011-1042.pdf>> [November 2018].

- United States Department of Energy (2010): U.S. Department of Energy critical materials strategy, 190 p., URL <https://energy.gov/sites/prod/files/DOE_CMS2011_FINAL_Full.pdf> [November 2018].
- United States Department of Energy (2016): Rare earth elements program; the Energy lab, National Energy Technology Laboratory, 19 p., URL <<https://www.netl.doe.gov/FileLibrary/Research/Coal/RareEarthElements/REE-Project-Portfolio-2016.pdf>> [November 2018].
- Wang, C., Wang, W., Qin, Y., Sang, S., Zhu, Y. and Weiss, D. J. (2008): Geochemistry of rare earth elements in a marine influenced coal and its organic solvent extracts from the Antaibao mining district, Shanxi, China; *International Journal of Coal Geology*, v. 76, p. 309–317.
- Wang, Z.Y., Ohtsuka, Y. and Tomita, A. (1986): Removal of mineral matter from coal by alkali treatment; *Fuel Processing Technology*, v. 13, no. 3, p. 279–289, URL <[https://doi.org/10.1016/0378-3820\(86\)90036-6](https://doi.org/10.1016/0378-3820(86)90036-6)> [November 2018].
- Waugh, A.B. and Bowling, K.M. (1984): Removal of mineral matter from bituminous coals by aqueous chemical leaching; *Fuel Processing Technology*, v. 9, no. 3, p. 217–233, URL <[https://doi.org/10.1016/0378-3820\(84\)90043-2](https://doi.org/10.1016/0378-3820(84)90043-2)> [November 2018].
- Zhang, Y., Liu, G., Chou, C.-L., Wang, L. and Kang, Y. (2007): Sequential solvent extraction for the modes of occurrence of selenium in coals of different ranks from the Huaibei coalfield, China; *Geochemical Transactions*, v. 8, no. 1, 8 p., URL <<https://doi.org/10.1186/1467-4866-8-14>> [November 2018].
- Zhang, W., Rezaee, M., Bhagavatula, A., Li, Y., Groppo, J. and Honaker, R. (2015): A review of the occurrence and promising recovery methods of rare earth elements from coal and coal by-products; *International Journal of Coal Preparation and Utilization*, v. 35, p. 295–330.
- Zheng, L., Liu, G., Chou, C., Qi, C. and Zhang, Y. (2007): Geochemistry of rare earth elements in Permian coals from the Huaibei coalfield, China; *Journal of Asian Earth Sciences*, v. 31, p. 167–176.
- Zheng, L., Liu, G., Qi, C., Zhang, Y. and Wong, M. (2008): The use of sequential extraction to determine the distribution and modes of occurrence of mercury in Permian Huaibei coal, Anhui Province, China; *International Journal of Coal Geology*, v. 73, no. 2, p. 139–155, URL <<https://doi.org/10.1016/j.coal.2007.04.001>> [November 2018].
- Zhou, C.-C., Zhang, N.-N., Peng, C.-B., Cong, L.-F., Ouyang, C.-H. and Han, R. (2016): Arsenic in coal: modes of occurrence, distribution in different fractions, and partitioning behavior during coal separation—a case study; *Energy and Fuels*, v. 30, no. 4, p. 3233–3240, URL <<https://doi.org/10.1021/acs.energyfuels.5b02669>> [November 2018].

Assessing British Columbia Porphyry Fertility Using Zircons

F. Bouzari, Mineral Deposit Research Unit (MDRU), The University of British Columbia, Vancouver, BC, fbouzari@eoas.ubc.ca

C.J.R. Hart, MDRU, The University of British Columbia, Vancouver, BC

Bouzari, F. and Hart, C.J.R. (2019): Assessing British Columbia porphyry fertility using zircons; *in* Geoscience BC Summary of Activities 2018: Minerals and Mining, Geoscience BC, Report 2019-1, p. 45–54.

Introduction

Distinguishing metal-fertile from barren plutons provides a significant advantage to exploration geologists seeking to discover porphyry copper deposits, particularly in British Columbia (BC), where many porphyry systems occur within or around the edges of large batholiths. Zircon ($\text{Zr}[\text{Hf}]\text{SiO}_4$) is a common accessory mineral in granitoid rocks that host porphyry copper deposits. Trace-element composition of zircon is used to determine the age of the rock, temperature and oxidation state of the parental melt. Zircon commonly shows detailed internal texture and zoning, which provide clues to the environment in which it formed and ore-forming processes. The development of stable, rapid, high-resolution geochemical methods of in situ mineral analysis, such as laser-ablation inductively coupled plasma–mass spectrometry (LA-ICP-MS) applied to zircon, has led to an enormous increase in the amount of high-quality isotopic and trace-element data that geochemists and petrologists can access to assist them in resolving problems associated with the geology of igneous and metamorphic rocks (Jackson et al., 2003). Investigations by Ballard et al. (2002) and Shen et al. (2015) correlated the relative uptake of $\text{Ce}^{4+}/\text{Ce}^{3+}$ in zircon with the oxidation state of barren and fertile porphyry copper-mineralized intrusive rocks in northern Chile and central Asia. Dilles et al. (2015), Lee et al. (2017b) and Banik et al. (2017) showed similar relationships for porphyry copper deposits in Chile and Nevada using the Eu concentration in zircon. Furthermore, Shen et al. (2015) demonstrated a correlation between zircon $\text{Ce}^{4+}/\text{Ce}^{3+}$ ratios and the size of the porphyry copper deposits in central Asia. These investigations concluded that zircon provides a most useful tool for evaluating the porphyry copper fertility of plutons.

This study investigates district- to batholith-scale fertility indicators of porphyry copper deposits in the Guichon Creek, Takomkane and Granite Mountain batholiths as well as those in the Toodoggone area (Figure 1) by characterizing the textural and geochemical features of zircon to

develop tools and strategies for the exploration of porphyry copper deposits in the BC magmatic belts. Results show that the geochemical as well as the textural characteristics of zircon can assist in distinguishing porphyry-fertile plutons from nonmineralized or poorly mineralized plutons.

Zircon for Fertility Studies

Zircon is a preferred heavy mineral to evaluate the potential of plutonic rocks to host porphyry copper deposits because it is a common accessory mineral in a broad range of magmas. Zircon is resistant to subsolidus (hydrothermal) alteration, and demonstrably retains critically important pre-alteration and pre-mineralization geochemical information. Zircon persists in surficial sediments for tens or hundreds of kilometres beyond the hydrothermal or geochemical footprint of magmatic-porphyry centres (Averill, 2011), thus enabling detection of fertile-porphyry clusters at substantial distances from their source and on the regional scale of Cordilleran magmatic provinces (Lee et al., 2017a). Zircon recovery from soil, rock and drillcore samples is both feasible and affordable. Furthermore, in situ U-Pb and Pb-Pb geochronology of zircon using laser ablation has matured to the extent that it constitutes a preferred method to accurately date mineralized and barren magmas (e.g., Stern et al., 2011; Chiaradia et al., 2013).

Geological Setting

The Quesnel terrane in south-central BC is characterized by an Upper Triassic to Lower Jurassic island-arc volcanosedimentary package with numerous contemporaneous plutons and batholiths, some with associated clusters of porphyry copper deposits (Logan and Mihalynuk, 2014). The plutons and batholiths occur as three arc-parallel belts that progressively young from west to east (Schiarrizza, 2015). The western Upper Triassic belt is characterized by the calcalkaline Guichon Creek and Granite Mountain granodioritic batholiths, which host the Highland Valley and Gibraltar porphyry copper districts, respectively (Figure 1). Similar plutonic rock types and potential porphyry copper deposits are expected to occur beneath the Neogene and Quaternary cover rocks. The central plutonic belt consists of the most recent Triassic alkaline plutons that are dominated by monzonitic rocks, including the Copper

This publication is also available, free of charge, as colour digital files in Adobe Acrobat® PDF format from the Geoscience BC website: <http://www.geosciencebc.com/s/SummaryofActivities.asp>.

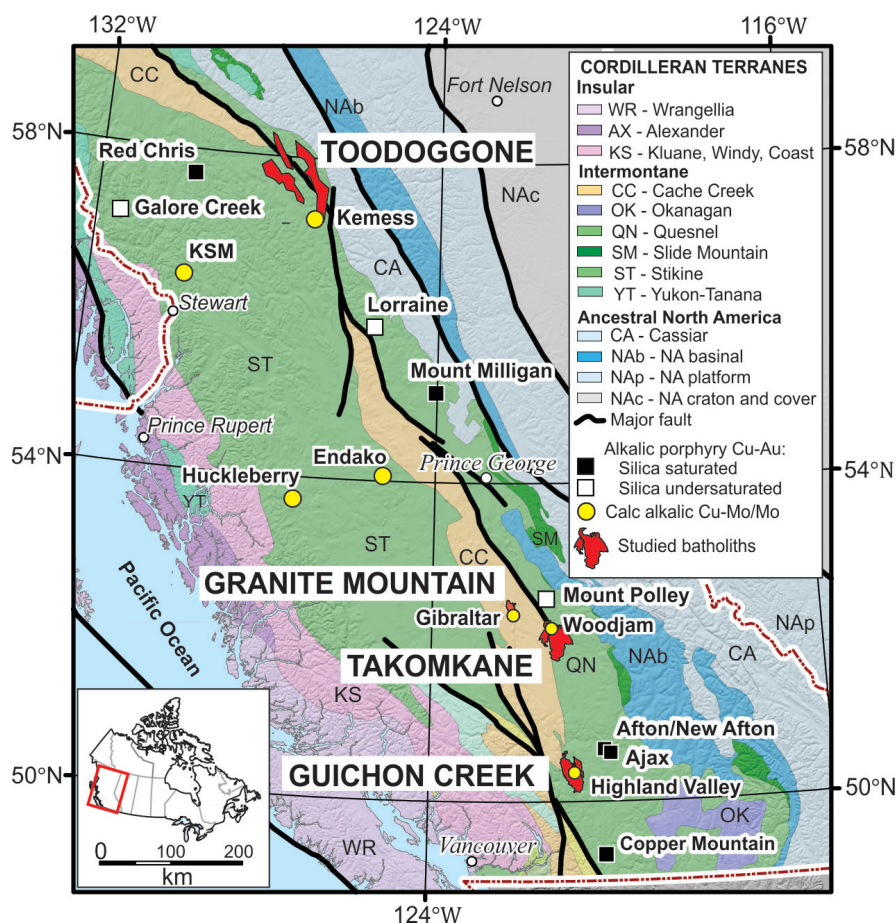


Figure 1. Location map, showing Cordilleran terranes, studied batholiths and major porphyry copper deposits in British Columbia (modified from Bissig and Cooke, 2014).

Mountain, Iron Mask and Mount Polley composite intrusions and related porphyry copper deposits. The easternmost belt consists of several Lower Jurassic calcalkaline granodioritic batholiths such as the Pennask and Takomkane batholiths, which host the Brenda and Woodjam property's Southeast Zone porphyry copper deposits, respectively.

Fertility characteristics of plutons of the Guichon Creek, Granite Mountain and Takomkane batholiths are considered, as well as those of plutons that occur in the Toadoggonne area. The geological setting of these areas is provided in Bouzari et al. (2016) and reference therein, a brief summary of each district is given here.

Guichon Creek Batholith

The Upper Triassic Guichon Creek batholith is a north-trending, approximately 65 by 30 km body that intruded and thermally metamorphosed the Upper Triassic Nicola Group basaltic to andesitic volcanic and volcanoclastic rocks (McMillan et al., 2009) of the Quesnel terrane. The batholith is composite and zoned, with earlier diorite and quartz diorite border phases that surround younger granodiorite phases in the centre (Casselman et al., 1995; Byrne

et al., 2013; D'Angelo et al., 2017). These mostly concentric phases, from the margins inward, are: the Border phase, the Highland Valley phases (consisting of the Guichon and Chataway subphases), the Bethlehem phases (consisting of the Bethlehem and Skeena subphases) and the Bethsaida phase. The Bethlehem and Skeena subphases and the Bethsaida phase host most of the Highland Valley porphyry copper-molybdenum deposits (Valley, Lornex, Highmont, Alwin, Bethlehem and JA).

Takomkane Batholith

The Takomkane batholith is a large (50 by 40 km) Upper Triassic–Lower Jurassic composite batholith that hosts several mineralized porphyry centres. It intrudes the Upper Triassic Spout Lake pluton and is cut by Lower Jurassic ultramafic–mafic plutons and the Lower Cretaceous Boss Mountain stock. The Takomkane batholith consists of two major units: the Upper Triassic–Lower Jurassic Boss Creek unit and the Lower Jurassic megacrystic Schoolhouse Lake unit. A smaller volume unit of

quartz-feldspar porphyry occurs within the Schoolhouse Lake unit. The Woodjam Creek unit is texturally distinct but compositionally similar to the Schoolhouse Lake unit and forms the northwestern part of the batholith (Scharizza et al., 2009). The Woodjam Creek unit (194.99 ± 0.16 Ma, del Real et al., 2017) has a similar age to the Schoolhouse Lake unit but has less quartz and does not contain the large K-feldspar megacrysts that characterize the latter. The Woodjam Creek unit is host to the major porphyry copper deposits, including the Southeast Zone (del Real et al., 2017).

Granite Mountain Batholith

The Upper Triassic Granite Mountain batholith (18 by 10 km), which hosts the Gibraltar porphyry copper mine, occurs near McLeese Lake in south-central BC. The batholith is subdivided into three main units, from the southwest to the northeast: Border phase diorite to quartz diorite, Mine phase tonalite and Granite Mountain phase leucocratic tonalite. The Burgess Creek stock (Panteleyev, 1978), to the northeast, comprises a heterogeneous assemblage of tonalite, quartz diorite and diorite that intrudes the Nicola Group. Mineralization at the Gibraltar mine is

hosted in the Mine phase tonalite of the Granite Mountain batholith. The age of the mineralization (215 ± 1.0 to 210 ± 0.5 Ma), determined based on three dates acquired using the rhenium-osmium method (Harding, 2012), indicates that the mineralization was penecontemporaneous with the emplacement of the Mine phase. But more recent fieldwork (C. Gallagher, pers. comm., 2017) suggests that porphyry dikes that cut the Mine phase were probably more closely associated with the mineralization event than the Mine phase. Samples of these dikes were not available in the course of this study.

Toodoggone Area Plutons

The Toodoggone area in north-central BC is a northwest-trending district located in the eastern part of the Stikine terrane. Geology of the Toodoggone area is described in detail by Diakow et al. (1993, 2005). Asitka, Takla and Hazelton group volcano-sedimentary rocks in the Toodoggone area are intruded by Upper Triassic to Lower Jurassic felsic to intermediate plutons and cogenetic dikes of the Black Lake suite (Diakow et al., 2005). The plutons are exposed at several locations, commonly forming elongated northwest-trending bodies. The Giegerich and Jock Creek plutons occur on the eastern margin of the area and the Duncan Hill pluton occurs in the western and central parts of the area. Small, and probably deeply eroded, porphyry copper mineralization at the Sofia prospect occurs within the Jock Creek pluton. Several smaller and presumably less eroded plutons, such as the Sovereign pluton near the Kemess deposit or those near the Brenda prospect, occur in the central part of the area. Kemess is the major porphyry copper-gold deposit in the district and is associated with the small Maple Leaf granodiorite pluton (Duuring et al., 2009).

Samples and Methods

A total of 127 rock samples were collected from various intrusive phases. Hand-sawn samples were described and further characterized using a petrographic microscope. A subset of 44 samples, representing main intrusive bodies, were selected for zircon separation and analysis, including 12 from the Guichon Creek, 12 from the Takomkane and 7 from the Granite Mountain batholiths, and 13 from the Toodoggone area.

Samples were disaggregated using a Spark 2 electric-pulse disaggregator at Overburden Drilling Management Limited (Nepean, Ontario) to break the rock along mineral-grain boundaries, providing a larger number of unbroken mineral grains. Subsequently, mineral separation was performed at the Mineral Deposit Research Unit, The University of British Columbia using Frantz[®] magnetic separation and conventional heavy-liquid methods.

Mineral grains were handpicked, mounted and polished in preparation for electron-probe microanalysis (EPMA) and trace-element laser-ablation inductively coupled plasma-mass spectrometry (LA-ICP-MS) at The University of British Columbia. A total of 1022 zircon grains were mounted and analyzed. These grains were studied and characterized by binocular, petrographic and cathodoluminescence (CL) microscopy. Properties such as colour, shape, inclusion populations and zoning were documented for each grain. Mineral grains and spots were then analyzed by EPMA for major elements and some trace elements before being analyzed by LA-ICP-MS for a full trace-element characterization. A total of 1620 spots were analyzed. In the case of smaller grains ($<100 \mu\text{m}$), one spot was analyzed per sample, whereas for larger grains ($>100 \mu\text{m}$), two spots were analyzed per grain, one at the grain centre and one at the rim.

Details on the samples and the analytical techniques used in this study will be published in a subsequent publication.

Zircon Texture

Zircon typically forms $100\text{--}500 \mu\text{m}$ long grains with complex internal zoning. Cathodoluminescence imaging was used to characterize the texture of the zircon grains. Oscillatory zoning is the most common type of zoning (Figure 2a), creating zones of green, dark green and grey luminescence. Fine zoning of <1 to $>10 \mu\text{m}$ for each zone is common and occurs around a larger core. Zircon grains locally have a black luminescent core, with an irregular shape resembling an antecryst. Elongated zircon grains display tabular zoning (Figure 2b), which occurs as parallel bands of green, light green, grey or black coloured luminescence; however, fine parallel zoning is not common. A combination of tabular and oscillatory zoning, known as tabular-oscillatory zoning, is also common (Figure 2c) and is characterized by the core of the zircon grains always showing tabular zoning rimmed by oscillatory zoning. However, zircon grains with oscillatory zoning rimmed by tabular zoning were not observed. This relationship suggests that zircons with tabular zoning always formed prior to the zircons with oscillatory zoning. Oscillatory zoning with sector zonation is another common type of zoning (Figure 2d). Zircon grains that show irregular zoning, which commonly occurs in zircon with oscillatory zoning, are distinctly different; in such grains, new growth zones crosscut older zones (Figure 2e, f), thus suggesting that new zircon zones formed by modifying or destroying older zones.

Zircon Trace-Element Chemistry

Zircon trace-element chemistry is a robust tool with which to study magmatic and ore-forming processes. Zircon structure can incorporate many trace elements and because of the slow rates of oxygen diffusion for these elements

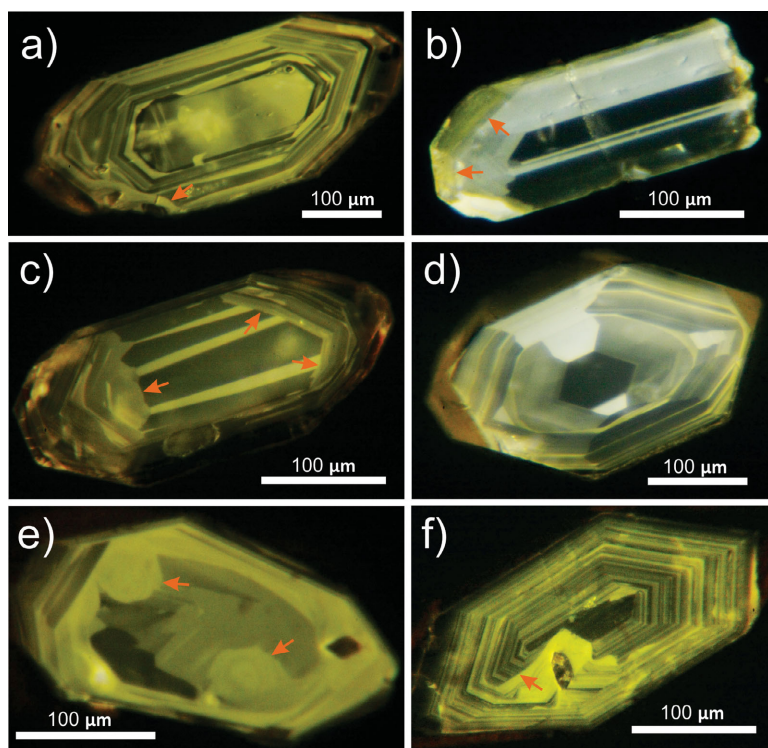


Figure 2. Cathodoluminescence images of zircon grains, showing various types of zoning: **a)** oscillatory zoning in a zircon grain, with some irregular zoning where younger zones crosscut older zones near the rim (indicated by the arrow); **b)** tabular zoning, with oscillatory zoning evident where it started to crystallize near the rim (indicated by the arrows); **c)** tabular zoning rimmed by oscillatory zoning (indicated by the arrows); **d)** oscillatory and sector zoning; **e)** and **f)** irregular zoning with the rim crosscutting the core zoning (indicated by the arrows).

(Cherniak et al., 1997), it retains initial compositions and thus provides a record of magmatic processes occurring during zircon growth such as oxidation state and temperature, which are important factors in the formation of porphyry copper deposits. Zircon in plutonic rocks of the porphyry belts typically display low abundances of light rare-earth elements (LREE) and high relative abundances of heavy rare-earth elements (HREE), with positive Ce and negative Eu anomalies (Ballard et al., 2002; Dilles et al., 2015). Typically, in mineralized intrusions, the Ce anomaly is larger and the Eu anomaly smaller in magnitude compared to nonmineralized intrusions (Ballard et al., 2002).

HREE Enrichment

The Th/U versus Yb/Gd plot shows zircon evolution following a curved path for all batholiths, with the Yb/Gd ratio increasing as the Th/U ratio decreases (Figure 3). The Guichon Creek batholith displays a wide range of Th/U and Yb/Gd ratios for zircons from both nonmineralized and mineralized phases (Figure 3a). However, zircon from the earlier phases, such as the Border and Guichon phases, have high Th/U and low Yb/Gd ratios (>0.45 and <15 , respectively), whereas mineralized phases, such as Bethsaida and Skeena, have zircons with lower Th/U and higher Yb/Gd

ratios (<0.45 and >15 , respectively). Similarly, at the Takomkane batholith, results from zircons recovered from the earlier phases of Spout Lake, Buster Lake and Boss Creek show a curved path, with a wide range of compositions but with higher Yb/Gd and lower Th/U ratios for the Boss Creek relative to the Spout Lake phase (Figure 3b). Zircon composition of the mineralized Woodjam Creek phase, clustered in the middle of the curve, presents a range of Yb/Gd and Th/U ratios strikingly similar to those of the Bethsaida phase of the Guichon Creek batholith. Zircons from the Schoolhouse Lake and quartz-feldspar porphyry phases of the Takomkane batholith appear scattered and fall largely off the main curve (Figure 3b). The zircons from the Granite Mountain batholith follow a similar curve on the Yb/Gd versus Th/U plot (Figure 3c), with the mineralized Mine phase, which occurs in the middle of the curve, displaying similar Th/U ratios to those of zircons from the Guichon Creek and Takomkane batholiths (between 0.2 and 0.45) but slightly lower Yb/Gd (>10). Samples from the Toodoggone area show a similar curved path, with overlap of the Th/U and Yb/Gd ratios of the various phases (Figure 3d). Zircons from the mineralized phases at Kerness and Sofia have low Th/U (<0.5) and high Yb/Gd (>20).

Crystal Fractionation

The increase in Th/U ratios in zircons is attributed to crystal fractionation producing residual melts with relatively high U and Th contents but low Th/U ratios (Miller and Wooden, 2004). The Yb/Gd increase is attributed to apatite, hornblende and titanite crystallization: as the magma cools and crystallizes, apatite, hornblende and titanite fractionation depletes the melt in middle rare-earth elements (MREE), causing an increase in zircon of HREE relative to MREE, and thus high Yb/Gd. The similarity of the Th/U and Yb/Gd ratios of zircons from all mineralized phases suggests that all fertile magmas require a certain amount of fractional crystallization. The variation in zircon compositions along the observed evolutionary paths reflects different proportions of apatite, hornblende and titanite in the sequence of crystallization (Lee et al., 2017b). This is more notable for zircons from the Mine phase of the Granite Mountain batholith that have lower Yb/Gd (10–25), which suggests less fractionated rock. The distribution pattern of the Th/U and Yb/Gd ratios of zircons from the poorly mineralized Schoolhouse Lake and quartz-feldspar porphyry units of the Takomkane batholith is quite scattered and does not follow the curved path of crystal fractionation (Figure 3b), which was probably due to the melts assimilating U-, Th-

and REE-enriched crustal materials. Lee et al. (2017b) came to the same conclusion and suggested that poorly mineralized rocks at El Salvador, in Chile, display evidence of crustal mixing and contamination, whereas the mineralized phases show evidence of simple crystal fractionation.

Eu Anomaly and Oxidation State

Europium in magma exists mainly as Eu^{2+} , which prefers partitioning into feldspar and thus generates a negative Eu anomaly in crystallizing zircon. Higher oxidation states promote an increase in the abundance of Eu^{3+} , which favours partitioning into zircon and thus decreases the negative Eu anomaly. The europium anomaly ($\text{Eu}_N/\text{Eu}_N^*$) is typically calculated as the ratio of chondrite-normalized Eu abundance relative to Sm and Gd. Hafnium is an incompatible element and its content in zircon is used as a proxy for percentage of crystallization and decrease in modal temperature (Dilles et al., 2015). The Eu anomaly versus Hf plot shows distinct variations in BC porphyry-related plutons (Figure 4a–d).

At Guichon Creek, zircons from the nonmineralized Border, Guichon and Chataway phases show an increase in Hf concentration as the Eu anomaly decreases; however, most nonmineralized samples have Eu anomalies <0.3 (Figure 4a). The increase in Hf concentration in zircon occurs as the temperature decreases and magma progressively crystallizes (Dilles et al., 2015). Zircons from the mineralized Bethsaida, Skeena and Bethlehem phases have variable Hf concentrations, with the samples from the Bethsaida and Skeena phases commonly showing higher Hf concentrations than those from the Bethlehem phase, which suggests that the Bethsaida and Skeena phases formed at lower temperatures than the Bethlehem phase. Lee et al. (2017a) reported a similar trend. More importantly, zircons from all three mineralized phases have Eu anomalies >0.35 , suggesting that magmatic cooling and crystallization in these mineralized phases occurred under higher oxidation states that prevented the decrease in Eu anomaly values, in sharp contrast to values of the nonmineralized phases.

Zircons from the Takomkane batholith show similar Eu and Hf relationships to those of the Guichon Creek zircons. Samples from the Spout Lake, Buster Lake and Boss Creek plutons show zircons with a wide range of Eu anomalies and Hf concentrations that plot roughly along a curved line (Figure 4b). Zircons from the mineralized Woodjam Creek unit display a distinct Eu anomaly >0.35 . Zircons from the younger but non-mineralized phases of the Schoolhouse Lake and quartz-feldspar porphyry units also display similar Eu

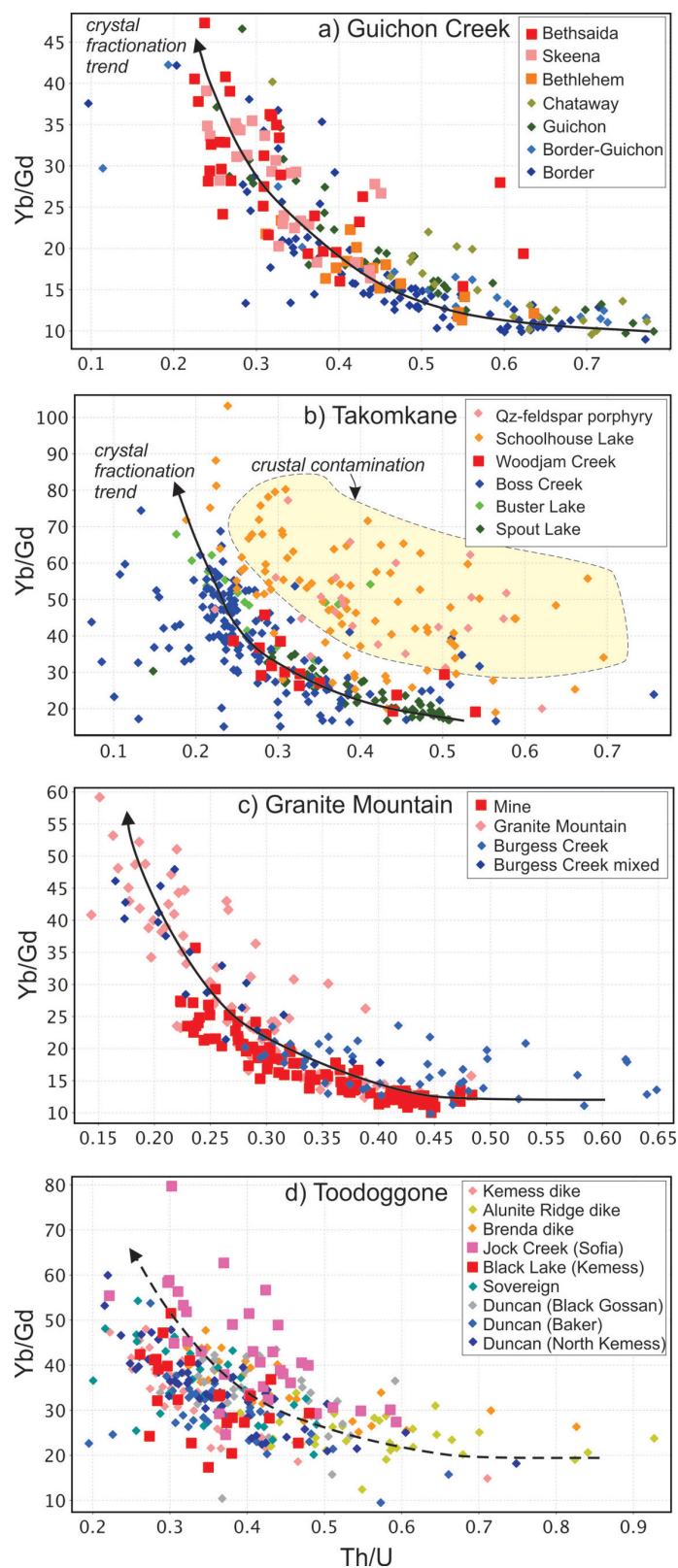


Figure 3. Binary diagram of Th/U versus Yb/Gd, showing a curved evolutionary path for zircons from porphyry-fertile plutons with moderate to high crystal fractionation, along with the scatter plot of plutons with crustal contamination and therefore lacking mineralization: **a)** Guichon Creek batholith; **b)** Takomkane batholith; **c)** Granite Mountain batholith; **d)** Toodoggone area. Abbreviation: Qz, quartz.

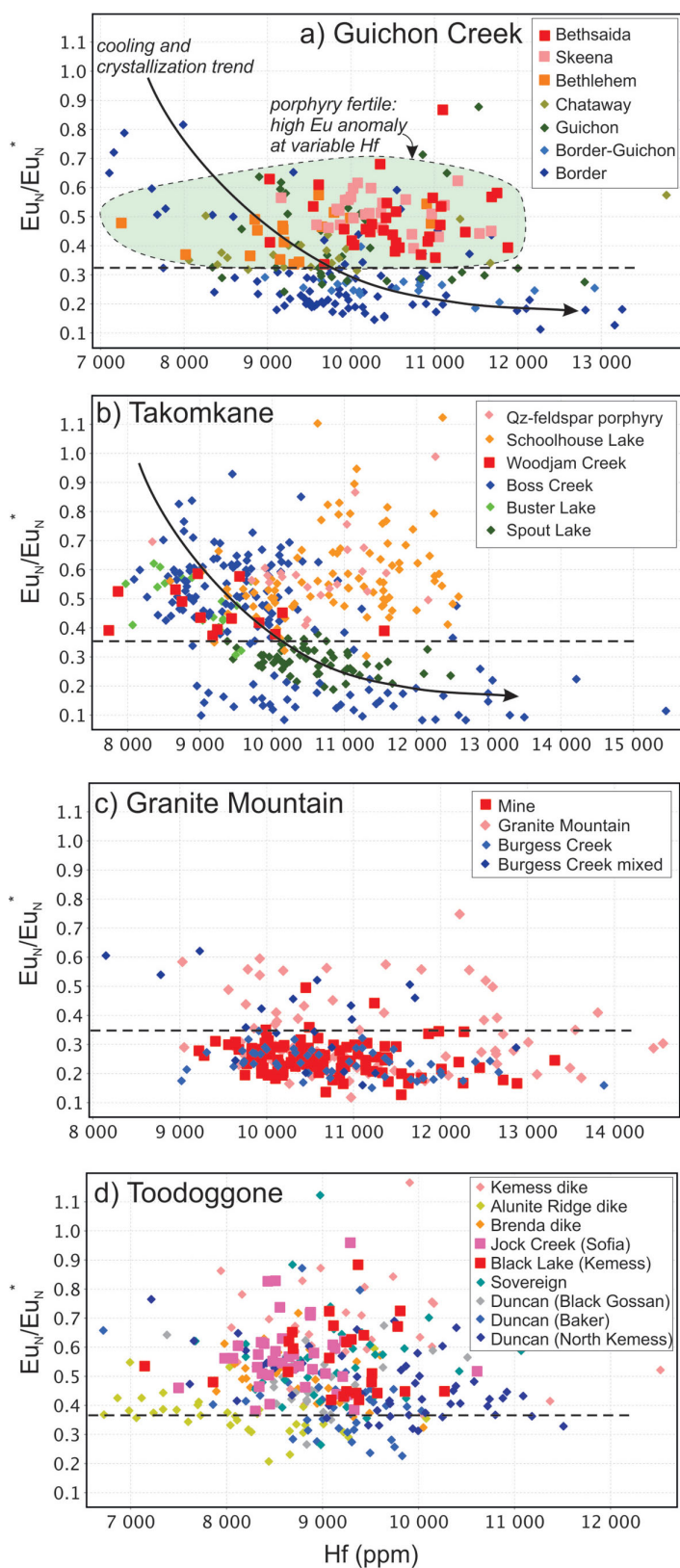


Figure 4. An Eu anomaly (Eu_N/Eu_N^*) versus Hf concentration plot, showing that zircons from mineralized phases have a Eu anomaly >0.35 regardless of Hf concentration, whereas zircons from nonmineralized phases have variable Eu values: **a)** Guichon Creek batholith; **b)** Takomkane batholith; **c)** Granite Mountain batholith; **d)** Toodoggone area. Abbreviation: Qz, quartz.

anomaly values >0.35 . However, zircons from these two units show a higher Hf concentration relative to that of the Woodjam Creek unit samples, suggesting that magmas were more fractionated in these younger units.

Zircons from the Granite Mountain batholith show a wide range of Hf concentrations, similar to those from the Guichon Creek and Takomkane batholiths, but the nonmineralized phases and apparently mineralized Mine phase both have zircons with a largely low Eu anomaly (<0.35), which suggests that much of this batholith crystallized under a low oxidation state (Figure 4c). Given the recent field observations on the occurrence of younger mineralized porphyry dikes that cut the Mine phase (see above), it may be that the Mine phase represents a slightly older phase of the mineralization.

Zircon samples from various plutons in the Toodoggone area also show a wide range of Hf concentrations, whereas they commonly show a Eu anomaly >0.35 , especially those from the mineralized phase of the Black Lake suite at Kemess and from the Jock Creek pluton at Sofia (Figure 4d). The zircon grains from other phases, such as those from the Duncan and Sovereign plutons, have variable Eu anomaly values ranging from low (<0.35) to high (>0.35).

Effect of Titanite and Apatite Crystallization versus Oxidation State and Magmatic Water

The Eu anomaly is commonly used to characterize the oxidation state of the magma such that at a higher oxidation state most Eu is present in the trivalent state and is not partitioned into fractionating plagioclase (Frey et al., 1978; Dilles et al., 2015). Alternatively, lack of a significant Eu anomaly can also be caused by high magmatic water contents, which suppresses plagioclase fractionation (Richards, 2011). Loader et al. (2017) argued that the fractionation of titanite and apatite has the potential to impart a positive Eu anomaly on residual melts, which may be inherited by zircon when it subsequently crystallizes.

Plots of Eu anomaly in zircon versus Yb/Gd (Figure 5) are used to further characterize the Eu anomaly and the effect of crystal fractionation, oxidation state and magmatic water. As discussed above, the Yb/Gd ratio is a proxy for fractionation of apatite, hornblende and titanite, which depletes the melt in MREE, causing an increase in zircon of HREE relative to MREE (high Yb/Gd). Zircons from the non-mineralized plutons have a wide range of Eu anomaly values (<0.2 to >0.6) and Yb/Gd (~ 10 to >40).

Zircons from the mineralized plutons, except the Mine phase of the Granite Mountain batholith, display a similar range of Yb/Gd but a distinctly higher Eu anomaly (≥ 0.35).

The above relationship suggests that apatite and titanite fractionation had different effects on mineralized and nonmineralized plutons. Zircons from the nonmineralized phases of all batholiths show a positive correlation between Yb/Gd and Eu_N/Eu_N^* (Figure 5a–d). Thus, as the melt became more fractionated with apatite and titanite (i.e., higher Yb/Gd), the Eu anomaly increased, becoming less negative. Therefore, the increase in the Eu anomaly could have been related to the apatite and titanite fractionation, as described by Loader et al. (2017), although the effect of an increase in oxidation state cannot be ruled out. However, the Eu anomaly values of zircons from the mineralized phases do not show any correlation with Yb/Gd (Figure 5). Thus, the mineralized phases have an Eu anomaly >0.35 whether Yb/Gd ratios are high or low, suggesting that apatite and titanite crystallization did not influence the Eu anomaly in zircons of the mineralized plutons.

The variation in Yb/Gd and petrographic evidence suggest that apatite and titanite fractionation occurred in the mineralized plutons, but the question remains as to why the fractionation processes did not affect the Eu anomaly in zircon? It could be that the effect of apatite and titanite crystallization on the Eu anomaly of zircon was largely minimized or nullified by the high oxidation state and water content of the mineralizing magma.

Correlation Between Trace Element and Zircon Texture

Zircon grains commonly display complex and fine textural zoning (see above). The correlation between these textures and zircon chemistry is usually difficult to establish because of the fine nature of the textural variations in zircon ($<10 \mu\text{m}$) and the laser-beam size selected for LA-ICP-MS analysis ($34 \mu\text{m}$ in this case). However, this study shows that there is a correlation between the type of zircon grains and their trace-element chemistry. Figure 6a shows the Eu anomaly plotted against Hf content for all studied zircon grains, classified according to their type of zoning. Zircon grains with an elongated shape and tabular zoning distinctly have a lower Eu anomaly, whereas granular zircon grains with oscillatory zoning display a wide range of Eu anomaly values, from low to high, although zircons with a high Eu anomaly (≥ 0.35) are more common. Zircon grains that display tabular-oscillatory zoning are commonly similar in

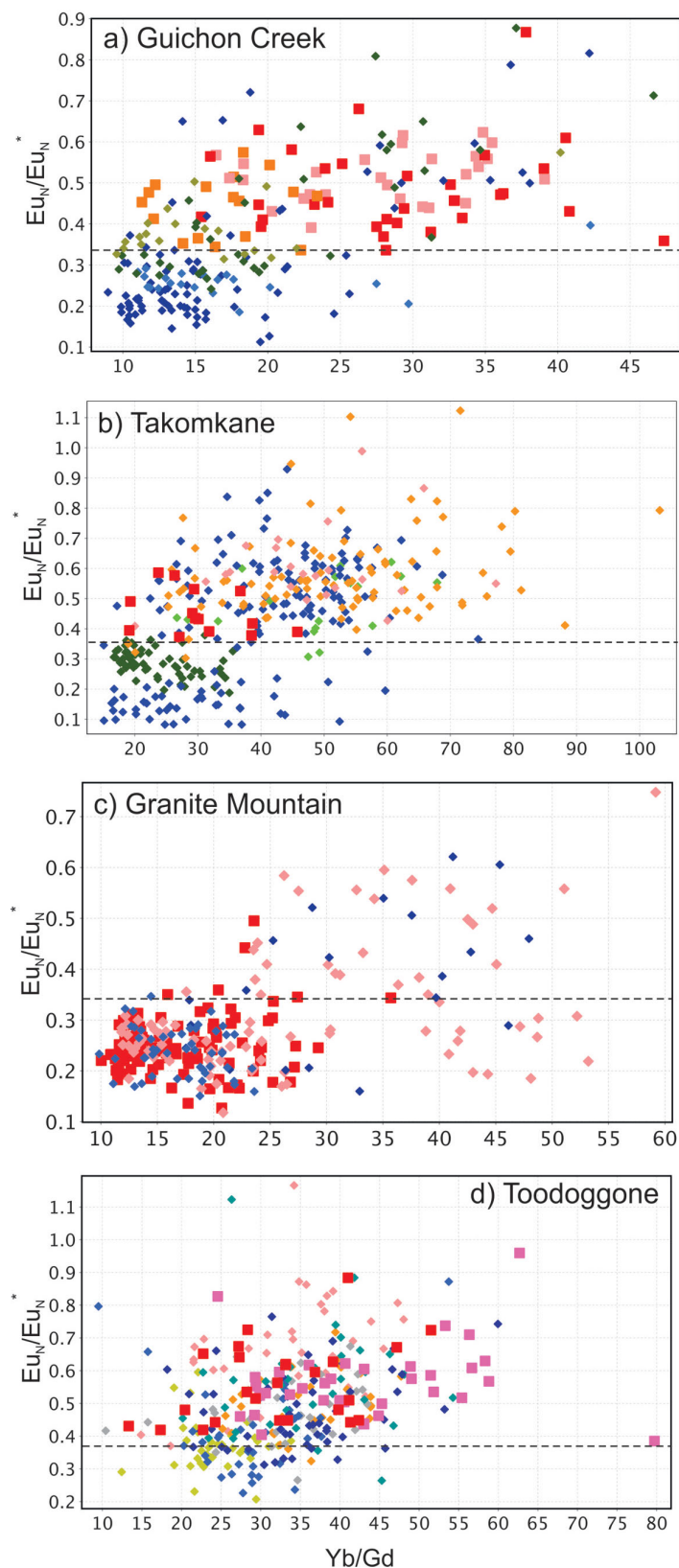


Figure 5. Europium anomaly in zircons and Yb/Gd as a proxy for apatite and titanite fractionation, showing that the Eu anomaly in the mineralized plutons is not affected by apatite and titanite fractionation: **a)** Guichon Creek batholith; **b)** Takomkane batholith; **c)** Granite Mountain batholith; **d)** Toodoggone area. Legend is the same as that used for Figure 4.

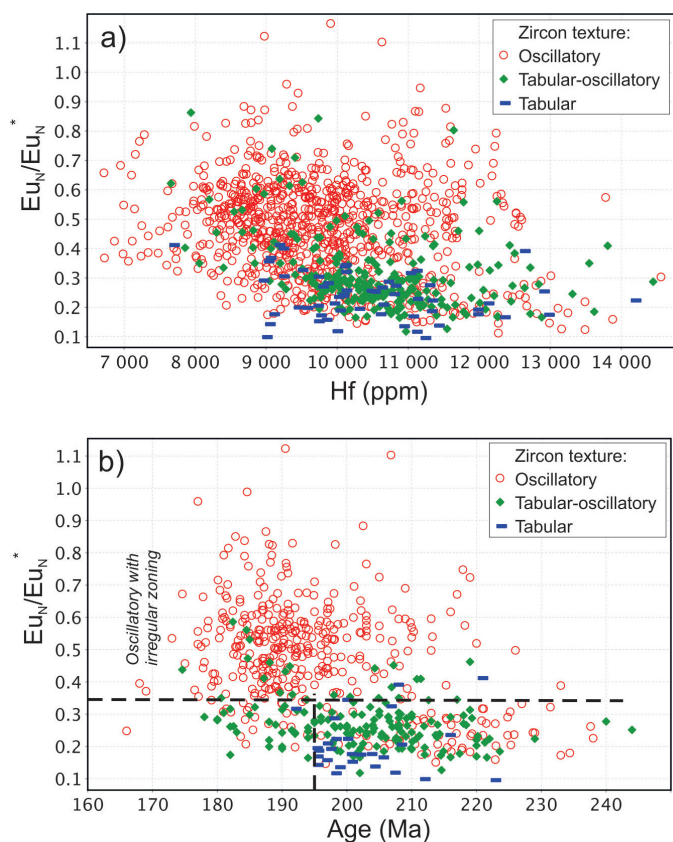


Figure 6. Diagram showing the correlation between zircon texture **a)** and age **b)** with the europium anomaly of zircon.

composition to those with tabular zoning; however, some zircon grains have a composition like that of zircons with oscillatory zoning. The reason for this is that, in the case of most of the grains, the core with tabular zoning was analyzed, whereas in the case of grains rimmed with oscillatory zoning, the rim was analyzed only if it was thick enough (>40 μm).

Age calculations based on U-Pb for a subset of grains (Figure 6b) show that zircon grains with tabular zoning and a low Eu anomaly are older than 195 Ma. The zircon grains with oscillatory zoning and a high Eu anomaly have a wide range of ages but are mostly younger than 200 Ma (ca. 180–200 Ma.). This relationship re-emphasizes, as was proposed in McMillan et al. (1995), that the plutons emplaced between 200–185 Ma are more likely to prove fertile. This is particularly true in terms of oxidation state and magmatic water content. More importantly, the shape and texture of zircon grains can be used to screen plutons for fertility since fertile plutons have abundant zircon with oscillatory zoning, which commonly shows irregularities where younger zones crosscut older zones (see above). These preliminary observations suggest that the study of zircon texture can be further developed to help in more efficiently identifying porphyry fertile plutons.

Conclusions

Zircons from the porphyry-fertile plutons in BC show several distinct characteristics that relate them to the ancient magmas that have an increased potential to generate porphyry copper deposits. Zircons from the mineralized plutons have small negative Eu anomalies ($Eu_N/Eu_N^* \geq 0.35$). This reflects 1) high magmatic water content and consequent suppression of early plagioclase crystallization (e.g., Ballard et al., 2002) and 2) late magmatic oxidation resulting in the loss of SO₂-rich magmatic-hydrothermal ore fluids during late-stage crystallization of granite (Dilles et al., 2015; Lee et al., 2017b). In each batholith complex, the mineralized plutons are associated with precursor plutons that are poorly mineralized or nonmineralized. These nonmineralized plutons show a variable Eu anomaly, which is interpreted to be largely controlled by crystal fractionation, particularly that of apatite and titanite (Loader et al., 2017). Therefore, the crystal fractionation of the magmas of these plutons did not produce ore deposits because of a low oxidation state or low magmatic water content, or both. Crystal fractionation also occurred during cooling of the mineralized plutons, but unlike the nonmineralized plutons, the effects of apatite and titanite crystallization were nullified by the high oxidation state and water content of the magma. Therefore, an Eu anomaly distribution in plutons that is not significantly affected by Hf concentration or Yb/Gd values suggests that both magmatic water and oxidation state were high during the entire cooling history of the magma and are potentially a better source of mineralization leading to the formation of porphyry copper deposits.

In summary, the key features of zircon that indicate porphyry-fertile plutons in BC are:

- zircons of Early Jurassic age (ca. 200–185 Ma);
- zircons with oscillatory zoning, particularly the ones that show some irregular zoning patterns crosscutting oscillatory zoning;
- zircons that show simple crystal fractionation, with values on the Yb/Gd versus Th/U plot forming a curved line, which suggests a lack of crustal contamination;
- zircons with an Eu anomaly ≥ 0.35 , which suggests a high magmatic water content and oxidation state; and
- zircons with an Eu anomaly not dependent on Hf concentration or Yb/Gd values, suggesting that magmatic water content and oxidation state were high and remained high during much of the magma crystallization.

Acknowledgments

Geoscience BC is thanked for its financial contribution in support of this project. B. Najafian helped with mineral separation, E. Chan helped with mineral-grain photography and H. McIntyre helped with laser ablation, inductively

coupled plasma–mass spectrometry analysis. The authors thank R. Lee of the Mineral Deposit Research Unit, The University of British Columbia for his review of and comments on this paper.

References

- Averill S.A. (2011): Viable indicator minerals in surficial sediments for two major base metal deposit types: Ni-Cu-PGE and porphyry Cu; *Geochemistry, Exploration, Environment, Analysis*, v. 11, p. 279–291.
- Ballard, J.R., Palin, J.M. and Campbell, I.H. (2002): Relative oxidation states of magmas inferred from Ce(IV)/Ce(III) in zircon: application to porphyry copper deposits of northern Chile; *Contributions to Mineralogy and Petrology*, v. 144, p. 347–364.
- Banik, T.J., Coble, M.A. and Miller, C.F. (2017): Porphyry Cu formation in the middle Jurassic Yerington batholith, Nevada, USA: Constraints from laser Raman, trace element, U-Pb age, and oxygen isotope analyses of zircon; *Geosphere*, v. 13, no. 4, p. 1113–1132, URL <<https://doi.org/10.1130/GES01351.1>> [November 2018].
- Bissig, T. and Cooke, D.R. (2014): Introduction to the special issue devoted to alkalic porphyry Cu-Au and epithermal Au deposits; *Economic Geology* v. 109, p. 819–825.
- Bouzari, F., Hart, C.J.R., Bissig, T. and Lesage, G. (2016): Mineralogical and geochemical characteristics of porphyry-fertile plutons: Guichon Creek, Takomkane and Granite Mountain batholiths, south-central British Columbia; *in* Geoscience BC Summary of Activities 2015, Geoscience BC, Report 2016-1, p. 17–22, URL <http://www.geosciencebc.com/i/pdf/SummaryofActivities2015/SoA2015_Bouzari.pdf> [November 2018].
- Byrne, K., Stock, E., Ryan, J., Johnson, C., Nisenson, J., Alva Jimenez, T., Lapointe, M., Stewart, H., Grubisa, G. and Sykora, S. (2013): Porphyry Cu-(Mo) deposits in the Highland Valley district, south-central British Columbia; *in* Porphyry Systems of Central and Southern BC, Tour of Central BC Porphyry Deposits from Prince George to Princeton, J. Logan and T. Schroeter (ed.), Society of Economic Geologists, Field Guidebook Series, v. 44, p. 99–116.
- Casselmann, M.J., McMillan, W.J. and Newman, K.M. (1995): Highland Valley porphyry copper deposits near Kamloops, British Columbia: a review and update with emphasis on the Valley deposit; *in* Porphyry Deposits of the Northwestern Cordillera of North America, T.G. Schroeter (ed.), Canadian Institute of Mining and Metallurgy, Special Volume 46, p. 161–191.
- Cherniak, D.J., Hanchar, J.M. and Watson, E.B. (1997): Diffusion of tetravalent cations in zircon; *Contributions to Mineralogy and Petrology*, v. 127, p. 383–390
- Chiaradia, M., Schaltegger, U., Spikings, R., Wotzlav, J.-F. and Ovtcharova, M. (2013): How accurately can we date the duration of magmatic-hydrothermal events in porphyry systems?—An invited paper; *Economic Geology*, v. 108, p. 565–584.
- D’Angelo, M., Miguel, A., Hollings, P., Byrne, K., Piercy, S. and Creaser, R. (2017): Petrogenesis and magmatic evolution of the Guichon Creek Batholith: Highland Valley Porphyry Cu±(Mo) District, south-central British Columbia; *Economic Geology*, v. 112, p. 1857–1888.
- del Real, I., Bouzari, F., Rainbow, A., Bissig, T., Blackwell, J., Sherlock, R., Thompson, J.F.H. and Hart, C.J.R. (2017): Spatially and temporally associated porphyry deposits with distinct Cu/Au/Mo ratios, Woodjam district, central British Columbia; *Economic Geology*, v. 112, p. 1673–1717.
- Diakow, L.J., Nixon, G.T., Rhodes, R. and Lane, B. (2005): Geology between the Finlay and Toadoggonne rivers, Toadoggonne river map area, north-central British Columbia (parts of NTS 94E/2, 6 and 7); BC Ministry of Energy, Mines and Petroleum Resources, Open File Map 2005-3, 1:50 000 scale, URL <<http://www.empr.gov.bc.ca/mining/geoscience/publicationscatalogue/openfiles/2005/pages/2005-3.aspx>> [November 2018].
- Diakow, L.J., Panteleyev, A. and Schroeter, T.G. (1993): Geology of the Early Jurassic Toadoggonne Formation and gold–silver deposits in the Toadoggonne river map area, northern British Columbia; BC Ministry of Energy, Mines and Petroleum Resources, 72 p., URL <<http://www.empr.gov.bc.ca/Mining/Geoscience/PublicationsCatalogue/BulletinInformation/BulletinsAfter1940/Documents/Bull86.pdf>> [November 2018].
- Dilles, J.H., Kent, A.J.R., Wooden, J.L., Tosdal, R.M., Koleszar, A., Lee, R.G. and Farmer, L.P. (2015): Zircon compositional evidence for sulfur-degassing from ore-forming arc magmas; *Economic Geology*, v. 110, p. 241–251.
- Duuring, P., Rowins, S.M., McKinley, B.S.M., Dickinson, J.M., Diakow, L.J., Kim, Y.-S. and Creaser, R.A. (2009): Magmatic and structural controls on porphyry-style Cu–Au–Mo mineralization at Kemess South, Toadoggonne district of British Columbia, Canada; *Mineralium Deposita*, v. 44, p. 463–496.
- Frey, F.A., Chappell, B.W. and Roy, S.D. (1978): Fractionation of rare-earth elements in the Tuolumne Intrusive Series, Sierra Nevada batholith, California; *Geology*, v. 6, p. 239–242.
- Harding, B. (2012): The characterization of molybdenum mineralization at the Gibraltar mines Cu-Mo porphyry, central British Columbia; B.Sc. thesis, Queen’s University, 52 p.
- Jackson, S.E., Gunther, D. and Sylvester, P.J. (2003): Applications of laser-ablation ICP-MS analysis: A tribute to Henry P. Longerich; *Canadian Mineralogist*, v. 41, p. 257–258.
- Lee, R.G., Byrne, K., Alfaro, M., D’Angelo, M., Hart, C.J.R., Hollings, P. and Gleeson, S.A. (2017a): Assessing the zircon compositional evolution from the Guichon Creek Batholith and Highland Valley Copper deposit, south-central B.C.; Abstract, Mineral Resources to Discover—14th SGA Biennial Meeting, Québec City, Quebec, August 2017, v. 3.
- Lee, R.G., Dilles, J.H., Tosdal, R., Wooden, J.L. and Mazdab, F.K. (2017b): Magmatic evolution of granodiorite intrusions at the El Salvador porphyry copper deposit, Chile, based on trace element composition and U/Pb age of zircons; *Economic Geology*, v. 112, p. 245–273.
- Loader, M.A., Wilkinson, J.J. and Armstrong R.N. (2017): The effect of titanite crystallisation on Eu and Ce anomalies in zircon and its implications for the assessment of porphyry Cu deposit fertility; *Earth and Planetary Science Letters*, v. 472, p. 107–119.
- Logan, J.M. and Mihalynuk, M.G. (2014): Tectonic controls on early Mesozoic paired alkaline porphyry deposit belts (Cu-Au±Ag-Pt-Pd-Mo) within the Canadian Cordillera; *Economic Geology*, v. 109, p. 827–858.
- McMillan, W.J., Anderson, R.G., Chan, R. and Chow, W. (2009): Geology and mineral occurrences (MINFILE), the Guichon Creek Batholith and Highland Valley porphyry copper dis-

- trict, British Columbia; Geological Survey of Canada, Open File 6079, 2 maps, URL <<http://geogratis.gc.ca/api/en/nrcan-rncan/ess-sst/78e93fdd-50d0-5877-a024-310362144149.html>> [November 2018].
- McMillan, W.J., Thompson, J.F.H., Hart, C.J.R. and Johnston, S.T. (1995): Regional geological and tectonic setting of porphyry deposits in British Columbia and Yukon Territory; *in* Porphyry Deposits of the Northwestern Cordillera of North America, T.G. Schroeter (ed.), Canadian Institute of Mining and Metallurgy, Special Volume 46, p. 40–57.
- Miller, J.S. and Wooden, J.L. (2004): Residence, resorption and recycling of zircons in Devils Kitchen Rhyolite, Coso volcanic field, California; *Journal of Petrology*, v. 45, p. 2155–2170.
- Panteleyev, A. (1978): Granite Mountain project (93B/8); *in* Geological Fieldwork 1977, BC Ministry of Energy, Mines and Petroleum Resources, BC Geological Survey, Paper 1977-1, p. 39–42.
- Richards, J.P. (2011): High Sr/Y magmas and porphyry Cu±Mo±Au deposits: Just add water; *Economic Geology*, v. 106, p. 1075–1081.
- Schiarizza, P. (2015): Geological setting of the Granite Mountain batholith, south-central British Columbia; *in* Geological Fieldwork 2014, BC Ministry of Energy, Mines and Petroleum Resources, BC Geological Survey, Paper 2015-1, p. 19–39, URL <http://www.empr.gov.bc.ca/Mining/Geoscience/PublicationsCatalogue/Fieldwork/Documents/2014/02_Schiarizza.pdf> [November 2018].
- Schiarizza, P., Bell, K. and Bayliss, S. (2009): Geology and mineral occurrences of the Murphy Lake area, south-central British Columbia (NTS 093A/03); *in* Geological Fieldwork 2008, BC Ministry of Energy, Mines and Petroleum Resources, BC Geological Survey, Paper 2009-1, p. 169–188, URL <http://www.empr.gov.bc.ca/Mining/Geoscience/PublicationsCatalogue/Fieldwork/Documents/2008/15_Schiarizza.pdf> [November 2018].
- Shen, P., Hattori, K., Pan, H., Jackson, S. and Seitmuratova, E. (2015): Oxidation condition and metal fertility of granitic magmas: zircon trace-element data from porphyry Cu deposits in the Central Asian orogenic belt; *Economic Geology*, v. 110, p. 1861–1878.
- Stern, C.R., Skewes, M.A. and Arevalo, A. (2011): Magmatic evolution of the giant El-Teniente Cu-Mo deposit, central Chile; *Journal of Petrology*, v. 52, p. 1591–1617.

IKE Copper-Molybdenum-Silver Porphyry Deposit, Southwestern British Columbia (NTS 092O): Early Halo-Type Veins as a Tool for Vectoring Toward Higher Grade Mineralization

M.M. Binner, Simon Fraser University, Burnaby, BC, mbinner@sfu.ca

D.D. Marshall, Simon Fraser University, Burnaby, BC

C.M. Rebagliati, Amarc Resources Ltd., Vancouver, BC

K.B. Riedell, Riedell Exploration Ltd., Vancouver, BC

Binner, M.M., Marshall, D.D., Rebagliati, C.M. and Riedell, K.B. (2019): IKE copper-molybdenum-silver porphyry deposit, southwestern British Columbia (NTS 092O): early halo-type veins as a tool for vectoring toward higher grade mineralization; *in* Geoscience BC Summary of Activities 2018: Minerals and Mining, Geoscience BC, Report 2019-1, p. 55–66.

Introduction

The IKE deposit is a Cu-Mo-Ag porphyry deposit located in the southern portion of the Canadian Cordillera in southwestern British Columbia (BC). It follows a calcalkalic porphyry model, as it is hosted in plutonic rock and has a large alteration footprint. Amarc Resources Ltd. drilled 21 discovery holes from 2014 to 2016 that cover an area of 1.2 km by 1.0 km to a depth of 875 m; all of these holes intersected long intervals of Cu and Mo mineralization. Significant amounts of early halo-type (EHT) veins are found throughout the deposit; such veins are typically associated with deep-seated porphyry deposits, such as Butte, Montana and Ann Mason, Nevada.

This project is an investigation of the geochemical properties of these early halo-type veins and how they relate to mineralization. Detailed petrographic studies were carried out on early halo-type veins in multiple parts of the system in order to identify the mineral assemblages that occur in the alteration haloes and how IKE compares to other deposits. Shortwave infrared (SWIR) spectroscopy was used on the hostrock at IKE to identify subtle geochemical changes in the alteration minerals. The main mineral picks, white mica absorption features and illite crystallinity values were examined to determine fluid composition and pathways in the deposit, and how they relate to grade and the formation of early halo-type veins.

The development of early halo-type veins is a key component of early high-temperature mineralization in the system and has the potential to aid in the exploration for high-grade zones at IKE and other deep-seated porphyry deposits.

This publication is also available, free of charge, as colour digital files in Adobe Acrobat® PDF format from the Geoscience BC website: <http://www.geosciencebc.com/s/SummaryofActivities.asp>.

Regional Geology

The IKE porphyry district is located on the eastern margin of the Coast Plutonic Complex (CPC) in southwestern BC, 33 km northwest of Gold Bridge (Figure 1). The CPC is Cretaceous to Eocene in age, and is thought to be linked to the subduction of the Pacific Plate beneath the western edge of the North American Plate, and partly a result of tectonic overlap and compressional thickening of crustal rocks during a collision between the North American Plate and two allochthonous terranes accreted to the western margin in the Mesozoic (Monger et al., 1982). Compared to the other morphogeological belts of the Canadian Cordillera, the Coast Belt is apparently lacking in mineral occurrences, and the exact mechanisms for this are not well understood (McMillan et al., 1996).

The IKE deposit is hosted in a late Cretaceous granodiorite intrusion that correlates with the Dickson-McClure batholith, which hosts several other calcalkaline porphyry occurrences. Rhenium-osmium dates from molybdenite at IKE yield ages of 46.4 ± 0.19 Ma and 47.55 ± 0.24 Ma, making it one of the few Eocene deposits in the region (Galicki and



Figure 1. Location of study area (modified from Galicki and Rebagliati, 2017).

Rebagliati, 2017). The majority of porphyry deposits in the Canadian Cordillera are early Mesozoic in age, and the porphyry deposits that are late Mesozoic to Cenozoic were formed in intracontinental settings after the accretion of the Quesnel and Stikine terranes onto continental North America. The distribution of postaccretionary deposits is linked to crustal structure and subduction geometries (McMillan et al., 1996).

Mineralization at IKE may be related to dilation zones from the Tchaikazan fault, as there is no evidence on surface or in the drillcore of a major structure at the deposit (Galicki and Rebagliati, 2017). The Tchaikazan fault is a mid-Cretaceous strike-slip fault with a postulated dextral displacement of up to 30 km, and is truncated to the south by the Dickson-McClure batholith (Schiarizza et al., 1997). There is evidence that the Tchaikazan fault was reactivated in the late Cretaceous and the Eocene (Umhoeffer and Kleinspehn, 1995). Mineral occurrences in the IKE district line up geographically with the southeasterly trend of the Tchaikazan fault, as seen in Figure 2. These mineral occurrences range in age from late Cretaceous to Eocene, and may to correlate with movement on the Tchaikazan fault.

IKE Property Geology

The IKE deposit is hosted in felsic to intermediate intrusive rocks. The host granodiorite, the most intersected intrusion, is a medium-grained, biotite-bearing hornblende granodiorite and is associated with most of the mineralization in the system. It predates mineralization but was enriched in grade during the mineralizing event. Uranium-lead dating of the mineralized granodiorite yielded 85.7 ± 1.1 Ma, which is correlative with the Cretaceous Dickson-McClure batholith (Galicki and Rebagliati, 2017). There are several different syn-mineralization intrusions at IKE that range from quartz monzonite to diorite and can be distinguished from the pre-mineralization granodiorite by their porphyritic texture. There are minor amounts of late-mineralization and post-mineralization dikes, but they are not linked to significant Cu and Mo grades (Galicki and Rebagliati, 2017). An example of dike orientation and how it relates to the drillcore is shown in Figure 3.

There is a general trend of high- to low-temperature alteration with time, with the most significant episodes of mineralization associated with high-temperature alteration

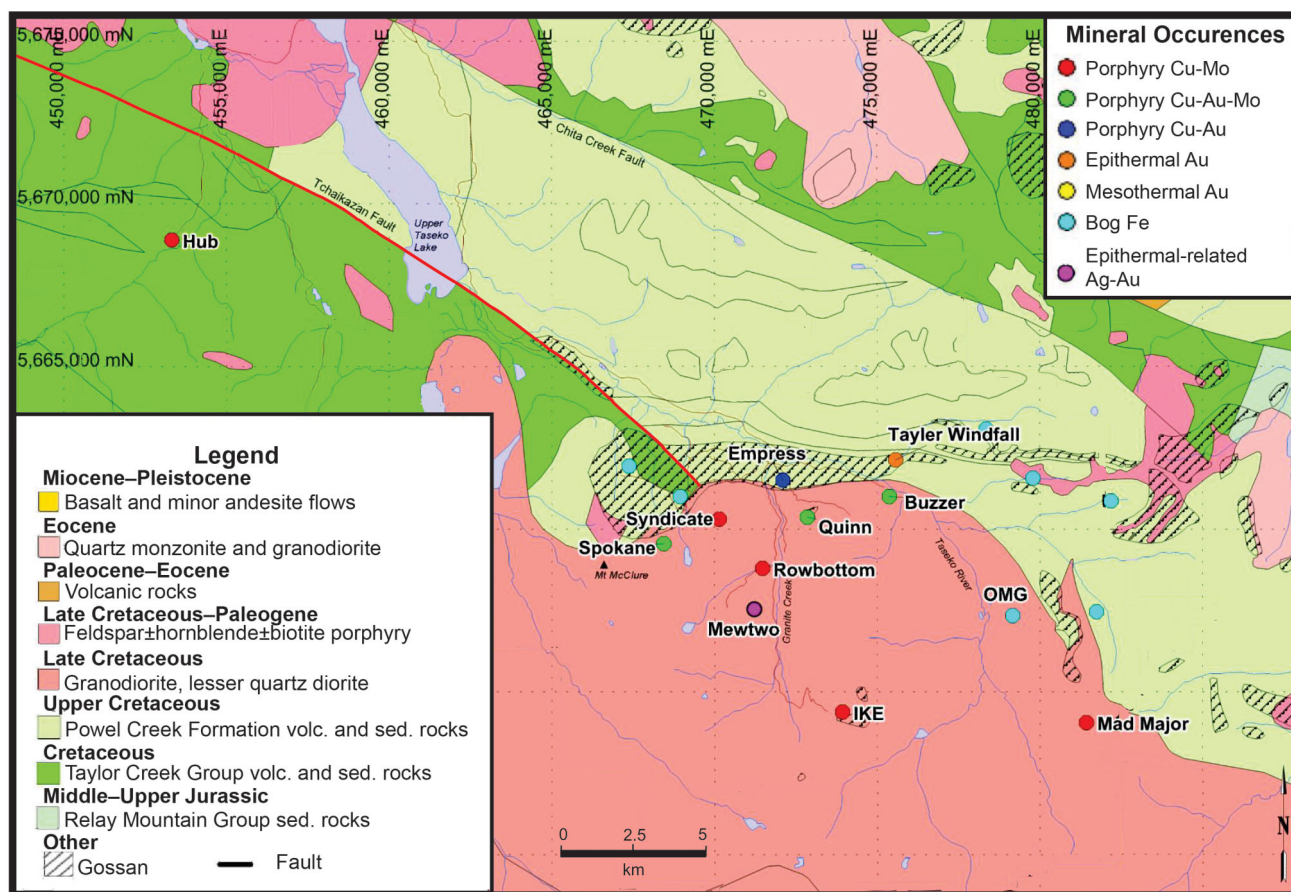


Figure 2. Regional geology of IKE and surrounding mineral occurrences. The Tchaikazan fault is outlined in red (modified from Galicki and Rebagliati, 2017). Abbreviations: sed., sedimentary; volc., volcanic.

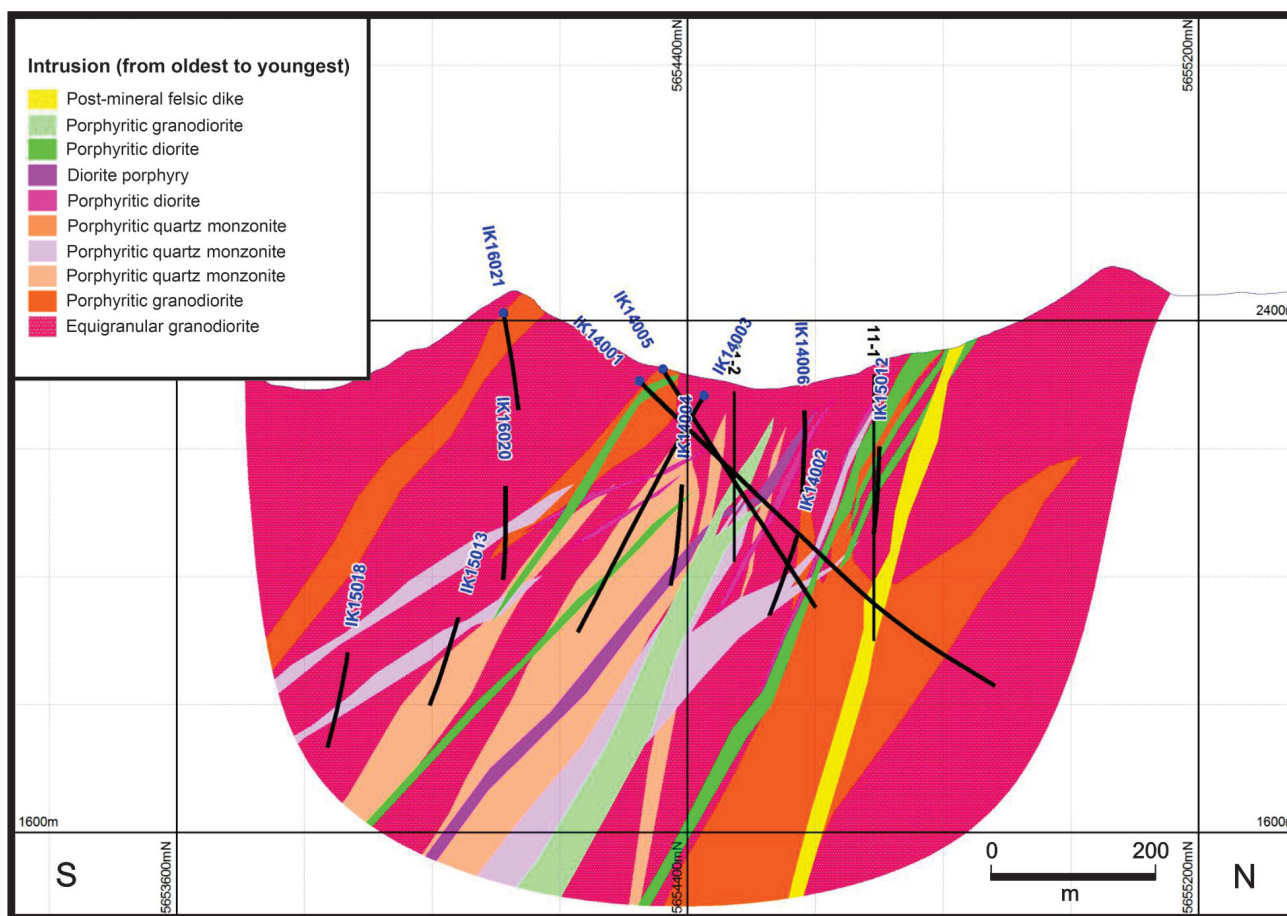


Figure 3. Geological cross-section of the IKE deposit, with location of some of the drillholes (modified from Galicki and Rebagliati, 2017).

(Galicki and Rebagliati, 2017). Potassium-silicate (biotite)±magnetite alteration is the earliest stage of hydrothermal alteration and involves the replacement of igneous biotite and hornblende with ‘shreddy’ hydrothermal biotite. Potassium-feldspar–quartz alteration consists of minor amounts of K-feldspar, generally found in alteration selvages of veins, most frequently in zones of high vein density. Propylitic alteration is relatively minor and is represented by a low-temperature assemblage of chlorite±carbonate±epidote. Rare quartz-chlorite-epidote-sulphide veins are associated with this alteration, suggesting sulphides were also introduced and/or remobilized at this stage of alteration. Phyllic alteration is the latest stage and consists of pyritic quartz veins with large sericite-pyrite-chlorite alteration haloes. It is minor in this deposit and is often seen in reopened, early halo-type veins and overprinting early-stage K-silicate alteration (Galicki and Rebagliati, 2017).

Mineralization in the system is both vein hosted and disseminated. The majority of Cu mineralization is attributed to early-stage potassic alteration and is mainly in the form of chalcopyrite; however, there is minor malachite in the shallow intervals of some drillholes, which could be a re-

sult of surface alteration. Chalcopyrite occurs in the veins and their alteration haloes as well as disseminated throughout the hostrock, where it replaces biotite and hornblende. Molybdenum is mainly vein hosted in the form of molybdenite and is often associated with later stage K-feldspar alteration.

Early Halo-Type Veins

Early halo-type (EHT) veins often occur in areas of high Cu grade in many deep-seated porphyry deposits. They are defined as veins with significant alteration haloes that are texture destructive, contain sericite island and sericite bowtie textures, and are one of the first veining events of the system (Proffett, 2009). Examples of deposits with significant amounts of EHT veins include Butte, Montana and Ann Mason, Nevada. Another interpretation of veins with significant alteration haloes in deep portions of porphyry deposits is that they are formed from degassing of overpressurized hydrothermal fluids during late crystallization and have compositions and textures similar to veins found in greisen-type Sn-W-Mo districts (Runyon et al., 2017). Although the vein haloes in IKE also have sericite and quartz as some of the main alteration minerals, they differ from veins in the Runyon study because they do not have open-

space-filling textures and are associated with the first stage of mineralization in the system.

The IKE deposit has an abundance of EHT veins, which are linked to early Cu mineralization in the system. They are found most frequently in the pre-mineralization granodiorite but occur in all of the syn-mineralization intrusions. It is important to note that they are absent from post-mineralization intrusions. Their crosscutting relationships with other vein types and occurrence in intrusion types suggest that they occur in the first stage of mineralization at IKE. The centrelines are thin (1 mm) and generally consist of quartz, chalcopyrite, pyrite and sometimes magnetite. Composition is variable, but the most common minerals in the alteration halo are sericite and biotite, along with chlorite, quartz and K-feldspar. The average sericite-rich alteration halo has a true width of about 1 cm, and haloes containing significant amounts of biotite are slightly thinner. The EHT veins can host a significant amount of mineralization, most commonly in the form of pyrite and chalcopyrite. Figure 4 shows some of the most commonly seen EHT veins in the IKE deposit.

Preliminary studies indicate that EHT veins at the IKE deposit seem to be linked to early mineralizing events in the IKE system, as they are concentrated in areas of higher Cu grade. Percentages of EHT veins were estimated visually in each sample interval (~3 m) of drillholes IK15013 and IK15018, where the EHT veins are prevalent. Both the vein and the alteration halo are included in the estimation. They occur through the entirety of both holes but are of higher intensity in areas of medium to strong K-silicate-biotite±magnetite alteration. Figure 5 shows a positive correlation between EHT veins and Cu grades, whereas Ag and Mo grades do not show strong correlations.

Petrography

Sixty-six polished thin sections and ten fluid-inclusion sections were prepared from the IKE deposit, many of them containing EHT veins. The most common minerals in the alteration haloes are sericite, biotite and quartz, and minor minerals include chlorite, feldspar, clinopyroxene and apatite. Sulphides are hosted in the alteration haloes: mainly chalcopyrite and pyrite, and some sphalerite. The composi-

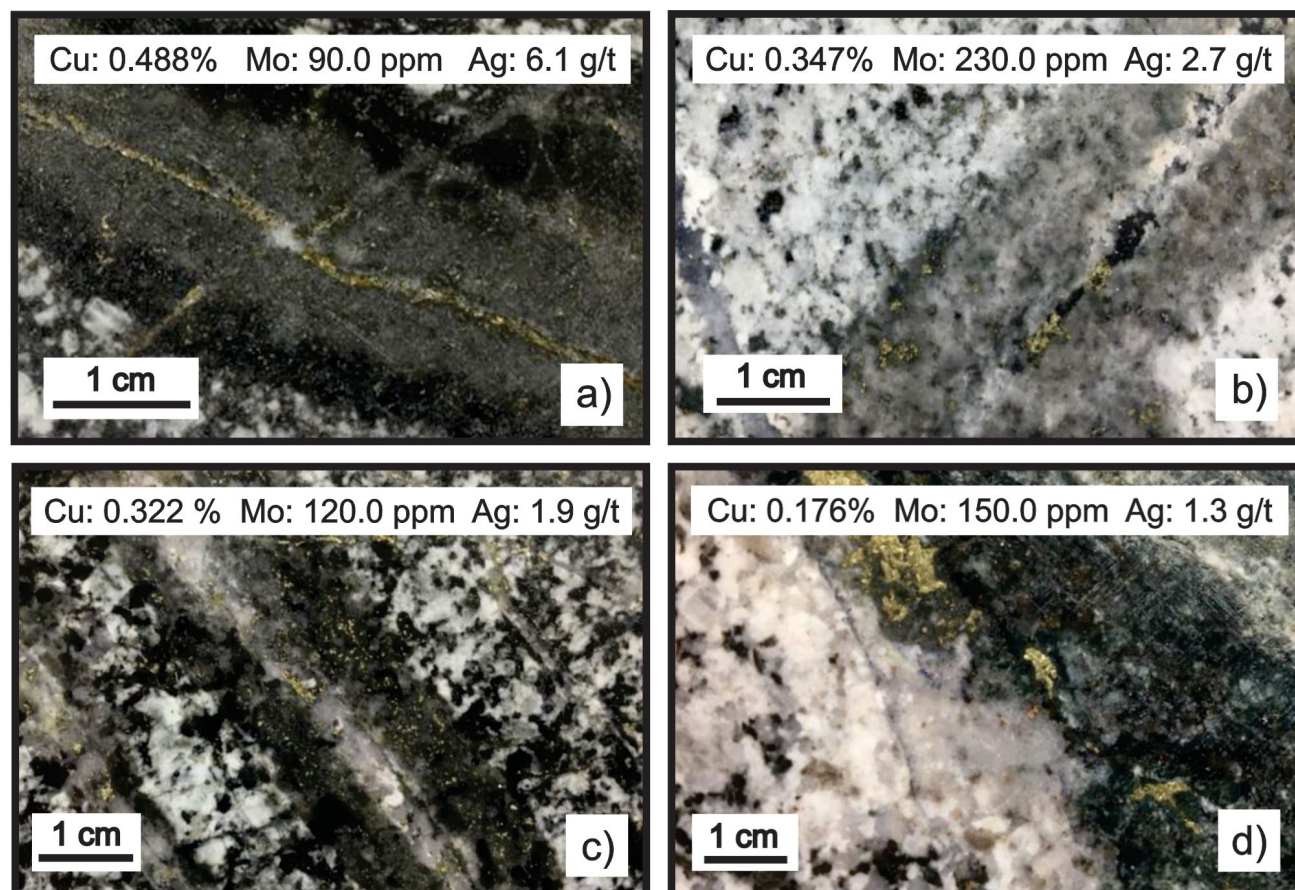


Figure 4. Examples of vein alteration haloes at IKE: **a)** zoned sericite-biotite alteration halo at 258 m in drillhole IK14001; **b)** sericite alteration halo at 630 m in drillhole IK15013; **c)** sericite-biotite alteration halo at 96 m in drillhole IK15013; and **d)** zoned sericite-biotite-chlorite alteration halo at 727 m in drillhole IK15018.

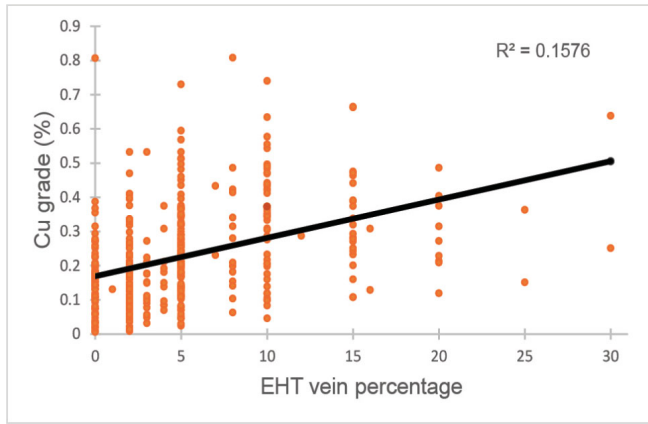


Figure 5. Copper grade versus percentage of early halo-type veins in drillholes IK15013 and IK15018, IKE deposit.

tion of alteration haloes does not appear to be affected by the hostrock because EHT veins that cross rock boundaries have the same alteration minerals in similar quantities, but the size of the alteration mineral grains reflects the grain size of the hostrock (Figure 6). The bowtie and sericite-island textures seen in the alteration haloes are diagnostic of EHT veins (Proffett, 2009).

Detailed petrographic studies were carried out on selected EHT veins at the IKE deposit in order to better understand the composition of the hydrothermal fluids and hostrock alteration. The veins highlighted in Figures 7–9 were chosen based on their variability of composition, sulphide content and position within the system. The veins studied were from drillholes IK14001, IK15013 and IK15018; their positions are shown in Figure 3. Sam-

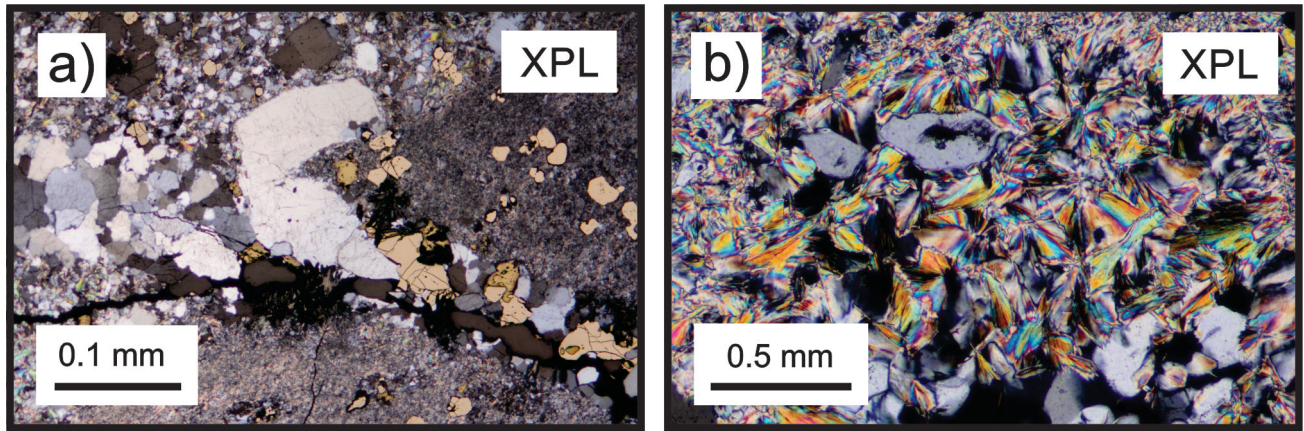


Figure 6. Thin-section photomicrographs from the IKE deposit: **a)** sericite alteration halo at the contact between equigranular granodiorite and porphyritic diorite at 434 m in drillhole IK15018; **b)** bowtie texture in sericite in the alteration halo at 249 m in drillhole IK14001. Abbreviation: XPL, cross-polarized light.

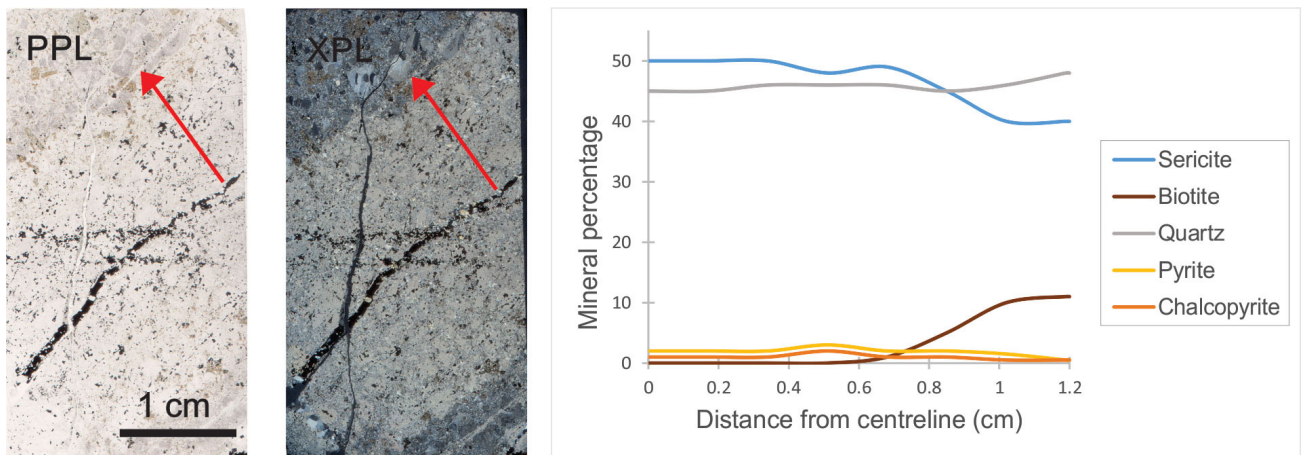


Figure 7. Mineral percentages in a zoned sericite-biotite alteration halo at 258 m in drillhole IK14001, with corresponding thin-section photomicrographs; cross-section indicated by red arrow, with tip of arrow denoting outer edge of alteration halo. Abbreviations: PPL, plane-polarized light; XPL, cross-polarized light.

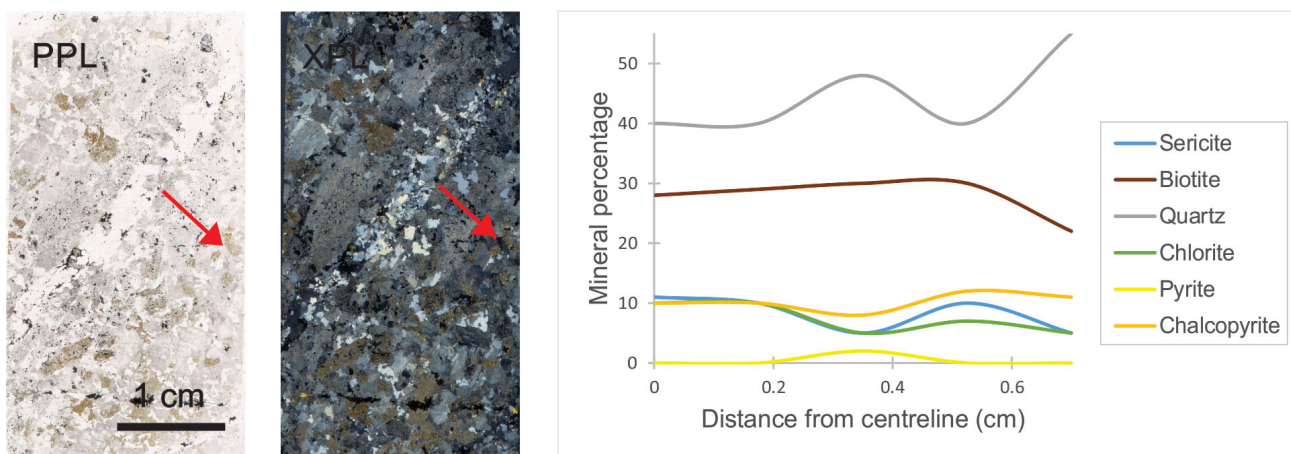


Figure 8. Mineral percentages in a sericite-biotite alteration halo at 96 m in drillhole IK15013, with corresponding thin-section photomicrographs; cross-section indicated by red arrow, with tip of arrow denoting outer edge of alteration halo. Abbreviations: PPL, plane-polarized light; XPL, cross-polarized light.

ple photos and interval grades of the EHT veins are shown in Figure 4. Mineral percentages were taken in portions of the alteration haloes that represented the general composition of the halo and did not include relict phenocrysts or crosscutting veinlets.

The sericite-biotite halo shown in Figure 7 demonstrates a common composition of zoned EHT veins found throughout the IKE deposit. The centreline consists of pyrite, chalcopyrite and quartz. The main alteration minerals are sericite and quartz, with biotite occurring at the outer edge of the alteration halo. Pyrite and chalcopyrite are disseminated throughout the halo, with chalcopyrite concentrated more closely to the centreline. Drillhole IK14001 is in the uppermost portion of the deposit, so the composition of the EHT vein may reflect cooling of the hydrothermal fluid as it moved to higher elevations in the system.

The vein highlighted in Figure 8 is an example of an unzoned EHT vein with biotite as the dominant vein mineral.

The centreline is composed of quartz, chalcopyrite, pyrite and molybdenite. This type of vein typically does not have an alteration halo in this system and, if a halo occurs, it is thin and composed of K-feldspar. The path of the centreline also does not perfectly follow the path of the alteration halo, which suggests that the original vein was reopened in a later mineralizing event. The alteration mineralization is relatively uniform throughout the halo. Biotite and quartz are the main alteration minerals, with less abundant sericite and chlorite. There are minor amounts of clinopyroxene in the alteration halo, but it was omitted from the graph for clarity. Chalcopyrite is the predominant sulphide in the alteration halo, with rare pyrite and trace molybdenite. Chalcopyrite often occurs with chlorite within the halo. Drillhole IK15013 is one of the deeper holes in the system and has the longest intervals of higher Cu grade (>0.3%), along with some of the highest percentages of EHT veins.

The EHT vein outlined in Figure 9 has a composition typical of higher grade Cu zones in deep porphyry deposits.

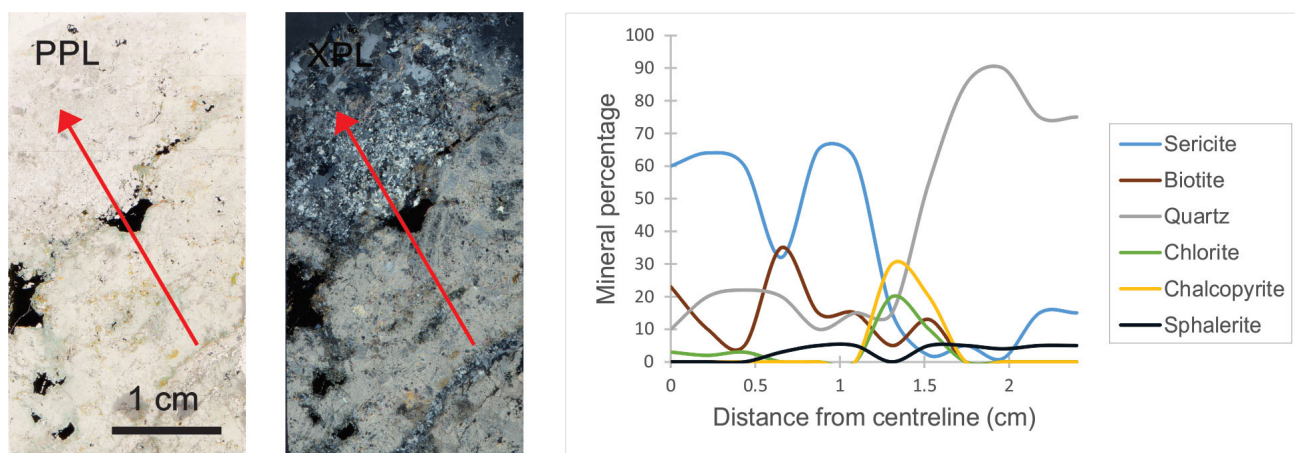


Figure 9. Mineral percentages in a zoned sericite-biotite-chlorite alteration halo at 727 m in drillhole IK15018, with corresponding thin-section photomicrographs; cross-section indicated by red arrow, with tip of arrow denoting outer edge of alteration halo. Abbreviations: PPL, plane-polarized light; XPL, cross-polarized light.

The centreline is composed of quartz, with small amounts of chlorite and calcite. The alteration halo is zoned, with green sericite, biotite and minor chlorite as the dominant alteration minerals closer to the centreline, and quartz and minor sericite on the outer edge of the halo. Minor amounts of K-feldspar, clinopyroxene and apatite are found throughout the alteration halo as well. Most of the chlorite occurs at the transition between the two portions of the alteration halo, along with larger grains of chalcopyrite. Smaller grains of sphalerite (<1 mm) are found in both zones of the alteration halo. This vein was in the last sample intervals of drillhole IK15018, which is the deepest hole of the system.

Preliminary fluid-inclusion studies have shown a variety of different fluid inclusions within the quartz veins at the IKE deposit. There are fluid inclusions that are liquid dominant or vapour dominant, and some that contain daughter minerals that appear to be halite and anhydrite. Two-phase fluid inclusions in the system are mostly liquid dominant; however, vapour-dominant two-phase inclusions are quite common as well. The porphyry boiling assemblage can be seen in a quartz-chalcopyrite-molybdenite vein, which involves a two-phase liquid-dominant fluid inclusion, a two-phase vapour-dominant fluid inclusion and a three-phase fluid inclusion, all occurring in the same quartz crystal (Figure 10). This is significant, as boiling of hydrothermal fluids in a porphyry system is thought to lead to mineralization (Nash, 1976). Detailed fluid-inclusion studies may not be suitable for this deposit, as fluid inclusions are very small and often appear to be secondary.

Shortwave Infrared Spectroscopy

Shortwave infrared (SWIR) spectroscopy has been used to identify alteration minerals and estimate crystallinity and mineral abundance. There is no sample preparation, it is nondestructive and measurements can be made directly on dry rock or pulp samples. Spectra are generated by measuring the electromagnetic radiation absorbed by submolecular vibrations related to covalent bonds, most notably Al-

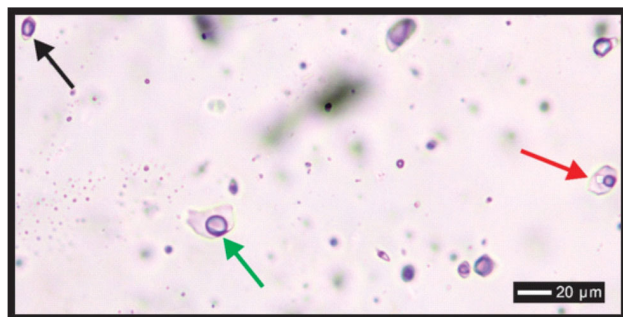


Figure 10. Fluid inclusions hosted within quartz of a quartz-chalcopyrite-molybdenite vein in sample 06-253.47, showing a typical porphyry 'boiling' assemblage of fluid inclusions ranging in composition from a three-phase (halite + liquid + vapour) fluid inclusion (red arrow) to a two-phase liquid-dominant (liquid + vapour) fluid inclusion (green arrow) to a two-phase vapour-dominant (vapour + liquid) fluid inclusion (black arrow).

OH, Fe-OH, Mg-OH and H₂O. (Simpson, 2015). Phyllosilicates, sorosilicates, carbonates and certain sulphates and ammonium-bearing minerals can be identified using this method. Some minerals, such as quartz, cannot be identified using this method as they do not yield a spectral response. Alteration minerals common in porphyry systems that can be measured using SWIR spectroscopy include muscovite, biotite, chlorite, epidote, calcite, kaolinite, illite and montmorillonite (Hauff, 2008). Minerals are identified based on patterns in the spectra. As an example, kaolinite is recognized by a doublet in the absorption features around 1400 and 2200 nm, and a relatively shallow water-absorption feature around 1900 nm (Figure 11). Multiple minerals can contribute the same absorption features in one spectrum, known as mixed spectra, which should be considered when performing calculations involving specific mineral groups (Halley, 2016).

There are many applications of SWIR spectroscopy, but this study focuses on mineral picks, illite crystallinity and wavelength positions around 2200 nm, and how they compare to grade and abundance of EHT veins. Pucks of core taken at every sample interval were analyzed for drillholes IK14001, IK15013 and IK15018, as they are from different parts of the system and contain significant amounts of EHT veins. The pucks often did not contain veins or alteration haloes, so the host rock was the focus of this alteration study. The analysis was done at The University of British Columbia using a TerraSpec 3 and the data were processed using The Spectral Geologist (TSG) 8 software. The spectral range for the instrument is 350–2500 nm, and the duration of the scans was 10 seconds. White references were taken hourly along with a Mylar™ standard to ensure consistent measurements. As a form of quality control, samples were rescanned if the absorption features were not pronounced.

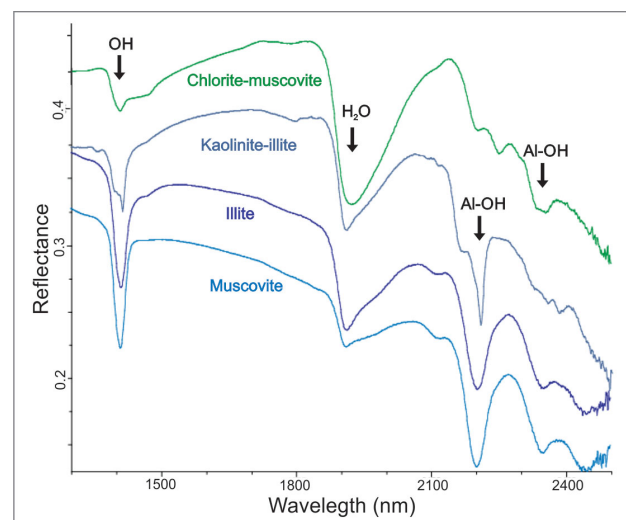


Figure 11. Example of spectra of common alteration minerals in the IKE deposit, with some absorption features labelled.

A vital function of SWIR spectroscopy is to quickly identify alteration minerals. The Spectral Geologist software generates mineral picks based on the spectral signatures, and can have up to three mineral picks for one spectrum. This study will focus on the main mineral pick, which is the most abundant mineral in a particular spectrum. The most common mineral picks in the IKE deposit are chlorite, muscovite, biotite, kaolinite, illite, montmorillonite, paragonite, phlogopite, siderite and tourmaline. Chlorite and muscovite are associated with the highest Ag, Cu and Mo grades (Figure 12). Some spectra yielded only one main mineral pick (e.g., epidote, hornblende and phengite), and

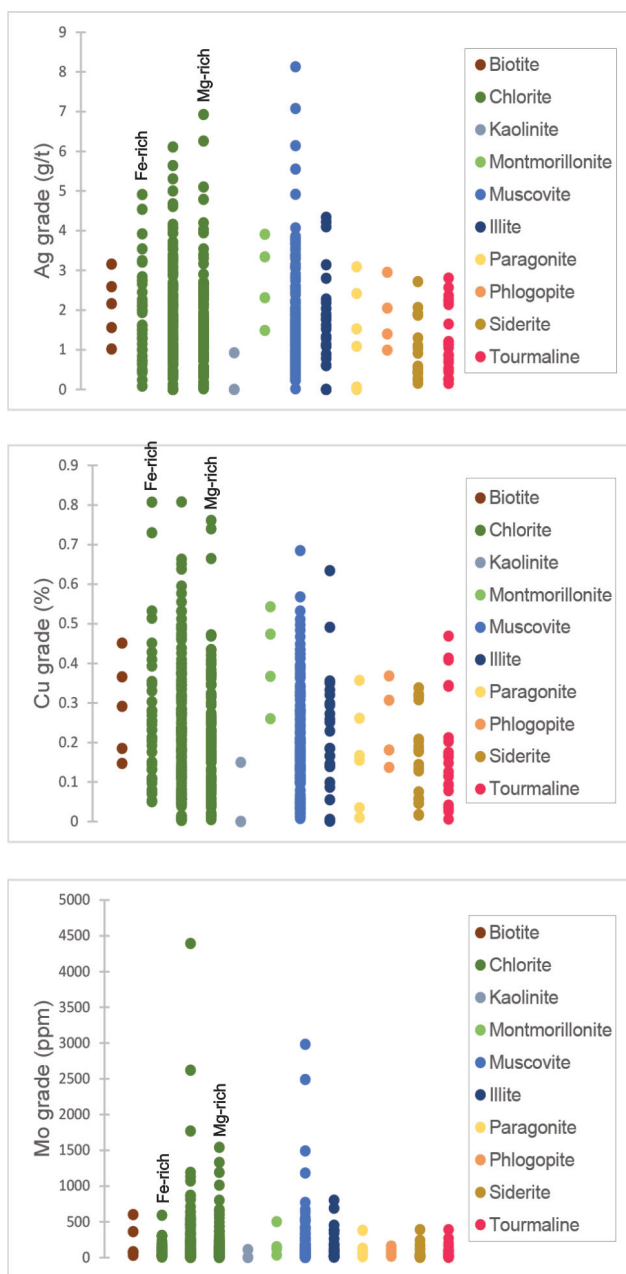


Figure 12. Grades of Ag, Cu and Mo related to the main mineral picks from SWIR spectroscopy data.

they were left out of the figure for simplicity. Muscovite, chlorite, biotite, tourmaline and siderite occur consistently in all of the drillholes. Biotite only occurred as the main mineral in drillholes IK15013 and IK15018, which are the deepest holes, elevation wise, in the deposit. It is interesting to note that all occurrences of kaolinite as the main mineral pick and the only occurrence of epidote as the main mineral pick occur in drillhole IK14001, which is the shallowest of the three drillholes studied.

Similar patterns are seen when comparing EHT vein percentage to the main mineral picks. As seen in Figure 13, the sample intervals with the highest amounts of EHT veins have mineral picks of chlorite, muscovite and illite. The EHT veins are more frequent in areas of Mg-rich chlorite than those of Fe-chlorite.

Illite crystallinity can be used as an estimation of the conditions of formation of alteration minerals. A broad measurement of illite crystallinity can be made using the ratio between the water and white mica absorption features at 1900 nm and 2200 nm, respectively (Halley, 2016). Once the spectra were obtained, the minimum values of the 1875–1925 nm and 2175–2225 nm ranges were plugged into equation 1. Higher values are associated with more crystalline phases, which tend to form at higher temperatures. Only data points with white micas and montmorillonite were used, to avoid the overestimation of water absorption from minerals like chlorite and biotite (Halley, 2016).

$$\text{Illite crystallinity} = \left(\frac{\text{minimum at 2200 nm}}{\text{minimum at 1900 nm}} \right) \quad (1)$$

Comparing illite crystallinity to ore grade in this system did not yield any clear relationships. As seen in Figure 14, Ag and Cu do not show a significant correlation with illite crystallinity, whereas Mo has a slightly positive correlation with higher crystallinity. Illite crystallinity plotted against EHT percentage shows no correlation as well, although removing points with minerals such as chlorite resulted in a small dataset. Further studies may be needed to establish

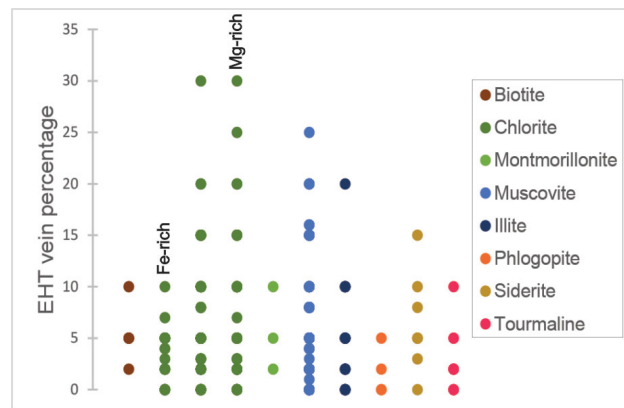


Figure 13. Percentage of early halo-type veins related to the main mineral picks from SWIR spectroscopy data.

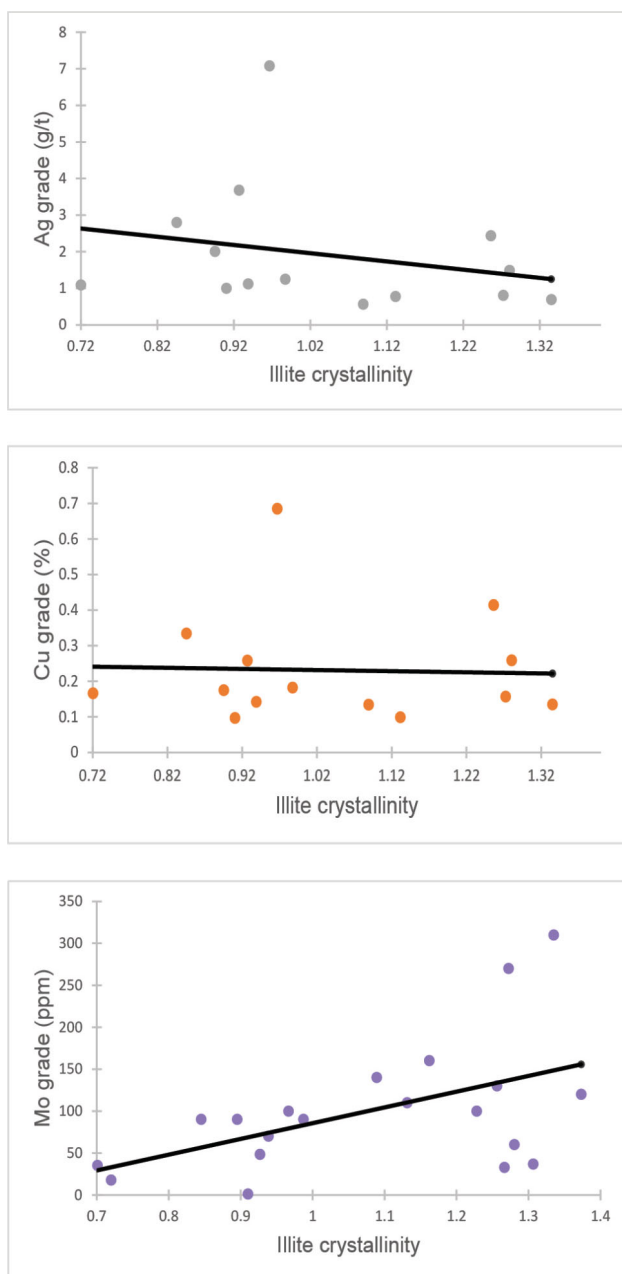


Figure 14. Grades of Ag, Cu and Mo compared to illite crystallinity.

this relationship. X-ray diffraction can also be used in conjunction with SWIR spectroscopy as an indicator of relative temperature of formation of illite and sericite, which would be useful in understanding conditions of the formation of certain phyllosilicates in the IKE deposit.

The composition of white mica can also be determined by the wavelength positions of Al-OH absorption features in the spectra. The wavelength at the minimum reflectance was recorded for the range 2185–2225 nm as a proxy for white mica composition (Harraden et al., 2013). When these values were plotted against grade and EHT vein percentage, the highest values of grade and EHT vein percent-

age tended to be in intervals where the minimum reflectance value was close to 2200 nm; however, there was no overall correlation.

Conclusions

It is clear that the presence of EHT veins is related to higher Cu grades in the system. Areas with higher percentages of EHT veins (>10%) have Cu grades of at least 0.1%. It is important to understand the processes that resulted in the formation of early halo-type veins, as they could be a tool for finding higher grade areas within the system.

Mineral assemblages seen in the alteration haloes of EHT veins at the IKE deposit reflect those of a deep-seated porphyry system. The EHT veins in drillhole IK14001, which is in the upper portion of the deposit, tend to have sericite as the dominant mineral, with some veins having significant amounts of biotite as well. Alteration haloes with sericite as the main component are thought to be a result of fluid cooling in shallower portions of the system. Studies on these types of veins provide an estimated formation temperature of 370–450°C (Rusk and Reed, 2008). In drillholes IK15013 and IK15018, which are the deeper holes in the system, there are still many sericite-dominant EHT veins; however, there are more occurrences of biotite-rich EHT veins, as well as green sericite and chlorite, in the alteration haloes. In deposits containing EHT veins, the presence of biotite, chlorite and green sericite indicate the most Cu-rich zone, as seen at Ann Mason, Nevada, where most of the Cu grade within the potassic B alteration zone is hosted in veins with alteration haloes containing chlorite (Dilles et al., 1992). Veins with alteration haloes consisting of chlorite, biotite and green sericite form at temperatures of around 475°C (Rusk and Reed, 2008). The presence of sphalerite in alteration haloes at the IKE deposit is interesting because, in Butte, Montana, it indicates the peripheral main-stage veins, which were formed at temperatures of 230–340°C (Rusk and Reed, 2008). A study done on the Butte deposit suggests that one hydrothermal-fluid composition may be responsible for alteration in the entire system. Differing compositions of alteration haloes can be due to changing temperature, varying extent of the reaction between the hydrothermal fluid and the host rock, and changing pressure (Reed et al., 2013). Compositions of EHT veins at the IKE deposit are quite similar to those seen in the main-stage mineralizing event at Butte, which would suggest similar fluid composition and temperature.

The SWIR spectroscopy alteration studies carried out on the IKE deposit suggest a large potassic-alteration footprint, as drillholes in opposite portions of the system seem to have predominantly high-temperature alteration minerals. The main mineral picks in this study were used to define the alteration zones in the system. Individual readings, by themselves, should not be overanalyzed too much, as re-

peating the reading could yield different mineral picks; however, identifying patterns in the data is useful in understanding fluid pathways (Halley, 2016). Drillhole IK14001 is the only hole that contains epidote and kaolinite, which would put it closer to the propylitic alteration zone; however, potassic minerals still seem to dominate. Illite crystallinity can be a useful estimate of the temperature of the mineralizing fluids. The Mo grade was the only factor that seemed to correlate with illite crystallinity, and the correlation would suggest that it is linked to hydrothermal fluids of higher temperature. The Cu grade may not show a correlation with illite crystallinity, as it is linked to the earlier stages of alteration and overprinting by later pulses of hydrothermal fluid could affect the results obtained in this alteration study. The conversion of illite to muscovite is a low-temperature reaction, occurring at 210–230°C (Garcia, 2013), so this method may not be suited for deeper portions of porphyry deposits.

Properties of the IKE deposit do not fit perfectly into a previously proposed Cu porphyry deposit model. The deposit is dominated by K-silicate alteration, lacks a defined propylitic alteration zone, and phyllic alteration is only seen in vein-alteration haloes, so it does not fit into the ‘classic’ porphyry model (Lowell and Guilbert, 1970). The alteration at IKE has more similarities to batholithic ore deposits, where the alteration zones are ‘inside-out’ with respect to the classic porphyry model, but differs in that it is not cut by a major fault and has more porphyritic rocks and quartz veins than expected in a batholithic deposit (Cheney and Trammell, 1966).

Future Work

Cathodoluminescence (CL) studies on quartz veins may be of use in this project. Temperature of the formation of quartz can be found comparatively using CL, where high intensity of luminescence would indicate a high temperature of formation (Rusk et al., 2006). Different quartz generations can be further defined using this method, assuming the physical and chemical characteristics were consistent throughout each vein-formation event. It would also be useful in determining primary and secondary fluid inclusions within quartz grains. Titanium diffusion within the quartz can also be measured using this technique, and may be a way to further constrain the timing of mineralization (Mercer et al., 2015).

Apatite luminescence, texture and geochemistry can be used to estimate the chemical compositions of the magmas that formed the hydrothermal fluids in a porphyry deposit (Bouzari et al., 2016). As apatite is found in a vein-alteration halo at IKE, CL studies on these particular apatites could aid in the understanding of how EHT veins contribute to mineralization in the system.

Further research using SWIR spectroscopy, in conjunction with X-Ray diffraction and microprobe work, could be useful in further constraining alteration patterns in the deposit. These studies would be done on more drillholes in the system, as well as the alteration haloes, to see how the spectra change with depth and mineralization.

Using data gathered from the above methods, as well as data already collected by Amarc Resources Ltd., a conceptual model for the IKE deposit will be developed. A model of this type of porphyry deposit could be useful because it will characterize not only this deposit but other porphyry deposits emplaced at greater depth, and could provide a new model for exploration.

Acknowledgments

In addition to Geoscience BC, major funding for the project was provided by the Geological Survey of Canada through the Targeted Geoscience Initiative, Phase 5. The authors thank the Mineral Deposit Research Unit at The University of British Columbia; F. Bouzari for assistance with the SWIR spectroscopy studies; and Amarc Resources Ltd. for consistent insight and support on the project. Lastly, thanks go to D. Thorkelson with the Petrology and Tectonics Research Group at Simon Fraser University for providing a review of the manuscript.

References

- Bouzari, F., Hart, C., Bissig, T. and Barker, S. (2016): Hydrothermal alteration revealed by apatite luminescence and chemistry: a potential indicator mineral for exploring covered porphyry copper deposits; *Economic Geology*, v. 111, p. 1397–1410, URL <<https://pubs.geoscienceworld.org/segweb/economicgeology/article/111/6/1397/152471/hydrothermal-alteration-revealed-by-apatite>> [November 2018].
- Cheney, E.S. and Trammell, J.W. (1996): The “inside-out” Quartz Creek quartz dioritic, batholithic, copper deposit, central Cascade Range, Washington; *in* *Geology and Ore Deposits of the American Cordillera*, Geological Society of Nevada, Reno/Sparks, Nevada, April 10–13, 1995, *Proceedings*, v. 3, p. 1521–1532.
- Dilles, J.H. and Einaudi, M.T. (1992): Wall-rock alteration and hydrothermal flow paths about the Ann Mason porphyry copper deposit, Nevada – a 6 km vertical reconstruction; *Economic Geology*, v. 87, no. 8, p. 1963–2001, <<https://pubs.geoscienceworld.org/segweb/economicgeology/article/87/8/1963/21087/wall-rock-alteration-and-hydrothermal-flow-paths>> [November 2018].
- Galicki, M. and Rebagliati, M. (2017): IKE project report 2016: Amarc Resources Ltd., internal report, 163 p. plus appendices.
- Garcia, L.A.G. (2013): Crystallinity variations of illite-smectite and kaolin hydrothermal alteration minerals by using SWIR spectroscopy: a study of the Rodalquilar Au-deposit, SE Spain; M.Sc. thesis, University of Twente, Enschede, Netherlands.
- Halley, S. (2016): Mineralogy maps for SWIR data: what works, what doesn’t, and why; *Geoconferences: Hyperspectral Analy-*

- sis for Exploration, URL <<http://www.scott-halley.com.au/public/documents/5/15/Mineralogy%20Maps%20from%20SWIR%20data.pdf>> [November 2018].
- Harraden, C., McNulty, B., Gregory, M. and Lang, J. (2013): Shortwave infrared spectral analysis of hydrothermal alteration associated with the Pebble porphyry copper-gold-molybdenum deposit, Iliamna, Alaska; *Economic Geology*, v. 108, no. 3, p. 483–494, URL <<https://pubs.geoscienceworld.org/segweb/economicgeology/article/108/3/483/128482/shortwave-infrared-spectral-analysis-of>> [November 2018].
- Hauff, P. (2008): An overview of VIS-NIR-SWIR field spectroscopy as applied to precious metal exploration; *Spectral International Inc.*, Arvada, Colorado, 71 p., URL <<http://www.spectral-international.com/files/50329239.pdf>> [November 2018].
- Lowell, J.D. and Guilbert, J.M. (1970): Lateral and vertical alteration-mineralization zoning in porphyry ore deposits; *Economic Geology*, v. 65, no. 4, p. 373–408, URL <<https://pubs.geoscienceworld.org/segweb/economicgeology/article/65/4/373/18036/lateral-and-vertical-alteration-mineralization>> [November 2018].
- McMillan, W.J., Thompson, J.F.H., Hart, C.J.R. and Johnston, S.T. (1996): Porphyry deposits of the Canadian Cordillera; *Geoscience Canada*, v. 23, no. 3, p. 125–134, URL <<https://journals.lib.unb.ca/index.php/GC/article/view/3905>> [November 2018].
- Mercer, C.N., Reed, M.H. and Mercer, C.M. (2015): Time scales of porphyry Cu deposit formation: insights from titanium diffusion in quartz; *Economic Geology*, v. 110, no. 3, p. 587–602, <<https://pubs.er.usgs.gov/publication/70142152>> [November 2018].
- Monger, J.W.H., Price, R.A. and Tempelman-Kluit, D.J. (1982): Tectonic accretion and the origin of the two major metamorphic and plutonic belts in the Canadian Cordillera; *Geology*, v. 10, no. 2, p. 70–75, URL <<https://pubs.geoscienceworld.org/gsa/geology/article/10/2/70/198326/tectonic-accretion-and-the-origin-of-the-two-major>> [November 2018].
- Nash, J.T. (1976): Fluid-inclusion petrology data from porphyry copper deposits and applications to exploration; *United States Geological Survey, Professional Paper 907-D*, 16 p., URL <<https://pubs.usgs.gov/pp/0907d/report.pdf>> [November 2018].
- Proffett, J.M. (2009): High Cu grades in porphyry Cu deposits and their relationship to emplacement depth of magmatic sources; *Geology*, v. 37, no. 8, p. 675–678, URL <<https://pubs.geoscienceworld.org/gsa/geology/article/37/8/675/103862/high-cu-grades-in-porphyry-cu-deposits-and-their>> [November 2018].
- Reed, H., Rusk, B. and Palandri, J. (2013): The Butte magmatic-hydrothermal system: one fluid yields all alteration and veins; *Economic Geology*, v. 108, no. 6, p. 1379–1396, URL <<https://pubs.geoscienceworld.org/segweb/economicgeology/article/108/6/1379/128521/the-butte-magmatic-hydrothermal-system-one-fluid>> [November 2018].
- Runyon, S.E., Steele-MacInnes, M., Seedorff, E., Lecumberri-Sanchez, P. and Mazdab, F.K. (2017): Coarse muscovite veins and alteration deep in the Yerington batholith, Nevada: insights into fluid exsolution in the roots of porphyry copper systems; *Mineralium Deposita*, v. 52, no. 4, p. 463–470, URL <<https://link.springer.com/article/10.1007/s00126-017-0720-1>> [November 2018].
- Rusk, B.G. and Reed, M.H. and Dilles, J.H. (2008): Fluid inclusion evidence for magmatic-hydrothermal fluid evolution in the porphyry copper-molybdenum deposit at Butte, Montana; *Economic Geology*, v. 103, no. 2, p. 307–334, URL <<https://pubs.geoscienceworld.org/segweb/economicgeology/article/103/2/307/127951/fluid-inclusion-evidence-for-magmatic-hydrothermal>> [November 2018].
- Rusk, B.G., Reed, H.R., Dilles, J.H. and Kent, A.J.R. (2006): Intensity of quartz cathodoluminescence and trace-element content in quartz from the porphyry copper deposit at Butte, Montana; *American Mineralogist*, v. 91, no. 8–9, p. 1300–1312, URL <<https://pubs.er.usgs.gov/publication/70028154>> [November 2018].
- Schiarizza, P., Gaba, R.G., Glover, J.K., Garver, J.I. and Umhoefer, P.J. (1997): Geology and mineral occurrences of the Taseko-Bridge River area; *BC Ministry of Energy, Mines and Petroleum Resources, Bulletin 100*, 191 p., URL <<http://www.empr.gov.bc.ca/Mining/Geoscience/Publications/Catalogue/BulletinInformation/BulletinsAfter1940/Pages/Bulletin100.aspx>> [November 2018].
- Simpson, M.P. (2015): Reflectance spectrometry (SWIR) of alteration minerals surrounding the Favona epithermal vein, Waihi vein system, Hauraki goldfield; *AusIMM, New Zealand Branch, Annual Conference, 2015*, p. 490–499, URL <https://www.researchgate.net/publication/282933781_Reflectance_spectrometry_SWIR_of_alteration_minerals_surrounding_the_Favona_epithermal_vein_Waihi_vein_system_Hauraki_Goldfield> [November 2018].
- Umhoefer, P. and Kleinspehn, K.L. (1995): Mesoscale and regional kinematics of the northwestern Yalakom fault system: major Paleogene dextral faulting in British Columbia, Canada; *Tectonics*, v. 14, no. 1, p. 78–94, URL <<https://agupubs.onlinelibrary.wiley.com/doi/10.1029/94TC01503>> [November 2018].

Evolution of Porphyry-Epithermal Gold Systems Using Trace Elements: Insights from the Iron Cap Deposit, Kerr-Sulphurets-Mitchell District, Northwestern British Columbia (NTS 104B)

H.C. Graham, School of Earth and Environment, University of Leeds, Leeds, United Kingdom, eehg@leeds.ac.uk

D.J. Morgan, School of Earth and Environment, University of Leeds, Leeds, United Kingdom

R.J. Chapman, School of Earth and Environment, University of Leeds, Leeds, United Kingdom

D.A. Banks, School of Earth and Environment, University of Leeds, Leeds, United Kingdom

Graham, H.C., Morgan, D.J., Chapman, R.J. and Banks, D.A. (2019): Evolution of porphyry-epithermal gold systems using trace elements: insights from the Iron Cap deposit, Kerr-Sulphurets-Mitchell district, northwestern British Columbia (NTS 104B); *in* Geoscience BC Summary of Activities 2018: Minerals and Mining, Geoscience BC, Report 2019-1, p. 67–74.

Introduction

Porphyry- and epithermal-style mineral deposits together account for approximately 28% of global gold endowment (based on past production, reserves and resources), making them collectively of comparable importance to orogenic and paleoplacer deposits as a source of gold on the world stage (Lipson, 2014). Similarly in British Columbia (BC), 31.5% of gold produced has originated from porphyry and epithermal deposits (BC Geological Survey, 2015). Porphyries, in particular, tend to be more sought after for their significant copper contents (making up three-quarters of global copper production; Sillitoe, 2010), yet the enrichment of gold in addition to copper makes them highly attractive exploration targets. With both epithermal and porphyry deposits forming from magmatic intrusions and their associated hydrothermal systems at active tectonic margins, there are often recognized spatial, temporal and genetic associations (Sillitoe, 2010). However, the transition from porphyry to epithermal conditions remains a key topic of discussion (e.g., Gammons and Williams-Jones, 1997; Hedenquist et al., 1998; Heinrich, 2005; Pudack et al., 2009; Maydagán et al., 2015). Further understanding of evolutionary processes is hence required to elucidate not only the above, but also the factors controlling the enrichment and distribution of gold in evolving magmatic-hydrothermal systems.

The variability in fluid characteristics, from the deep porphyry to shallow epithermal environments, is one particular aspect of porphyry-epithermal system evolution that lacks sufficient understanding. Change in parameters such as temperature, pH and phase (i.e., liquid vs. vapour) can significantly affect the solubility and transport of metals, as

has been discussed by numerous workers in the case of gold (e.g., Gammons and Williams-Jones, 1997; Archibald et al., 2001; Stefánsson and Seward 2003, 2004; Simon et al., 2005; Williams-Jones and Heinrich, 2005). Genetic models tend to outline broad characteristics, such as alteration zones, as indicators of fluid conditions (e.g., Seedorff et al., 2005; Sillitoe, 2010). However, the range of conditions implicit in the accepted nomenclature for porphyry-epithermal alteration does not necessarily correlate with the behaviour of economic metals. Few researchers have succeeded in accurately defining the fluid parameters associated with discrete periods of ore genesis in an evolving magmatic-hydrothermal system. Because fluids are a key control on the distribution and speciation of resources, knowledge of the precise physicochemical conditions that facilitate metal transport and induce deposition in certain parts of a porphyry-epithermal system has significant implications for the advancement of exploration and processing methodologies.

Fluid-inclusion studies have been instrumental in interpreting the conditions of ore formation, since their inception almost half a century ago (e.g., Roedder, 1971; Heinrich et al., 1992; Wilkinson, 2001). However, there remain significant shortcomings with the technique: primarily the ambiguity of associations between the characterized inclusions and adjacent ore minerals. Moreover, primary inclusions that have strong indicated relationships to ore minerals can be relatively scarce. The study of trace elements may provide an alternative, supplementary and potentially more accurate method to interpret fluid conditions at specific points within mineralizing environments. Variations in trace elements have been recognized on the deposit scale, macro scale (e.g., between vein generations) and micro scale (e.g., within individual ore minerals) in numerous deposits worldwide (e.g., Cioaca et al., 2014; Pašava et al., 2016; Sykora et al., 2018; Zarasvandi et al., 2018). However, there remains a paucity of research explaining these

This publication is also available, free of charge, as colour digital files in Adobe Acrobat® PDF format from the Geoscience BC website: <http://www.geosciencebc.com/s/SummaryofActivities.asp>.

variations in detail, with the physicochemical characteristics of the fluids likely being a key variable.

This project focuses on a comprehensive sample suite from deep-porphyry to shallow-vein environments at the Iron Cap deposit in the Kerr-Sulphurets-Mitchell (KSM) district, northwestern British Columbia (Figure 1). The research will study the use of trace elements (including gold) to interpret the evolution of the magmatic-hydrothermal system. Specifically, variation in the speciation of certain trace elements (i.e., Au, As, Sb, Pd, Se, Te, Hg) and their subsequent partitioning to ore minerals will be investigated to provide a window to the physicochemical conditions

prevalent at different stages of porphyry-epithermal development, both in time and space. In addition, a population of detrital gold grains collected from drainages within the KSM district will be scrutinized to identify geochemical variations and infer the source and formation process of gold, both in the district as a whole and at Iron Cap. Lastly, the thermodynamic properties of the above trace elements will be assessed to determine the suitability of trace element studies for interpreting the conditions of ore formation in a given porphyry-epithermal system. In the present paper, the geology of the case study area at KSM is described, the sampling procedures and rationale are outlined, and the various methodologies and plans for future work are presented.

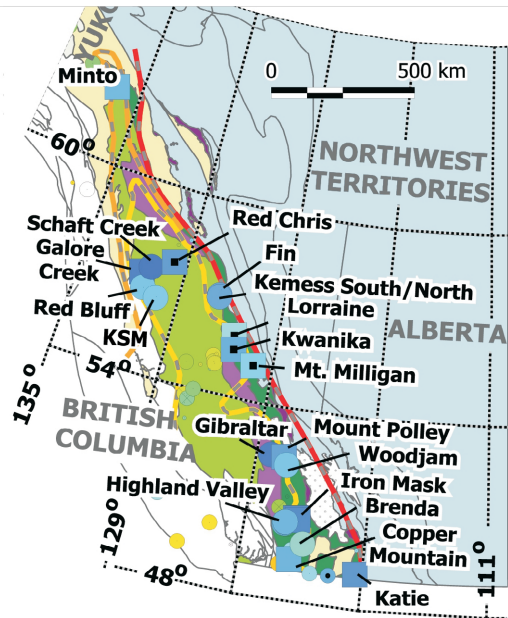
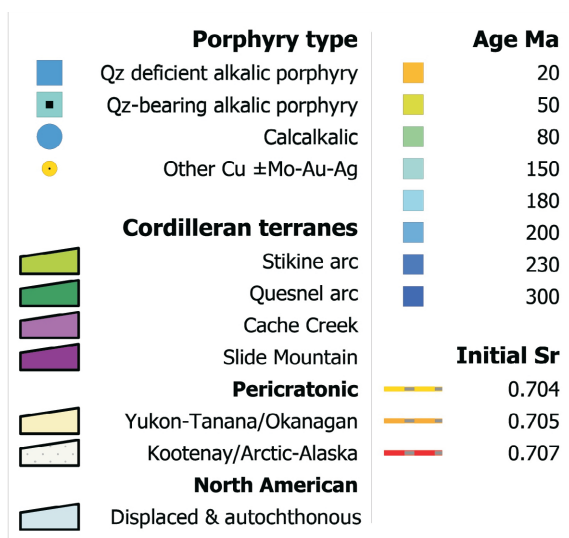


Figure 1. Location of the Kerr-Sulphurets-Mitchell (KSM) district in northwestern British Columbia (modified from Logan and Mihalynuk, 2014). Other porphyry deposits of the Canadian Cordillera are also shown, with porphyry type represented by symbol shape, and the age of deposits depicted by colouration.

Study Area

The Kerr-Sulphurets-Mitchell (KSM) district is host to four Cu-Au, predominantly porphyry-style deposits: Kerr, Sulphurets, Mitchell and Iron Cap. Together they host proven and probable reserves of 38.8 million ounces of Au, 10.2 billion pounds of Cu, 207 million pounds of Mo and 183 million ounces of Ag, at grades of 0.55 g/t Au, 0.21% Cu, 42.6 g/t Mo and 2.6 g/t Ag, making KSM one of the largest undeveloped Cu-Au prospects in the world and particularly one of the most gold rich in terms of total contained metal (Seabridge Gold, 2018b). The Iron Cap deposit at KSM will be studied in detail as part of this research. It has not yet been investigated in terms of the magmatic-hydrothermal system and therefore presents a unique opportunity to characterize the nature of fluids throughout evolution from deep porphyry to shallower, near-epithermal environments.

Regional Geology

The Stikine arc terrane of the Canadian Cordillera is significantly endowed with magmatic-related mineral deposits, including those of the KSM district (Figure 1). Most mineralizing activity occurred during a short ~15 m.y. period at the Triassic–Jurassic boundary, producing the abundance of deposits in western BC that form a 60 km long trend stretching north-northwest from the town of Stewart to the mining district around KSM (Logan and Mihalynuk, 2014; Febbo et al., 2015). The dominant hosts for mineralization within the Stikine terrane are the volcanosedimentary sequences of the Late Triassic Stuhini Group and Early Jurassic Hazelton Group (Nelson and Kyba, 2014). The Stuhini sequences are unconformably overlain by those of the Hazelton, the latter group representing the waning of island-arc magmatism prior to accretion in the Middle Jurassic (Nelson and Colpron, 2007; Nelson and Kyba, 2014). Several deformation events have affected the Stikine successions, the most significant being a mid-Cretaceous sinistral transpression associated with the Skeena fold-and-thrust belt that produced north-northwest-trending struc-

tures (Nelson and Kyba, 2014). The present geology of northwestern BC is shown in Figure 2.

Local Geology

The four deposits of the KSM district (Kerr, Sulphurets, Mitchell and Iron Cap) are centred on a series of Early Jurassic diorite to syenite intrusions, with adjacent wallrocks comprising the volcanoclastic and sedimentary units of the Late Triassic Stuhini Group and Early Jurassic Hazelton Group (Figure 3). Radiometric dating suggests that the KSM intrusions, and hence the associated mineralization, were emplaced between 197 and 189.6 Ma (Febbo et al., 2015 and references therein). The porphyry style is dominantly calcalkaline, although discrete areas exhibit features consistent with alkaline-style mineralization (Campbell and Dilles, 2017). The four deposits are hosted mainly within the footwall of the east-verging Sulphurets thrust fault (STF), which is linked to the Skeena fold-and-thrust belt (Kirkham and Margolis, 1995; Febbo et al., 2015). A

splay of the STF, the Mitchell thrust fault, also separates the Iron Cap and Mitchell deposits at the northern end of the district (Febbo et al., 2015).

At Iron Cap, mineralization is hosted primarily within porphyritic monzonite, unclassified intrusions containing a high volume (>80%) of quartz veins and, to a lesser extent, the surrounding wallrock of mudstone, sandstone, conglomerate and volcanic breccia (Campbell and Dilles, 2017). The orebody plunges to the northwest, with the central section exhibiting potassic alteration, zoning outward to chlorite±sericite, and peripheral phyllic and silicic alteration in the wallrocks (Campbell and Dilles, 2017). While porphyry-style mineralization dominates, features more characteristic of the upper parts of a magmatic-hydrothermal system, such as sericite-quartz-clay alteration, hydrothermal breccias and increases in sulphosalt minerals, are identified in the near surface (Seabridge Gold, 2018a). This suggests that the Iron Cap deposit may represent a transition from porphyry to epithermal environments.

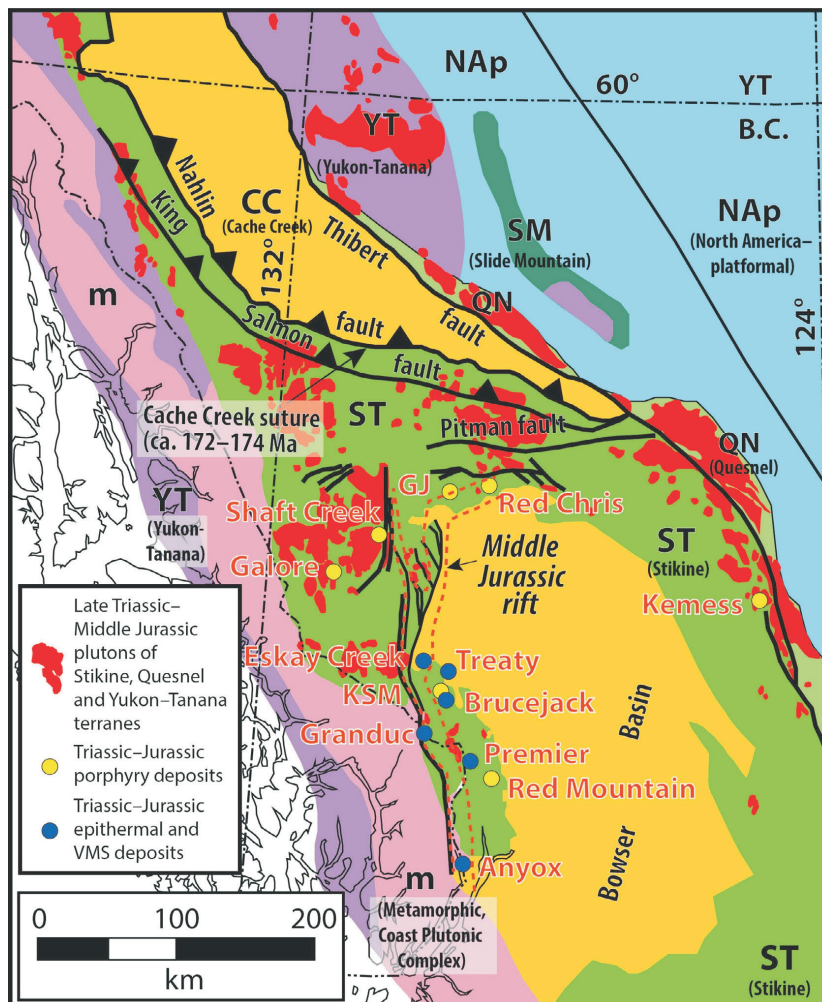


Figure 2. Geology of northwestern BC, showing the general north-northwest-trending terranes and major structures (from Campbell and Dilles, 2017). The locations of the prolific Triassic–Jurassic intrusive rocks are also shown, with associated mineral deposits of porphyry, epithermal and volcanogenic massive sulphide (VMS) types.

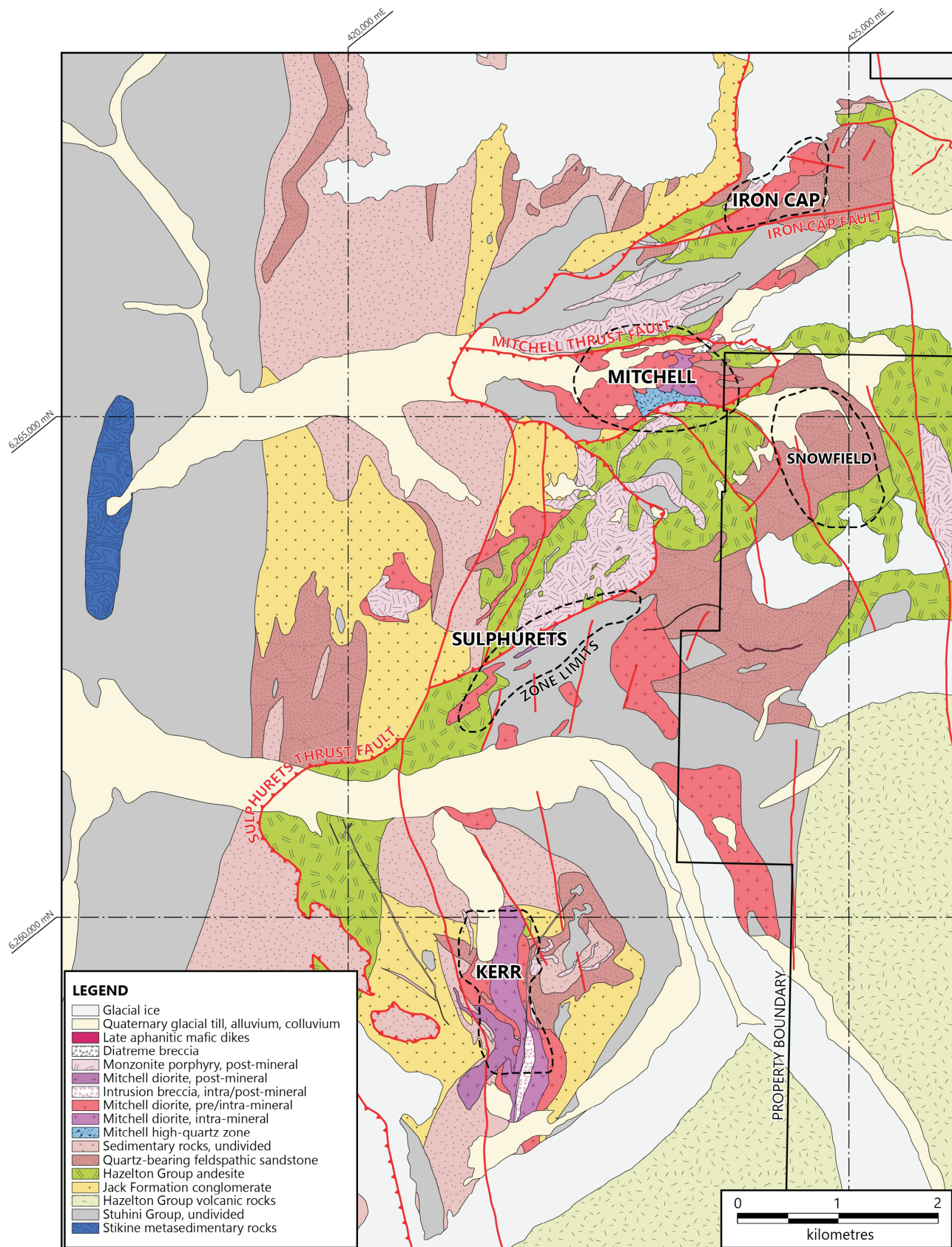


Figure 3. Geology of the Kerr, Sulphurets, Mitchell and Iron Cap deposits within the rocks of the KSM district (modified from Campbell and Dilles, 2017). Snowfield is a porphyry deposit located in the adjacent licence area and is purported to be the displaced cap of the Mitchell deposit (Febbo et al., 2015). UTM zone NAD83-9V.

Sampling

Drillcore

More than 60 samples have been collected from drillcore of the Iron Cap deposit. The selection of certain samples from the available core was informed by various criteria. Firstly, acquiring a transect through a majority of the deposit is necessary to attain a comprehensive understanding of system evolution, so samples were collected from a range of different holes at varied depths, ensuring representation of vertical or lateral variations. Secondly, a number of the targeted trace elements (Au, As, Sb, Pd, Se, Te, Hg) must be present to carry out the proposed analysis, so samples that recorded the presence of these elements (recognized from assays) in varied amounts were selected. Lastly, distinct fluid phases must be distinguished to identify evolutionary processes. The drillcore was therefore scrutinized to ensure that features allowing identification of fluid phases were present, with core containing several vein generations being preferentially sampled. At present, the collected samples are being prepared for analysis.

Detrital Gold

A period of detrital gold sampling was originally planned to be completed during September 2018 but has now been postponed to 2019 due to unforeseen circumstances. Nevertheless, the sampling procedure will not change, focusing on collection of natural gold grains from a range of water courses draining the KSM deposits. The samples will not represent exclusively Iron Cap but a wider population encompassing all four deposits of the district, and likely other nearby deposits (i.e., Snowfield and Brucejack). It may, however, be possible to identify grains that show comparable features (e.g., Au:Ag ratios) to the gold recognized in Iron Cap core samples, and interpretation of the data from detrital gold analysis may establish discrete populations. One possibility is to crush a number of the core samples collected to retrieve an appreciable amount of hypogene gold from Iron Cap for comparison with the detrital. However, there is an issue that gold recovered in this way would mostly not be constrained to an individual vein generation or fluid phase, and thus have limited use in interpreting fluid evolution. Yet, it would allow characterization of Iron Cap gold in a wider sense and provide a benchmark for recognizing gold from Iron Cap in the detrital environment.

Methodology and Future Work

Petrography

A full petrographic study of the drillcore samples will be carried out first, using transmitted and reflected light microscopy, augmented by scanning electron microscopy (SEM). From these data, an initial paragenesis for Iron Cap can be constructed, which will detail the sequence of events

that took place during its formation. Importantly, different vein generations will be identified. Each generation will relate to a fluid (or fluids in some cases) that had a different composition and experienced different conditions to the fluids that formed earlier and later vein generations. Understanding the temporal relationship between the veins will ensure that fluid evolution can be studied and interpreted. Linking the veins (and their forming fluids) to certain petrographic features, such as the presence of gold-bearing minerals, will also provide an initial understanding of the physicochemical parameters of the fluids (e.g., gold bearing). The petrographic study thus forms an important basis for subsequent analysis, allowing additional data collected to be placed into a geological context.

Analytical Process

Following core-sample characterization and the initial identification of fluid phases, trace-element analyses will proceed by electron microprobe analysis (EMPA) and laser-ablation inductively coupled plasma–mass spectrometry (LA-ICP-MS). The aim of this analysis is to define the concentration, distribution and speciation of each target element (Au, As, Sb, Pd, Se, Te, Hg) relating to a discrete fluid phase, in order to understand the physicochemical characteristics of that fluid. To begin, EMPA will be used to analyze minerals containing the trace elements, such as sulphides, selenides and tellurides (identified on the SEM). This will define their chemical compositions and highlight targets for further analysis by LA-ICP-MS. As a non-destructive method with a high spatial resolution, EMPA is initially preferred over LA-ICP-MS, which will follow once a target mineral has been characterized by EMPA. The low detection limits of LA-ICP-MS will be used to analyze a suite of minerals, predominantly sulphides such as pyrite and molybdenite, and gold, to identify heterogeneities in their compositions between vein generations and within individual minerals. Such information will highlight differences between fluid phases and describe the changes in a single fluid phase over time.

To complement the trace-element study, fluid inclusions will first be analyzed by cathodoluminescence to identify how inclusions identified in the petrographic study could relate to certain fluid and mineral phases. Microthermometry will then provide an indication of fluid conditions, by measurement of inclusion-trapping conditions and elemental compositions. Lastly, LA-ICP-MS will be applied to specific inclusions, to determine the concentration of elements in the fluid and to identify elements in the fluid that have not precipitated. An element's absence from the petrographic and trace-element analysis but presence in fluid inclusions will raise questions on the solubility, transport and deposition of that element.

The detrital gold grains will be characterized using two approaches. If the grains are sufficiently large to permit sectioning, inclusions of other minerals will be identified by SEM. Determination of gold-alloy compositions will then be established by EMPA. If the gold particles collected are exceedingly small (<50 µm), then information will be gained through ablation of the entire grain. These datasets illuminate the mineralogical context of the hypogene source and, at KSM, they may indicate which of the local potential sources has liberated the most particulate gold. In addition, gold mineralogy at the trace-element level can be used as another window to the trace-element suite present in the mineralizing fluid.

Interpretation

The physicochemical characteristics of the hydrothermal fluid(s) that formed Iron Cap will be interpreted using the acquired data. Fluid phases will be characterized based on petrography, the concentration of trace elements they contained, fluid-inclusion data (where possible) and subsequent consideration of the thermodynamic properties of various trace elements within the system. This information will be evaluated with the aim of defining the fluid conditions in terms of temperature, pressure, salinity, pH, type (liquid or vapour), sulphur fugacity and oxygen fugacity, and interpreting the transport mechanism for gold and the target trace elements.

The next step will be to propose a detailed fluid-evolution model for Iron Cap, describing the processes that took place to induce changes in the fluid, and the deposition of gold and the suite of trace elements in certain sites and states. Fluid-rock interaction, fluid mixing, phase separation, and partitioning are all important processes that can influence fluid changes and element deposition, and they will thus be considered in this context. The outcomes of the Iron Cap study will be subsequently assessed to establish whether a transferrable methodology can be developed.

Conclusions

This project investigates trace-element behaviour in the magmatic-hydrothermal system of the Iron Cap deposit at KSM, to shed light on the evolution from porphyry to epithermal conditions and to improve understanding of the processes leading to gold enrichment and linked deposit formation. A comprehensive sample suite, from deep porphyry to shallow vein environments at Iron Cap, will be analyzed by microscopy, EMPA, LA-ICP-MS and fluid-inclusion microthermometry to determine the concentration, distribution and speciation of trace elements (Au, As, Sb, Pd, Se, Te, Hg) within the deposit, and identify discrete fluid phases. Characterization of detrital gold grains and, if possible, gold from ore will provide additional information on the partitioning of trace elements in the magmatic-hydrothermal system whilst augmenting the existing database

of detrital gold in BC to increase its potential as an indicator mineral during exploration. The collected data will be interpreted in light of the thermodynamic properties of the studied elements, to describe the changing fluid conditions during magmatic-hydrothermal evolution and construct a genetic model for the Iron Cap deposit. Subsequent examination of trace-element behaviour may allow characterization of the physicochemical parameters of fluids in a given magmatic-hydrothermal system, enabling prediction of metal transport and deposition, and helping lead to discovery of mineralization. Such a technique would have wide application in exploration and resource targeting on regional and local scales.

Acknowledgments

This project is funded by the Natural Environment Research Council, United Kingdom. The lead author thanks Geoscience BC for funds provided through the scholarship program, and the Society of Economic Geologists is acknowledged for financial support provided through a Graduate Student Fellowship. Seabridge Gold Inc. is gratefully acknowledged for access to the KSM project, and for logistical support and accommodation provided during sample collection. Lastly, T. Torveja is thanked for a helpful review of this manuscript.

References

- Archibald, S.M, Migdisov, A.A. and Williams-Jones, A.E. (2001): The stability of Au-chloride complexes in water vapor at elevated temperatures and pressures; *Geochimica et Cosmochimica Acta*, v. 65, p. 4413–4423.
- BC Geological Survey (2015): Gold in British Columbia; BC Ministry of Energy, Mines and Petroleum Resources, BC Geological Survey, Information Circular 2015-16, 2 p., URL <https://www2.gov.bc.ca/assets/gov/farming-natural-resources-and-industry/mineral-exploration-mining/documents/mineral-development-office/gold_september_2015.pdf> [October 2018].
- Campbell, M.E. and Dilles, J.H. (2017): Magmatic history of the Kerr-Sulphurets-Mitchell copper-gold porphyry district, northwestern British Columbia (NTS 104B); *in* Geoscience BC Summary of Activities 2016, Geoscience BC, Report 2017-1, p. 233–244, URL <http://cdn.geosciencebc.com/pdf/SummaryofActivities2016/SoA2016_Campbell.pdf> [October 2018].
- Cioaca, M.E., Munteanu, M., Qi, L. and Costin, G. (2014): Trace element concentrations in porphyry copper deposits from Metaliferi Mountains, Romania: a reconnaissance study; *Ore Geology Reviews*, v. 63, p. 22–39.
- Febbo, G.E., Kennedy, L.A., Savell, M., Creaser, R.A. and Friedman, R.M. (2015): Geology of the Mitchell Au-Cu-Ag-Mo porphyry deposit, northwestern British Columbia, Canada; *in* Geological Fieldwork 2014, BC Ministry of Energy, Mines and Petroleum Resources, BC Geological Survey, Paper 2015-1, p. 59–86, URL <http://www.empr.gov.bc.ca/Mining/Geoscience/PublicationsCatalogue/Fieldwork/Documents/2014/04_Febbo_etal.pdf>. [October 2018].

- Gammons, C.H. and Williams-Jones, A.E. (1997): Chemical mobility of gold in the porphyry-epithermal environment; *Economic Geology*, v. 92, p. 45–59.
- Hedenquist, J.W., Arribas, A. and Reynolds, T.J. (1998): Evolution of an intrusion-centered hydrothermal system: Far Southeast-Lepanto porphyry and epithermal Cu-Au deposits, Philippines; *Economic Geology*, v. 93, p. 373–404.
- Heinrich, C.A. (2005): The physical and chemical evolution of low-salinity magmatic fluids at the porphyry to epithermal transition: a thermodynamic study; *Mineralium Deposita*, v. 39, p. 864–889.
- Heinrich, C.A., Ryan, C.G., Mernagh, T.P. and Eadington, P.J. (1992): Segregation of ore metals between magmatic brine and vapor: a fluid inclusion study using PIXE microanalysis; *Economic Geology*, v. 87, p. 1566–1583.
- Kirkham, R. and Margolis, J. (1995): Overview of the Sulphurets area, northwestern British Columbia; in *Porphyry Deposits of the Northwestern Cordillera of North America*, T.G. Schroeter (ed.), Canadian Institute of Mining, Metallurgy and Petroleum, Special Volume 46, p. 473–483.
- Lipson, R. (2014): The promise and perils of porphyry deposits in the future of gold production; *Society of Economic Geologists Newsletter*, v. 98, p. 1, 14–21.
- Logan, J.M., and Mihalynuk, M.G. (2014): Tectonic controls on Early Mesozoic paired alkaline porphyry deposit belts (Cu-Au ± Ag-Pt-Pd-Mo) within the Canadian Cordillera; *Economic Geology*, v. 109, p. 827–858.
- Maydagán, L., Franchini, M., Rusk, B., Lentz, D.R., McFarlane, C., Impiccini, A., Ríos, F.J. and Rey, R. (2015): Porphyry to epithermal transition in the Altar Cu-(Au-Mo) deposit, Argentina, studied by cathodoluminescence, LA-ICP-MS, and fluid inclusion analysis; *Economic Geology*, v. 110, p. 889–923.
- Nelson, J.L. and Colpron, M. (2007): Tectonics and metallogeny of the British Columbia, Yukon and Alaskan Cordillera, 1.8 Ga to the present; in *Mineral Deposits of Canada: A Synthesis of Major Deposit-Types, District Metallogeny, the Evolution of Geological Provinces, and Exploration Methods*, W.D. Goodfellow (ed.), Geological Association of Canada, Mineral Deposits Division, Special Publication 5, p. 755–791.
- Nelson, J.L., and Kyba, J. (2014): Structural and stratigraphic control of porphyry and related mineralization in the Treaty Glacier–KSM–Brucejack–Stewart trend of western Stikinia; in *Geological Fieldwork 2013*, BC Ministry of Energy, Mines and Petroleum Resources, BC Geological Survey, Paper 2014-1, p. 111–140, URL <http://www.empr.gov.bc.ca/Mining/Geoscience/PublicationsCatalogue/Fieldwork/Documents/2013/07_Nelson_Kyba.pdf> [October 2018].
- Pašava, J., Svojtka, M., Veselovský, F., Ďurišová, J., Ackerman, L., Pour, O., Drábek, M., Halodová, P. and Haluzová, E. (2016): Laser ablation ICPMS study of trace element chemistry in molybdenite coupled with scanning electron microscopy (SEM) – an important tool for identification of different types of mineralization; *Ore Geology Reviews*, v. 72, p. 874–895.
- Pudack, C., Halter, W.E., Heinrich, C.A. and Pettke, T. (2009): Evolution of magmatic vapor to gold-rich epithermal liquid: the porphyry to epithermal transition at Nevados de Famatina, northwest Argentina; *Economic Geology*, v. 104, p. 449–477.
- Roedder, E. (1971): Fluid inclusion studies on the porphyry-type ore deposits at Bingham, Utah, Butte, Montana and Climax, Colorado; *Economic Geology*, v. 66, p. 98–118.
- Seabridge Gold Inc. (2018a): KSM (Kerr-Sulphurets-Mitchell) geology; Seabridge Gold Inc., URL <http://seabridgegold.net/ksm_geology.php> [October 2018].
- Seabridge Gold Inc. (2018b): Mineral reserves and resources, February 2018; Seabridge Gold Inc., URL <<http://seabridgegold.net/resources.php>> [October 2018].
- Seedorff, E., Dilles, J.H., Proffett, J.M., Jr., Einaudi, M.T., Zurcher, L., Stavast, W.J.A., Johnson, D.A. and Barton, M.D. (2005): Porphyry deposits: characteristics and origin of hypogene features; *Economic Geology*, v. 100, p. 251–298.
- Sillitoe, R.H. (2010): Porphyry copper systems; *Economic Geology*, v. 105, p. 3–41.
- Simon, A.C., Frank, M.R., Pettke, T., Candela, P.A., Piccoli, P.M. and Heinrich, C.A. (2005): Gold partitioning in melt-vapor-brine systems; *Geochimica et Cosmochimica Acta*, v. 69, p. 3321–3335.
- Stefánsson, A. and Seward, T.M. (2003): Stability of chlorido-gold(I) complexes in aqueous solutions from 300 to 600°C and from 500 to 1800 bar; *Geochimica et Cosmochimica Acta*, v. 67, p. 4559–4576.
- Stefánsson, A. and Seward, T.M. (2004): Gold(I) complexing in aqueous sulphide solutions to 500°C at 500 bar; *Geochimica et Cosmochimica Acta*, v. 68, p. 4121–4143.
- Sykora, S., Cooke, D.R., Meffre, S., Stephanov, A.S., Gardner, K., Scott, R., Selley, D. and Harris, A.C. (2018): Evolution of pyrite trace element compositions from porphyry-style and epithermal conditions at the Lihir gold deposit: implications for ore genesis and mineral processing; *Economic Geology*, v. 113, p. 193–208.
- Wilkinson, J.J. (2001): Fluid inclusions in hydrothermal ore deposits; *Lithos*, v. 55, p. 229–272.
- Williams-Jones, A.E. and Heinrich, C.A. (2005): Vapor transport of metals and the formation of magmatic-hydrothermal ore deposits; *Economic Geology*, v. 100, p. 1287–1312.
- Zaravandi, A., Rezaei, M., Raith, J.G., Pourkaseb, H., Asadi, S., Saed, M. and Lentz, D.R. (2018): Metal endowment reflected in chemical composition of silicates and sulfides of mineralized porphyry copper systems, Urumieh-Dokhtar magmatic arc, Iran; *Geochimica et Cosmochimica Acta*, v. 223, p. 36–59.

Preliminary Field Results from Kinskuch Lake, Northwestern British Columbia (NTS 103P/11): a Study of the Boundary between the Stuhini and Hazelton Groups

E.A. Miller, Department of Earth, Ocean and Atmospheric Sciences, The University of British Columbia, Vancouver, BC, emilymillergeo@gmail.com

L. Kennedy, Department of Earth, Ocean and Atmospheric Sciences, The University of British Columbia, Vancouver, BC

B.I. van Straaten, British Columbia Geological Survey, Victoria, BC

Miller, E.A., Kennedy, L. and van Straaten, B.I. (2019): Preliminary field results from Kinskuch Lake, northwestern British Columbia (NTS 103P/11): a study of the boundary between the Stuhini and Hazelton groups, *in* Geoscience BC Summary of Activities 2018: Minerals and Mining, Geoscience BC, Report 2019-1, p. 75–86.

Introduction

The Late Triassic and Early Jurassic intrusive suites of the Stikine terrane of British Columbia (BC) are associated with significant Cu-Au-Mo porphyry and intrusion-related mineralization (Nelson et al., 2013; Logan and Mihalynuk, 2014; Campbell and Dilles, 2017). The Stewart mining camp includes the Early Jurassic KSM area Cu-Au porphyry deposits (MINFILE 104B 103, 173, 182 and 191; BC Geological Survey, 2018), the Big Bulk Au-Cu porphyry system (MINFILE 103P 016), the Red Mountain Au deposit (MINFILE 103P 086) and the Brucejack epithermal Au deposit (MINFILE 104B 022).

Porphyry Cu-Au-Mo systems, especially those formed along continental active margins, are generally considered to have formed in a contractional environment (e.g., Sillitoe, 2010). The tectonic environment of porphyry systems formed in island arcs, such as those located within the Stikine terrane of northwestern BC, are not as well understood. Within the Sulphurets area, at the Kerr-Sulphurets-Mitchell (KSM) project, recent geological studies suggest that normal faulting, active sedimentation and olistolith formation accompanied Early Jurassic porphyry emplacement (Nelson and Kyba, 2014; Febbo et al., 2015; Kyba and Nelson, 2015; Febbo, 2016). Febbo (2016) proposed a model where small pull-apart basins along reactivated basement structures localized porphyry Cu-Au-Mo formation at the KSM project, hence, porphyry emplacement did not occur in a purely contractional environment.

To test this model and its applicability to the broader region, in the 2018 field season, 1:20 000 scale structural and stratigraphic mapping of two sites was completed: Kinskuch Lake, surrounding the Big Bulk Au-Cu porphyry system and the Red Mountain Au deposit. Both study areas are lo-

cated south of the better-studied Sulphurets area. They were selected because they are underlain by similar rocks, also deposited in the Early Jurassic, with mineralization thought to be of comparable age to the rocks studied at KSM.

The aim of this paper is to present preliminary lithological descriptions, stratigraphic sequences and structural elements resulting from the 2018 fieldwork at the Kinskuch Lake site and is part of a M.Sc. research project undertaken by E. Miller. The goals of the fieldwork were to delineate the Late Triassic to Early Jurassic stratigraphy and to record the geometry and kinematics of the structural elements in the area, with the aim of reconstructing the geological setting into which the Big Bulk porphyry system was emplaced. To determine whether porphyry and related mineralization was intruded into extensional pull-apart basins, the following questions will ultimately be addressed by the research:

- What are the ages of porphyry intrusion and mineralization?
- What is the sedimentological/volcanic environment in which the deposit was formed?
- Is there geological evidence for porphyry emplacement contemporaneous with high-energy sedimentation?
- What was the structural architecture during porphyry emplacement?

Regional Geology and Tectonic Setting

The study area is dominated by Late Triassic and Early Jurassic volcano-sedimentary rocks that form part of the Stikine terrane, the largest accreted terrane in BC (2000 by 300 km, Figure 1). The Stikine terrane comprises three unconformity-bounded, island-arc volcano-sedimentary successions that include the upper Paleozoic Stikine assemblage, the Middle to Upper Triassic Stuhini and Takla groups and the uppermost Triassic to Middle Jurassic Hazelton Group (Greig, 1992; Logan et al., 2000; Colpron and Nelson, 2011; Nelson et al., 2013). Mesozoic

This publication is also available, free of charge, as colour digital files in Adobe Acrobat® PDF format from the Geoscience BC website: <http://www.geosciencebc.com/s/SummaryofActivities.asp>.

arc-related intrusions include the Late Triassic Stikine and Galore Creek plutonic suites (coeval and comagmatic with the Stuhini Group), as well as the latest Triassic Tatogga and Early Jurassic Texas Creek plutonic suites, which are coeval and comagmatic with the Hazelton Group (Nelson et al., 2018).

The Stuhini Group represents the oldest rocks in the study area and locally comprises Triassic arc-related mafic volcanic rocks typified by the presence of augite and sedimentary rocks.

Generally, the base of the Hazelton Group is a regional unconformity above Triassic and older rocks (Nelson and Kyba, 2014), although locally this contact is paraconformable to conformable (van Straaten and Nelson, 2016). The lower Hazelton Group is a latest Triassic to Toarcian andesitic volcanic sequence with local felsic centres. In the Sulphurets area, the base of the Hazelton Group is represented by granitoid-cobble conglomerate and quartz-rich

arkose of the Jack Formation. The overlying rocks are assigned to the Betty Creek Formation (Nelson et al., 2018), consisting mainly of the Unuk River Formation andesite unit, the lowest part of which (andesitic pyroclastic and epiclastic deposits) may correlate with the Hazelton Group volcanic succession at Kinskuch Lake. The upper Hazelton Group in the Sulphurets area (Pliensbachian to Bajocian) includes sedimentary strata of the Spatsizi Formation and bimodal, rift-related volcano-sedimentary rocks of the Iskut River Formation (Gagnon et al., 2012; Nelson et al., 2018).

The Middle Jurassic to mid-Cretaceous sedimentary rocks of the Bowser Lake Group (Evenchick et al., 2007) occupy a large area of the central Stikine terrane east of the Sulphurets area.

During the mid-Cretaceous, strata of the Stuhini, Hazelton and Bowser Lake groups were deformed as part of the sinistral-transpressive Skeena fold-and-thrust belt

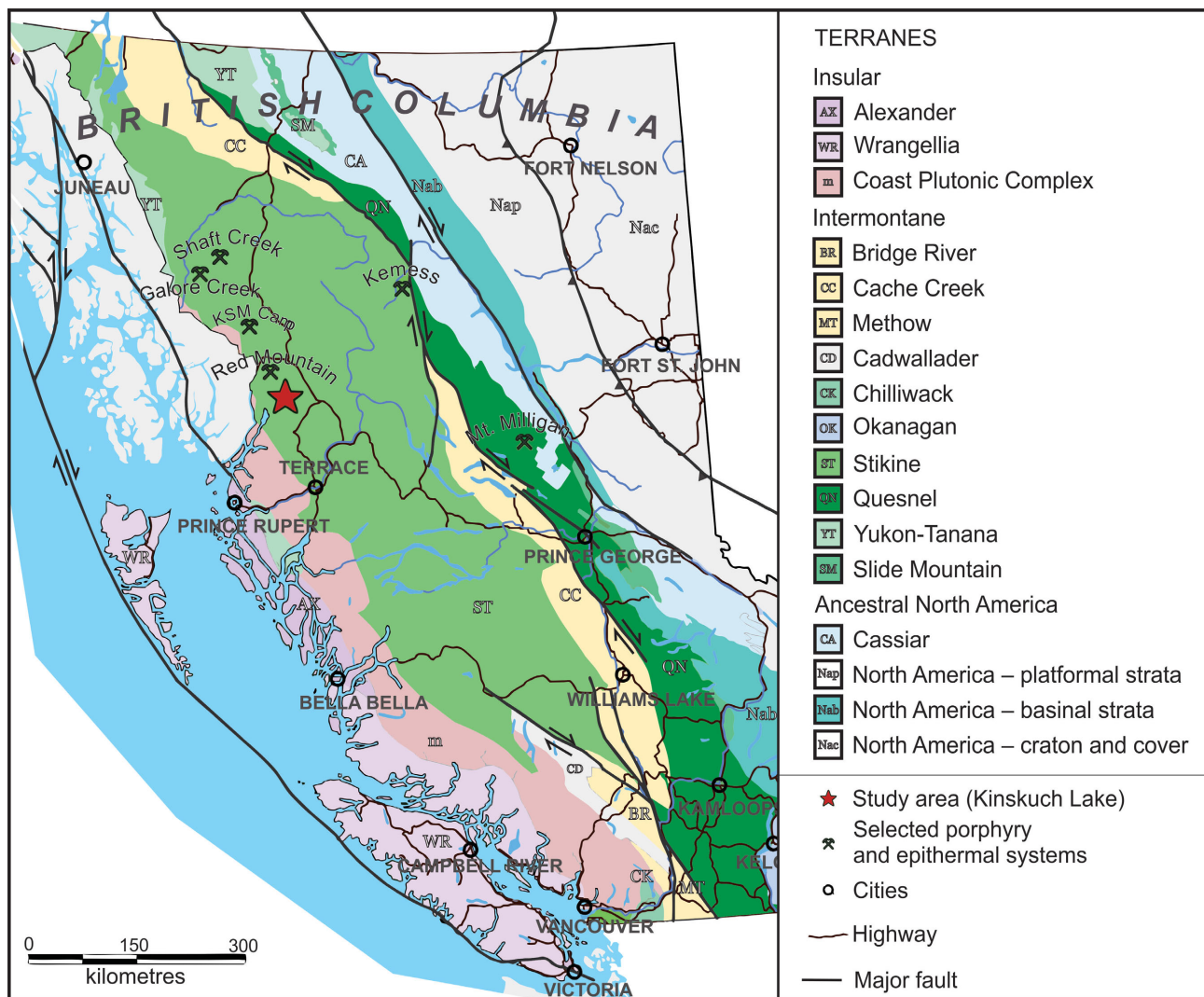


Figure 1: Location of the Kinskuch Lake study area, showing the terranes of British Columbia (Colpron and Nelson, 2011), the KSM project and selected porphyry and epithermal prospects and deposits.

(Evenchick et al., 2007). This resulted in the formation of northwest- and northeast-trending folds and sinistral shear zones.

Fieldwork and Preliminary Observations

The Kinskuch Lake area is underlain by Stuhini Group and Hazelton Group rocks but also includes an intervening transitional unit and a dioritic to monzonitic stock that hosts the Big Bulk Cu-Au porphyry system (Figure 2). The field area is cut by numerous faults and well-bedded rocks (mainly from the Stuhini Group) that are deformed by two generations of folds. Regional metamorphic grade is sub-greenschist.

Three weeks were spent at Kinskuch Lake in July 2018, mapping stratigraphy and structural geology at 1:20 000 scale. Fieldwork goals were to create several stratigraphic sections across the field area, paying attention to changes in the type of sedimentation (i.e., low-energy deposits versus high-energy deposits), bedding orientations, and fold and fault orientations and kinematics. Based on this fieldwork, the Stuhini and Hazelton groups are subdivided into lithostratigraphic units, which are in turn subdivided into facies. The preliminary map presented in Figure 2 shows

the divisions down to the unit level, whereas the descriptions and stratigraphic section (Figure 3) depict the generalized distribution of facies within these units. Stratigraphic subdivisions and lithological descriptions presented here are preliminary and may be revised with further study.

Stuhini Group (uTrS)

The oldest rocks within the study area are part of the Stuhini Group and are subdivided into a volcanic and volcanic-derived sedimentary rock unit (uTrSv) and a sedimentary rock unit (uTrSs).

Volcanic and Volcanic-Derived Sedimentary Rock Unit (uTrSv)

The Stuhini Group volcanic and volcanic-derived sedimentary rock unit is the lowest stratigraphic unit in the Kinskuch Lake area. The lower part of this unit is typified by well-stratified, mafic volcanic clast-bearing conglomerate to volcanic-derived, sandstone interstratified with lesser mafic volcanic breccia (uTrSvs). These are overlain by mafic volcanic breccia (uTrSvbx) with rare interstratified volcanic-derived sandstone and minor augite-phyrlic coherent mafic rocks (uTrSvb).

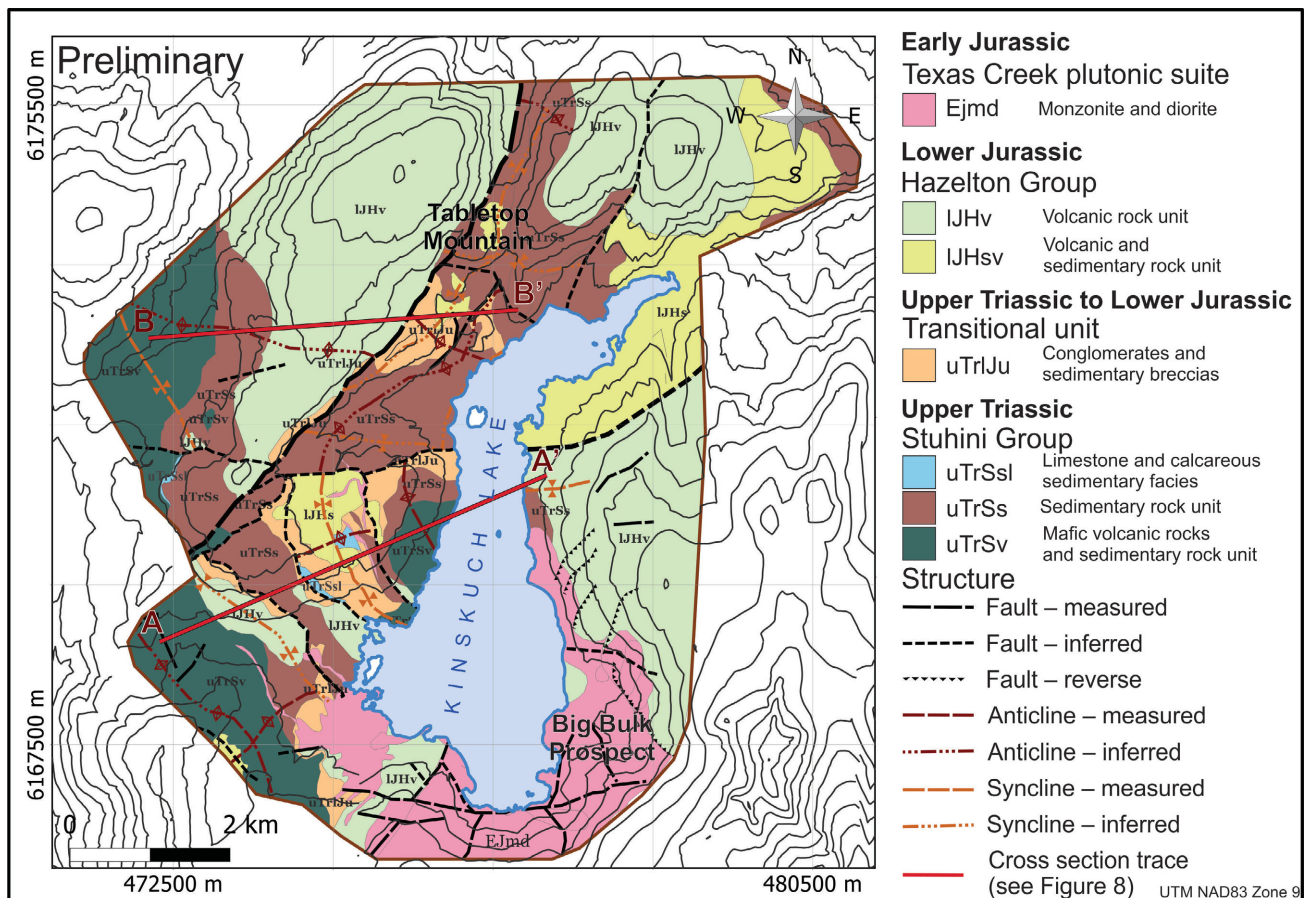


Figure 2. Preliminary geological interpretation for the Kinskuch Lake area, northwestern British Columbia, based on mapping completed in 2018, location of Big Bulk porphyry mineralization, referenced geographic features (including Kinskuch Lake and Tabletop Mountain) and cross-section traces for the schematic sections presented in Figure 8.

Volcanic Breccia and Volcanic-Derived Sedimentary Facies (uTrSvs)

This facies is characterized by grey to green weathering, rhythmically bedded, mafic volcanic-derived sedimentary rocks (Figure 4a). It typically forms 10–20 m thick, fining-upward sequences progressing from basal clast- to matrix-supported pebble conglomerate (with 30–70% round augite-phyric volcanic clasts in an augite crystal-bearing sandy matrix) to sandstone to siltstone. Generally, each fin-

ing-upward sequence is underlain by the volcanic breccia as described in facies uTrSvbx (Figure 4b).

Volcanic Breccia Facies (uTrSvbx)

This is a monomictic volcanic breccia with 30–70% clast- to matrix-supported, subangular to angular volcanic clasts (1–40 cm). The volcanic clasts contain 10–40% blocky augite phenocrysts (2–5 mm, locally up to 8 mm in diameter), up to 15% feldspar phenocrysts (1–4 mm in diameter)

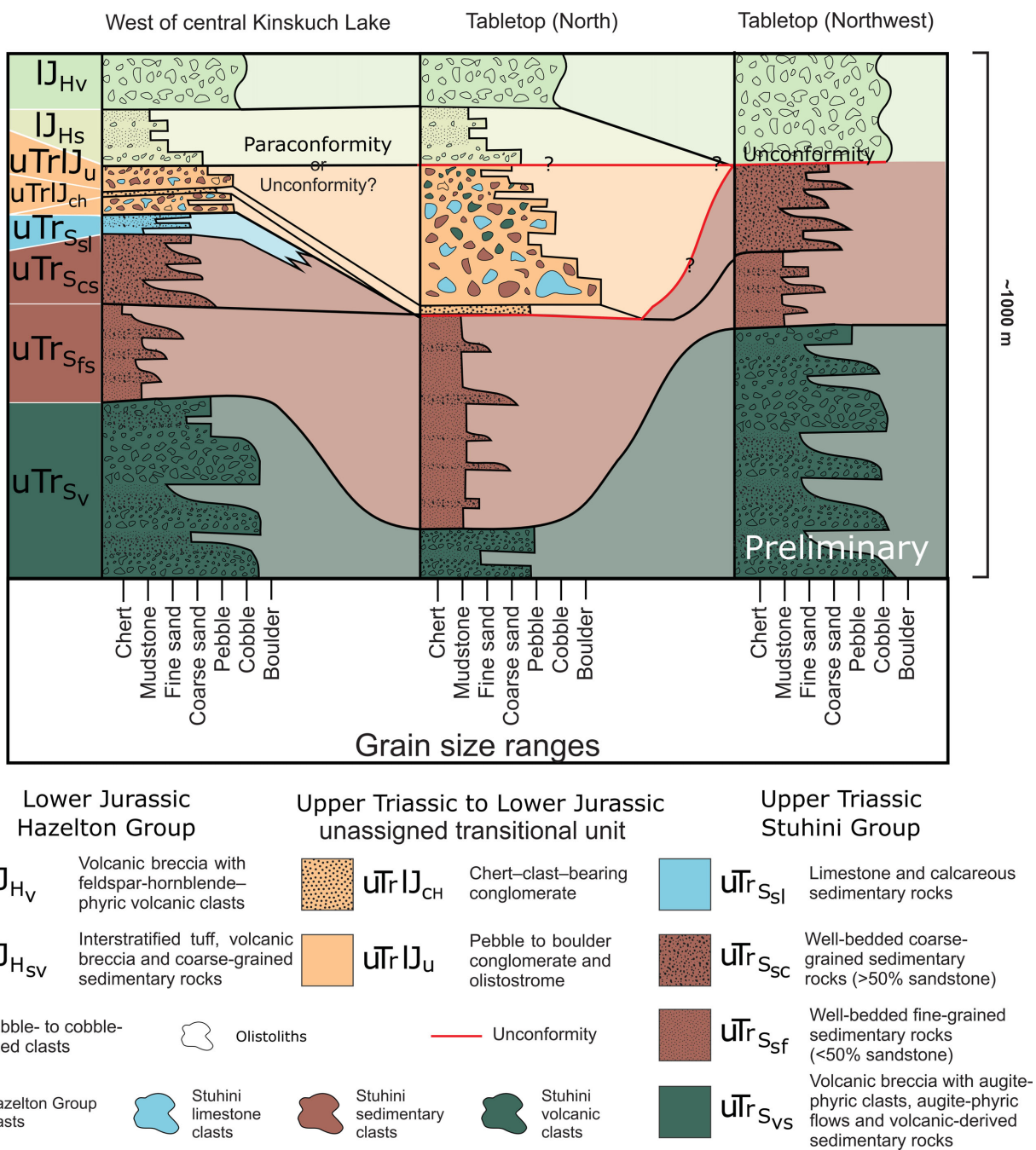


Figure 3. Preliminary Kinskuch Lake area schematic stratigraphic columns, showing the stratigraphic variation from just west of central Kinskuch Lake across Tabletop Mountain to the north and to the far west of the study area, west of Tabletop Mountain.

and up to 5% calcite-filled amygdules (1–3 mm in diameter) set in a dark green to black aphanitic groundmass. The matrix is fine-grained and mafic, with 10–40% euhedral augite crystals (2–5 mm in diameter) and is dark green to grey weathering, dark green to black on fresh surfaces (Figure 4b). The breccia also contains rare interstratified sandstone beds.

Augite-Phyric Coherent Mafic Facies (uTrSvb)

These green to black mafic coherent rocks contain 20–30% augite phenocrysts (2–4 mm, locally 5–8 mm) and up to 5% calcite-filled amygdules (1–3 mm). This facies was only observed in the southwestern portion of the map as massive, 1–5 m thick, bedding-parallel layers within dominantly mafic volcanic breccia, and it may represent flows or sills.

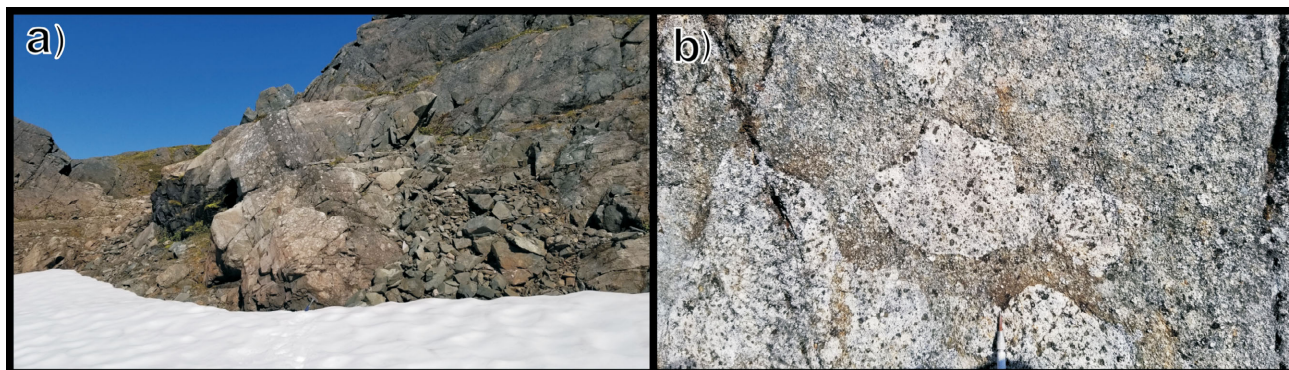


Figure 4. Stuhini Group volcanic and volcanic-derived sedimentary rocks in the study area: **a)** well-stratified volcanic breccia and volcanic-derived sedimentary rocks (uTrSvs; UTM NAD83 Zone 9, 472194E, 6172116N; looking west); **b)** volcanic breccia with angular augite-phyric clasts (uTrSvbx; 473840E, 6168792N).

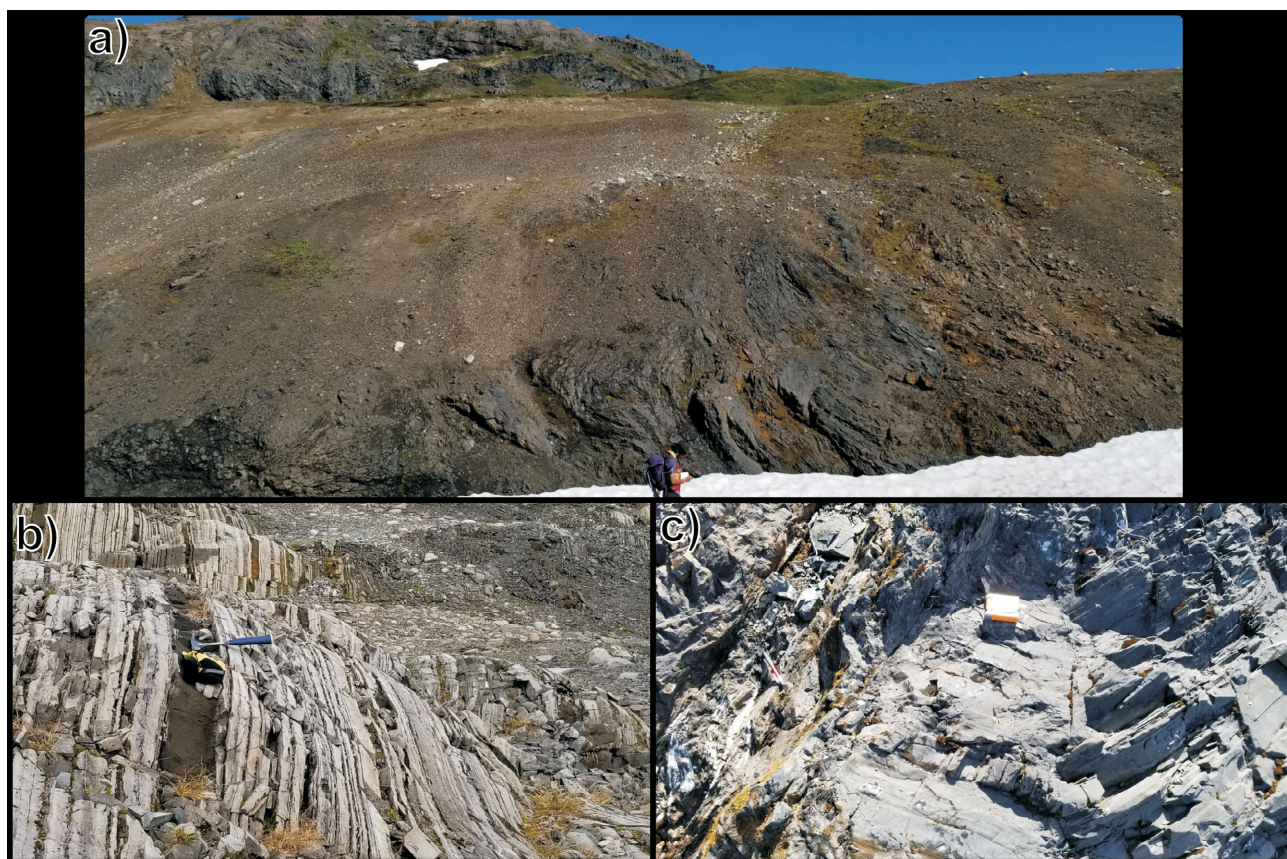


Figure 5. Stuhini Group sedimentary rocks in the study area: **a)** strongly deformed, well-stratified fine-grained sedimentary rocks (uTrSsf) underlying coarser cliff-forming sedimentary rocks in background (uTrSsc; UTM NAD83 Zone 9, 475930E, 6173794N; photo taken facing east); **b)** well stratified, coarse-grained sedimentary rocks (uTrSsc), white weathering feldspathic sandstone interbedded with black recessively weathering argillite (475014E, 6169985N; photo taken facing north); and **c)** a fault-related fold hinge in grey weathering calcareous siltstone to sandstone (uTrSsl) showing carbonate vein fill in fault (476883E, 6170665N; photo taken looking east).

Sedimentary Rock Unit (uTrSs)

Stuhini Group sedimentary rock unit includes interstratified argillite, chert, feldspathic sandstone, conglomerate, limestone and calcareous sandstone and siltstone. Quartz is absent in all rock types. The exact stratigraphic superposition varies across the area, but generally follows the following pattern: basal augite-phyric volcanic clast-bearing conglomerate facies (uTrSsac), overlain by well-bedded, predominantly fine-grained sedimentary facies (uTrSsf), grading upward into a package of similar, but predominantly coarser grained sedimentary facies

(uTrSsc), which is capped by limestone and calcareous sedimentary facies (uTrSsl). A stratified chert facies (uTrSsch) occurs locally, generally near the top of the well-bedded sedimentary rocks (uTrSsf).

Heterolithic Conglomerate Facies (uTrSsac)

A thin massive conglomerate, just a few metres thick, is locally observed at the base of the Stuhini Group sedimentary unit, directly overlying the volcanic unit. It is a heterolithic pebble to cobble conglomerate, predominantly clast supported, with rounded to angular, augite-phyric volcanic



Figure 6. Conglomerates from the unassigned transitional unit (uTrJ): **a)** mafic volcanic clast-bearing conglomerate (uTrJJa; UTM NAD83 Zone 9, 476579E, 6172416N); **b)** heterolithic conglomerate (uTrJh; 475243E, 6172200N); **c)** sandstone and limestone clast-bearing conglomerate (uTrJc; 476017E, 6172826N); **d)** fragment from a 50 m diameter fossiliferous limestone sampled at 476579E, 6172416N (uTrJc); **e)** angular chert-clast-bearing sedimentary breccia (uTrJch; 475695E, 6179268N).

clasts, sandstone clasts and bedded sedimentary clasts, in a fine-grained feldspathic sandstone matrix.

Fine-Grained Sedimentary Facies (uTrSsf)

Fine-grained sedimentary rocks of the Stuhini Group exhibit black to dark grey to orange weathering (dark grey on fresh surfaces). This sedimentary facies is composed of >50% well-bedded argillite to mudstone (locally graphitic) interbedded with lesser siltstone and very fine to fine-grained sandstone and minor medium-grained sandstone. Rare (<5%) coarse-grained sandstone and pebbly sandstone was seen in the coarse-grained sedimentary facies (uTrSsc). Bed thicknesses are variable, but predominantly very thin to medium (<1–20 cm). The fine-grained sedimentary rocks often display metre- to decimetre-scale tight folds and it is likely that this package has, at least locally, been structurally thickened (Figure 5a).

Stratified Chert Facies (uTrSch)

The stratified chert is distinctive but only observed at two localities in the study area: in the sedimentary unit near the central-west shore of Kinskuch Lake, and directly underlying coarse-grained sedimentary facies under Tabletop Mountain to the northwest of Kinskuch Lake. The chert is grey and distinctly glassy in appearance, is stratified on a millimetre to centimetre scale and is occasionally interstratified with mudstone and siltstone. It is generally fractured, faulted and boudinaged, suggesting that the chert was a relatively strong package during deformation.

Coarse-Grained Sedimentary Facies (uTrSsc)

The coarse-grained sedimentary facies is predominantly dark grey and weathers to variable shades of buff, orange and grey. It comprises >50% well-bedded siltstone, lithic sandstone, feldspathic sandstone and pebbly sandstone, with <50% argillite and mudstone (Figure 5b). These sequences show normal grading with load structures and crossbedding observed locally. Bed thickness varies from very thin to thin bedded (2–10 cm) to locally medium bedded (up to 30 cm). Pebbly sandstone is generally matrix supported with 3–10% angular and often ‘flame-like’ argillite clasts (3 to 5 mm), likely derived from unconsolidated Stuhini Group argillite. In general, this sedimentary facies represents increasing proportions of higher energy sediment influx compared to the underlying fine-grained sedimentary facies (uTrSsf) but is otherwise very similar in character and composition.

Limestone and Calcareous Sedimentary Facies (uTrSsl)

The limestone and calcareous sedimentary rocks weather pale to medium grey with a distinctive recessive to pitted chalky weathering surface (Figure 5c). The limestone is generally massive and is commonly fossiliferous. It is interbedded with, and overlain by, medium- to fine-grained, very thin to thin-bedded calcareous sandstone and siltstone. The limestone and calcareous sedimentary facies is only observed locally within the area and has limited along-strike continuity; it is unclear how much of this is due

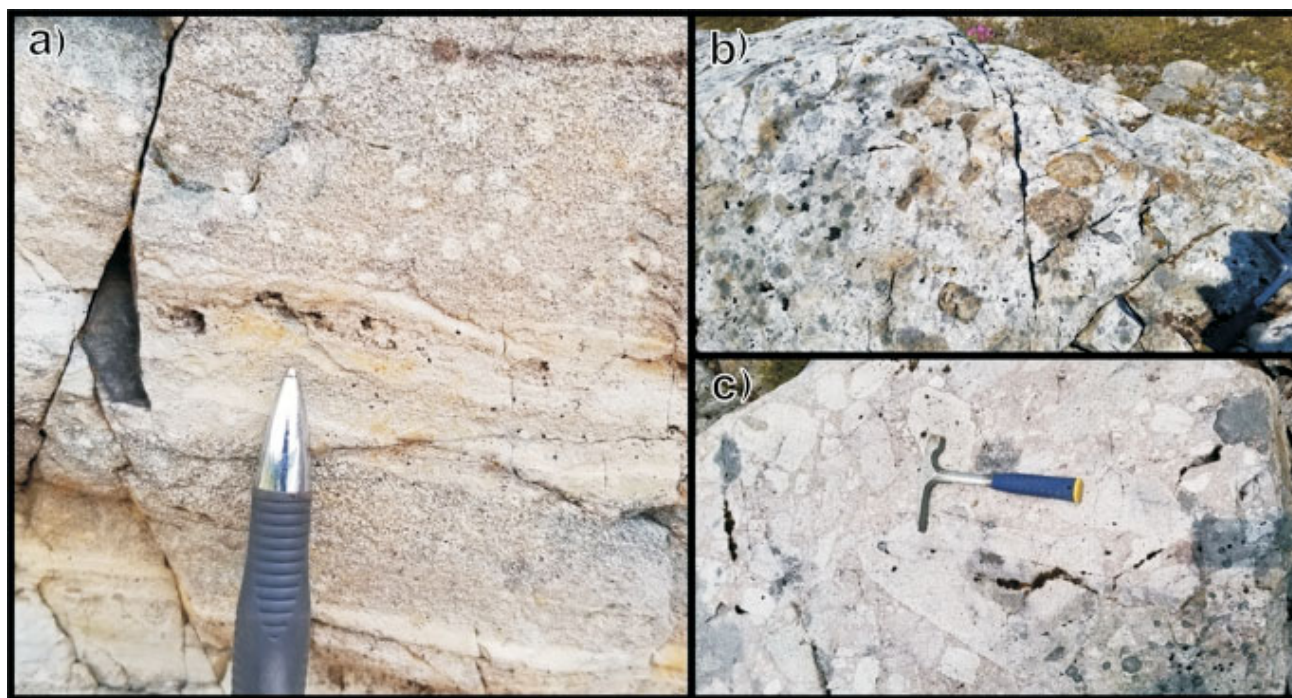
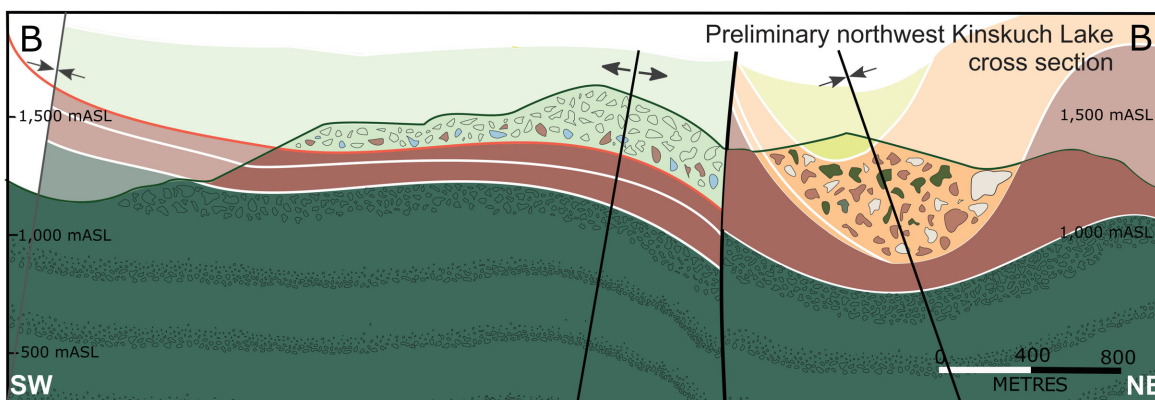
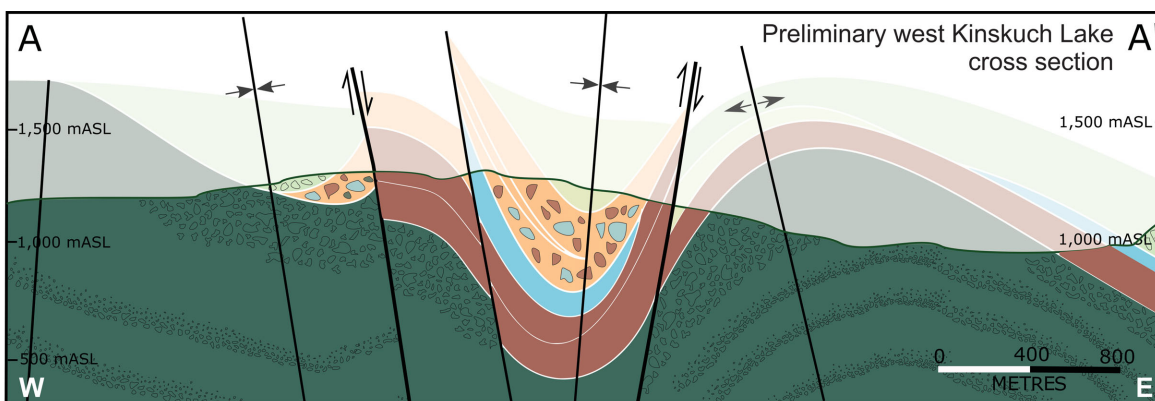


Figure 7. Hazelton Group volcanic and sedimentary rocks: **a)** interbedded sandstone, siltstone and feldspar-crystal tuff (IJHsvt; UTM NAD83 Zone 9, 477193E, 6171770N; photo taken looking northwest); **b)** volcanic breccia containing significant Stuhini Group sedimentary clasts (IJHvh; 474381E, 6169968N); **c)** monomictic volcanic breccia (IJHvbx) with angular ‘jigsaw’ poorly sorted juvenile pebble to cobble clasts (475626E, 6173255N).



Lower Jurassic Hazelton Group

- IJ_{HV} Volcanic breccia with feldspar-hornblende-phyric volcanic clasts
- IJ_{HSV} Interstratified tuff, volcanic breccia and coarse-grained sedimentary rocks
- Pebble- to cobble-sized clasts
- Hazelton Group clasts

Upper Triassic to Lower Jurassic unassigned transitional unit

- uTr_IJ_{CH} Chert-clast-bearing conglomerate
- uTr_IJ_U Pebble to boulder conglomerate and olistostrome
- Olistoliths
- Stuhini limestone clasts
- Stuhini sedimentary clasts
- Stuhini volcanic clasts

Upper Triassic Stuhini Group

- uTr_SSl Limestone and calcareous sedimentary rocks
- uTr_SSC Well-bedded coarse-grained sedimentary rocks (>50% sandstone)
- uTr_SSf Well-bedded fine-grained sedimentary rocks (<50% sandstone)
- uTr_SVS Volcanic breccia with augite-phyric clasts, augite-phyric flows and volcanic-derived sedimentary rocks

- Unconformity
- Faults
- Anticline trace
- Syncline trace

Figure 8. Preliminary schematic cross sections for traces A-A' and B-B' in Figure 2. Cross section A-A' is orthogonal to F₁ folds and north-trending faulting. It shows the apparent thinning of the Stuhini Group limestone unit and coarse-sediment unit. Cross section B-B' is somewhat oblique to the trends, displaying the broad F₂ folds in the southwestern portion of the section and a tighter F₁ syncline in the north-eastern portion of the section.

to lateral facies changes, postdepositional erosion and/or subsequent deformation.

Stuhini Group or Hazelton Group (uTrIJ)

Transitional Unit (uTrIJu)

Rocks of the transitional unit are not currently assigned to either the Stuhini Group or the Hazelton Group. The transi-

tional unit consists of pebbly sandstone, conglomerate and olistostromal deposits with cobbles, boulders and olistoliths up to at least 50 m in diameter.

The transitional unit is composed of four conglomerate facies differentiated primarily based on dominant clast composition; contacts appear to be gradational. They show significant lateral and vertical variability in matrix

composition, clast size and clast angularity. Particularly where this unit is thick (e.g., below Tabletop Mountain), there are local sandstone-filled, crossbedded channels ranging from 20 cm up to 2 m in width cutting the mostly massive, poorly sorted conglomerate facies.

Mafic Volcanic Clast-Bearing Conglomerate Facies (uTrIJa)

This facies is a pebble to cobble to rare boulder conglomerate with subrounded, predominantly augite-phyric clasts and lesser limestone and other sedimentary clasts in a feldspathic to lithic sandstone matrix (Figure 6a). Within this conglomerate there are relatively large areas, up to at least 20 m in width and of unknown lateral continuity in size, of mafic volcanic breccia that are difficult to distinguish from the bulk of the conglomerate due to similar weathering characteristics. These may be extremely large clasts or mass flow deposits intercalated with the conglomerate.

Heterolithic Conglomerate Facies (uTrIJh)

A very poorly to poorly sorted heterolithic pebble, cobble to rare boulder conglomerate, this facies includes clasts up to 40 cm in diameter. Matrix- to locally clast-supported, this conglomerate contains 40–70% subrounded to angular sandstone, limestone, augite-phyric volcanic, feldspar-phyric volcanic, mudstone, bedded sedimentary and maroon rare aphanitic clasts in a feldspathic to lithic sandstone matrix (Figure 6b). Relative proportions of rock types of the clasts are highly variable, but sandstone, limestone and augite-phyric volcanic clasts typically predominate.

Sandstone Clast-Bearing Conglomerate Facies (uTrIJs)

A very poorly sorted pebble, cobble to rare boulder conglomerate includes clasts averaging 5–10 cm, but with limestone olistoliths up to 50 m in diameter in some localities. Clast- to matrix-supported, this conglomerate has 40–75% subrounded to subangular sandstone clasts and subordinate limestone, argillite and mudstone clasts, in a variably feldspathic to lithic sandstone matrix (Figure 6c). Locally, this facies is olistostromal with limestone boulders and olistoliths up to 50 m in diameter; this limestone is often fossiliferous (Figure 6d). Most sandstone clasts are composed of feldspathic to lithic sandstone of similar composition to the matrix, but some contain significant augite. At a single outcrop, below Tabletop Mountain, a large portion (~30%) of the sandstone clasts contain detrital biotite.

Chert-Clast-Bearing Conglomerate to Sedimentary Breccia Facies (uTrIJch)

The chert-clast-bearing conglomerate to sedimentary breccia is a generally poorly sorted, clast-supported heterolithic pebble (0.5–5 cm) conglomerate containing 5–20% angular grey chert fragments (Figure 6e). The chert is accompanied by clasts derived from the Stuhini Group sedimentary

unit, including thinly bedded argillite (uTrSsf), sandstone, siltstone and granule to pebble conglomerate (uTrSsc). Rounding is variable, from subrounded to angular, with argillite generally showing more rounding than the more resistant fragments. The matrix of the conglomerate is a fine-grained feldspathic sandstone to siltstone.

Hazelton Group (IJH)

The Hazelton Group at Kinskuch Lake comprises a volcanic and sedimentary unit (IJHsv), which is overlain by a volcanic unit (IJHv) comprised primarily of volcanic breccia.

Volcanic and Sedimentary Rock Unit (IJHsv)

This unit is composed of roughly equal proportions of sedimentary and volcanic rocks. It is the most variable of the two Hazelton Group units recognized in the area and is not always present at the base of the group. The authors distinguished three facies that are commonly interbedded; any one of these lithological packages can form the base of the Hazelton Group at a given locality. The exact stratigraphic superposition varies across the area, but generally follows the following pattern: basal conglomerate to sedimentary breccia facies (IJHsvcon) or interbedded sandstone and tuff facies (IJHsvt), overlain by well-bedded to locally massive, coarse-grained sandstone and siltstone facies (IJHsvs), capped by conglomerate and sedimentary breccia facies (IJHsvcon).

Heterolithic Conglomerate and Sedimentary Breccia Facies (IJHsvcon)

This unit is primarily a mixture of massive to crudely stratified heterolithic conglomerate containing rounded to subrounded pebbles and rare cobbles of crowded feldspar-hornblende-phyric volcanic rock, sandstone and argillite. It is clast to matrix supported with a feldspathic sandstone matrix. This conglomerate is locally interstratified with more typical massive Hazelton Group monomictic volcanic breccia described below as facies IJHvbx.

Interbedded Sandstone and Tuff Facies (IJHsvt)

This facies includes well-bedded, distinctively pale-weathering siltstone to coarse-grained sandstone (Figure 7a) that may contain up to 5% quartz granules, with significant (up to 40% of the rock volume) very thin to thin interbeds of crystal tuff containing broken angular to euhedral feldspar crystals.

Coarse-Grained Sandstone and Siltstone Facies (IJHsvs)

This is a medium- to coarse-grained sandstone and siltstone that is thin bedded to lesser medium to thick bedded and locally massive with rare mudstone interbeds. It appears similar to Stuhini Group coarse-grained sedimentary rocks (uTrSsc) but is conformably above right-way-up Hazelton

Group conglomerate beds (IJHsvcon) and may contain hornblende crystals or hornblende-phyric clasts (pending petrographic confirmation).

Volcanic Rock Unit (IJHv)

The Hazelton Group volcanic rock unit comprises three facies that occur in a generally predictable sequence as presented below, although interfingering is common and not all facies are present in all stratigraphic sections observed across the study area. The heterolithic volcanic breccia facies, for example, is only observed where the unit of volcanic and sedimentary rocks is thin to absent, and the volcanic unit occurs near the base of the Hazelton Group.

Heterolithic Volcanic Breccia Facies (IJHvh)

The heterolithic volcanic breccia contains clast- to matrix-supported accessory clasts and hornblende-feldspar-phyric juvenile clasts set in a hornblende and feldspar crystal-rich matrix. The accessory clasts include bedded mudstone, sandstone and limestone, likely derived from underlying Stuhini Group rocks (Figure 7b). This lithological package is similar to the monomictic volcanic breccia (IJHvbx) but is differentiated by the presence of accessory clasts.

Feldspar±Hornblende Crystal Tuff and Lapilli Tuff Facies (IJHvt)

Crystal tuff with variable feldspar±hornblende crystal content is observed only locally within the monomictic volcanic breccia facies and is not present across the entire study area. Locally, the tuff closely resembles the matrix of the volcanic breccia and can contain up to 5% lapilli- to block-sized accessory sedimentary fragments, or juvenile clasts similar to those of the monomictic volcanic breccia. This package can be very similar in appearance and weathering character to intrusive rocks in the Big Bulk porphyry system, making differentiation difficult.

Monomictic Volcanic Breccia Facies (IJHvbx)

The predominant rock type of the highest stratigraphic levels of the Hazelton Group throughout the study area is the monomictic volcanic breccia. It is a massive, poorly to very poorly sorted volcanic breccia that has a typically densely packed euhedral to angular hornblende and feldspar crystal-rich matrix with 40–70% hornblende-feldspar-phyric volcanic clasts (Figure 7c). This facies shows significant lateral and vertical variation in both clast size and proportion of clasts to matrix. Clasts range from lapilli to block sized, rarely as large as 10 m.

Intrusive Units

The predominant intrusive unit in the study area is a multiphase stock that hosts the Big Bulk Cu-Au porphyry system in the southern part of the study area. This unit is provisionally correlated with the Early Jurassic Texas Creek Plutonic Suite, and likely represents the intrusive

equivalents of lower Hazelton Group volcanic rocks. Three separate dike sets are also recognized; one is probably related to the Big Bulk stock and the other two may be considerably younger. The complete characterization of the intrusive units awaits petrological, geochemical and geochronological study.

Multiphase Big Bulk Diorite to Monzonite Unit (EJmd)

The multiphase Big Bulk diorite to monzonite can be characterized as hornblende diorite, hornblende monzonite and hornblende-biotite monzonite. It ranges from equigranular to sparsely porphyritic to crowded porphyritic and locally includes intrusive breccia. Porphyritic varieties contain 10–30% lath-shaped plagioclase phenocrysts (1–2 mm), 5–15% acicular hornblende phenocrysts (1–2 mm), locally up to 30% K-feldspar phenocrysts and rarely up to 10% distinctive porphyritic platy biotite books in a predominantly fine-grained (<1 mm) feldspar-hornblende-dominated groundmass ranging from plagioclase dominant to a nearly 1:1 ratio of plagioclase:K-feldspar. Alteration is variable and includes weak sericitization, chlorite alteration, patchy epidote alteration and intense quartz-sericite-pyrite alteration that strongly obscures original textures and composition and displays the local development of significant cleavage associated with folding and imbricate thrust faulting.

Early Jurassic Dioritic Dikes (EJdyk)

Observed extending radially from the Big Bulk stock, these dikes are typically dioritic with 10–30% strongly elongated lath-shaped plagioclase phenocrysts that often show radial ‘flower’ textures and 10–15% acicular hornblende phenocrysts in a fine to very fine grained groundmass of mainly hornblende and plagioclase. They contain up to 3% disseminated pyrite and locally patchy chlorite-epidote replacement of mafic minerals.

Late Dioritic Dikes (E?d)

Texturally and compositionally similar to the Jurassic dikes but lacking alteration and sulphides, these dikes are generally traceable for up to several kilometres of strike length. The age of these dikes is unknown; they could be part of the Eocene Hyder plutonic suite.

Late Mafic Dikes (E?m)

Dark green, recessive weathering aphanitic dikes commonly show chilled margins and/or flow banding along their margins. These dikes are only rarely observed, may be traced for up to 100 m, and occur within east-west-trending, steeply dipping faults. They cut the Big Bulk stock, as well as Stuhini Group and lower Hazelton Group rock units. Locally these dikes contain up to 5% calcite-filled amygdules and appear to be significantly less deformed and altered than surrounding rocks, suggesting that this is one of the youngest rock units represented in the area.

Preliminary Structural Observations

Two generations of folds were observed at Kinskuch Lake, with F_1 trending mainly northerly and F_2 represented by open folds with easterly trending axial traces. Map-scale faults show a similar orthogonal pattern, with north to northeast and west to northwest trends.

Rock type exerts a significant control on structural style, with deformation expressed primarily as faulting in the strong units (i.e., volcanic breccia [JHvbx] and granitoid intrusions [EJmd]) that predominate the east side of Kinskuch Lake, whereas the well-stratified rocks on the west side of the lake display a combination of folds and faults. Furthermore, on the west side of the lake, the fine-grained sedimentary facies locally display abundant metre- to decimetre-scale tight folds, whereas the more competent sandstone facies only display larger-scale folds (>50 m wavelength). Axial planar cleavage occurs only locally, within some of the argillite and in areas of strong phyllic alteration. Overall cleavage is very poorly developed except locally within some of the argillite packages and in areas of strong phyllic alteration.

The preliminary cross-sectional interpretation of the fold and faulting pattern in the west portion of the Kinskuch Lake study area is shown in Figure 8. It illustrates the thinning of several units across the area and shows the contrast between the clearly unconformable contact between Hazelton Group volcanics and Stuhini Group sedimentary rocks in the far west of the study area and displays a potentially paraconformable or conformable contact between Stuhini Group and the conglomerate to olistostromal transitional unit nearer to Kinskuch Lake.

Discussion and Future Work

There is significant variation in stratigraphic architecture within the Stuhini Group and lower Hazelton Group across the field area. These variations could be explained by lateral facies changes, differential erosion levels at the boundary between the Hazelton and Stuhini groups, distance from volcanic vents and sediment sources and/or the effects of synsedimentary faults or other topographic disruption causing localized deposition of higher energy deposits.

The transitional unit represents a dramatic change in sedimentation style from the well-stratified sedimentary rocks that characterize the underlying Stuhini Group. The transitional unit olistostromal deposits and conglomerate may have resulted from basin instability and/or tectonic uplift in the latest Triassic to Early Jurassic and may correlate with similar units observed in the KSM area by Kyba and Nelson (2015) and Febbo (2016).

The next steps in this research include

- compiling a similar preliminary summary of the Red Mountain Au deposit area;
- conducting litho-geochemistry and petrography to accurately characterize the volcanic and intrusive units;
- completing component analysis for accurate characterization and correlation of sedimentary, volcanic-derived sedimentary and volcanic units;
- determining biostratigraphy and isotope geochronology to assess the age, stratigraphic position and provenance of units; and
- analyzing in detail the structural data including petrographic studies.

In addition, in 2019, the Big Bulk area will be mapped at a scale of 1:5000 (or more detailed) to assess the role of imbricate faulting and folding on the distribution of porphyry-related Cu-Au mineralization and better define the emplacement environment and relationship to pre-existing and/or syn-intrusion faults. Also, a palinspastic restoration of conditions prior to Cretaceous deformation will be attempted to more accurately represent the structural environment into which the Cu-Au porphyry system was emplaced.

Acknowledgments

Funding for this research has been generously provided by a Natural Resources Canada—Targeted Geoscience Initiative Grant and a 2018 Geoscience BC scholarship.

This project would not have been possible without the extremely generous in-kind support provided by Dolly Varden Silver Corp., IDM Mining Ltd., Hecla Mining Company and OK2 Minerals.

Special thanks to P. Schiarizza for reviewing and providing an extremely helpful review of and suggestions for this manuscript.

The authors deeply appreciate H. McIntyre's assistance as she generously provided her field descriptions, thoughts and mapping data from work completed at Big Bulk and Red Mountain during the 2017 field season. These have proven to be invaluable both in guiding mapping traverse selection and in supplementing this season's interpretations and map work.

References

- BC Geological Survey (2018): MINFILE BC mineral deposits; BC Ministry of Energy, Mines and Petroleum Resources, BC Geological Survey, URL <<http://minfile.ca/>> [October 2018].
- Campbell, M.E. and Dilles, J.H. (2017): Magmatic history of the Kerr-Sulphurets-Mitchell copper-gold porphyry district, northwestern British Columbia (NTS 104B), in Geoscience BC Summary of Activities 2016, Geoscience BC, Report

- 2017-1, p. 233–244, URL <http://cdn.geosciencebc.com/pdf/SummaryofActivities2016/SoA2016_Campbell.pdf> [October 2018].
- Colpron, M. and Nelson, J. (2011): A digital atlas of terranes for the northern Cordillera; BC Ministry of Energy, Mines and Petroleum Resources, BC Geological Survey, GeoFile 2011-11, URL <<http://www.empr.gov.bc.ca/Mining/Geoscience/PublicationsCatalogue/Geofiles/Pages/2011-11.aspx>> [October 2018].
- Evenchick, C.A., McMechan, M.E., McNicoll, V.J. and Carr, S.D. (2007): A synthesis of the Jurassic-Cretaceous tectonic evolution of the central and southeastern Canadian Cordillera: exploring links across the orogen; Geological Society of America, Special Paper, v. 433, p. 117–145.
- Febbo, G.E. (2016): Structural evolution of the Mitchell Au-Cu-Ag-Mo porphyry deposit, northwestern British Columbia; M.Sc. thesis, Department of Earth, Oceanic and Atmospheric Sciences, The University of British Columbia, 340 p.
- Febbo, G.E., Kennedy, L.A., Savell, M., Creaser, R.A. and Friedman, R.M. (2015): Geology of the Mitchell Au-Cu-Ag-Mo porphyry deposit, northwestern British Columbia, Canada; *in* Geological Fieldwork 2014, BC Ministry of Energy, Mines and Petroleum Resources, BC Geological Survey, Paper 2015-1, p. 59–86, URL <http://www.empr.gov.bc.ca/Mining/Geoscience/PublicationsCatalogue/Fieldwork/Documents/2014/04_Febbo_et_al.pdf> [October 2018].
- Gagnon, J.-F., Barresi, T., Waldron, J.W.F., Nelson, J.L., Poulton, T.P., Cordey, F. and Colpron, M. (2012): Stratigraphy of the upper Hazelton Group and the Jurassic evolution of the Stikine terrane, British Columbia; Canadian Journal of Earth Sciences, v. 49, p. 1027–1052.
- Greig, C.J. (1992): Fieldwork in the Oweegee and Snowslide ranges and Kinskuch Lake area, northwestern British Columbia; *in* Current Research, Part A, Geological Survey of Canada, Cordillera and Pacific Margin, p. 145–156, URL <http://ftp.maps.canada.ca/pub/nrcan_rncan/publications/ess_sst/132/132780/pa_92_1a.pdf> [October 2018].
- Kyba, J. and Nelson, J. (2015): Stratigraphic and tectonic framework of the Khyber-Sericite-Pins mineralized trend, lower Iskut River, northwest British Columbia; *in* Geological Fieldwork 2014, BC Ministry of Energy, Mines and Petroleum Resources, BC Geological Survey, Paper 2015-1, p. 41–58, URL <http://www.empr.gov.bc.ca/Mining/Geoscience/PublicationsCatalogue/Fieldwork/Documents/2014/03_Kyba%20Nelson.pdf> [October 2018].
- Logan, J.M., Drobe, J.R. and McClelland, W.C. (2000): Geology of the Forest Kerr–Mess Creek area, northwestern British Columbia; BC Ministry of Energy, Mines and Petroleum Resources, BC Geological Survey, Bulletin 104, 164 p., URL <<http://www.empr.gov.bc.ca/Mining/Geoscience/PublicationsCatalogue/BulletinInformation/BulletinsAfter1940/Pages/Bulletin104.aspx>> [October 2018].
- Logan, J.M. and Mihalynuk, M.G. (2014): Tectonic controls on early Mesozoic paired alkaline porphyry deposit belts (Cu–Au±Ag–Pt–Pd–Mo) within the Canadian Cordillera; Economic Geology, v. 109, p. 827–858.
- Nelson, J.L., Colpron, M. and Israel, S. (2013): The Cordillera of British Columbia, Yukon, and Alaska: Tectonics and Metallogeny; Society of Economic Geologists, Special Publication, v. 17, p. 53–109.
- Nelson, J. and Kyba, J. (2014): Structural and stratigraphic control of porphyry and related mineralization in the Treaty Glacier–KSM–Brucejack–Stewart trend of western Stikinia; *in* Geological Fieldwork 2013, BC Ministry of Energy, Mines and Petroleum Resources, BC Geological Survey, Paper 2014-1, p. 111–140, URL <http://www.empr.gov.bc.ca/Mining/Geoscience/PublicationsCatalogue/Fieldwork/Documents/2013/07_Nelson_Kyba.pdf> [October 2018].
- Nelson, J., Waldron, J., van Straaten, B., Zagorevski, A. and Rees, C. (2018): Revised stratigraphy of the Hazelton Group in the Iskut River region, northwestern British Columbia; *in* Geological Fieldwork 2017, BC Ministry of Energy, Mines and Petroleum Resources, BC Geological Survey, Paper 2018-1, p. 15–38, URL <http://www.empr.gov.bc.ca/Mining/Geoscience/PublicationsCatalogue/Fieldwork/Documents/2017/02Nelson_et_al.pdf> [October 2018].
- Sillitoe, R.H. (2010): Porphyry copper systems; Economic Geology, v. 105, p. 3–41.
- van Straaten, B.I. and Nelson, J. (2016): Kitsault – Red Mountain (KRM): following the Early Jurassic Texas Creek metallogenic epoch southward; Mineral Exploration Roundup, Vancouver, BC, January 27, 2016, presentation.

Producing Clean Coal from Western Canadian Coalfields Using the Water-Based Roben Jig Process: Refining the Process

M.L. Mackay, Trillium Geoscience Ltd., mmackay@trilliumgeoscience.com

L. Giroux, Natural Resources Canada, CanmetENERGY, Ottawa, ON

R.L. Leeder, Leeder Consulting Inc., Surrey, BC

H. Dexter, GWIL Industries–Birtley Coal & Minerals Testing Division, Calgary, AB

J. Halko, Teck Coal Ltd., Calgary, AB

M. Holuszko, The University of British Columbia, Vancouver, BC

D. Thomas, CWA Engineers, Vancouver, BC

Mackay, M.L., Giroux, L., Leeder, R.L., Dexter, H., Halko, J., Holuszko, M. and Thomas, D. (2019): Producing clean coal from western Canadian coalfields using the water-based Roben Jig process: refining the process; *in* Geoscience BC Summary of Activities 2018: Minerals and Mining, Geoscience BC, Report 2019-1, p. 87–100.

Introduction

There are a number of coalfields in British Columbia (BC): several thermal coalfields and two major metallurgical coalfields, the Kootenay and Peace River (Figure 1). Metallurgical coals are destined mainly for use in commercial coke ovens to produce coke for use in blast furnaces in steelworks.

One of the main challenges after finding and identifying coal seams is evaluating the quality of the coal resource during the exploration stage. Understanding coal quality can be a complex process and is key to a sound economic evaluation of the resource. During the exploration phase of coal-mine development, evaluation of metallurgical-coal quality is often done using samples collected from drillcore. Although many coal seams outcrop, the bulk of the coal deposit is generally deep underground. Coal near the surface can be sampled using test pits or adits, but drilling is the method most often used to obtain representative coal-seam samples. During the feasibility stage of an exploration property, a bulk sample of more than a tonne is required for testing the coal in a pilot-scale coke oven to fully understand the coking potential of the coal. Sufficient sample can be obtained using several 6-inch drill-program cores, although this is costly, particularly for thinner seams.

Coal samples collected during exploration are prepared by screening and then lab-scale or pilot-scale washing that simulates the coal behaviour in commercial coking coal-wash plants. The coarser sized coal is processed using mixtures of organic liquids and the finer fraction is cleaned by a



Figure 1. Location of coalfields in southeastern British Columbia from which the coal samples used in this study originated.

process called froth flotation. The quality of the coal produced by these smaller scale washing methods is critical to understand the market potential of the coal. These processes must produce the same quality coal as a commercial plant.

On the lab scale, the float-and-sink procedure (Figure 2) is used to separate coal from dirt, rock and mineral matter using a density separation, the same process used in commercial plants. The lower density solutions tend to float mainly the coal. During the float-and-sink process, the coal sample is separated at relative densities (specific gravities, sg) between roughly 1.40 and 1.80 using tanks of organic mixtures made from white spirit (1.40 sg), perchloroethylene (PCE; 1.60 sg) and methylene bromide (1.80 sg; ASTM

This publication is also available, free of charge, as colour digital files in Adobe Acrobat® PDF format from the Geoscience BC website: <http://www.geosciencebc.com/s/SummaryofActivities.asp>.

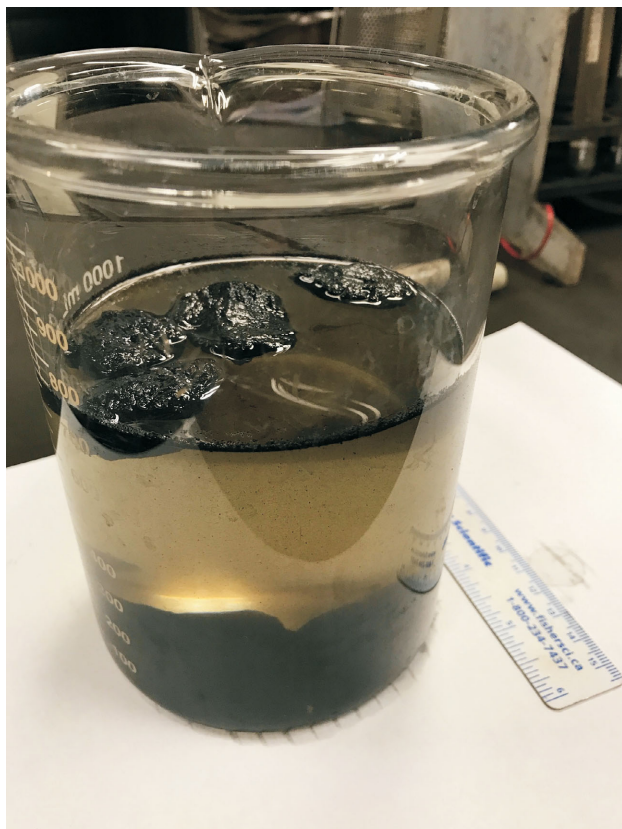


Figure 2. Coal particles floating in perchloroethylene.

D4371-06, 2012). This produces clean-coal samples at the target ash, sulphur and calorific content typical of what would be produced in a commercial coal-washing plant.

Commercial plants separate the coal into size fractions that are processed in equipment that separates the coal from waste (rock, dirt and minerals) using differences in density—coal being less dense than the waste. The equipment uses water-magnetite mixtures of controlled density in cyclones and baths, centrifugal force for coal-water mixtures



Figure 3. Operator working with organic liquids in a specially designed fume hood.

in cyclones, and relative settling rates of the coal particles of differing densities in water to isolate/separate the ‘clean’ coal in jigs and settling tanks. The finest sizes are treated by water-based froth flotation, which can ‘float’ the coal from the waste. Exploration samples are treated/cleaned in a similar fashion.

Project economics are based on the results of the float-and-sink testing, which produces information on the yield of clean coal as well as the quality of the cleaned coal and resulting coke quality. The coking characteristics, in particular, for a metallurgical coal deposit are critical in evaluating project economics (i.e., expected price for the clean coal). It is important to ensure that coal/coking properties are correctly assessed from drillcore samples to properly evaluate project economics.

Background

For years, a major concern in the handling and use of organic liquids such as perchloroethylene (PCE) was the safety risks associated with human exposure. Perchloroethylene is a known carcinogen and poses a safety hazard for laboratory operators, so it must be handled carefully. Figure 3 shows a laboratory technician working in a specially designed fume hood wearing personal protective equipment, including a respirator mask.

In addition to the health issues, there are increasing concerns about whether the solvents impact the quality of coking coal. Many Canadian geologists have found that cleaned drillcore coal samples often had lower caking/coking properties than bulk or production coal samples, an observation that goes back many decades. A number of investigations looked at how PCE and other organic solvents may impact the coking quality of coal samples, including Australian and American work (DuBroff et al., 1985; Campbell, 2010; Iveson and Galvin, 2010, 2012). These studies found that there were different impacts depending on the quality characteristics of the coal being assessed. Coals similar to the western Canadian coking coals (higher inert, lower thermal rheological coals) appeared to have been negatively impacted.

Based on these observations, the Canadian Carbonization Research Association (CCRA) undertook a preliminary program to investigate the impact of the organic solvents used in float-and-sink procedures on the coal and coke properties of a higher inert, low-fluidity western Canadian coal sample (Holuszko et al., 2017). This study looked at the effects of perchloroethylene on coal rheology and coke quality. It was found that an 80% decrease (relative to the control sample) in Gieseler maximum fluidity occurred in the perchloroethylene-treated coal immediately following treatment. The coke resulting from the treated sample showed a 16-point decrease in coke strength after reaction (CSR) when compared to the control sample. These two

coal- and coke-quality parameters are key when evaluating coal resources and reserves. The ramifications of using the wrong numbers for these parameters when determining the characteristics of product for sale are severe and could result in unwarranted project abandonment or false overvaluing of the property.

After the initial study outlined above, the CCRA also completed an exploratory study that examined an alternative to organic liquids by washing coal samples in a jig. A lab-scale Roben Jig (Figures 4, 5) was used to clean several coals using only water, and the resulting quality characteristics of the clean coal and its coke were compared to those of coal that was processed using the traditional process of washing with organic chemicals.

It was found that it was possible to produce a clean-coal product with quality properties very similar to those obtained using the organic liquids. The Roben Jig-cleaned coals had the same/similar results for coal-quality parameters and better results for coal-rheology parameters. These findings are important because they demonstrate that the Roben Jig can be used to produce clean-coal composites similar to those obtained from traditional float-and-sink methods.

Objectives

The objective of this project was to revise the existing operating methodology for the Roben Jig in order to minimize misplaced material (Mackay et al., 2018). Another goal was to answer the following questions:

- At what apparent relative density is misplacement of coal particles occurring?
- What are the characteristics of the misplaced coal particles?
- What is the preferred method of operating the Roben Jig?
- How does the Roben Jig compare to an industrial processing plant?
- How many coal types need to be tested so that results are statistically significant?
- How is the perchloroethylene interacting and affecting the coal chemistry to cause a reduction in rheology and an increase in Hardgrove Grindability Index?

If successful, this project would benefit the coal industry by eliminating of use of PCEs and other organic liquids in the production of small-mass exploration samples for the determination of coal- and coke-quality parameters, and reduce the exposure of lab technicians/operators to carcinogenic organic liquids.



Figure 4. Roben Jig equipment used in this study.



Figure 5. Inverted Roben Jig with coal slice to be removed.

Experimental Washing Methodology

The research group devised two Roben Jig methodologies that could yield products with lower ash content while minimizing misplaced coal and rock particles. These methodologies were compared to the original coal-washing methodologies from the Phase 1 research (Mackay et al., 2018). The clean coals from all processes were then compared to the product from an industrial coal-washing plant.

The coarse coal particles in each sample (greater than 0.50 mm) were washed during this study in several different ways:

- Raw coal was washed in an industrial coal-washing plant.
- Raw coal was segregated into one coarse fraction (12.5 × 0.5 mm) and washed in organic liquids using the float-and-sink method and following the ASTM D4371 standard (Phase 1 Method: Float-and-Sink, One Coarse Fraction)
- Raw coal was segregated into one coarse fraction (12.5 × 0.5 mm) and washed in the Roben Jig (Phase 1 Method: Roben Jig, One Coarse Fraction)
- Clean coal resulting from the jiggling of one coarse fraction was then rejigged (New Method A: Re-Jiggling).
- Raw coal was segregated into two coarse fractions (12.5 × 2 mm and 2 × 0.5 mm) and washed in organic liquids using the float-and-sink method and following the ASTM D4371 standard (New Method B: Float-and-Sink, Two Coarse Fractions).
- Raw coal was segregated into two coarse fractions (12.5 × 2 mm and 2 × 0.5 mm) and washed using the Roben Jig (New Method C: Roben Jig, Two Coarse Fractions).

Common to all methodologies, the fine coal (particle sizes of less than 0.5 mm) was washed using the froth flotation method (ASTM D5114-90(2010)). The clean coal resulting from this method was recombined with the coarser coal (greater than 0.5 mm) when creating clean-coal composite samples.

Industrial Coal-Washing Plant Method

This research project had a unique opportunity to piggy-back on a single-seam run at an operating industrial-processing plant at a mine in southeastern BC. Mine operations seldom schedule ‘single-seam’ runs unless it is part of the natural release of coal from the mine plan; it is more usual to see many seams being processed through the plant together. The ability to be able to compare laboratory-washed coal to that cleaned in an industrial-sized wash plant is considered the gold standard in validating a laboratory method for washing coal. As much as possible, companies want to be able to predict the actual clean-coal product that will be delivered from a mine’s washing plant. As the single seam was being run through the plant, raw coal was collected

from the ‘feed’ side of the plant. This coal was used in the laboratory processing by organic liquids and the Roben Jig. Clean coal was also collected from the plant and analyzed for clean-coal quality and coke quality. Industrial-sized processing plants do not achieve perfect separation, and material is misplaced. A simple float-and-sink using organic liquids was also done to determine where the misplaced particles originated.

Phase 1 Method: Float-and-Sink, One Coarse Fraction

The specific gravity of a coal particle is dependent on mineral-matter content and maceral composition. Coal particles containing the lowest amount of mineral matter will float when separated in a 1.30 sg liquid, whereas those with the highest mineral-matter content are separated at 1.80 sg.

The float-and-sink method (ASTM D4371-06, 2012) was used in this project. This technique fractionates coal and mineral-matter particles based on particle density by allowing particles to settle in organic-liquid mixtures with known specific gravities. Mixtures of white spirits, perchloroethylene and methylene bromide are used to produce media densities ranging from 1.30 sg to 1.80 sg.

Phase 1 Method: Roben Jig, One Coarse Fraction

The Roben Jig is a device that enables the sorting of coal particles based on density to occur as the coal is jiggled up and down in a column of water. Although no published standard (ASTM, ISO or Australian) exists for the use of the Roben Jig, the following procedure was developed by the inventor. Approximately 15 kg of 12.5 mm × 0.25 mm coal and tracers (glass marbles) of a known specific gravity (2.70) were added to the jig tube with a 0.25 mm screen at the bottom. This mesh base allowed water to enter during the jig downstroke and particles to be sorted during the jig upstroke. This tube, with coal added, was gently lowered into the jig vessel. Water level was adjusted so that it was approximately 100 mm above the level of the coal. The jig tube was attached to the pneumatic jiggling mechanism. Once turned on, this mechanism moved the jig tube up and down. The down stroke was rapid to suspend particles individually, the upstroke was slower to allow the particles to sort according to density. The jiggling time was 15 minutes. When the jig cycle was complete, the coal sample was presumed to have been sorted into a density continuum column, heaviest material (discard) at the bottom grading to lightest (best) coal at the top.

After jiggling was completed, the jiggling tube was lifted from the jig vessel, allowing the water to drain from the coal. A sample pusher was inserted in the jig tube and pressed to allow more water to drain. The entire tube was then inverted to allow the coal to be pushed upward. Once

the jig tube was inverted, and the screen removed, the marbles were visible, as they had the highest specific gravity; this was evidence that the jiggling was successful. A tray was attached to the top of the tube and the sample pusher was rotated, causing the coal to be pushed above the jig tube and allowing the operator to scrape off the layer. The layer was then carefully scraped into the apparent relative density (ARD) basket. Note that, because the jig tube was inverted after jiggling, the first fraction collected was the highest density (heaviest or highest ash content). The thickness of the layers was dictated by the particle-size distribution of the coal and by how many fractions one expected to remove from the sorted column. Since the wet ARDs were calculated immediately, the depth of the layers could be increased or decreased to obtain a range of ARDs and subsequent range of ash contents.

Each wet coal layer was weighed and air dried, and a dry ARD calculated. Samples were then prepped for laboratory testing. Similar ARDs were added together before prepping or tested first to confirm ash results. The calculated ARD is an average for that layer.

New Method A: Re-Jiggling

In this method, the clean coal from the coarse size fraction was re-jiggled to see if it was possible to further segregate the particles based on density. First, a slice was taken that had an average ARD of 1.29 and an ash value of 10.20%. The slice was added back into the Roben Jig and processed. Through this ‘re-jiggling’ action, it was possible to further clean the coal by removing 158 g of a higher ash (22.77%), higher ARD (1.39) coal; this allowed for a selection of a lower ash product (<7%) compared to the starting value of 10.20%. This method showed promise for being effective at cleaning coal to lower ash cut points. In this study, the clean coal resulting from jiggling the coarse fraction (12.5 × 0.5 mm) was added back into the empty jig and re-jiggled.

New Method B: Float-and-Sink, Two Size Fractions

The coarse coal was first divided into two size fractions (12.5 × 5 mm and 2 × 0.5 mm) instead of one (12.5 × 0.5 mm) before being washed using the float-sink method (ASTM D4371-06, 2012). It is common in the coal industry to wash different coarse fractions separately in organic liquids.

New Method C: Roben Jig, Two Size Fractions

Pielot (2010) studied the results of various widths of grain-size classes being fed to jigs and found that the narrower the grain-size classes of the coal feed, the more precise was the jiggling. To test Pielot’s theory, this method separated the coarse coal into size classes, each of which was jiggled on its own.

Analysis

Clean-Coal Analysis

Each clean-coal composite was analyzed for various quality characteristics and was coked in the sole-heated oven (12 kg capacity) at CanmetENERGY in Ottawa, with coke characteristics subsequently being quantified. The clean coal resulting from the industrial-scale coal-washing plant was carbonized in the Carbolite pilot coke oven. The clean-coal composites were analyzed at GWIL Industries–Birtley Coal & Minerals Testing Laboratory for yield (percent), proximate analysis, free swelling index (FSI), specific gravity (sg), total sulphur, Hardgrove Grindability Index (HGI), calorific value (kcal/kg), mercury, ultimate analysis, mineral analyses of the ash, phosphorus in coal (calculated, percent), Gieseler maximum fluidity, Ruhr dilatation, ash fusion (oxidizing and reducing), chlorine, fluorine, alkali extraction–light transmittance test, Sapozhnikov X and Y indices, and caking index (G). Petrographic analysis of the coal and coke was carried out at both CanmetENERGY (Ottawa, ON) and David E. Pearson & Associates (Victoria, BC).

Carbonization

Coal samples (~20 kg each) from the float-and-sink washing with organic liquids and the Roben Jig washing with water were received at CanmetENERGY in Ottawa on August 7 and 10, 2018. In the case of 100% Plant Clean #183147, a significantly larger quantity of approximately 450 kg (three 45-gallon drums full) was received for carbonization tests in both the small-scale sole-heated oven (12 kg) and the pilot-scale coke oven (340 kg).

Upon reception, coals were air dried in open air in the laboratory for 12 hours (24 hours in the case of the larger sample of 100% Plant Clean) and homogenized prior to preparing charges for coking in CanmetENERGY’s 12 kg capacity sole-heated oven and its 340 kg capacity Carbolite pilot coke oven.

This section provides a description of the features and operating conditions for carbonization of coal in the sole-heated oven, including the preparation of coke samples from coals in this project for measurement of coke strength after reaction (CSR) and coke reactivity index (CRI) following a procedure developed at CanmetENERGY (MacPhee et al., 2013). It also provides a description of the Carbolite pilot oven used to carbonize a larger amount of the sample of 100% Plant Clean and assess its resulting coke quality.

Sole-Heated Oven (ASTM D2014-97(2010))

A 12 kg sample of coal (70–80%–3.35 mm or –6 mesh) was divided equally and each half charged into one chamber (approximately 280 mm in width, length and depth) of a double-chambered oven. A weighted piston applied a con-

stant force corresponding to a pressure of 15.2 kPa (2.2 psi) to the top of the coal bed (thickness in the 76–90 mm range), which was heated from below according to a prescribed temperature program. The sole temperature was raised from 554°C to 950°C at a heating rate of 0.9–1°C/min during the test. The movement of the load was continuously monitored during the test, which was complete when the temperature at the top of the coal bed reached 500°C (normally reached after a period of 6–7 hours). The measured expansion or contraction of the sample was converted to a reference base of 833 kg/m³ (52 lbs./cu. ft.) and 2% moisture.

After carbonization, the semi-coke was removed from the sole-heated oven and reheated in a stainless-steel holding box (229 mm wide, 292 mm long and 305 mm deep) that is hermetically sealed on top with a 3 mm thick section of stainless steel and lined with a 3 mm thick layer of ceramic-fibre insulation. The steel has an exit hole 1 cm in diameter in the centre for venting the hot coke gases. Also, the holding box is fitted on the bottom with a stainless-steel inlet tube (150 mm long and 6 mm inside diameter) connected to a cylinder of nitrogen gas, which allows for continuous flushing of the coke with the gas (5–10 L/min flow rate) to prevent its combustion. This treatment heated the semi-coke to 1100°C to complete the annealing of the coke.

A schematic of a sole-heated oven is presented in Figure 6 and a photo of the sole-heated oven used in this project is shown in Figure 7.

Cokes from the sole-heated oven were assessed for apparent specific gravity (ASG) and hot-strength properties, including CSR and CRI (following the ASTM D5341M-14 standard), and were analyzed for proximate (moisture, ash, volatile matter and fixed carbon), sulphur and carbon forms/textures using an optical microscope.

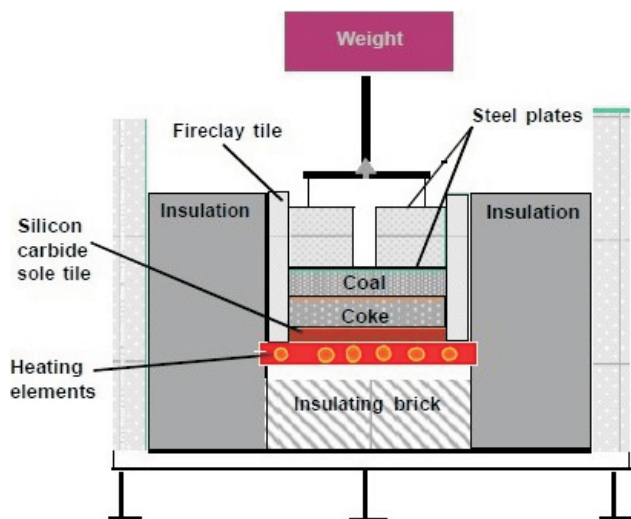


Figure 6. Schematic diagram of the CanmetENERGY sole-heated oven.

The ASG of coke is defined as the ratio of the mass of a volume of dry coke to the mass of an equal volume of water. Coke ASG varies with the rank and ash content of the coal carbonized, the bulk density of the coal charge in the oven, the carbonization temperature and the coking time (Price and Grandsen, 1987). In this project, the ASG of cokes was determined following a method developed at Canmet-ENERGY and related to the ASTM D167-93 (2004) and ISO 1014:1985 standards.

According to ASTM D5341-14, the CRI is the percentage weight loss of the coke sample after reaction in CO₂ at 1100°C for 2 hours. The cooled, reacted coke is then tumbled in an I-drum for 600 revolutions at 20 rpm. The cumulative percentage of +9.5 mm coke after tumbling is denoted as the CSR.

Microscopic analysis of the textures was also performed on the sole-heated cokes to measure the carbon forms. This technique is extremely useful for understanding the behaviour of coal during coking and for interpreting pressure generation and coke-quality results.

Carbon-form analysis in cokes in this project was carried out using a combination of the US Steel method (Gray and DeVaney, 1986) and the CanmetENERGY method, which is based on work carried out by Marsh in 1978–1981 and published in the book *Introduction to Carbon Science* (Edwards et al., 1989). A single point count is made for each measured field of view. For each field, the stage is rotated in order to determine the possible highest rank carbon form. Normally, 500-point counts are performed on a sample. Each carbon form is derived from an assumed parent-coal vitrinite type. From the coke-texture analysis, one can determine the effective coal reflectance (%Ro).

Carbolite Pilot Oven

Specifications of the Carbolite pilot-scale movable-wall coke oven (Carbolite Gero Ltd., Sheffield, United Kingdom) are listed in Table 1 and the oven is shown in Figure 8.



Figure 7. CanmetENERGY sole-heated oven (12 kg capacity) used in this study.

Table 1. Specifications of the CanmetENERGY Carbolite pilot movable-wall coke oven.

Coke-oven specification	Carbolite pilot-scale movable-wall coke oven
Chamber width (mm)	460
Chamber volume (m ³)	0.401
Charge weight (kg)	340–350
Percentage of coal passing 3.35 mm	80–85
Charge density in oven (dry; kg/m ³)	809–825
ASTM bulk density (wet; kg/m ³)	773–783
Charge moisture (%)	2.5–3.2
Heating control (flue temperature; °C)	875°C start; increase 15°C/h to 1130°C
Pushing time (h)	3 h after centre temperature reaches 950°C (usually around 18 h)
Quench	Water (wet) normally; N ₂ gas (dry) is also possible
Coke treatment (conditioning)	Client specified (usually 1 or 3 drops from 3 m height)

To simulate industrial coking, the temperature of the oven is kept low (875°C) at the beginning of the carbonization cycle, to limit the heat input to the coal, and then gradually raised (15°C/h) until the flue temperature reaches 1130°C. The oven is normally charged with coal 85 ±5% of which is less than 3 mm, and the coal moisture is adjusted so as to achieve a dry-coal bulk density in the oven in the range 810–825 kg/m³. The oven is discharged 3 hours after the centre temperature of the coke reaches 950°C. The coke is water quenched and dropped 3 m onto a concrete floor in order to condition or stabilize it. This process is carried out in preparation for the drum testing, followed by measurement of the resultant coke properties.

The coke discharged from the Carbolite oven is assessed for size distribution, proximate analysis, sulphur, coke stability and hardness using the ASTM tumbler method, the cold strength drum index (DI) test of the Japanese Industrial Standard (JIS), CSR/CRI, ASG and texture.

Fundamentals of Coal Science

A small budget was set aside to further investigate the science behind the chemical reaction between perchloroethyl-

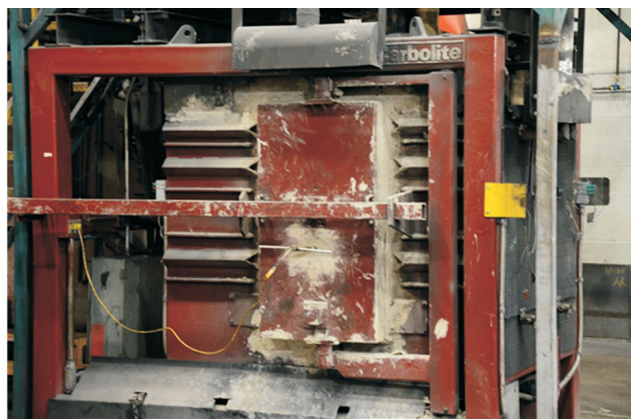


Figure 8. CanmetENERGY Carbolite pilot-scale coke oven (340 kg capacity) used in this study.

ene and coal macerals. The intent was to carry out the investigation using the micro-FTIR machine, but the work could not be completed during 2018. Therefore, the applicability of a family of liquids called Novec 7000 series in washing coal was tested, in collaboration with a research scientist at 3M.

Novec 7000, also known as 1-methoxyheptafluoropropane, is an engineered liquid developed by 3M. It has a low toxicity, is not known or suspected to cause cancer, and is nonflammable and noncorrosive. It has a specific gravity of 1.40. Novec 7700, also known as Furan (2,3,3,4,4-pentafluorotetrahydro-5-methoxy-2,5-bis[1,2,2,2-tetrafluoro-1-(trifluoromethyl)ethyl]), was also engineered by 3M. This liquid has the same benign characteristics as Novec 7000; in fact, it is suggested that it can be ingested without any medical concerns. The specific gravity of Novec 7700 is 1.797. The two liquids are miscible and can be used to create a range of liquids from 1.40 to 1.80 sg.

To complete detailed washability studies with coal, customers often require float densities over that range. This Novec fluid is a potential candidate for the replacement of harmful organic liquids in the float/sink procedure. Since 3M was prepared to donate the liquids for use in this research, it was thought that this was the opportune time to carry out the research. Novec 7000 and 7700 liquids were mixed in varying proportions to create heavy liquid baths with the following specific gravities: 1.40, 1.50, 1.60, 1.70 and 1.80. Raw coal underwent float-and-sink analysis according to ASTM D4371 in both traditional organic liquids (perchloroethylene, white spirits and methylene bromide) and the Novec solutions. The float-and-sink data were then compared for yield and quality characteristics. Clean coals resulting from both studies were also compared for a range of quality parameters. Results are not finalized as yet.

Results

This research project had the opportunity to obtain raw and clean coal from a single-seam plant run. Because of this, clean-coal samples derived from a number of methodologies were compared. As mentioned, the ability to compare laboratory-washed coal to that cleaned in an industrial-sized wash plant is considered the gold standard in validating a laboratory method for washing coal. Table 2 shows how these clean-coal samples compared.

On an ash basis, the clean coal derived from the float-and-sink process was a cleaner product, with ash less than 7%. The float/sink process in organic liquids provides ‘perfect separation’ between coal and rock. Care was taken not to create a clean-coal product that would be impossible to create in an industrial plant. Therefore, the specific gravity cut point remained less than 1.70, which is the cut-off achiev-

able for a processing plant. The two factors, limiting the specific gravity cut point and the organic liquids achieving perfect separation (with no misplaced particles), resulted in the ash of the clean coal being lower than those from the Roben Jig or the industrial plant.

Other coal-quality parameters remained similar between the samples washed with organic liquids and those washed in the jig, even when changing the coarse size fractions. Re-jigging the clean coal that resulted from the traditional jigging method resulted in a lowering of the ash content from 7.80 to 6.68%. The petrography for these samples is still outstanding.

The free-swelling index of the six clean-coal composites ranged from 8.0 to 8.5, with only two of the composites obtaining the 8.5 value. The chlorine content was higher in the clean-coal composites washed in the perchloroethylene

Table 2. Clean-coal quality parameters (air-dried basis). Abbreviations: CCC, clean-coal composite; db, dry basis; ddpm, dial divisions per minute; FS, float-and-sink; REJIG, re-jigging; RJ, Roben Jig; SD 2.5, dilatation based on a 60 mm pencil per gram of air-dried coal in the test sample, multiplied by a constant of 2.5.

Clean coal quality (air-dried basis)	2018					
	FS CCC sizes	JIG CCC sizes	FS CCC 12.5 x 0.5 mm	JIG CCC 12.5 x 0.5 mm	REJIG CCC 12.5 x 0.5 mm	Plant product
Moisture (%)	1.29	1.21	1.20	1.38	1.22	1.00
Ash (%)	6.81	7.51	6.74	7.80	6.68	8.01
Volatile matter (%)	29.32	30.15	29.59	29.15	29.36	28.42
Fixed carbon (%)	62.58	61.13	62.47	61.67	62.74	62.57
Sulphur (%)	0.54	0.54	0.54	0.54	0.55	0.53
Free swelling index	8.5	8.0	8.0	8.0	8.0	8.5
Chlorine (ppm)	2280	365	2570	432	321	-
Flourine (ppm)	171	172	158	162	163	143
Hardgrove grindability index	79	78	78	79	80	-
Specific gravity	1.37	1.37	1.31	1.35	1.36	-
% phosphorus in coal (db)	0.040	0.042	0.043	0.045	0.044	0.045
Gieseler maximum fluidity (ddpm)	290	274	281	298	322	212
Ruhr dilatation						
% contraction	25	25	28	25	26	28
% dilatation	107	121	112	118	125	149
% total dilatation	132	146	140	143	151	177
% SD 2.5	108	120	118	127	133	150
Mineral analysis of ash						
SiO ₂ (%)	58.50	59.76	57.56	59.57	58.27	58.86
Al ₂ O ₃ (%)	31.44	29.60	32.79	29.61	31.16	29.78
TiO ₂ (%)	1.57	1.47	1.56	1.41	1.52	1.53
CaO (%)	1.43	1.46	1.97	1.26	1.83	1.48
BaO (%)	0.28	0.31	0.31	0.32	0.29	0.28
SrO (%)	0.15	0.14	0.14	0.14	0.17	0.12
Fe ₂ O ₃ (%)	1.46	1.59	1.50	1.62	1.60	3.17
MgO (%)	0.48	0.58	0.53	0.56	0.51	0.48
Na ₂ O (%)	0.08	0.08	0.05	0.07	0.07	0.09
K ₂ O (%)	1.16	1.51	1.22	1.66	1.41	1.22
P ₂ O ₅ (%)	1.32	1.26	1.46	1.30	1.49	1.28
SO ₃ (%)	0.27	0.27	0.30	0.23	0.23	0.21
Undetermined (%)	1.86	1.97	0.61	2.25	1.45	1.50

float-and-sink process. This was expected due to the chlorine content of the liquids. The Hardgrove Grindability Index, fluorine, % phosphorus in coal, and mineral analysis of ash were similar for all six composites.

The Gieseler maximum fluidity was measured on all composites within a two-day period, the values ranging from 212 to 322 dial divisions per minute (ddpm). Although small differences were observed, the fluidity of this coal did not appear to be significantly decreased due to the treatment with perchloroethylene.

The timeline for the dilatation testing was not kept as tight for all six samples. Therefore, the difference between the plant dilatation value of 149% and those of the other samples (107 to 125%) could have been partially due to aging.

Phase 1 Method: Float-and-Sink and Roben Jig, One Coarse Fraction

As was found with the work completed in 2017, the Roben Jig was able to create a clean-coal composite similar to that created using organic liquids except that, in the work reported here, the ash in the clean coal from the jig was higher. This was because the specific gravity cut-point was limited to what the processing plant could achieve at the mine. It is known that organic liquids provide a perfect separation and there is usually a ‘plant factor’ added to yield information coming from studies such as these to account for the imperfection of a processing plant. If the limitation was not imposed on the cut point, it would have been possible to make the ashes the same.

Also of note is that the Gieseler maximum fluidity values were comparable between the water-based method and the organic liquids. This could be due to there being less fusinite and semifusinite macerals in the coal. The petrography results will confirm this.

Misplaced Material

One of the objectives of this project was to identify and quantify the misplaced material that occurs in the column during the jigging process. A few clean slices were taken from the jigged clean coal and washed in organic liquids. Figure 9 illustrates the specific gravities of the particles that made up slice #13, one of the cleaner slices, which had an average relative density of 1.18. Washing the slice by float-and-sink showed that most of the particles fell at or below the 1.30 sg, but there were also particles from the 1.40, 1.60 and +1.90 specific gravities.

Figure 10 shows slice #1 from the Roben Jig. This was the slice with the highest ash content and had an average apparent relative density of 2.28. The float-and-sink process separated the coal particles into the correct specific gravity baths. Most of the particles fell into the +1.90 sg class, which is what one would expect to see as the highest ash

‘sink’. This would be where one would find the rock. Particles contained in slice #1 also fell into the -1.30, 1.30, 1.40, 1.50, 1.60, 1.70 1.80 classes.

A further step was to take the clean-coal composite, as compiled from the Roben Jig method, and wash it in organic liquids to determine the density of the particles. The cut-point of the clean-coal composite had an ARD of 1.54. Table 3 shows the mass percentage falling into each specific-gravity class. Approximately 94% of the particles fell below the 1.54 sg. Five percent of the particles forming the clean-coal composite was misplaced from higher specific gravities, including 1.3% from the rock particle (+1.80 sg) sink. Although these misplaced particles exist, they do not seem to negatively impact the clean-coal quality parameters.

New Method A: Re-Jigging

The clean coal resulting from the Roben Jig traditional method was re-jigged to determine if a second cleaning action could remove misplaced particles. After re-jigging, the clean coal created during the second jigging process underwent float-and-sink analysis in organic liquids. Table 4 shows the percentage of particles falling into each specific gravity range. After re-jigging, only 2.9% of the particles in the clean-coal composite were misplaced from other higher specific gravity ranges. Re-jigging was confirmed to be a useful method of reducing the amount of misplaced material.

New Methods B and C: Float-and-Sink and Roben Jig, Two Size Fractions

Changing the size range of the coarse particles that undergo float-and-sink washing is a standard practice in the laboratory washing of coal. It was because of this, and some information from Pielot (2010), that it was proposed to investigate washing different coarse fractions separately in the Roben Jig. Pielot thought that narrowing the size fraction resulted in more precise jigging. In this study, no difficulties were encountered while jigging the 12.5 × 2 mm frac-

Table 3. Float-and-sink mass percentages falling within specific-gravity ranges of a re-washed clean coal produced by the Roben Jig. Abbreviations: FLT, float; SNK, sink.

Specific gravity	Mass percentage
1.30 FLT	67.4
1.30 - 1.40	22.6
1.40 - 1.50	4.1
1.50 - 1.60	1.4
1.60 - 1.70	0.9
1.70 - 1.80	0.7
1.80 SNK	3.0

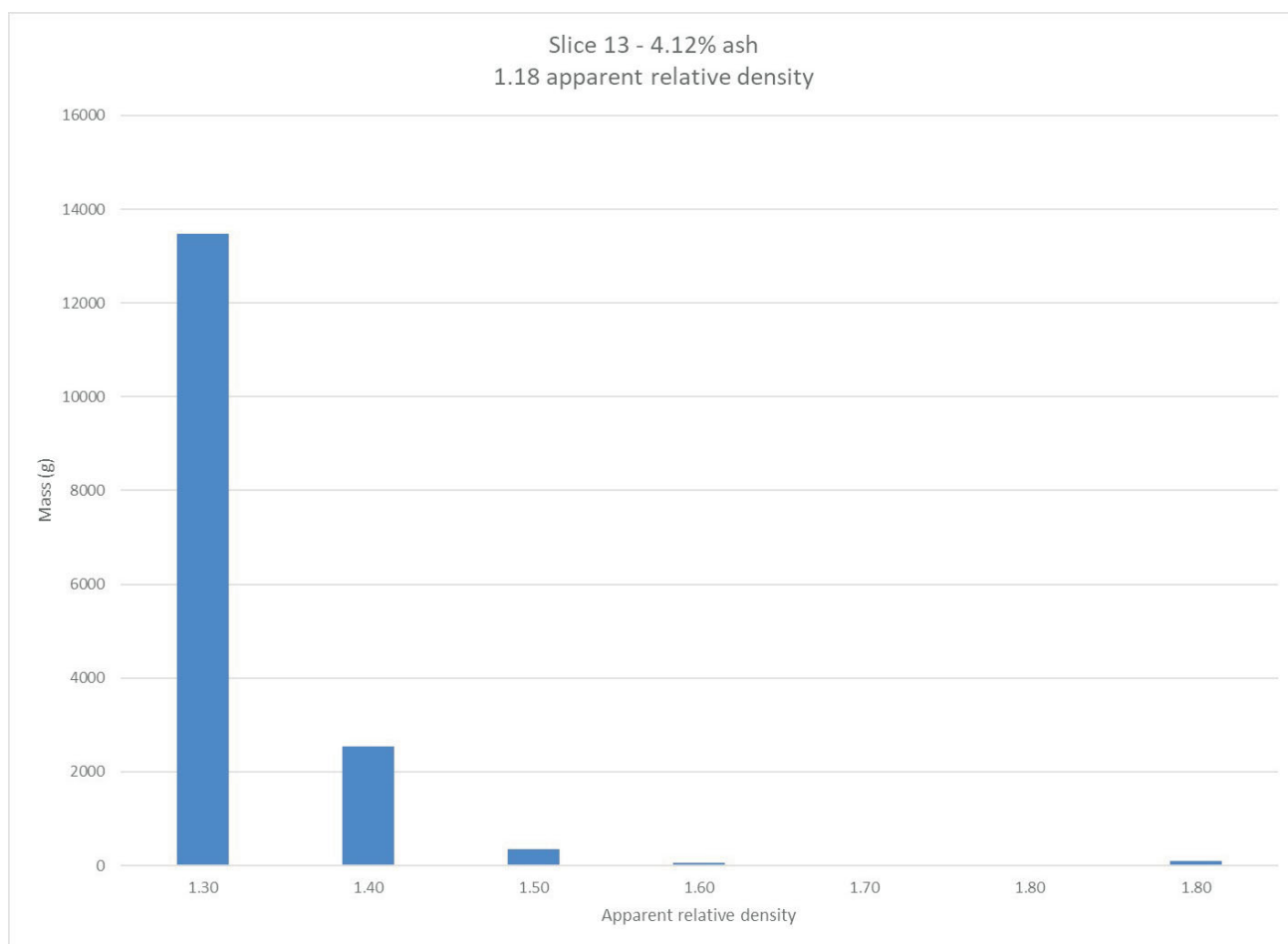


Figure 9. Particle-density distribution, expressed as proportions by mass, of low-density jig slice.

tion. However, jiggling the finer 2×0.5 mm fraction proved difficult: it was found that there were inconsistencies between slices. Usually, the relative density of slices behaves predictably: the highest relative density occurs at the bottom of the column, with lower relative densities occurring in a stepwise fashion moving to the top of the column. The inconsistencies between slices of the finer fraction suggested that there was misplaced material. When the clean

coal from this fraction was washed by float-and-sink, it was found that there were 9% misplaced particles. Table 5 shows the specific-gravity distribution of the coal particles at the 1.40 sg cut point.

From an operational standpoint, jiggling the finer size fraction was also more time consuming, as the operator had to continually check the work that was done. This method of misplaced-material mitigation did not prove to be the best method.

Clean-Coal Carbonization

Table 6 presents analytical data (available thus far) for cokes made in the sole-heated oven from coals studied in this project.

Contraction levels range from -15% for 100% plant clean product crushed to 12.5 mm to -9% for 100% JIG CCC 12.5×0.5 and 100% REJIG 12.5×0.5 . The type of washing medium, namely organic liquids for float-and-sink and water for Roben Jig, had a minor effect on the level of sole-heated oven contraction observed, -11% and -10% , respectively. The low amount of volatile matter remaining in the cokes ($<1\%$) provides clear evidence that the coals were

Table 4. Float-and-sink mass percentages falling within specific-gravity ranges of a re-washed clean coal produced by re-jiggling. Abbreviations: FLT, float; SNK, sink.

Specific gravity	Mass percentage
1.30 FLT	69.9
1.30 - 1.40	23.8
1.40 - 1.50	3.5
1.50 - 1.60	1.0
1.60 - 1.70	0.6
1.70 - 1.80	0.4
1.80 SNK	0.9

Table 5. Float-and-sink mass percentages falling within specific-gravity ranges of a rewashed clean coal produced by jigging the 2 x 0.5 mm size fraction. Abbreviations: FLT, float; SNK, sink.

Specific gravity	Mass percentage
1.30 FLT	72.2
1.30 - 1.40	18.8
1.40 - 1.50	3.7
1.50 - 1.60	1.8
1.60 - 1.70	0.8
1.70 - 1.80	0.5
1.80 SNK	2.2

essentially fully carbonized by a combination of coking in the sole-heated oven and heat treatment of the resulting semi-coke to 1100°C under nitrogen to complete the annealing of the coke.

The apparent specific gravity (ASG) of coke ranged between 0.96 (100% REJIG 12.5 x 0.5) and 1.01 (100% plant

clean product crushed to 12.5 mm). As stated earlier, the rank and ash content of the carbonized coal dictates the coke ASG. The low ash content of 6.8% (db) in 100% REJIG 12.5 x 0.5 results in the lowest ASG coke, whereas the high ash content of 8.2% (db) in 100% plant clean product crushed to 12.5 mm results in the highest ASG coke.

The coke strength after reaction (CSR) of the clean coal resulting from all washing methods was compared. Comparison of New Methods B (FS CCC sizes) and C (JIG CCC sizes) revealed that Method C (Roben Jig) washing improved the CSR by 5 points relative to Method B (float-and-sink). Method C (JIG CCC sizes) also resulted in a 6-point increase in CSR when compared to the Phase 1 Method (JIG CCC 12.5 x 0.5). Washing the coal using New Method B (FS CCC sizes) resulted in a 3 point decrease in the CSR compared to the Phase 1 Method (FS CCC 12.5 x 0.5).

A comparison of the CSRs resulting from coal washed using the Phase 1 methods of jigging and float-and-sink (one coarse fraction of 12.5 x 0.5 mm) shows that Roben Jig washing led to a CSR 4 points lower than float-and-sink

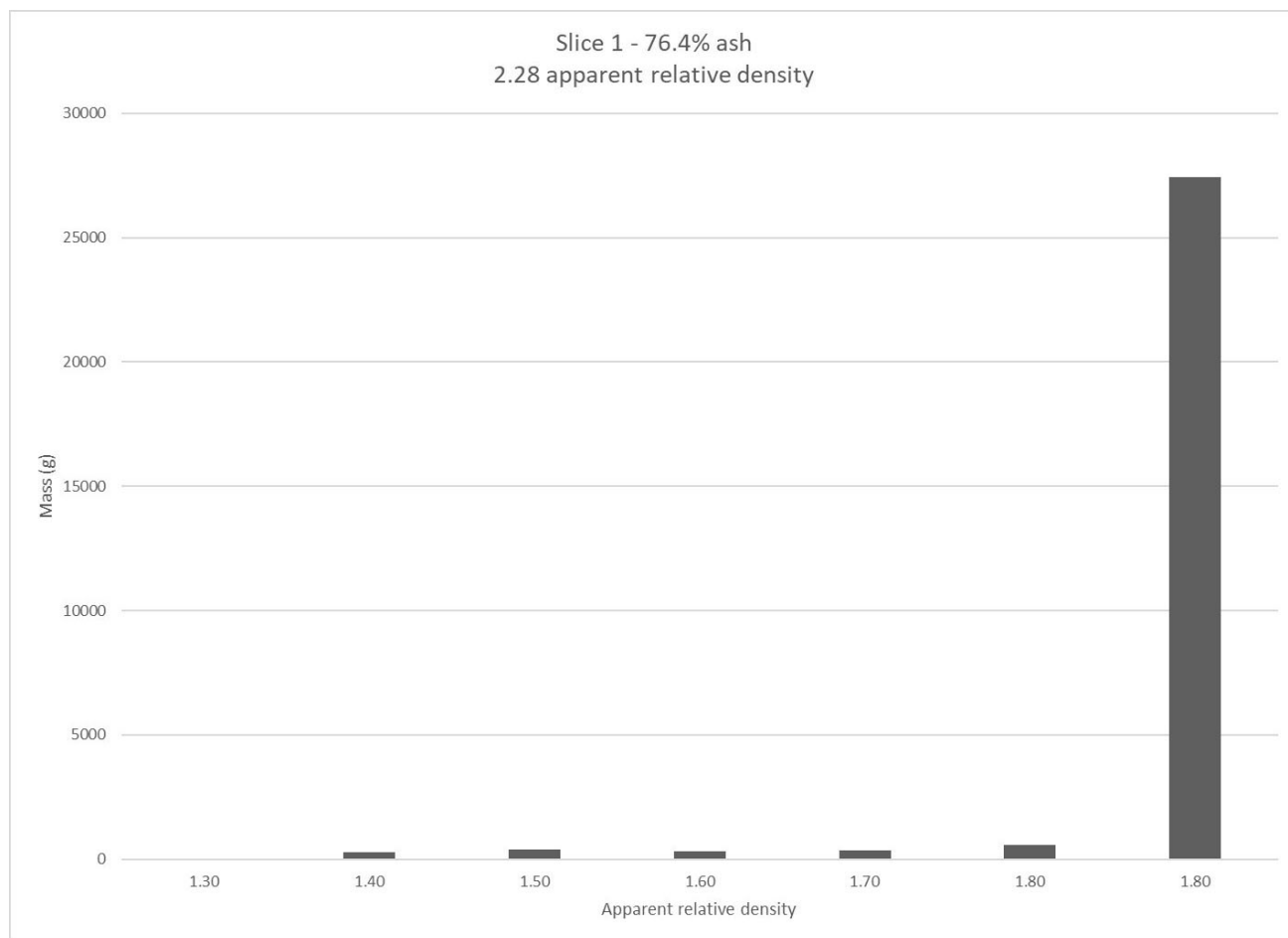


Figure 10. Particle-density distribution, expressed as proportions by mass, of high-density jig slice.

Table 6. Quality of coke samples obtained from sole-heated oven tests. Abbreviations: CCC, clean-coal composite; FS, float-and-sink; JIG, Roben Jig; REJIG, re-jigging.

Coke property	2018						Crushed plant product
	FS CCC sizes	JIG CCC sizes	FS CCC 12.5 x 0.5	JIG CCC 12.5 x 0.5	REJIG CCC 12.5 x 0.5	Plant product	
Expansion/contraction	-11.8	-11	-11	-9.2	-9.4	-11.6	-14.5
Coke strength after reaction (CSR)	65.5	70.5	68.3	64.3	65.0	61.5	64.2
Coke reactivity index (CRI)	21.3	17.2	18.5	19.2	20.6	25.2	23.0
Apparent specific gravity (ASG)	0.970	0.995	0.988	0.989	0.963	1.004	1.012

washing. Re-jigging of this coal led to a negligible change/improvement in CSR.

The CSR of the plant-washed coal (plant product) was 61.5. After crushing the plant-washed coal to pass 12.5 mm, the CSR increased to 64.2. Crushing of the product to 12.5 mm led to a 3 point improvement in CSR relative to the complete size range. It should be noted that the repeatability of this test is 3.3. This would indicate that the CSRs are actually quite similar.

Table 7 presents analytical data for coke made in the Carbolite oven from 100% plant clean product (sample #183147).

Assessment of the quality of cokes made in the sole-heated oven and the Carbolite pilot oven from 100% plant clean product found ASTM stability and hardness of 56 and 66, respectively; JIS DI30/15 and DI150/15 of 94 and 85, respectively; and CSR and CRI of 58 and 27, respectively. The CSR and CRI from the larger pilot-scale coke oven (340 kg) are found to be inferior to those from the smaller sole-heated oven (12 kg), which are 62 and 25, respectively (Figure 11).

The superior CSR and CRI of coke produced in the smaller sole-heated oven is expected, since the carbonization process took place under a significantly higher load/pressure (15.2 kPa) than that in the larger pilot oven (4–8 kPa). This led to the formation of a coke with higher apparent density (ASG of 1.00), and thus lower porosity, from the sole-heated oven compared to that from the larger pilot oven (ASG of 0.92).

Conclusions

The Canadian coal industry needs a reliable method of washing small metallurgical-coal samples whereby the exposure of both the coal sample and the laboratory technicians to perchloroethylene and other toxic organic liquids can be eliminated. This study evaluated the use of the Roben Jig and varying methodologies, as well as two engineered liquids (Novec 7000 and 7700), in satisfying these requirements.

When comparing the quality characteristics of clean coal samples, it is apparent that the Roben Jig was able to produce a clean-coal sample similar to that from the industrial coal-washing plant that uses the float-and-sink method

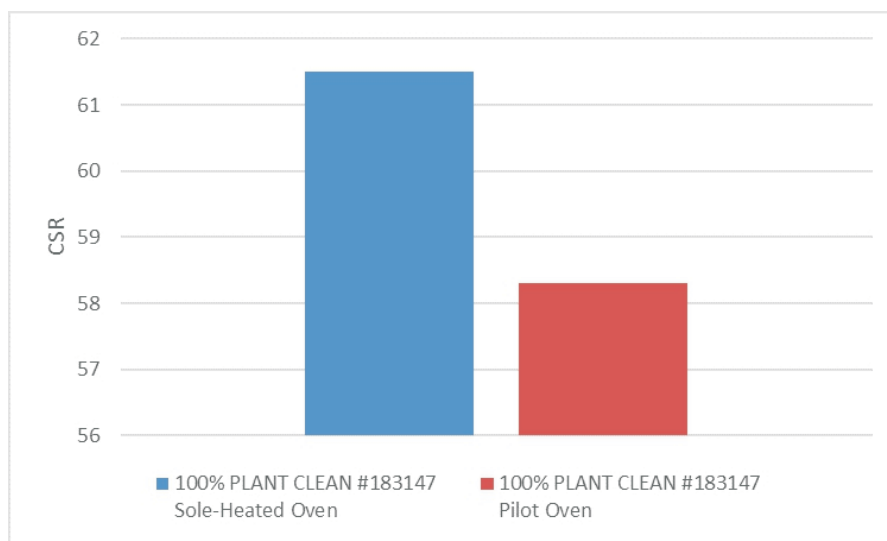


Figure 11. CSR comparison of cokes made in the sole-heated oven and Carbolite pilot-scale oven from 100% plant clean product (sample #183147).

Table 7. Quality of coke samples obtained from Carbolite pilot oven tests on 100% plant clean #183147.

	Date received		AUG/7/18
	Weight received		3-DRUMS
	Project		CCRA 90 - Roben Jig
	Coal index		Phase 2 26799
	Description		100% PLANT CLEAN #183147 C-2733
Sole-heated oven test	Expansion/contraction	%	-11.6
Coke moisture	Moisture	%	x
Coke proximate (db)	Ash	%	x
	Volatile matter	%	x
	Fixed carbon	%	x
	Sulphur	%	x
Carbonization results	Oven test number		C-2733
	Test date		SEP/7/18
	Moisture in charge	%	3.0
	Net dry charge weight	kg	336.8
	ASTM BD	kg/m ³	773.7
	Oven dry BD	kg/m ³	815.6
	Coking time	h:min	18:14
	Final centre temperature	°C	1074
	Time to 900°C	h:min	14:48
	Time to 950°C	h:min	15:14
	Time to 1000°C	h:min	15:51
	Time to max. wall pressure	h:min	2:45
	Max. wall pressure	kPa	4.1
	Max. gas pressure	kPa	6.7
	Coke yield	%	72.4
Sieve analysis of coke (cumulative)	100 mm sieve	%	0.4
	75 mm sieve	%	7.6
	50 mm sieve	%	51.3
	37.5 mm sieve	%	83.6
	25.0 mm sieve	%	94.3
	19.0 mm sieve	%	95.3
	12.5 mm sieve	%	96.1
	Passing 12.5 mm sieve	%	3.9
	Mean coke size	mm	53.0
ASTM coke tumbler test	Stability		56.3
	Hardness		66.3
JIS coke tumbler test	50 mm sieve, 30 rev.		21.2
	25 mm sieve, 30 rev.		90.6
	15 mm sieve, 30 rev.		93.6
	50 mm sieve, 150 rev.		8.0
	25 mm sieve, 150 rev.		79.4
	15 mm sieve, 150 rev.		85.1
	CSR		58.3
	CRI		27.2
	ASG		0.920
Coke texture	Isotropic	%	2.7
	Very fine mosaic	%	7.4
	Fine mosaic	%	34.9
	Medium mosaic	%	32.3
	Coarse mosaic	%	3.8
	Total mosaic	%	78.4
	Elongated fine flow	%	4.2
	Elongated medium flow	%	0.9
	Elongated coarse flow	%	0.0
	Total flow	%	5.1
	Domain flat flow	%	0.0
	Domain undulating	%	0.0
	Domain ribbon	%	0.0
	Total domain	%	0.0
	Fusinite	%	3.5
	Semifusinite	%	9.5
	Unidentified inerts	%	0.8
	Altered vitrinite	%	0.0
	Total inert	%	13.8
	Coal Ro calculated		1.04
	Coke mosaic index		2.02

with organic liquids. The ash value of the clean coal from the jig was higher than that from the float-and-sink method, but only because of limitations on cut-points imposed by the methodology. Misplaced material was found in clean-coal composites created in the jig, but in small enough proportions that it did not have a negative effect the clean-coal quality. A re-jigging action was found to be the most useful in reducing the percentage of misplaced particles. Narrowing the size range of particles during jigging proved to be operationally difficult for the finer size fraction (2×0.5 mm).

With respect to carbonization, evaluation of the cokes produced from the plant clean-coal product after washing of the complete size range of coal particles in the two types of media showed that the Roben Jig (New Method C) had a CSR of 70 compared to values of 65.5 and 68.3 for the float-sink methods (Phase 1 Method and New Method B). The New Method C of washing two coarse size fractions separately in the Roben Jig led to a 6-point improvement in CSR relative to washing only the 12.5×0.5 mm size fraction. Re-jigging the coal (New Method A) led to a negligible change/improvement in CSR.

Future Work

Study in this research project is ongoing. Future work will involve summarizing the results from the following tasks:

- Coal petrography
- Coke-texture petrography
- Novac 7000 series washability

Acknowledgments

The project members thank the peer reviewer, E. Gravel (P.Geo.), Independent Consultant. Thanks also go to Geoscience BC, the Canadian Carbonization Research Association, Teck Resources Ltd., 3M Canada and GWIL Industries–Birtley Coal & Minerals Testing Division for their financial and in-kind contributions that made this project possible.

References

Campbell, M. (2010): Options for sink/float analysis – economic and technical review; *in* Proceedings of 37th Symposium on the Geology of the Sydney Basin, Pokolbin, Australia, May 2010.

DuBroff, W., Kaegi, D.D., Knoerzer, J.J. and Spearin, E.Y. (1985): Solvent pretreatment of coal to improve coke strength; United States Patent and Trademark Office, patent number 4528069, URL <<http://patft.uspto.gov/netacgi/nph-Parser?Sect1=PTO2&Sect2=HITOFF&p=1&u=%2Fmetahtml%2FPTO%2Fsearch-bool.html&r=3&f=G&l=50&col=AND&d=PTXT&s1=4528069&OS=4528069&RS=4528069>> [November 2017].

Edwards, A.S., Marsh, H. and Menendez, R. (1989): Introduction to Carbon Science; Butterworth & Co. (Publishers) Ltd.,

348 p., URL <<http://www.sciencedirect.com/science/book/9780408038379>> [November 2018].

Gray, R.J. and DeVanney, K.F. (1986): Coke carbon forms: microscopic classification and industrial applications; *International Journal of Coal Geology*, v. 6, p. 277–297.

Holuszko, M.E., Leeder, R., Mackay, M., Giroux, L., MacPhee, J.A., Ng, K.W. and Dexter, H. (2017): Effects of organic liquids on coking properties of a higher-inert western Canadian coal; *Fuel Processing Technology*, v. 155, p. 225–231.

Iveson, S. and Galvin, K.P. (2010): Influence of organic liquids on coal carbonisation properties; Australian Coal Association Research Program (ACARP), Brisbane, Australia, Project C17051.

Iveson, S. and Galvin, K.P. (2012): The effect of perchloroethylene on coking properties; *Fuel*, v. 95, p. 504–513.

Mackay, M.L., Leeder, R.L., Giroux, L., Dexter, H., Holuszko, M., Halko, J., Howey, C. and Thomas, D. (2018): Producing clean coal from western Canadian coal fields using the water-based Roben Jig process; *in* Geoscience BC Summary of Activities 2017, Geoscience BC, Report 2018-1, p. 69–86.

MacPhee, J.A., Giroux, L., Ng, K.W., Todoschuk, T., Conejeros, M. and Kolijn, C. (2013): Small-scale determination of metallurgical coke; *Fuel*, v. 114, p. 229–234, URL <<https://doi.org/10.1016/j.fuel.2012.08.036>> [November 2018].

Pielot, J. 2010: An analysis of effects of coal jigging after changes in the grain composition of a feed; *Archives of Mining Sciences*, v. 55, no. 4, p. 827–846.

Price, J.T. and Gransden, J.F. (1987): Metallurgical coals in Canada: resources, research, and utilization; Energy, Mines and Resources Canada, CANMET Report 87-2E. ASTM D4371-06(2012): Standard test method for determining the washability characteristics of coal; ASTM International, West Conshohocken, PA, 2012, URL <[http://www.astm.org/cgi-bin/resolver.cgi?D4371-06\(2012\)](http://www.astm.org/cgi-bin/resolver.cgi?D4371-06(2012))> [November 2018].

ASTM and ISO Standard Methods

ASTM D2014-97(2010): Standard test method for expansion or contraction of coal by the sole-heated oven; ASTM International, West Conshohocken, PA, 2010, URL <[http://www.astm.org/cgi-bin/resolver.cgi?D2014-97\(2010\)](http://www.astm.org/cgi-bin/resolver.cgi?D2014-97(2010))> [November 2018].

ASTM D4371-06(2012): Standard test method for determining the washability characteristics of coal; ASTM International, West Conshohocken, PA, 2012, URL <[http://www.astm.org/cgi-bin/resolver.cgi?D4371-06\(2012\)](http://www.astm.org/cgi-bin/resolver.cgi?D4371-06(2012))> [November 2018].

ASTM D5114-90(2010): Standard test method for laboratory froth flotation of coal in a mechanical cell; ASTM International, West Conshohocken, PA, 2010, URL <[http://www.astm.org/cgi-bin/resolver.cgi?D5114-90\(2010\)](http://www.astm.org/cgi-bin/resolver.cgi?D5114-90(2010))> [November 2018].

ASTM D5341 / D5341M-14: Standard test method for measuring coke reactivity index (CRI) and coke strength after reaction (CSR); ASTM International, West Conshohocken, PA, 2014, URL <<http://www.astm.org/cgi-bin/resolver.cgi?D5341D5341M-14>> [November 2018].

ISO 1014:1985: Coke – determination of true relative density, apparent relative density and porosity; International Organization for Standardization, Geneva, Switzerland, URL <<https://www.iso.org/standard/5483.html>> [November 2018].

Soil Amendments in Mine Closure, New Afton Mine, South-Central British Columbia: Proposed Work

L.H. Fraser, Department of Natural Resource Sciences, Thompson Rivers University, Kamloops, BC, lfraser@tru.ca

Fraser, L.H. (2019): Soil amendments in mine closure, New Afton mine, south-central British Columbia: proposed work; in Geoscience BC Summary of Activities 2018: Minerals and Mining, Geoscience BC, Report 2019-1, p. 101–104.

Introduction

Environmental laws and regulations govern mining and oil-and-gas extraction in Canada, including reclamation. Prior to development, resource-extraction companies are required to post a bond as a promissory that their activity and closure will meet approved government environmental standards. Despite the rising demand for restoration management, there is limited research on environmental restoration and there are few dedicated university postgraduate training programs in Canada to address the complexities of ecosystem reclamation. There is a critical need to work with the mining and oil-and-gas industries, in partnership with governmental agencies, to develop better management practices for successful ecosystem restoration, and to train Highly Qualified Personnel (HQP) for reclamation work.

Current restoration plans and mine-closure proposals for land reclamation are generally not based on sound scientific evidence. They are more likely to be based on past practice and administrative and logistical constraints. In order to rectify this lack of information, optimize reclamation methods and allow for a more harmonious coexistence between industry and environment, research focused on understanding and mastering ecosystem reclamation is needed.

This project is located at the New Afton mine in south-central British Columbia (Figure 1) and will study topsoil stored in a stockpile at the mine (Figure 2) to explore the use of soil amendments as they relate to enhancing viability of stored topsoil.

Project Location

During mine operation, topsoil stockpiles are established for use in reclamation upon closure of the mine. The height of these piles can reach up to 30 m. In addition, stockpiles can sit for the entire duration of mine operation, which may be decades. A major question is “Does topsoil stored in piles remain viable after so many years?” In order to ad-

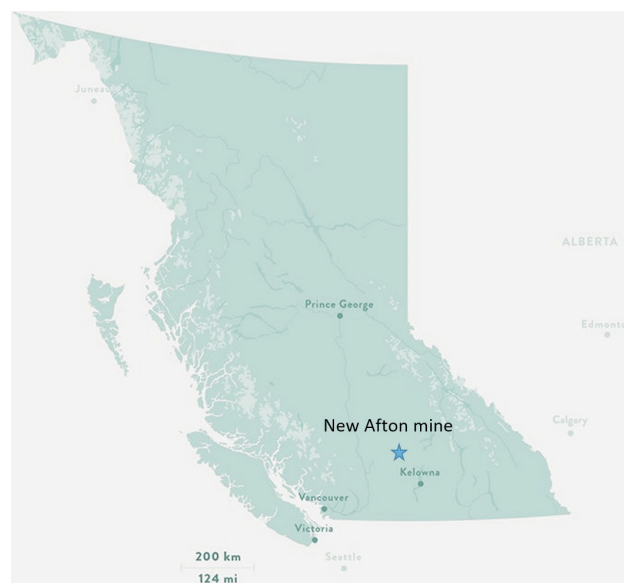


Figure 1. Location of the New Afton mine, south-central in British Columbia.

dress this question, the viability of the topsoil stockpile must be characterized over time and by depth. Furthermore, strategies must be developed to increase the viability of stored stockpiles.

A large stockpile on the site of the new New Afton mine (Figure 3) was selected for study. One way to assess viability is to measure the soil microbiota through DNA sequencing. A sampling protocol has been established to measure differences in the microbial community by depth in the stockpile. Experimental plots will also be established to test methods of rejuvenating the viability of a stockpile, which will include the use of soil amendments, such as ‘fresh’ topsoil from an undisturbed site, biochar, compost and wood chips.

Objective

The easiest way to restore topsoil and microbial communities after mine closing to their full pre-closing health status (i.e., equivalent soil characteristics and microbial community composition and function), and therefore the most likely route to achieve fully functional reclamation, would be to simply replace the excavated overburden with the

This publication is also available, free of charge, as colour digital files in Adobe Acrobat® PDF format from the Geoscience BC website: <http://www.geosciencebc.com/s/SummaryofActivities.asp>.

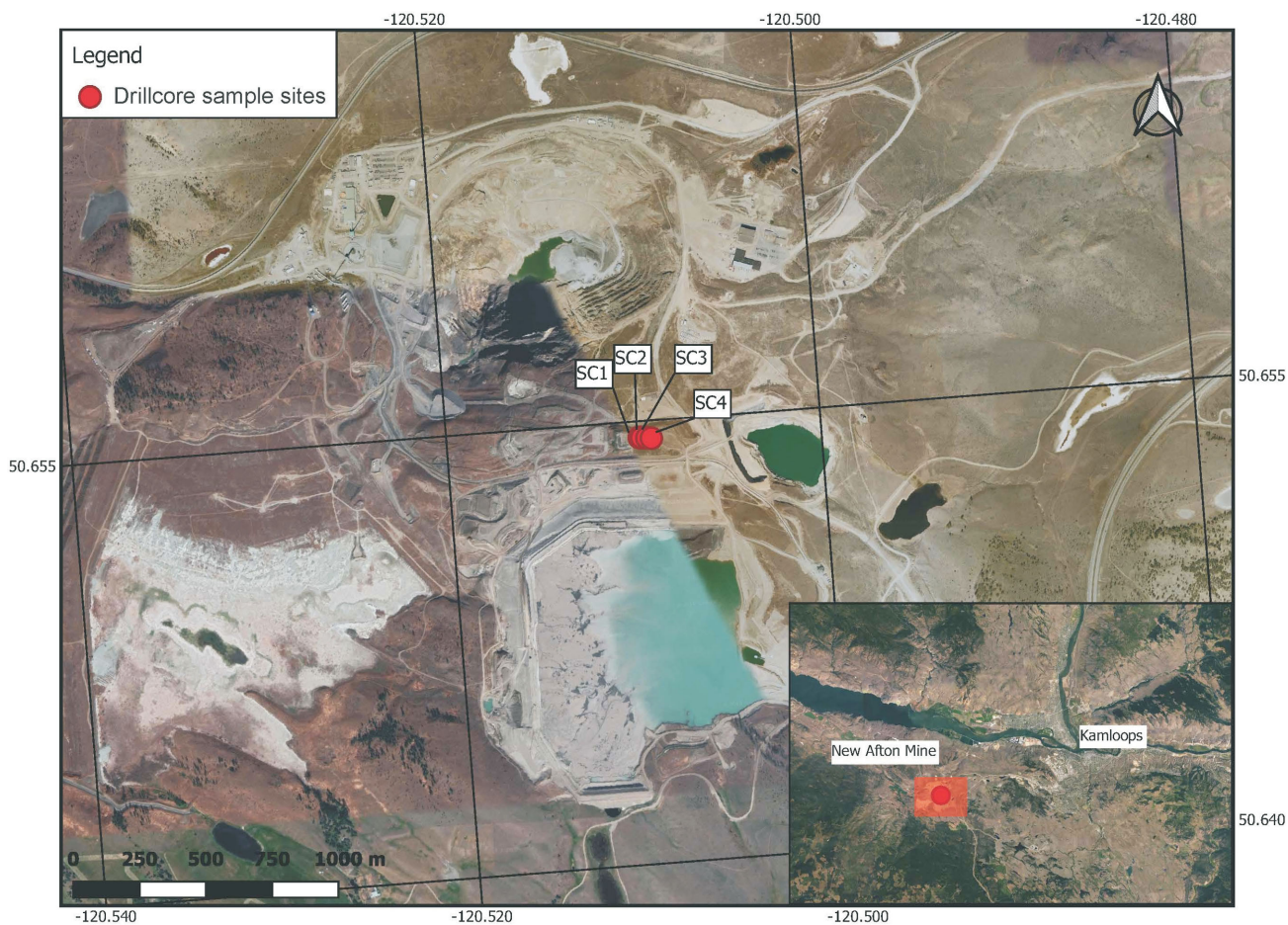


Figure 2. Site of stockpile and drill locations at the New Afton mine.

stockpiles of these materials kept on site. Unfortunately, it is known that microbial composition and functions degrade significantly over time, likely depending on factors such as depth of the stockpile, exposure to sun and weather, temperature, and chemical and microbial interaction.



Figure 3. Topsoil stockpile at New Afton mine, with drill rig on top.

Methodology

The project will investigate factors that affect changes to microbial health in topsoil stockpiles by evaluating such a stockpile at the New Afton mine. The soil and microbial characteristics, and microbial functions in these stockpiles will be characterized.

Soil samples will be collected at soil depths of 0–30 cm, 30–60 cm, 60–90 cm, 90 cm–1.2 m, 1.2–1.5 m, 1.5–3.0 m, 3.0–4.5 m, 4.5–6.0 m, 6.0–7.5 m, 7.5–10.5 m, 10.5–13.5 m, and at 3 m intervals until the bottom of the stockpile has been reached (Figure 4).

Soil characterization will include mineralogy and organic-matter content. High molecular weight, bulk DNA extracts will be collected. High throughput DNA sequencing will be done on the Thermo Fisher Scientific Ion S5 XL System.

Bulk soils collected at each depth interval will be stored in a –20°C freezer until the greenhouse trials are established. The basic premise is to take soils at each depth, treat with different combinations of soil amendment, and grow a phytometer (model plant species) as a test species to deter-



Figure 4. Drill operation and sample collection at the New Afton mine topsoil stockpile, September 26, 2018.

mine relative growth potential under different treatment conditions.

Acknowledgments

In addition to Geoscience BC, funding for this project is being provided through a Natural Sciences and Engineering Research Council of Canada Industrial Research Chair in Ecosystem Reclamation, with the following industry partners: Metro Vancouver, New Afton mine, Highland Valley Copper mine, Genome BC, Arrow Transportation, the Real Estate Foundation of BC, Kinder Morgan Canada and the BC Cattlemen's Association. Peer reviewed by J. Van Hamme and A. Gilbert.

Biodiversity in Ecosystem Mine Reclamation, South-Central British Columbia: Proposed Work

L.H. Fraser, Department of Natural Resource Sciences, Thompson Rivers University, Kamloops, BC, lfraser@tru.ca

Fraser, L.H. (2019): Biodiversity in ecosystem mine reclamation, south-central British Columbia: proposed work; in Geoscience BC Summary of Activities 2018: Minerals and Mining, Geoscience BC, Report 2019-1, p. 105–108.

Introduction

Environmental laws and regulations govern mining and oil-and-gas extraction in Canada, including reclamation. Prior to development, resource-extraction companies are required to post a bond as a promissory that their activity and closure will meet approved government environmental standards. Despite the rising demand for restoration management, there is limited research on environmental restoration and there are few dedicated university postgraduate training programs in Canada to address the complexities of ecosystem reclamation. There is a critical need to work with the mining and oil-and-gas industries, in partnership with governmental agencies, to develop better management practices for successful ecosystem restoration, and to train Highly Qualified Personnel (HQP) for reclamation work.

Current restoration plans and mine-closure proposals for land reclamation are generally not based on sound scientific evidence. They are more likely to be based on past practice and administrative and logistical constraints. In order to rectify this lack of information, optimize reclamation methods and allow for a more harmonious coexistence between industry and environment, research focused on understanding and mastering ecosystem reclamation is needed.

This project will study biodiversity of the invertebrate community along a chronosequence of reclamation sites at the New Afton mine and Highland Valley Copper mine in south-central British Columbia (Figure 1).

Biodiversity

Biodiversity describes the variety and variability of living species in an environment and can be used as a measure for ecosystem health, especially if baseline data are available and are followed over time at locations of interest. Patterns in plant diversity, and the measures to identify plant diversity, use standardized sampling and field guides; however, during biodiversity assessments, the identification of spe-

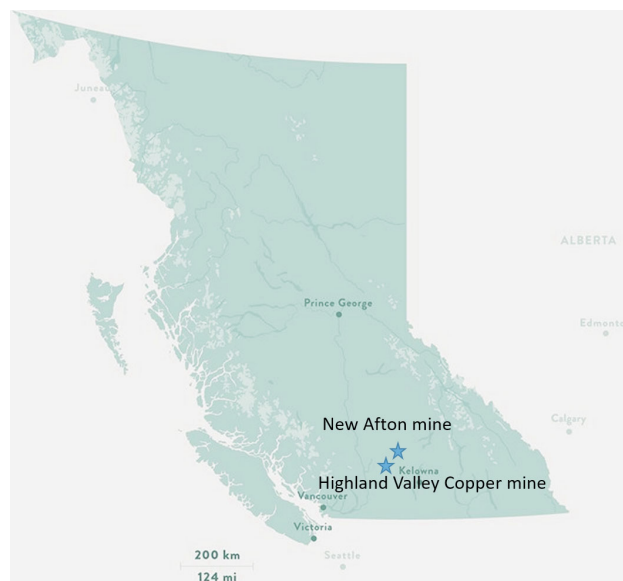


Figure 1. Locations of the New Afton mine and the Highland Valley Copper mine, south-central British Columbia.

cies, particularly invertebrates, is often best achieved using genetic analyses. Much effort has gone into finding signature genes, called ‘DNA bar codes’ for different groups of invertebrates. Each species can now be rapidly and cost-effectively identified and, with the proper sampling protocols, quantified in terms of relative abundance and diversity by site. New Gold’s New Afton mine, the industry partner for this project, is the first in Canada to employ DNA bar-coding as part of their commitment to measuring and ensuring environmental sustainability. Tracking biodiversity against pre-mining benchmarks informs restoration efforts in real time and allows changes and adjustments when needed. Restoration of animal communities to date has been based primarily on vegetation recovery, with the assumption that the animals will naturally follow. This ignores the growing scientific evidence that feedback from animals can cause top-down control that determines the abundance and diversity of plants, as well as the rate at which nutrients cycle through ecosystems. Whole ecosystem-based approaches will be employed in this study, including biodiversity planning and monitoring of all ecosystem functions and services, to guide restoration efforts throughout the entire life cycle of the mine. DNA bar-cod-

This publication is also available, free of charge, as colour digital files in Adobe Acrobat® PDF format from the Geoscience BC website: <http://www.geosciencebc.com/s/SummaryofActivities.asp>.

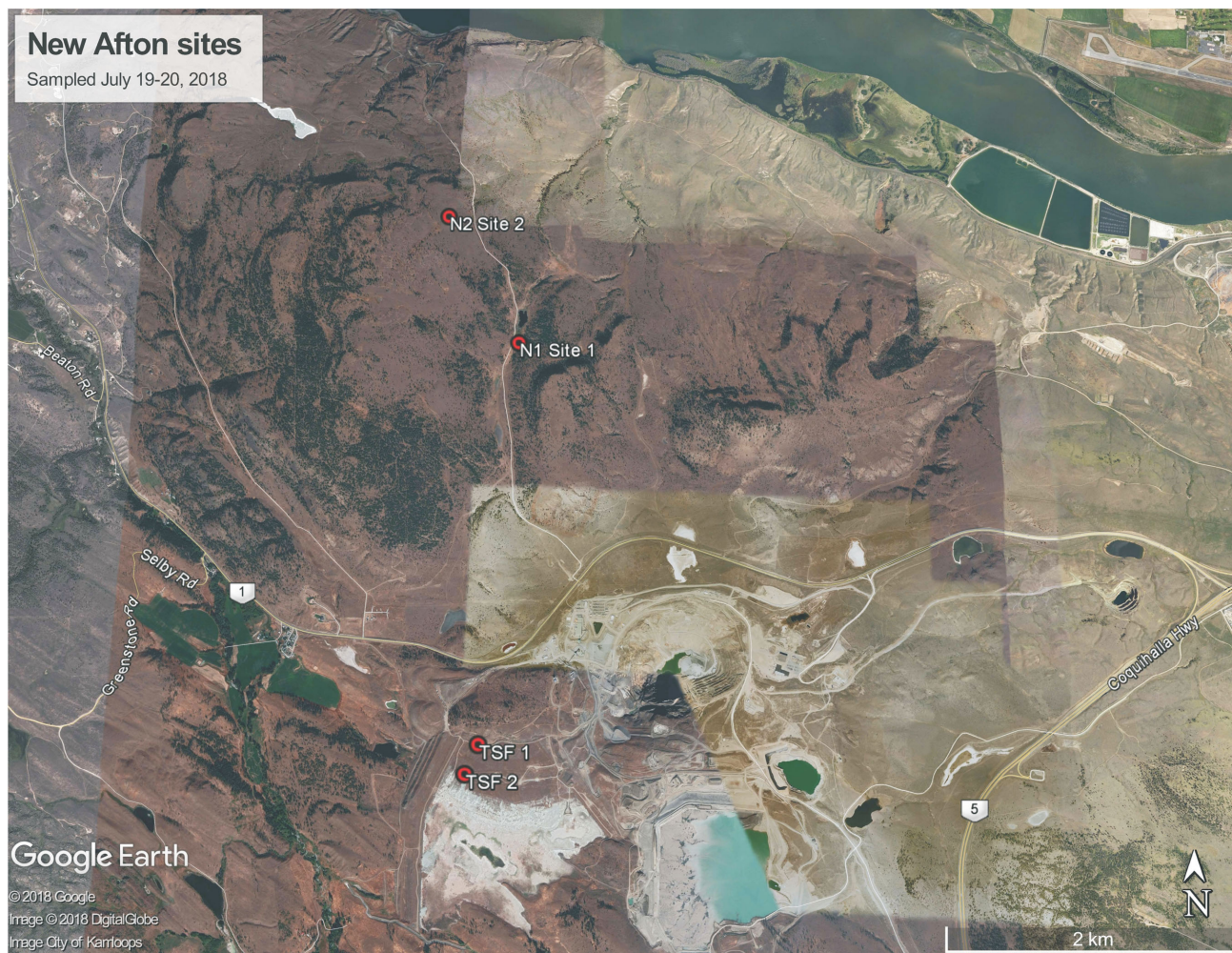


Figure 2. New Afton mine with locations of sample sites: reference sites (N1 Site 1 and N2 site 2) and old tailings storage facility (TSF 1 and TSF 2).

ing, a tool for rapid species inventory and food-web structure, will be utilized for testing species diversity and composition by focusing on invertebrates, a technique successfully adapted by New Gold Inc. for biodiversity assessment.

Methodology

Malaise traps and pitfall traps will be used at the New Afton mine and the Highland Valley Copper mine in undisturbed control sites and mine-reclamation sites. At the New Afton mine, two reference sites (Figure 2, N1 Site 1 and N2 Site 2) and two reclamation sites on the old tailings storage facility (Figure 2, TSF 1 and TSF 2) were sampled. At the Highland Valley Copper mine, thirteen sites have been selected (Figure 3). Malaise traps are tent-like structures that are used to capture flying insects. The trap intercepts insects that then fly upward toward the light and are captured in a container of an ethanol solution. Pitfall traps are small ground-insect collection traps that consist of a hole in the ground approximately 10 cm deep filled with a collection cup that contains

an ethanol solution to preserve the specimens for DNA analysis. Pitfall traps will be placed approximately every 10 m on a 90 m transect at each site for a total of 10 traps per site. One malaise trap will be placed randomly at every site. Specimens from both the pitfall and malaise traps will be collected and identified to order-level taxonomic assignment, then stored individually in ethanol solution to be sent for molecular phase analysis. Tissue samples will be collected to recover the bar code region of the cytochrome c oxidase I gene. After implementing methods used in DNA bar-coding within a genomics lab, the DNA bar codes will be compared with existing records on the Barcode of Life Database (BOLD; Ratnasingham and Hebert, 2007) to obtain species identifications for all study sites.

Conventional soil, plant and larger animal sampling will help develop a better understanding of food-web structure and complement the molecular analyses. Standard operating procedures will be drafted for users so tools incorporating markers from bar-coding and metadata can be tested, revised and validated by mine operators.



Figure 3. Highland Valley Copper mine with locations of 13 sample sites in a range of reclamation areas.

Acknowledgments

In addition to Geoscience BC, funding for this project is being provided through a Natural Sciences and Engineering Research Council of Canada Industrial Research Chair in Ecosystem Reclamation, with the following industry partners: Metro Vancouver, New Afton mine, Highland Valley Copper mine, Genome BC, Arrow Transportation, the Real Estate Foundation of BC, Kinder Morgan Canada and the

BC Cattlemen’s Association. Peer reviewed by J. Van Hamme and C. Gervan.

References

Ratnasingham, S. and Hebert, P.D.N. (2007): BOLD: The Barcode of Life Data System (www.barcodinglife.org). *Molecular Ecology Notes*, v. 7, p. 355–364, URL <<https://doi.org/10.1111/j.1471-8286.2007.01678.x>> [December 2018].

Targeting Highly Reactive Labile Magnesium in Ultramafic Tailings for Greenhouse-Gas Offsets and Potential Tailings Stabilization at the Baptiste Deposit, Central British Columbia (NTS 093K/13, 14)

S.S.S. Vanderzee, Bradshaw Research Initiative for Minerals and Mining, The University of British Columbia, Vancouver, BC, svander@eoas.ubc.ca

G.M. Dipple, Bradshaw Research Initiative for Minerals and Mining, The University of British Columbia, Vancouver, BC

P.M.D. Bradshaw, FPX Nickel Corp., Vancouver, BC

Vanderzee, S.S.S., Dipple, G.M. and Bradshaw, P.M.D. (2019): Targeting highly reactive labile magnesium in ultramafic tailings for greenhouse-gas offsets and potential tailings stabilization at the Baptiste deposit, central British Columbia (NTS 093K/13, 14); *in* Geoscience BC Summary of Activities 2018: Minerals and Mining, Geoscience BC, Report 2019-1, p. 109–118.

Introduction

The products of mining are essential for modern society, the renewable energy infrastructure and transportation systems of the future; however, their recovery produces an enormous volume of solid waste and is a significant contributor to anthropogenic greenhouse-gas emissions. The amount of mine waste produced worldwide is on the same order of magnitude as that of natural Earth-shaping erosional processes: some tens of billions of tonnes of waste per year (Fyfe, 1981; Förstner, 1999; Blight, 2011), most of which consists of tailings (Kossoff et al., 2014). Mine tailings (pulverized rock that remains after the extraction of economic metals and minerals) are often disposed of within dammed impoundments called tailings storage facilities. The physical stability of mine tailings is important because the failure of the impoundment walls can result in the release of large volumes of waste, which can cause significant environmental and economic damage, and in some cases, loss of human life (do Carmo et al., 2017). The focus of this paper is achieving optimal management of mine tailings and reducing greenhouse-gas (GHG) emissions, which is important to the sustainability of extractive industries and society as a whole (Intergovernmental Panel on Climate Change, 2014; Kossoff et al., 2014).

One method for stabilizing mine tailings suggested by Choi et al. (2009) is the addition of binders such as Portland cement. Choi et al. (2009) found that a Portland cement content of 5 wt. % was sufficient to stabilize the tailings and satisfy unconfined compressive strength guidelines of 0.35 MPa (50 psi.), which is generally accepted to represent stabilized waste that can withstand overburden pressures in a landfill (LaGrega et al., 1994). This approach would,

however, increase a mine's carbon footprint because approximately 800 kg of CO₂ is produced by manufacturing 1 t of Portland cement (Worrell et al., 2001). It would also add significant costs because Portland cement is approximately US\$100/t (Statista, 2018); therefore, 5 wt. % consumption per tonne of tailings would add \$5/t to the mining costs.

For mines that produce ultramafic tailings, an attractive and potentially cost-effective option is to promote the sequestration of CO₂ in the tailings, which has the potential to promote stabilization by the formation of cementitious secondary magnesium carbonate minerals within the tailings after they are deposited. This can be accomplished through the exposure of the tailings to atmospheric CO₂ and/or concentrated CO₂ steam such as flue gas. This results in the alteration of magnesium hydroxide minerals (e.g., brucite {Mg(OH)₂} and hydrotalcite-group minerals such as iowaite {Mg₆Fe₂(OH)₁₆Cl₂·H₂O}) that are typically present in trace abundance in ultramafic tailings (Wilson et al., 2014) along with the more abundant magnesium silicate minerals (e.g., serpentine {Mg₃Si₂O₅(OH)₄}). During the process, termed carbon mineralization, magnesium ions (Mg²⁺) are released into the pore water of the tailings where they can then react with dissolved CO₂ species such as HCO₃⁻ to precipitate magnesium carbonate minerals such as nesquehonite {MgCO₃·3H₂O}, dypingite {Mg₅(CO₃)₄(OH)₂·5H₂O} and hydromagnesite ({Mg₅(CO₃)₄(OH)₂·4H₂O}; Wilson et al., 2014). These reactions effectively turn the CO₂ gas into an environmentally benign mineral. The most economically viable method to accelerate these reactions is likely to target tailings that contain enriched levels of highly reactive labile magnesium so that energy- and chemical-intensive acceleration technologies are not required to overcome the relatively slow bulk dissolution rates of magnesium silicate minerals (Daval et al., 2013).

This publication is also available, free of charge, as colour digital files in Adobe Acrobat® PDF format from the Geoscience BC website: <http://www.geosciencebc.com/s/SummaryofActivities.asp>.

The authors define labile magnesium as being sourced from highly reactive hydroxide minerals—brucite and hydrotalcites—and from the surface of serpentine, where the very outer layers of the sheet silicate will readily release their magnesium ions but the bulk of the mineral grain will not (Thom et al., 2013). Based on Thom et al. (2013), Harrison et al. (2015) and our preliminary flow-through dissolution experiments, this paper considers 100% of the magnesium in brucite and hydrotalcites to be labile and 2.5% of the magnesium in serpentine to be labile. The labile magnesium ions are much more rapidly released into the pore water of tailings at atmospheric temperature and pressure; therefore, secondary magnesium carbonate cement can be readily produced at low cost and within a relatively short time frame. In the case of the Mount Keith nickel mine in Western Australia, 11% of annual CO₂ emissions were unintentionally offset due to the uptake of CO₂ from the atmosphere by labile magnesium-bearing tailings without any additional costs, and reactive transport models infer that small changes in tailings management practices could allow the labile magnesium to fully react and offset up to 60% of the mine’s emissions (Wilson et al., 2014).

A problem with using this process at a mine site to stabilize tailings and significantly offset greenhouse-gas emissions is that the labile magnesium content within a single mineral deposit, and therefore within mine tailings, is highly variable due to the inherent geological variability. The abundance and spatial distribution of labile magnesium throughout a mineral deposit can be inferred by measuring mineral abundance in exploration drillcore through Rietveld X-ray diffraction; however, this technique is time and cost intensive and is not practical for mine planning reconnaissance studies that can require a mineral abundance analysis of several tens of thousands of samples. Alternatively, the problem can be solved by using estimations of mineral abundance that can be rapidly and inexpensively computed from whole-rock analytical data that are routinely collected on drillcore during exploration. In this paper, the authors apply the projection method of computing mineral abundance (Thompson, 1982; Gordon and Dipple, 1999) to the whole-rock analytical data from exploration drillcore from the Baptiste nickel deposit (MINFILE 093K 116; BC Geological Survey, 2018), which is part of the Decar nickel district in central British Columbia (BC). This deposit is unique in that the nickel is hosted within a highly magnetic and dense nickel-iron alloy called awaruite (Britten, 2017; Milidragovic et al., 2018). The mineral abundance computations are used to estimate the labile magnesium content of the Baptiste nickel deposit, and therefore, the carbon sequestration potential. This allows the spatial distribution of the labile magnesium to be mapped and the enriched zones to be targeted for the creation of cemented and stabilized tailings impoundment walls. If successful at a mine operating scale, this could

reduce the cost of tailings storage as well as the magnitude of environmental risk.

Methods

Whole-Rock Chemical Compositions

The whole-rock chemical composition of 9990 exploration drillcore pulps from the Baptiste nickel deposit were determined by four-acid digestion followed by inductively coupled plasma–optical emission spectrometry (ICP-OES) analysis and were supplied by FPX Nickel Corp. These data were reduced to 7604 samples by removing samples labeled as wasterock (2323 samples) and dikes (63 samples). Included in these data are measurements of loss on ignition (LOI), which can be derived from the volatilization of H₂O from hydroxyl within brucite and serpentine, CO₂ from carbonate minerals and SO₂ following the oxidation of sulphide minerals during ignition. It is assumed that the LOI is derived solely from H₂O loss because carbonate-bearing rock types such as listwanite (which is composed of magnesite and quartz and is not a source of labile magnesium) were removed from the dataset by the wasterock query filter, and the sulphur content of the Baptiste samples was negligible (mean of 0.02 wt. %). The major-element composition for the test set of 30 samples with high MgO that was used for model calibration and validation is shown in Table 1.

Rietveld X-ray Diffraction

In this paper, Rietveld X-ray diffraction (R-XRD) data on 10 samples were used to determine the model minerals, which are minerals that are characteristic of the deposit—or at least characteristic of specific zones of interest within the deposit—and to calibrate the mineral abundance computation model. An additional 20 samples were used to validate the computations of the model. The samples analyzed by R-XRD were coarse rejects from exploration pulps and were prepared for XRD analysis by first reducing the material’s particle size in a steel ring mill for 5 minutes. The material was then further pulverized as an ethanol slurry in a vibratory McCrone micronizing mill for 7 minutes (Wilson et al., 2006). The R-XRD results are shown in Table 2.

Computing Mineral Abundance from Whole-Rock Elemental Compositions

A mass balance relationship is used to determine what proportion of the model minerals best explains the whole-rock chemical assay data. There must be a mass balance for each of the m constituents (commonly the oxides that represent most of the rock) of the analyses with the computed model mineral abundances n . These mass balances can be expressed as follows:

$$\sum_{j=1}^n a_{ij}x_j = b_i \quad \begin{matrix} i = 1, 2, \dots, m \\ j = 1, 2, \dots, m \end{matrix} \quad (1)$$

where a_{ij} represents the amount of constituent i in mineral j , b_i represents the amounts of constituent i in the whole-rock chemical composition and x_j represents the unknown abundance of model minerals. In this approach, exchange components are allowed for (Thompson, 1982), which in this paper allows Fe^{2+} to substitute for Mg^{2+} (FeMg_{-1}) and $\text{Fe}^{3+}\text{Al}^{3+}$ to substitute for $\text{Fe}^{2+}\text{Si}^{4+}$ (AlSi_{-1}) within minerals to an extent that best fits the projected mineral abundance to the whole-rock chemical assay data, and allows each sample to have a unique computed mineral composition.

The computations were performed in MATLAB by describing the mass balance equation (equation 1) as the system of equations shown below. Based on the R-XRD data in Table 2, brucite $\{\text{Mg}(\text{OH})_2\}$, magnetite $\{\text{Fe}_3\text{O}_4\}$, forsterite $\{\text{Mg}_2\text{SiO}_4\}$, serpentine $\{\text{Mg}_3\text{Si}_2\text{O}_5(\text{OH})_4\}$ and diopside $\{\text{CaMgSi}_2\text{O}_6\}$ were used as model minerals to explain the whole-rock chemical assay data; however, the addition of the FeMg_{-1} exchange component introduces an unknown into the computation formula without adding an equation because no new major chemical constituents are introduced. As a result, if all the model minerals identified in Ta-

ble 2 were retained in addition to the exchange components, the system would become underdetermined and a unique solution for mineral abundance would not be obtainable. This necessitates the removal of one of the model minerals so that the number of unknowns will equal the number of equations. Magnetite was selected for removal because the R-XRD and whole-rock composition assay data showed that the magnetite abundance was not proportional to the total amount of Fe in the sample, and the measured abundance in the 10 calibration samples showed a relatively low degree of variability (~1–5 wt. % magnetite). A constant magnetite abundance of 3.8 wt. % was assumed in all samples, which was estimated based on petrographic and geochemical data. Now that the model minerals, their constituents (Table 1) and exchange components have been identified, the system of equations can be described in matrix form, as seen in Figure 1.

The projection model was then empirically refined based on the quantitative R-XRD data by adjusting a series of parameters (serpentine composition and the percentage of LOI associated with the dihydroxylation of serpentine and

Table 1. Major-element chemical composition of the test set of 30 samples with high MgO used for model calibration validation. Abbreviation: LOI, loss on ignition.

Sample code	Fe ₂ O ₃ (wt. %)	MgO (wt. %)	CaO (wt. %)	SiO ₂ (wt. %)	Al ₂ O ₃	LOI	Total
Model calibration samples							
1423082	7.81	43.07	0.04	33.74	0.06	14.21	98.93
1423072	7.9	42.85	0.02	34.65	0.15	14.73	100.3
1423092	7.97	42.89	0.09	35.41	0.06	13.97	100.39
1423128	7.02	42.39	0.05	37.35	0.21	12.71	99.73
1423127	7.88	42.52	0.1	36.05	0.4	12.74	99.69
1423090	8.07	39.65	0.47	37.1	1.12	12.66	99.07
1423106	7.37	40.68	0.2	38.95	0.82	12.28	100.3
1423149	8.39	40.83	0.54	37.99	0.84	11.68	100.27
1423108	7.36	37.39	1.5	38.99	1.86	11.56	98.66
1423111	8.32	37.69	0.86	39.45	1.75	11.51	99.58
Model validation samples							
1423073	7.62	41.93	0.01	35.72	0.08	14.19	99.55
1423078	7.84	43.12	0.03	36.45	0.29	12.18	99.91
1423079	8.18	42.41	0.03	35.03	0.19	14.25	100.09
1423083	7.77	42.57	0.03	34.9	0.06	14.48	99.81
1423084	7.22	42.27	0.01	33.67	0.06	14.08	97.31
1423086	7.87	42.15	0.01	34.41	0.12	14.05	98.61
1423088	7.63	42.47	0.02	35.39	0.24	12.83	98.58
1423091	7.48	41.41	0.03	34.28	0.12	14.01	97.33
1423094	7.63	42.51	0.01	33.81	0.06	14.28	98.3
1423096	6.64	43.09	0.02	35.69	0.18	13.45	99.07
1423116	7.96	37.13	0.85	39.19	1.48	11.96	98.57
1423117	8.49	38.34	0.75	38.81	1.36	12.33	100.08
1423118	8.26	36.99	1.13	38.55	1.7	12.02	98.65
1423134	7.69	40.86	0.26	36.47	0.72	12.99	98.99
1423132	8.47	40.66	0.14	37.22	0.89	13.09	100.47
1423162	7.64	38.3	0.82	38.5	1.46	12.28	99
1423167	7.84	38.22	1.43	37.74	1.07	12.49	98.79
1423178	8.19	38.14	1.71	39	1.21	12.32	100.57
1423188	7.98	38.7	1.48	39.19	1.29	11.98	100.62
1423189	7.87	39	1.58	38.87	1.25	11.99	100.56

Table 2. Results of Rietveld X-ray diffraction refinement on course rejects of exploration pulps.

Sample code	Brucite (wt. %)	Magnetite (wt. %)	Forsterite (wt. %)	Serpentine (wt. %)	Diopside (wt. %)
Model calibration samples					
1423082	12.61	3.55	4.79	78.4	0.66
1423072	10.12	4.08	3.44	81.84	0.52
1423092	9.79	2.48	2.95	83.52	1.26
1423128	6.77	3.57	8.33	81.33	0
1423127	4.58	2.2	11.56	81.65	0
1423090	1.84	1.82	10.95	84.56	0.83
1423106	1.44	1.65	11.04	85.61	0.25
1423149	1.15	1.32	17.6	78.97	0.96
1423108	0.53	3.09	5.88	87.51	2.99
1423111	0.24	4.6	3.92	88.88	2.37
Model validation samples					
1423073	10.68	5.94	3	79.85	0.53
1423078	5.8	1.98	20.5	71.42	0.3
1423079	9.62	3.42	6.42	80.11	0.43
1423083	12.19	4.79	3.52	78.95	0.56
1423084	12.57	6.46	4.19	76.28	0.5
1423086	10.78	4.5	5.48	78.87	0.37
1423088	7.46	3	13.32	76.19	0.01
1423091	10.81	6.71	4.52	77.69	0.28
1423094	10.74	2.8	3.46	82.25	0.73
1423096	9.58	4.29	7.42	78.3	0.41
1423116	0.56	4.17	2.74	90.44	2.08
1423117	0.68	3.43	4.21	90.07	1.59
1423118	0.29	3.12	5.32	89.59	1.68
1423134	4.97	3.1	7.27	83.92	0.73
1423132	1.82	2.69	4.43	90	1.06
1423162	0.74	2.66	7.78	87.14	1.7
1423167	1.09	1.54	10.47	84.45	2.45
1423178	0.78	2.78	4.93	88.1	3.43
1423188	0.77	2.73	8.92	84.6	2.99
1423189	0.89	2.39	9.51	83.9	3.17

$$\begin{matrix}
 \mathbf{X} & & \mathbf{A} & & \mathbf{B} \\
 \left[\begin{array}{cccccc}
 n_{\text{Brc},1} & n_{\text{Fo},1} & n_{\text{Di},1} & n_{\text{FeMg},1,1} & n_{\text{Atg},1} & n_{\text{AlSi},1,1} \\
 n_{\text{Brc},2} & n_{\text{Fo},2} & n_{\text{Di},2} & n_{\text{FeMg},1,2} & n_{\text{Atg},2} & n_{\text{AlSi},1,2} \\
 \dots & \dots & \dots & \dots & \dots & \dots \\
 n_{\text{Brc},n} & n_{\text{Fo},n} & n_{\text{Di},n} & n_{\text{FeMg},1,n} & n_{\text{Atg},n} & n_{\text{AlSi},1,n}
 \end{array} \right] & \cdot & \left[\begin{array}{cccccc}
 0 & 1 & 0 & 0 & 0 & 1 \\
 0 & 2 & 0 & 1 & 0 & 0 \\
 0 & 1 & 1 & 2 & 0 & 0 \\
 1 & -1 & 0 & 0 & 0 & 0 \\
 0 & 3 & 0 & 2 & 0 & 2 \\
 0 & 0 & 0 & -1 & 1 & 0
 \end{array} \right] & = & \left[\begin{array}{cccccc}
 n_{\text{Fe},1} & n_{\text{Mg},1} & n_{\text{Ca},1} & n_{\text{Si},1} & n_{\text{Al},1} & n_{\text{H}_2\text{O},1} \\
 n_{\text{Fe},2} & n_{\text{Mg},2} & n_{\text{Ca},2} & n_{\text{Si},2} & n_{\text{Al},2} & n_{\text{H}_2\text{O},2} \\
 \dots & \dots & \dots & \dots & \dots & \dots \\
 n_{\text{Fe},n} & n_{\text{Mg},n} & n_{\text{Ca},n} & n_{\text{Si},n} & n_{\text{Al},n} & n_{\text{H}_2\text{O},n}
 \end{array} \right]
 \end{matrix}$$

Figure 1. System of equations used to compute mineral abundances within the Baptiste nickel deposit, where the 'X' matrix is the unknown and defines the number of moles of each model mineral or exchange component per 100 g of material, with column dimensions defined by the number of model minerals plus the number of exchange components, and row dimensions by the number of samples (n). The 'A' matrix represents the molar stoichiometry of each model mineral and exchange component. As shown by the labels adjacent to the A matrix, the column dimensions are defined by the major chemical constituents (e.g., Fe, Mg, H₂O) and the row dimensions are defined by the model minerals and exchange components. Lastly, the 'B' matrix defines the number of moles of each chemical component per 100 g of material, with column dimensions defined by the number of major chemical components and row dimensions defined by the number of samples (n). The values in the B matrix are obtained by converting whole-rock geochemical assay data (Table 1) from weight percent oxide to molar concentrations. Abbreviations: Atg, antigorite; Brc, brucite; Di, diopside; Fo, forsterite.

brucite) through a least squares approach. The serpentine composition was refined so that the magnesium to silicon ratio was 1.57 to 1.0, and the LOI was adjusted by a factor of 0.96 to reflect structurally bound water. The mineral abundance computation model was refined based on R-XRD results for 10 samples and 20 additional samples were used to verify the computations of the model.

Results

Brucite and serpentine are the predominant sources of labile magnesium in the Baptiste nickel deposit. Accurate estimation of their abundance is therefore important for estimating labile magnesium abundance. A comparison between the measured and computed abundance of brucite is shown in Figure 2. The first 10 samples were used to calibrate the projection model and an additional 20 samples were analyzed after the projection model was built to test its accuracy. Figure 2 shows that the projection model could provide useful mineralogical computations with an average difference between the measured and computed brucite abundance of -0.1 wt. % and a standard deviation of 1.1 wt. %. Where the projection model produced negative computed brucite abundances (1477 samples out of 7604), the values were set to zero and might be explained by the presence of trace or amorphous minerals that were not included as model minerals.

Figure 3 shows the comparisons between the measured and computed abundances of all the model minerals that were included in the projection model and shows that the projection model also has strong predictive capability for serpentine content, which is important because the mineral surfaces of serpentine are also a significant source of labile magnesium. The forsterite and diopside computations are significantly less reliable; however, this is not important

because forsterite and diopside do not contribute a significant amount of labile magnesium (or calcium) to mine tailings because of low reactive surface area density and slow dissolution kinetics, respectively.

The projection model was then applied to all 7604 whole-rock assays from the Baptiste deposit to assess the mineralogical heterogeneity, the labile magnesium content as a measure of the carbon sequestration capacity and the fraction and location of future tailings material that has sufficient labile magnesium to potentially stabilize the tailings through carbon mineralization. Histograms of computed brucite and serpentine content within the Baptiste deposit are shown in Figure 4. Although more than 25% of the deposit is computed to have no brucite, 75% contains brucite ranging from trace amounts to in excess of 10%. Serpentine dominates the mineralogy of all samples.

Implications

Labile magnesium content estimated from computed mineral content is plotted as weight percent MgO in Figure 5. This provides a preliminary assessment of the carbon sequestration capacity of mine tailings. To estimate greenhouse-gas emissions from mine operations production data from the Mount Keith nickel mine in Western Australia, a serpentinite-hosted nickel deposit was used. At Mount Keith, natural gas is used to generate electricity for the ore processing facility (which accounted for $\sim 66\%$ of their CO_2 emissions) and diesel-powered mining haul trucks account for the remaining $\sim 34\%$ (WMC Resources Ltd., 2002). In total, the mine produced $33.6 \text{ t CO}_2/\text{kt}$ rock mined (Wilson et al., 2014); therefore, mines that use hydroelectric power still need to sequester $11.4 \text{ t CO}_2/\text{kt}$ rock mined to be GHG neutral due to emissions from the haul truck fleet. From these data, it can be estimated that an average of 1.3 wt. %

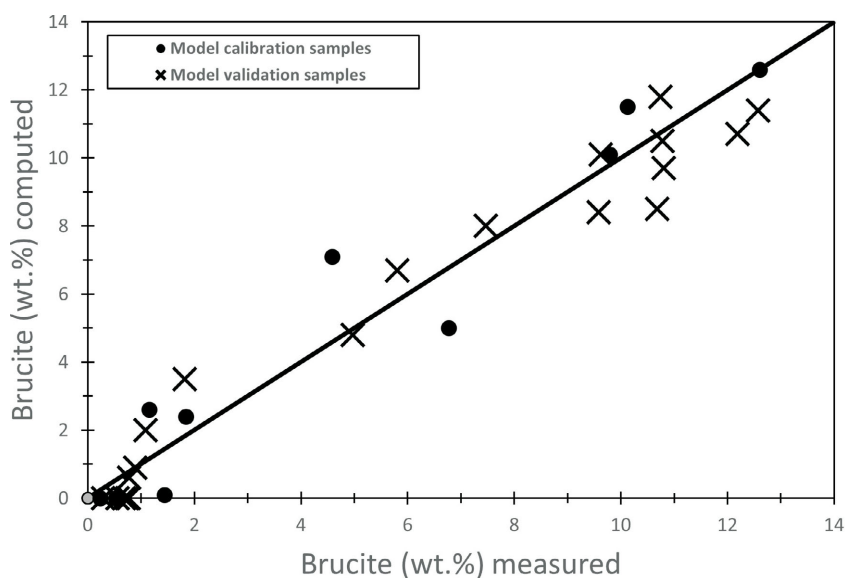


Figure 2. Abundance of brucite computed by the projection model versus the brucite abundance measured by Rietveld X-ray diffraction.

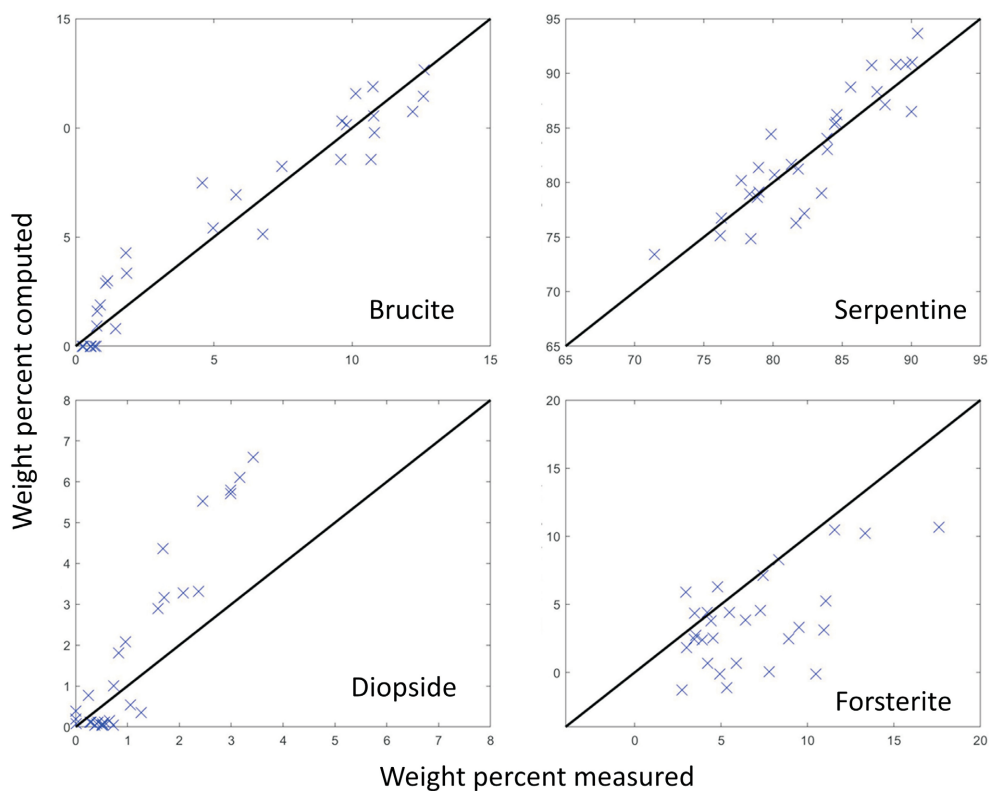


Figure 3. Mineral abundance for brucite and three other minerals computed by the projection model versus the mineral abundance measured by Rietveld X-ray diffraction.

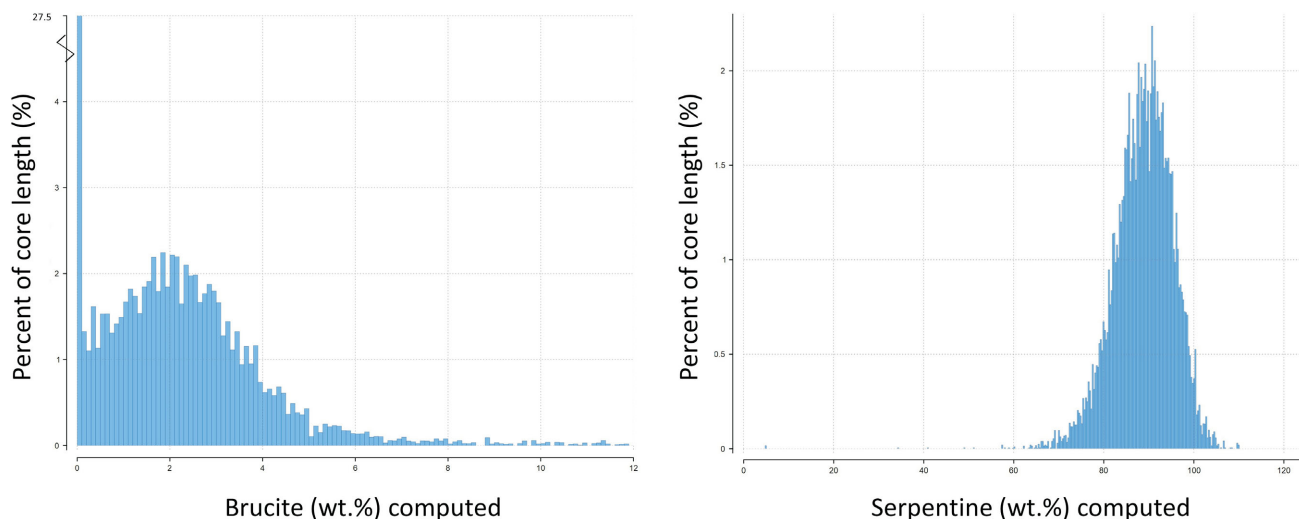


Figure 4. Abundance of brucite and serpentine computed by the projection model across the Baptiste nickel deposit. Samples described as wasterock or dikes in the geochemistry dataset were omitted. The mean brucite and serpentine content is 1.8 wt. % and 88.8 wt. % respectively.

labile MgO is sufficient to make an open-pit nickel mine carbon neutral assuming hydroelectricity is used, and 3.9 wt. % labile MgO if natural gas is used for electricity generation. The Baptiste nickel mine is located near hydro-electric infrastructure; therefore, an estimated average of 1.3 wt. % labile MgO would provide sufficient capacity for carbon-neutral mining. Figure 5 shows that the projection model computations give an average labile magnesium

content of 2.3 wt. %. This suggests that the Baptiste mine has more than enough carbon sequestration capacity from labile magnesium to become a carbon neutral mine. Figure 6 shows that if carbon mineralization efforts are focused on the most labile magnesium-rich tailings, only 30% of the tailings need to react with CO₂ to make the Baptiste mine carbon neutral over its lifetime. In addition, this same labile magnesium-rich 30% fraction of the tail-

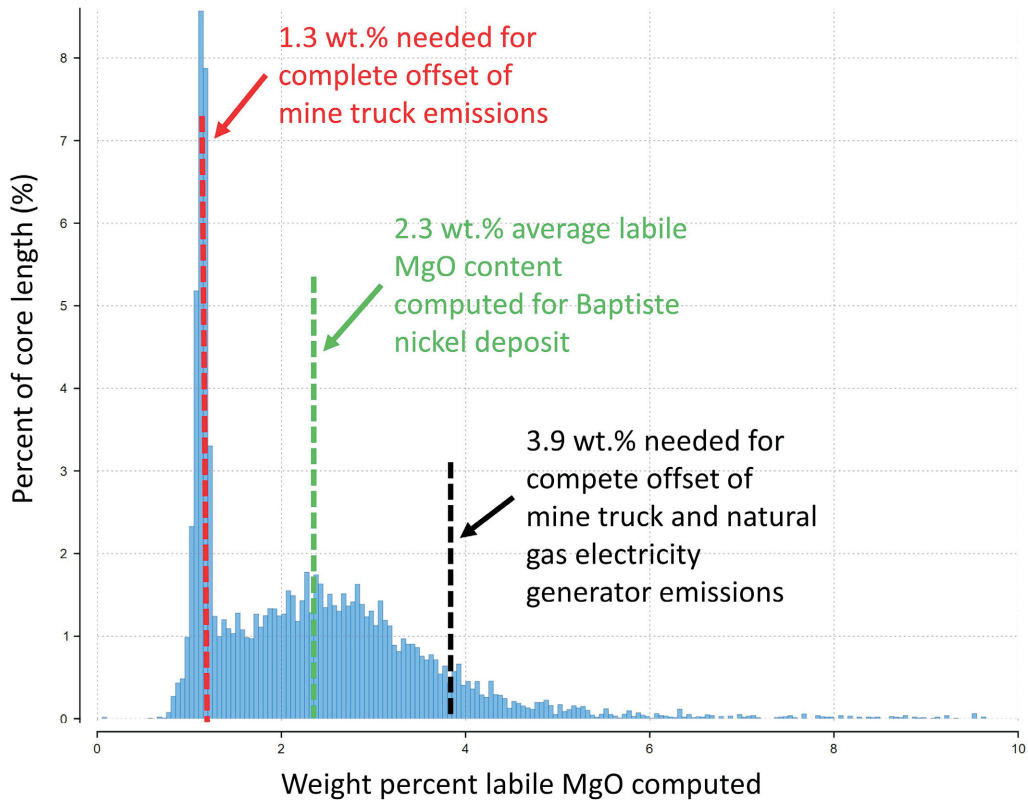


Figure 5. Histogram of the computed labile magnesium content of drillcore from the Baptiste nickel deposit.

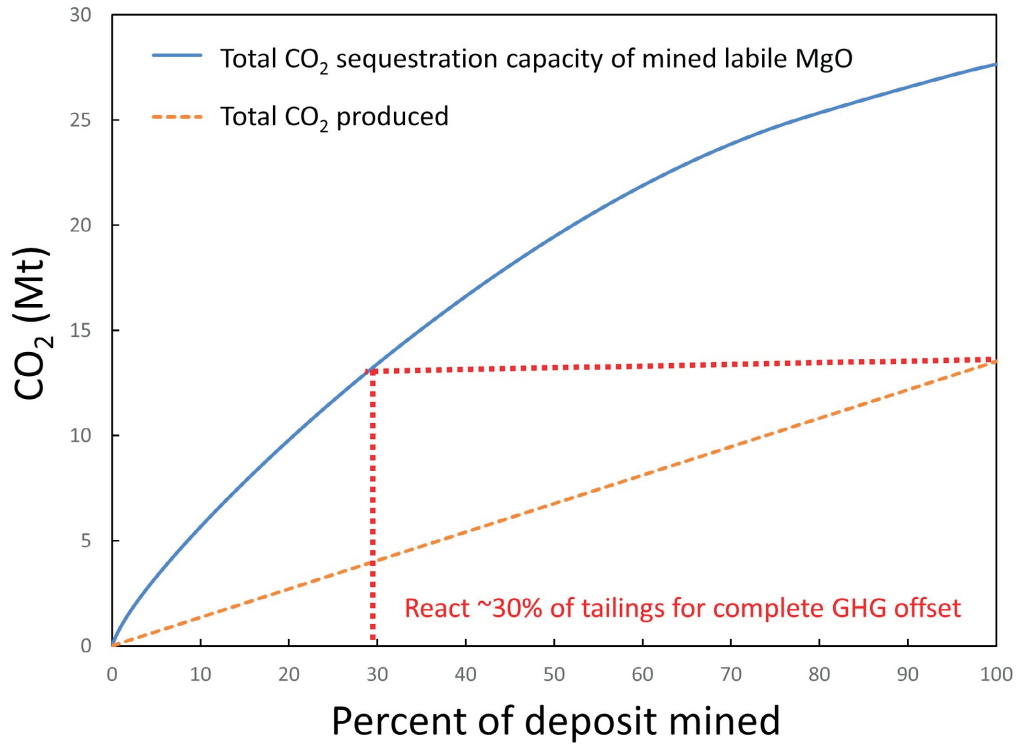


Figure 6. Anticipated CO₂ emissions from nickel mining as a function of the percentage of the deposit that has been mined. The authors assume 1.8 Gt of rock will be mined because this represents the indicated reserve of the Baptiste deposit (FPX Nickel Corp., 2018). The solid line shows the potential rate of carbon sequestration if the most labile magnesium-rich (MgO) zones are used first. Hydroelectricity is assumed for computed complete greenhouse-gas (GHG) offset.

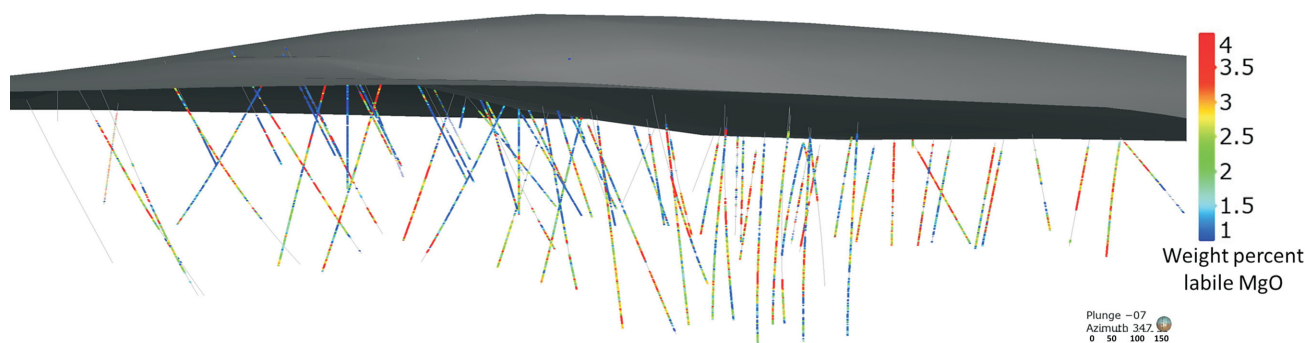


Figure 7. Computed labile magnesium (in wt. % MgO) in mineralized drillcore sections of the Baptiste nickel deposit, central British Columbia. Wasterock sections are shown in grey and were excluded from labile magnesium computations.

ings has the potential to become stabilized by the formation of magnesium carbonate cement, as indicated by lab-scale tests that showed that tailings with approximately 3 wt. % brucite or more can achieve unconfined compressive strengths of approximately 4137 kPa (600 psi.) to more than 5516 kPa (800 psi.) after sequestering 10% CO₂ for two weeks (Vanderzee et al., 2018).

These results may be typical of serpentinite-hosted nickel deposits. For example, carbon mineralization in tailings of the Mount Keith nickel mine has been documented (Wilson et al., 2014) and the potential at the Dumont nickel mine in Quebec is being explored (Kandji et al., 2017). To help target the labile magnesium-rich areas of mineral deposits for carbon mineralization purposes, the authors propose using exploration geochemical data to make mineral abundance computations so that 3-D maps of labile magnesium (Figure 7) can be incorporated into the mine plan.

Conclusions and Future Work

This study, in combination with Vanderzee et al. (2018), has demonstrated at the lab scale that the Baptiste mine likely contains enough labile magnesium to potentially sequester all the CO₂ produced by its mining trucks (11.4 t CO₂/kt rock mined). This would make Baptiste GHG neutral if it used hydroelectric power, which is likely to be the case in BC, and may stabilize the tailings at the same time. To improve, or at least complement, the accuracy of the labile magnesium estimations, other methods of computing mineral abundance can be applied to Baptiste. These methods include linear programming (Gordon and Dipple, 1999), phase equilibria (Connolly, 2005) and MINSQ (Herrmann and Berry, 2002). Furthermore, the authors' laboratory work on tailings stabilization has been very encouraging and the next steps include investigating methods to further accelerate the reaction rates by promoting the transport of CO₂ into the tailings and conducting larger field-scale experiments. These experiments will include measurements of CO₂ sequestration rates, stabilization tests and reactive transport modelling. If the laboratory work can be verified at the field scale, Baptiste could be revolutionary for tail-

ings management and climate change mitigation efforts, as well as for being the first awaruite deposit in the world to be mined.

Acknowledgments

In addition to Geoscience BC, the authors acknowledge FPX Nickel Corp. and the Natural Sciences and Engineering Research Council for financial support of this project. The authors also thank D. Milidragovic from the BC Geological Survey for reviewing this paper.

References

- BC Geological Survey (2018): MINFILE BC mineral deposits database; BC Ministry of Energy, Mines and Petroleum Resources, BC Geological Survey, URL <<http://minfile.ca/>> [November 2018].
- Blight, G. (2011): Mine waste: a brief overview of origins, quantities and methods of storage; *in* Waste: A Handbook for Management, p. 77–88.
- Britten, R. (2017): Regional metallogeny and genesis of a new deposit type-disseminated awaruite (Ni₃Fe) mineralization hosted in the Cache Creek terrane; *Economic Geology*, v. 112, p. 517–550.
- do Carmo, F.F., Kamino, L.H.Y., Junior, R.T., de Campos, I.C., de Carmo, F.F., Silvino, G., da Silva, K.J., de Castro, X., Mauro, M.L., Rodrigues, N.U.A., de Souza Miranda, M.P. and Pinto, C.E.F. (2017): Fundão tailings dam failures: the environment tragedy of the largest technological disaster of Brazilian mining in global context; *Perspectives in Ecology and Conservation*, v. 15, no. 3, p. 145–151.
- Choi, W.H., Lee, S.R. and Park, J.Y. (2009): Cement based solidification/stabilization of arsenic-contaminated mine tailings; *Waste Management*, v. 29, no. 5, p. 1766–1771.
- Connolly, J.A.D. (2005): Computation of phase equilibria by linear programming: a tool for geodynamic modeling and its application to subduction zone decarbonation; *Earth and Planetary Science Letters*, v. 236, p. 524–541.
- Daval, D., Hellmann, R., Martinez, I., Gangloff, S. and Guyot, F. (2013): Lizardite serpentine dissolution kinetics as a function of pH and temperature, including effects of elevated pCO₂; *Chemical Geology*, v. 351, p. 245–256.
- Dipple, G.M., Raudsepp, M. and Gordon, T.M. (2001): Assaying wollastonite in skarn; *in* CIM Special Volume: Industrial Minerals in Canada, p. 1–10.

- Förstner, U. (1999): Introduction; *in* Environmental Impacts of Mining Activities: Emphasis on Mitigation and Remedial Measures, Springer, Heidelberg, p. 1–3.
- FPX Nickel Corp. (2018): Developing Canada’s next nickel district; FPX Nickel Corp., URL <<https://fpxnickel.com/wp-content/uploads/2017/08/FPX-Nickel-Corporate-Presentation.pdf>> [November 2018].
- Fyfe, W. (1981): The environmental crisis: quantifying geosphere interactions; *Science*, v. 213, p. 105–110.
- Gordon, T.M. and Dipple, G.M. (1999): Measuring mineral abundance in skarn. II. A new linear programming formulation and comparison with projection and Rietveld methods; *The Canadian Mineralogist*, v. 37, p. 17–26.
- Harrison, A.L., Dipple, G.M., Power, I.M. and Mayer, K.U. (2015): Influence of surface passivation and water content on mineral reactions in unsaturated porous media: implications for brucite carbonation and CO₂ sequestration; *Geochimica et Cosmochimica Acta*, v. 148, p. 477–495.
- Herrmann, W. and Berry, R.F. (2002): MINSQ – a least squares spreadsheet method for calculating mineral proportions from whole rock major element analyses; *Geochemistry: Exploration, Environment, Analysis*, v. 2, no. 4, p. 361–368.
- International Panel on Climate Change (2014): Summary for policymakers; *in* Climate Change 2014: Impacts, Adaptation, and Vulnerability, Part A: Global and Sectoral Aspects, Contribution of Working Group II to the Fifth Assessment Report of the Intergovernmental Panel on Climate Change. C.B. Field, V.R. Barros, D.J. Dokken, K.J. Mach, M.D. Mastrandrea, T.E. Bilir, M. Chatterjee, K.L. Ebi, Y.O. Estrada, R.C. Genova, B. Girma, E.S. Kissel, A.N. Levy, S. MacCracken, P.R. Mastrandrea and L.L. White (ed.), Cambridge University Press, Cambridge, UK, p. 1–32.
- Kandji, E.H., Plante, B., Bussière, B., Beaudoin, G. and Dupont, P.P. (2017): Geochemical behavior of ultramafic waste rocks with carbon sequestration potential: a case study of the Dumont Nickel Project, Amos, Québec; *Environmental Science and Pollution Research*, v. 24, p. 11734–11751, URL <<https://doi.org/10.1007/S11356-017-8735-9>> [November 2018].
- Kossoff, D., Dubbin, W.E., Alfredsson, M., Edwards, S.J., Macklin, M.G. and Hudson-Edwards, K. (2014): Mine tailings dams: characteristics, failure, environmental impacts, and remediation; *Applied Geochemistry*, v. 51, p. 229–245.
- LaGrega, M.D., Buckingham, P.L. and Evans, J.C. (1994): Hazardous Waste Management; McGraw-Hill Inc., New York, 1202 p.
- Mildragovic, D., Grundy, R. and Schiarizza, P. (2018): Geology of the Decar area north of Trembleur Lake, NTS 93K/14; *in* Geological Fieldwork 2017, BC Ministry of Energy, Mines and Petroleum Resources, BC Geological Survey, Paper 2018-1, p. 129–142.
- Statista (2018): Cement prices in the United States from 2007 to 2017; URL <<https://www.statista.com/statistics/219339/us-prices-of-cement/>> [November 2018].
- Thompson, J.B., Jr. (1982): Reaction space: an algebraic and geometric approach; *in* Characterization of Metamorphism through Mineral Equilibria; *Reviews in Mineralogy and Geochemistry*, v. 10, p. 33–52.
- Thom, J.G.M., Dipple, G.M., Power, I.M. and Harrison, A.L. (2013): Chrysotile dissolution rates: implications for carbon sequestration; *Applied Geochemistry*, v. 35, p. 244–254.
- Vanderzee, S.S.S., Power, I.M., Dipple, G.M. and Bradshaw, P.M.D. (2018): Carbon mineralization in ultramafic tailings, central British Columbia: a prospect for stabilizing mine waste and reducing greenhouse gas emissions; *in* Geoscience BC Summary of Activities 2017: Minerals and Mining, Geoscience BC, Report 2018-1, p. 109–112.
- Wilson, S.A., Raudsepp, M. and Dipple, G.M. (2006): Verifying and quantifying carbon fixation in minerals from serpentine-rich mine tailings using the Rietveld method with X-ray powder diffraction data; *American Mineralogist*, v. 91, p. 1331–1341.
- Wilson, S.A., Harrison, A.L., Dipple, G.M., Power, I.M., Barker, S.L.L., Mayer, K.U., Fallon, S.J., Raudsepp, M. and Southam, G. (2014): Offsetting of CO₂ emissions by air capture in mine tailings at the Mount Keith Nickel Mine, Western Australia: rates, controls and prospects for carbon neutral mining; *Journal of Greenhouse Gas Control*, v. 25, p. 121–140.
- WMC Resources Ltd. (2002): WMC Resources Ltd Sustainability Report 2002; WMC Resources Ltd., URL <<https://www.bhp.com/-/media/bhp/documents/investors/reports/2002/wmcsustainability2002.pdf?la=en>> [November 2018].
- Worrell, E., Price, L., Martin, N., Hendriks, C. and Meida, L.O. (2001): Carbon dioxide emissions from the global cement industry; *Annual Review of Energy and the Environment*, v. 26, p. 303–329, URL <<https://doi.org/10.1146/annurev.energy.26.1.303>> [November 2018].



Geoscience BC

t: 604 662 4147

e: info@geosciencebc.com

SUITE 1101-750 WEST PENDER ST
VANCOUVER, BC V6C 2T7

www.geosciencebc.com